

REMOBILIZATION AND PRIMARY URANIUM GENESIS
IN THE DAMARAN OROGENIC BELT, NAMIBIA.

by

ALAN GERALD MARLOW, M.Sc.

Submitted in fulfilment of the requirements for
the Degree of Doctor of Philosophy

Department of Earth Sciences,
The University of Leeds.

September, 1981.

ABSTRACT

The Damaran belt in Namibia represents a highly eroded orogenic area, the root zone of which is exposed between Swakopmund on the coast and Karibib in the west. Primary uranium deposits located in these structurally lower regions of the orogen, have been studied in an attempt to assess the importance of geological processes associated with remobilization in the genesis of the uraniumiferous Damaran granitoids.

The pre-Damaran basement consists of a sequence of up to 1600m of shallow water clastic and carbonate rocks with interbedded meta-basaltic and pyroclastic horizons. The 'meta-basalts' range in composition from basalt to andesite, and are characterized by chemical features diagnostic of a tholeiitic, and in some cases komatiitic affinity. This sequence, previously assigned to the Abbabis Formation, is intruded locally by 2.0 Ga gneisses which range in composition from diorites, through granodiorites to alkali-rich granites. Pb-isotope ratios of sulphides from the basement and the Damaran metasedimentary cover indicate that the basement was enriched in U/Pb at 1.7 Ga, and that the Damaran uranium province has been in existence for at least 1.7 Ga.

The Damara Sequence consists of a lower Nosib Group and an upper Swakop Group. The former consists of fluvial clastics (Etusis Formation), followed by shallow-water calcareous, feldspathic sandstones (Khan Formation). Uranium minerals, in the form of uranyl silicate inclusions, found within detrital constituents of the Etusis quartzites, provide direct evidence of radioactive material within the pre-Damaran basement prior to its erosion, transportation and deposition within the

Damara Sequence. The Swakop Group represents a typical geosynclinal sequence starting with carbonates, quartzites, conglomerates and pelites (Rössing Formation); followed by mixtites (Chuos Formation) and a dominantly calcareous succession (Karibib Formation); and ending with a monotonous series of biotite schists (Kuseb Formation). Primary uranium minerals including uraninite and betafite located within schists and calc silicates of the Rössing Formation are considered to have recrystallized during the Damaran metamorphism from syngenetic uranium associated with stratabound copper deposits.

The Damaran belt underwent regional deformation between about 650 and 550 Ma, and although early mafic granitoids were emplaced locally, the major granite forming event post-dates the major regional deformation. Between 540 and 460 Ma dome structures were developed by a process involving diapirism and the upward movement and subsequent ballooning of large volumes of granitic material. The Damaran granitoids may be broadly divided into syn- to post-tectonic Salem type granites and red granites, and late- to post-tectonic leucogranites and alaskites. Field relationships indicate that the Salem type granites are derived from a source deeper than the Damara Sequence, whilst the alaskites appear to be derived from migmatized basement and Damaran metasedimentary cover rocks.

The earlier Damaran granitoids, which tend to be more mafic in character, show relatively low Sr-isotope ratios and contain chemical and mineralogical features in common with I-type granitoids. These various factors are considered to reflect derivation from the lower crust or upper mantle. In contrast the later granitoids are normally leucocratic in nature, commonly radioactive and occasionally mineralized.

They display relatively high Sr-isotope ratios, and an affinity with S-type granitoids, and they are considered to be derived from basement and Nosib source rocks.

The mineralized alaskites contain primary uranium minerals including uraninite, betafite and metamict thorite which crystallized from melts enriched in U and Th. Primary mineralizations are not restricted to alaskites, but also occur within red granites. Secondary uranium minerals within the mineralized Damaran granitoids include uranyl silicate, thorogummite, calciothorite, ferrothorite and uranophane. These minerals formed during a deuteritic stage of alteration, and also during a recent stage of surface enrichment and secondary alteration.

Dedicated to Hans Breytenbach

ACKNOWLEDGEMENTS

Foremost, I would like to express my sincere thanks to C. Hawkesworth and M. Coward, firstly for initiating this project and secondly for their enthusiastic supervision both in the field and the laboratory. Special thanks also go to G. Hornung for his help throughout the period of research.

I would like to thank the following mining companies for permission to work within their concessions. Anglo American Corp. of S.W.A., Falconbridge of S.W.A., General Mining and Finance Corp. of S.W.A., Goldfields of S.W.A., Trust and Mining Company Ltd. and Rössing Uranium Ltd. Without this permission the work would not have been done, and their help and logistical support is gratefully acknowledged. I would also like to express my gratitude to the geologists and prospectors who assisted me in the field, in particular A. Ransom, R. Miller, B. Fletcher, J. Hartleb, R. Corrans, H. Versfeld and H. Breytenbach.

My thanks go to the people in Leeds for their invaluable discussions and criticisms, in particular to J. Kramers, A. Gray, E. Condliffe, P. Ruxton, K. Downing, J. Barnes, M. Powell, R. Cliff, P. Nixon and F. Johnston. Many thanks also to my mother, P. Marlow for helping with the diagrams.

I am grateful to those at the Open University responsible for providing me with unpublished geochemical data.

Finally, I acknowledge the financial support provided by Trust and Mining Company Ltd., and N.E.R.C.

DEFINITION OF NOTATIONS AND ABBREVIATIONS

X, Y, Z	are the three mutually perpendicular axes of the strain ellipsoid where $X \geq Y \geq Z$.
L	lineation
S	schistosity
n	no. of measurements
P.P.L.	plane polarised light
XN	crossed nicols
B.E.I.	back scattered electron image
X.R.F.	X-ray fluorescence spectrometry
L.O.I.	loss on ignition
Fe_2O_3 (t)	total Fe as Fe_2O_3
λ_{Rb}	decay constant for Rb = $1.42 \times 10^{-11} \text{ yr}^{-1}$
M.S.W.D.	mean square weighted deviate
$(^{87}\text{Sr}/^{86}\text{Sr})_0$	initial $^{87}\text{Sr}/^{86}\text{Sr}$
R.E.E.	rare earth elements

CONTENTS

	<u>Page No.</u>
ABSTRACT	i
DEDICATION	iv
ACKNOWLEDGEMENTS	v
DEFINITION OF NOTATIONS AND ABBREVIATIONS	vi
CONTENTS	vii
CHAPTER I. INTRODUCTION	1
I.1. Preliminary discussion	1
I.2. Location	2
I.3. Previous work	5
I.4. The aim of the study	6
I.5. Details of the field study	7
I.6. Physiography	8
CHAPTER II. THE GEOLOGY OF THE PRE-DAMARAN BASEMENT	9
II.1. Introduction	9
II.2. The metasedimentary, metavolcanic and pyroclastic sequences of the Abbabis Formation	10
(i) The quartzites	12
(ii) The schists	14
(iii) The conglomerates	16
(iv) The marbles and calc silicates	16
(v) The meta-basalts and pyroclastic rocks	17
(vi) Sulphide mineralization	21
(vii) Geochemistry of the basalts	22
(vii) A. Major element chemistry	23
(vii) B. Trace element chemistry	28
II.3. The gneisses of the Abbabis Formation	31
(i) The granodioritic gneiss	33
(ii) The leucocratic gneiss and augen gneisses	33
(iii) Geochemistry of the Abbabis gneisses	35
II.4. The amphibolite dykes	37
II.5. Conclusions	39
CHAPTER III. THE GEOLOGY OF THE DAMARA SEQUENCE	40
III.1. Introduction	40
III.2. The Damara Sequence	42

		<u>Page No.</u>
	(i) The Etusis Formation	42
	(ii) The Khan Formation	44
	(iii) The Rössing Formation	45
	(iv) The Chuos Formation	49
	(v) The Karibib Formation	52
	(vi) The Kuiseb Formation	54
III.3.	Conclusions	56
CHAPTER IV.	THE GEOLOGY OF THE DAMARAN INTRUSIVES	58
IV.1.	Introduction	58
IV.2.	The Salem type granites	59
IV.3.	The red granites	62
IV.4.	The leucogranites	68
IV.5.	The alaskites	72
IV.6.	The gabbros	74
IV.7.	Conclusions	78
CHAPTER V.	STRUCTURAL EVOLUTION	80
V.1.	Introduction	80
V.2.	Structural evolution of the Valencia area	81
V.3.	Structural evolution of the Goanikontes area	88
V.4.	Structural evolution of part of the Abbabis inlier	94
V.5.	Structural evolution of the Stinkbank-Namibfontein area	99
V.6.	Structural evolution of the Otjua area	101
V.7.	Regional correlations	104
V.8.	Conclusions	106
CHAPTER VI.	URANIUM MINERALIZATION IN THE DAMARAN BELT	108
VI.1.	Introduction	108
VI.2.	Uranium in the pre-Damaran basement	109
VI.3.	Uranium in the Damara Sequence	113
	(i) Uranium in the Etusis Formation	113
	(ii) Uranium in the Khan Formation	115
	(iii) Uranium in the Rössing Formation	116
VI.4.	Uranium in the Damaran intrusives	121
	(i) The radioactive Salem granites	122
	(ii) The radioactive red granites	125
	(iii) The radioactive leucogranites	131
	(iv) The radioactive alaskites	132
	(iv) A. The primary uranium minerals in the alaskites	133
	B. The secondary uranium minerals in the alaskites	140
VI. 5.	Conclusions	147

	<u>Page No.</u>	
CHAPTER VII	CHEMISTRY OF THE URANIUM MINERALS	151
VII.1.	Introduction	151
VII.2.	Uraninite	152
VII.3.	Betafite	154
VII.4.	Metamict thorite	157
VII.5.	Uranyl silicate	159
VII.6.	Thorogummite	162
VII.7.	Uranophane	163
VII.8.	Conclusions	165
CHAPTER VIII	GEOCHRONOLOGY	166
VIII.1.	Introduction	166
VIII.2.	Rb/Sr results	168
	(i) Abbabis gneiss	171
	(ii) Stinkbank Salem granite	172
	(iii) Otjua red granite	172
	(iv) Stinkbank leucogranite	174
	(v) Ida dome alaskite	174
	(vi) Goanikontes alaskite	175
	(vii) Valencia alaskite	180
	(viii) Discussion	182
VIII.3.	Pb/Pb results	184
	(i) U-Pb systematics	189
	(ii) Th-Pb systematics	196
VIII.4.	Conclusions	198
CHAPTER IX	GEOCHEMISTRY	201
IX.1.	Introduction	201
IX.2.	Geochemical characteristics of the Damaran granitoids	203
IX.3.	Discussion	214
IX.4.	Conclusions	223
CHAPTER X	EVOLUTION OF THE DAMARAN URANIUM PROVINCE	225
REFERENCES		236
APPENDIX 1.	ANALYTICAL TECHNIQUES AND LABORATORY PROCEDURES	248
APPENDIX 2.	CONTOUR FIGURES FOR THE STEREOGRAMS SHOWN IN FIGURES 15, 17, 18, 19 AND 20.	257
APPENDIX 3.	PARTIAL ANALYSES OF THE URANIUM MINERALS	258
APPENDIX 4.	Rb/Sr WHOLE-ROCK ANALYTICAL RESULTS	267
APPENDIX 5.	MAJOR AND TRACE ELEMENT ANALYSES AND NORMATIVE COMPOSITIONS	272

- FOLDER 1. GEOLOGICAL MAP OF PART OF THE ABBABIS INLIER
- FOLDER 2. GEOLOGICAL MAP OF PART OF OTJUA 37
- FOLDER 3. GEOLOGICAL MAP OF THE GOANIKONTES AREA
- FOLDER 4. GEOLOGICAL MAP OF PART OF VALENCIA 122
- FOLDER 5. GEOLOGICAL MAP OF PARTS OF NAMIBFONTEIN 91 AND
STINKBANK 62.

CHAPTER I

INTRODUCTION

1.1. Preliminary discussion

During the evolution of an orogenic belt rocks are formed by the addition of new material from the mantle and by remobilization of pre-existing crust by erosion and sedimentation, metamorphism, deformation and magmatism. The products of these processes have all been recognized within the intra-cratonic branch of the Damaran orogen, and it is the subject of this thesis to assess the role played by remobilization in the genesis of primary uranium deposits which occur within the high temperature portion of the Damaran orogenic belt in Namibia.

The genesis of uranium enriched granites is currently discussed in terms of two opposing hypotheses. The first involves the concentration of uranium in anatectic melts formed by remobilization of pre-existing basement, in areas of thickened sialic crust (Moreau, 1976; Beckinsale et al., 1979). The alternative hypothesis is that metalliferous granitoids are generated directly from the mantle or from deep crustal levels, and are subsequently enriched in uranium and associated metals by hydrothermal processes involving the redistribution of uranium in meteoric fluids (Stemprok, 1963, 1979; Simpson et al., 1979; Plant et al., 1980). However, it is highly likely that both models are represented by real examples, and as proposed by Rogers et al. (1978) the two hypotheses probably correspond to ideal end members of most granitic uranium deposits.

The Damaran orogenic belt of Namibia belongs to the widespread

tectonothermal event first designated as Pan-African by Kennedy (1964). It consists of two branches: the first trending sub-parallel to the present coast-line from southern Angola to southwestern Namibia where a probable link with the Gariep belt has been established (Kröner and Jackson, 1974; Kröner and Hawkesworth, 1977; Kröner, 1981; Davies and Coward, 1981); and the second trending NE-SW forming the intra-cratonic branch. The coastal branch and the intra-cratonic branch constitute an orogenic triple junction (Coward, 1981a), and together with the Ribeira belt of Brazil and Uruguay they form a major Damara-Ribeira orogen which developed during the contemporaneous Pan-African and Brasiliano cycles (Porada, 1979). The main intra-cratonic Damaran branch extends across the territory of Namibia from Swakopmund on the coast to the Botswanan border, where it is largely obscured by younger rocks (Fig. 1). It is bounded by the Congo craton in the N, and by the Kalahari craton in the S; and the rock sequences within the belt constitute a typical geosynclinal assemblage which has been grouped lithostratigraphically into the Damara Sequence (S.A.C.S., 1980).

1.2. Location

The area investigated lies within the central portion of the Damaran belt between Swakopmund and Karibib. It forms the northern fringe of the Namib Desert and is bounded roughly by latitudes 22° and 23° south, and by the coast and longitude 16° east. Detailed geological mapping was undertaken in five separate parts of this area, and their location within the Damaran belt is shown on the simplified geological map (Fig. 2). Mapping was performed with the aid of aerial photographs,

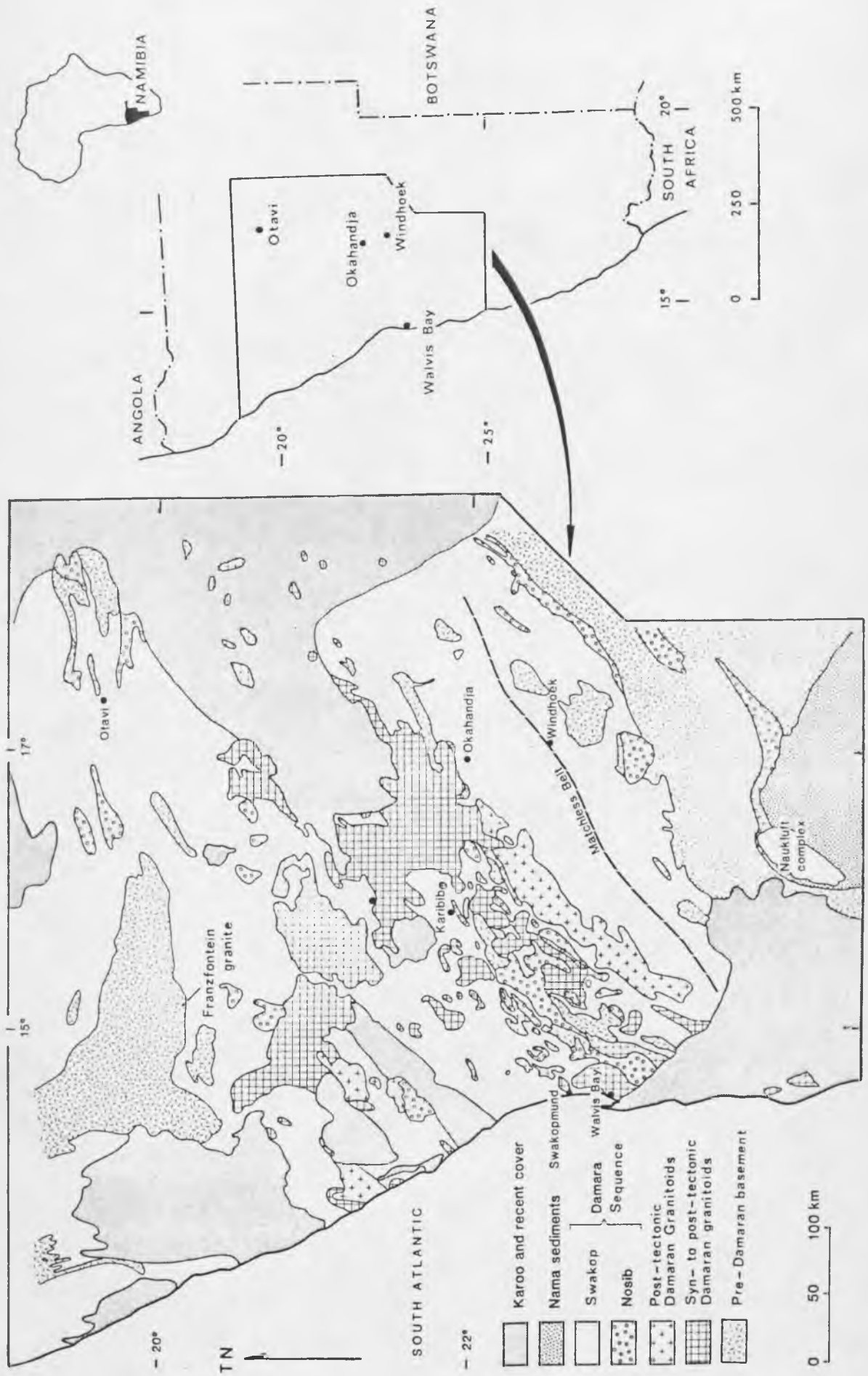


Fig. 1. Location and simplified geology of the intra-cratonic branch of the Damaran belt in Namibia.

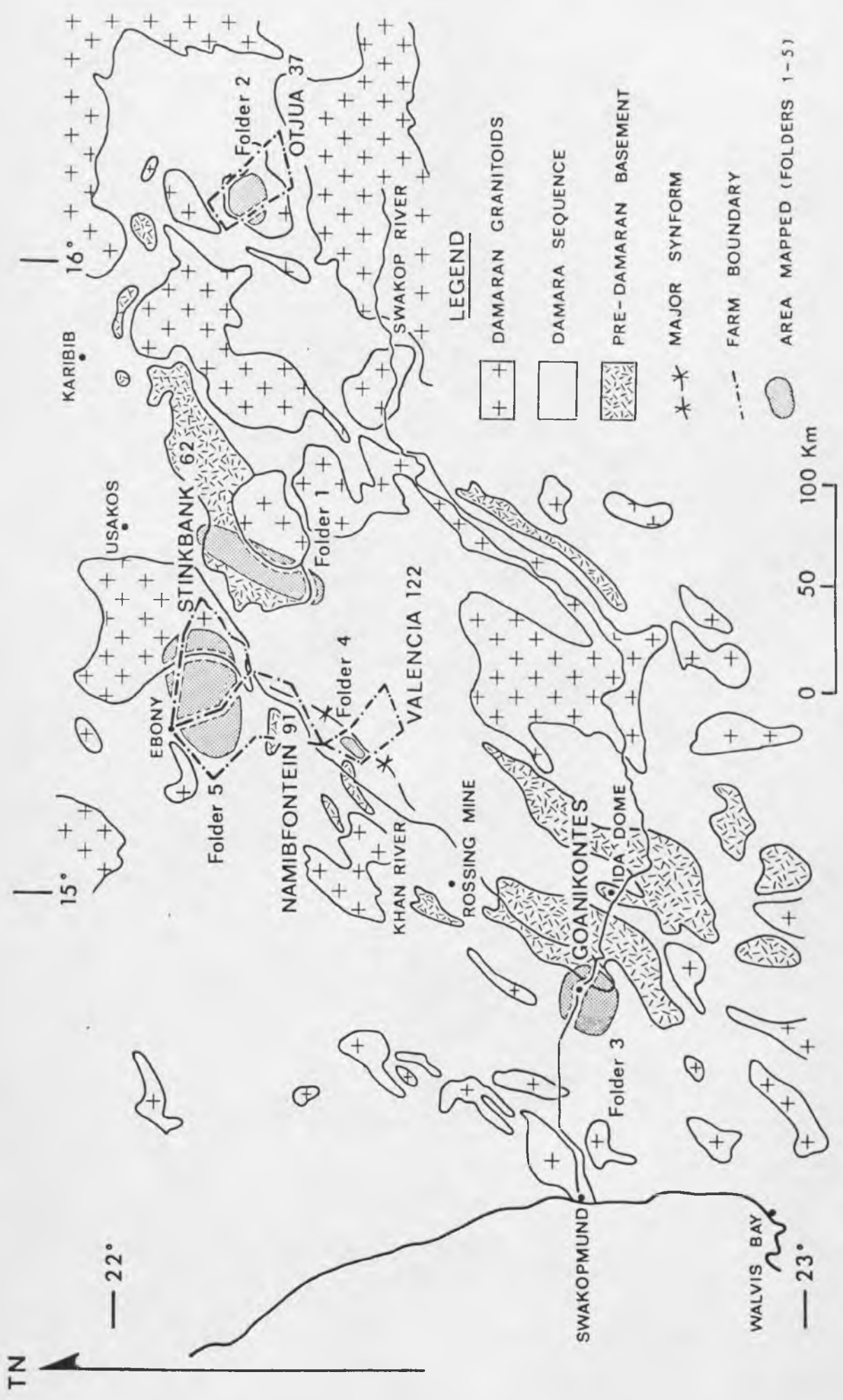


Fig. 2. Simplified geological map of the central portion of the Damaran belt, illustrating the location of areas mapped in detail.

and geological maps were compiled from uncontrolled print layoffs of the appropriate photographs. The maps are presented in Folders 1 to 5, and the farms and approximate areas covered by the maps, as well as the numbers of the aerial photographs used, are given in Table 1.

Table 1. Details relating to the geological maps presented in

Folders 1 to 5

<u>Folder No.</u>	<u>Farms covered</u>	<u>Approximate area mapped</u>	<u>Scale of mapping</u>	<u>Photograph Nos.</u>	<u>Strip Nos.</u>	<u>Job No.</u>
1.	Naob 69, Ubib 76, Tsawisis 16 and Tsawisis Suid 95.	95 sq. km	1:50,000	5325, 5360, 5362 and 4550	13, 14 and 15	760
2.	Otjua 37	30 sq. km	1:25,000	0656 (x 2 enlargement)	7	578
3.	Goanikontes 40	sq. km	1:25,000	4840 (x 2 enlargement)	21	760
4.	Valencia 122	6 sq. km	1:10,000	028 and 030	13 (in-house job)	
5.	Namibfontein 91, Stinkbank 62 and Lukasbank 63.	120 sq. km	1:42,000	6796, 6794, 6792 and 7177	6 and 7	596

1.3. Previous work

Large parts of the central portion of the Damaran belt have previously been mapped by Smith (1966) and Jacob (1974a) at scales of 1:125,000 and 1:100,000, respectively. Smaller areas have been investigated by Barnes (1981) and Downing (in prep.), who have undertaken detailed mapping in regions bordering the lower Swakop River. Previous studies relating to structural, petrological and geochemical aspects of

the Damaran belt will be discussed in the introductory sections to the following chapters.

The source of the uranium mineralization in the alaskites was first discussed by Jacob (1974b) who considered that during the Damaran metamorphism uraniumiferous anatectic melts were derived from a group of rocks he designated 'red granite-gneiss'. This group consists of rocks from both the pre-Damaran basement, and the Nosib Group which represents the lower part of the Damara Sequence. Berning et al. (1976) were also of the opinion that the alaskites were derived by anatexis, but they considered the basement rocks to represent the source of the protore. Jacob and Hambleton-Jones (1977) state that the uraniumiferous granitic melts were produced through mobilization of radioactive basement, and possibly also through anatexis of the Damara Sequence. Although these hypotheses may be quite sound, they need to be justified by further geological evidence, and the purpose of this work is to test the hypotheses by a multi-disciplinary approach involving the assessment of structural, petrological, geochemical and isotopic data.

1.4. The aim of the study

The Damaran belt represents a highly eroded orogenic area, the root zone of which lies within the central portion of the belt between Swakopmund and Karibib. Exposures in this region are good, particularly in the areas occupied by gorges of the Khan and Swakop Rivers, and therefore the Damaran belt offers an ideal opportunity for studying the structurally lower regions of an orogenic belt. The aim of this study therefore was to assess the importance of geological processes associated with remobilization in the genesis of the uraniumiferous Damaran

granitoids exposed in the root zone of the Damaran belt.

With the exception of certain parts of Stinkbank 62 and Namibfontein 91, exposures within the detailed study areas are excellent. The aim of the mapping in the region occupied by the farms Naob 69, Ubib 76, Tsawisis 16 and Tsawisis Suid 95 (Folder 1) was to establish a stratigraphic succession for the pre-Damaran metasedimentary rocks assigned to the Abbabis Formation (Gevers, 1931). The Goanikontes and Valencia areas (Folders 3 and 4, respectively) represent regions where mining companies are actively exploring mineralized alaskites, and the two areas were selected for detailed mapping in an attempt to determine the source of the uranium mineralization within the alaskites. Since the radioactive anomalies are not restricted to the alaskites, two further areas were mapped where other radioactive Damaran granitoids are exposed. These regions have also been investigated by mining companies, and include a portion of Otjua 37 (Folder 2) as well as parts of Stinkbank 62 and Namibfontein 91 (Folder 5).

1.5. Details of the field study

The fieldwork was undertaken during two separate field seasons, the first in 1978 during the months August through to October, and the second in 1979 during the months May through to October. During the course of the field studies, excursions were made with the following prospectors and geologists: H. Bachran, H. Breytenbach, M.P. Coward, C.J. Hawkesworth, P. Ruxton, K. Downing, J.F.H. Barnes, H. Clemmey, A. Ransom, R. McG. Miller, B. Fletcher, J. Hartleb, R. Corrans, H. Versfeld and T. Richards, and their assistance is gratefully acknowledged.

A front-wheel drive vehicle was used for transport, and financial

assistance during the course of the fieldwork was provided by N.E.R.C. In certain areas field accommodation was made available by Anglo American Corp. of S.W.A., General Mining and Finance Corp. of S.W.A., Goldfields of S.W.A., Trust and Mining Company Ltd., and Rössing Uranium Ltd.

1.6. Physiography

The average rainfall along the northern margins of the Namib desert varies between about 15mm/year on the coast and about 150mm/year around Karibib, and the rain falls mainly within the summer months between November and March. The temperatures in the interior are high, especially within the deeper gorges, but on the coast thick fogs generated by the cold off-shore Benguella Current produce cool, damp climates. Night temperatures are variable depending upon the season, but they may fall below freezing point during the winter months of May and June.

Vegetation over most of this region is minimal, consisting of low shrub and grass, and sheep rearing, particularly caracul farming, is the principal occupation of the local inhabitants. The Namib plains are modified by rivers such as the Khan and Swakop (Fig. 2), which may be incised to a depth of over 150m. They are sand filled, but the walls of the gorges frequently provide spectacular two-dimensional exposures.

CHAPTER II

THE GEOLOGY OF THE PRE DAMARAN BASEMENT

II.1. Introduction

The rocks comprising the Abbabis Inlier were initially recognized and named by Gevers (1931), and subsequently mapped to a scale of 1:125,000 by Smith (1966). Smith (1965) divided the rocks of the Abbabis Formation into dolomitic marble and calc silicate rocks; biotite schist; orthoamphibolite and Abbabis gneiss. These units were shown in their correct stratigraphic order on the published geological map (Smith, 1966) with the Abbabis gneisses-post dating the metasediment and ortho-amphibolite of the Abbabis Formation. However, during the discussion of these rock units (Smith, 1965), the Abbabis gneiss and the biotite schist were taken to represent the bottom and top of the succession respectively, and the orthoamphibolites were considered to be basic intrusives which transgressed the other rock units.

The Abbabis Inlier, measuring approximately 40 x 10km represents the largest outcrop of pre-Damaran rocks exposed within the N.E. trending arm of the Damaran geosyncline. The distribution of basement rocks within the Damaran belt is shown in Fig. 2. Much of the inlier is poorly exposed, but a N.E trending zone which runs across the centre of the inlier between the Gamgamchab Mountain in the N. and the Chuos Mountains in the S. is better exposed, and in places forms very prominent topography such as the Klein Chuos Mountain. Smith's (1966) map shows this zone to be dominated by biotite schist and gneiss, but also to include outcrops of his dolomitic marble and orth-amphibolite units.

Since the geology of the basement rocks was relatively little understood compared with that of the Damaran rocks, the well exposed zone of the Abbabis Inlier described above was mapped to a scale of 1:50,000 (Folder 1). A simplified geological map of this part of the Abbabis inlier is shown in Fig. 3. The aim of the mapping was to establish a stratigraphic succession for the metasedimentary rocks within the Abbabis Formation, as well as to define the chronology of the Abbabis gneisses relative to the rest of the pre-Damaran rocks. The mapped zone is approximately 20km in length, and is well exposed along its northern and southern contacts where overlain by the Damara Sequence.

Mapping of this zone indicates the pre-Damaran rocks may be divided into an older metasedimentary, volcanic and pyroclastic sequence, and a younger series of gneisses. The former are described below under the heading of "the metasedimentary, metavolcanic and pyroclastic sequences of the Abbabis Formation", whilst the latter are described under the heading of "the Abbabis gneisses".

II.2. The metasedimentary, metavolcanic and pyroclastic sequences of the Abbabis Formation

The sequence consists of up to 1600m of quartzites, schists, conglomerates, calc silicates and marbles, with interbedded meta-basaltic and pyroclastic horizons, which outcrop in a N.E. trending belt either side of the Usakos-Nordenburg road (Folder 1, H4). The regional distribution of the main penetrative fabric within these rocks, as well as their overall outcrop pattern indicate the area has undergone at least two major phases of deformation, and the extent to which tectonic thickening has increased the measured thickness is not clear.

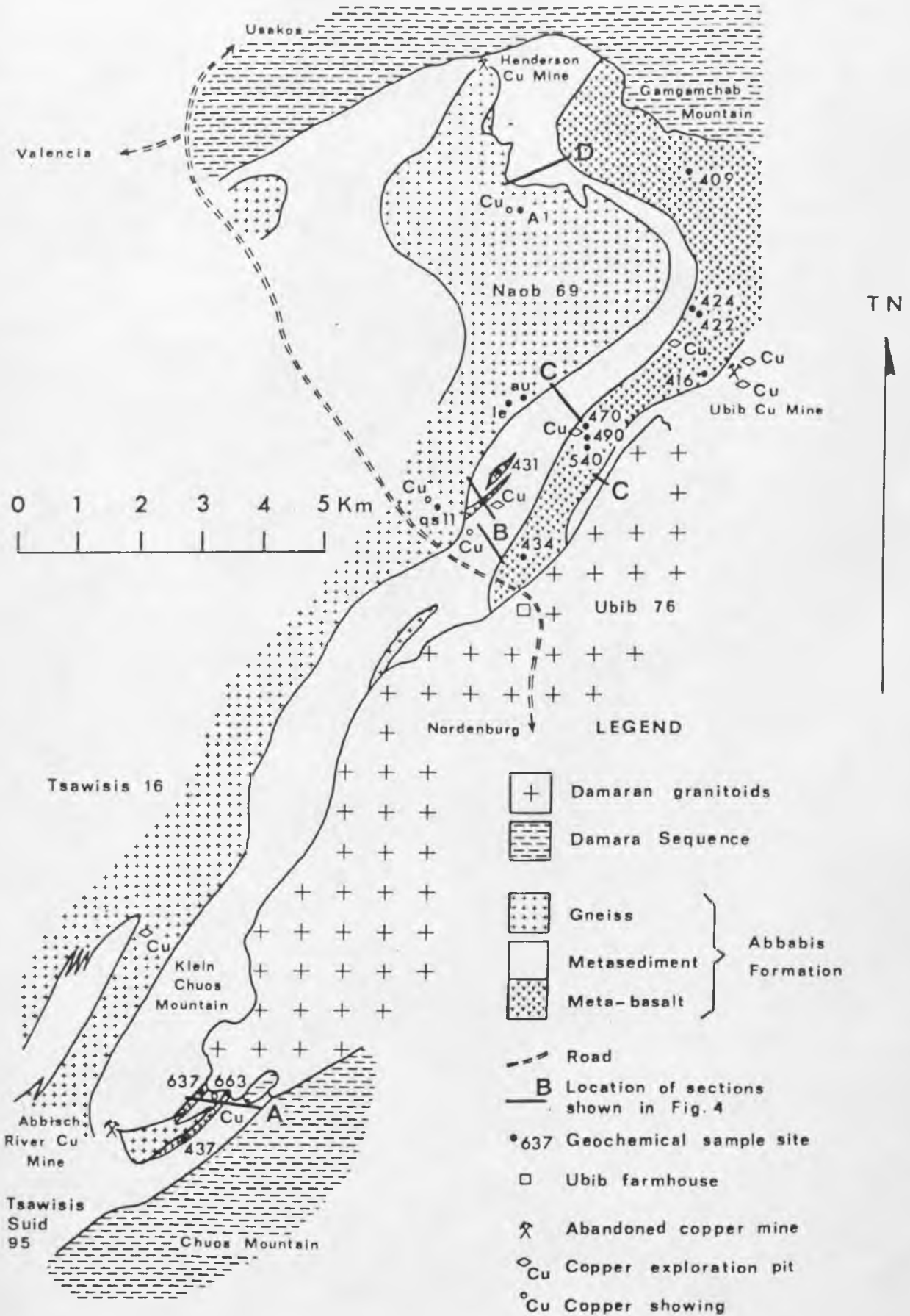


Fig. 3. Simplified, geological map of part of the Abbabis inlier, showing the location of the mineralization, measured sections and geochemical samples.

The age of this group of rocks is unknown. Locally they are intruded by the Abbabis gneisses which give ages of around 2 Ga, but it is not known whether they form part of the same chelogenic cycle as the gneisses, or whether they were deposited during a much earlier stage in the evolution of the southern African continent.

The sequence is characterised by both vertical and lateral variations in lithology, illustrated by the four measured sections in Fig. 4, whose locations are shown on the simplified geological map of part of the Abbabis Inlier (Fig. 3).

(i) The quartzites

The quartzites are restricted to those parts of the meta-sedimentary succession directly associated with the volcanic and pyroclastic sequences, and are totally absent elsewhere. They are better developed on Naob 69 in the N.E., and they thin towards the S.W. where on Sawisis Suid 95 they reach maximum thicknesses of only a few metres.

The quartzites range from fine to coarse grained, and may locally be trough X-stratified (Fig. 4, Section C), consistently indicating way-up towards the N.W. The most prominent quartzite unit occurs directly above the volcanic sequence on Naob 69 reaching a maximum thickness of approximately 35m (Folder 1, 6-4). It has a lateral extent of about 12km and over most of this length consists of coarse grained, slightly feldspathic quartzite, but in the vicinity of the Usakos-Nordenburg road it grades into a fine grained, impure quartzite.

Mineralogically the quartzites consist of an interlocking mosaic of recrystallized quartz, orthoclase and plagioclase with interstitial muscovite, biotite, garnet, sillimanite, magnetite, sphene, hornblende, epidote, chlorite and calcite, and accessory zircon and apatite. The

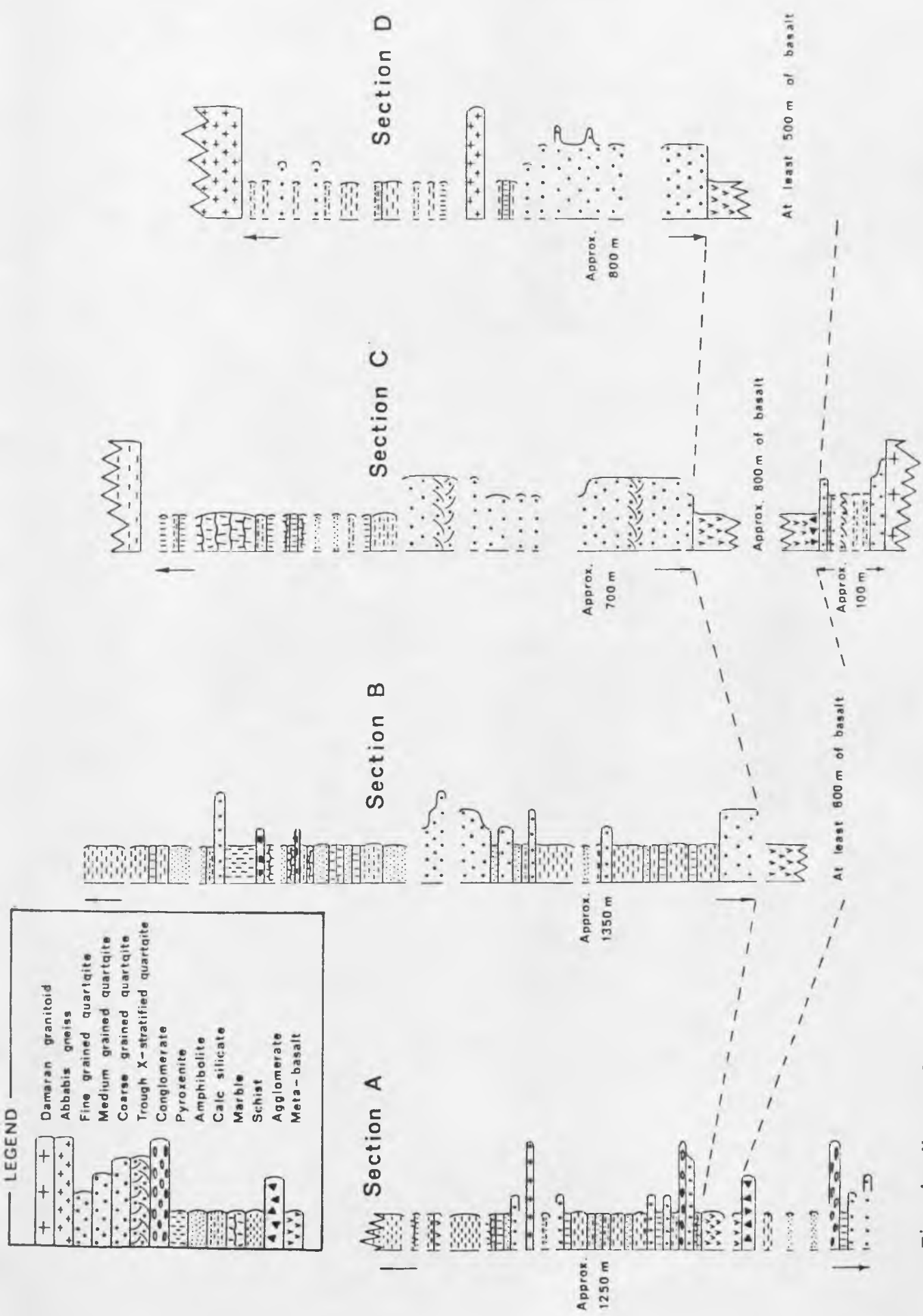


Fig. 4. Measured sections of the metasedimentary, metavolcanic and pyroclastic sequences over part of the Abbas inlier. For locations of sections see Fig. 3.

quartz grains commonly display triple junctions, and may contain inclusions of biotite, plagioclase, muscovite, orthoclase, Fe-oxide, apatite, sphene and zircon. The feldspars are commonly sericitized, saussuritized and calcitized. The magnetite porphyroblasts in the prominent quartzite described above, reach a maximum size of 7mm in a major tributary of the Naob River (Folder 1, F2), whilst tourmaline crystals in a quartzite band in contact with a Damaran granitoid (Folder 1, H3) are probably the result of crystallization from hydrothermal solutions associated with this granite.

Opaque Fe-oxides occur as large interlocking grains, as interstitial grains or as inclusions along mica cleavage planes. The muscovite may be present as interstitial prismatic grains, as alteration products after biotite, or as poikiloblasts which occasionally show partial retrogression to chlorite. The biotite which is commonly partially or totally altered to chlorite and muscovite, occurs mainly as prismatic interstitial grains, but may also be present as reaction rims around the Fe-oxides. When present the hornblende is prismatic and interstitial, whilst the sphene occurs as inclusions within quartz or as clusters of small rounded grains. Accessory zircon and apatite occur as rounded, interstitial grains or as subhedral to euhedral inclusions in quartz.

(ii) The schists

The schists form the dominant rock type within the meta-sedimentary succession, and although they may be extremely variable in their mineralogy within the portion of the metasedimentary sequence associated with the volcanics and pyroclastics, they form a monotonous series of biotite-, garnet- and sillimanite-bearing schists elsewhere in the

area. These rocks consist of a recrystallized mosaic of quartz and orthoclase, containing pre-tectonic garnet and post-tectonic biotite and sillimanite, with accessory Fe-oxide. The garnet grains form clusters of subhedral grains separated by thin chlorite skins, which are drawn out in the direction of the main penetrative fabric, whilst the sillimanite forms radiating bundles of needles, and the biotite forms randomly oriented prisms which show slight alteration to chlorite and muscovite. Smith (1965) described the mineralogical and textural characteristics of these rocks, and concluded that the mineral assemblage is indicative of high-pressure and high-temperature metamorphism.

Schistose rocks within the metasedimentary sequence associated with the volcanics and pyroclastics may contain metamorphic hornblende, diopside, enstatite, rutile, magnetite, muscovite and tourmaline as well as garnet, sillimanite and biotite. The assemblage diopside, tremolite and Fe-oxide is common, as is the muscovite, magnetite and biotite assemblage. Within the former the diopside forms pre-tectonic, slightly muscovitized prismatic grains, whilst the tremolite forms pre-tectonic, zoned porphyroblasts containing dense clouds of minute Fe-oxide inclusions. Within the latter assemblage the pre-tectonic muscovite and magnetite form trains which parallel the fabric, whilst the large post-tectonic biotite prisms cut across the fabric. The tourmaline forms slate-blue grains in thin section, which are commonly nucleated along a muscovite-biotite interface,

Rose coloured, zoned porphyroblasts of beryl which commonly reach 3cm in length, are present within the sillimanite-, biotite- and muscovite-bearing schists which outcrop just N.E. of the Usakos-Nordenburg road on Naob 69 (Folder 1, J5).

(iii) The conglomerates

The conglomerates are not common, but occur in association with quartzites and are occasionally well developed as on Tsawisis Suid 95 (Fig. 4, Section A and Folder 1, S9), where a deposit measures a few metres in thickness and some tens of metres in strike length. Pebbles which vary in size from small to over 15cm and which may be angular or rounded, consist predominantly of quartzite, and to a lesser extent of fine grained amphibolite. The pebbles are moderately packed in a fine grained, epidotized, feldspar-, garnet-, pyroxene- and ilmenite-bearing siliceous matrix, containing epidote-, garnet- and quartz-bearing skarn. Approximately 250m to the N.W. of the conglomerate, a boulder bed of similar dimensions is developed. The boulders which are scarce and which vary in size from 2 to 25cm consist of medium grained, biotite-bearing granite and vein quartz. The matrix consists of biotite schist which intercalates with fine grained, biotite-bearing, quartzite.

(iv) The marbles and calc silicates

The marble and calc silicate units like the quartzite units, are restricted to that part of the metasedimentary succession associated with the volcanics and pyroclastics. The marble and calc silicate bands reach maximum thicknesses of approximately 60 and 20m respectively, along the measured Section C (Fig. 4), but they are normally only a few metres thick and their lateral extent rarely exceeds 1km. The calc silicates display a range in grain size, and a vertically bedded unit a few metres thick on Ubib 76 (Folder 1, G4) shows a coarsening to the N.W., which may represent graded bedding. This is in accordance with younging directions to the N.W. defined by trough X-stratification within the quartzites.

Smith (1965) recognized these rocks on Tsawisis 16 and Tsawisis Suid 95, and described yellow-brown dolomitic marbles consisting of dolomite and calcite with accessory graphite, tremolite, forsterite and epidote, and calc silicate bands consisting of quartz, plagioclase and diopside with accessory garnet, sphene and epidote.

(v) The meta-basalts and pyroclastic rocks

These rocks outcrop over a strike length of at least 12km on Naob 69 and Ubib 76, as well as for a further 2km on Tsawisis Suid 95, and although the sequence is very restricted in thickness in the S. compared with that in the N., it is very likely to have been continuous prior to the emplacement of the Damaran granitoids which now separate the two areas. The maximum thickness of the main meta-basaltic unit is about 1km N.W. of the Ubib mine on Naob 69 (Folder 1, F2). Smith (1966) mapped these rocks as orthoamphibolites, but recognized only two narrow bands; one in the Naob River on Naob 69, and a second on Ubib 76 in the vicinity of the Usakos-Nordenburg road. In the discussion of these rocks Smith (1965) confused them with basic intrusives which transgress all the other pre-Damaran formations, even though he recognized their concordant nature and their amygdaloidal texture.

As well as forming one large unit, the meta-basalts also outcrop to the N. and W. of the main outcrop, forming units a few tens of metres in thickness on Naob 69 (Folder 1, B5, H5 and I5), and Tsawisis Suid 95 (S10). The pyroclastics occur interlayered within that part of the metasedimentary sequence occupied by the quartzites, conglomerates, calc silicates and marbles, and they reach maximum thicknesses of about 5m. Two well developed agglomerates occur about 1km N.E. of the Usakos-

Nordenburg road on Naob 69 (Section B, Fig. 4 and Folder 1, I5), whilst on Tsawisis Suid 95 an agglomerate unit occurs directly to the S.E. of a narrow sequence of meta-basalts in the Abbisch River (Fig. 4, Section A and Folder 1, S9).

The meta-basalts display pillow structures in the vicinity of the Naob-Ubib farm boundary (Plate 1), and the absence of pillows throughout the rest of the outcrop may be due to their obliteration by the Damaran tectonism, which has resulted in vertical to subvertical penetrative fabrics and strong steeply plunging lineations within most of the meta-basalt units. The basalts are normally amygdaloidal (Plate 2) the amygdales being filled with quartz and epidote, and they show varying degrees of alteration to epidosite. Garnet- and epidote-bearing skarns are also widespread within the meta-basalts and very well developed boudinaged garnet "cigars" have formed within the skarns which have undergone prolate deformation (Plate 3).

The pyroclastics consist of agglomerate units which show a variety of clast types and sizes, but the clasts are normally angular in shape and commonly elongated and rotated into conformity with the regional fabric by the Damaran deformation (plate 4). Clast types include ilmenite- and pyroxene-bearing calc silicate; pyroxenite; quartzofeldspathic gneiss, pyroxene- and hornblende-bearing schist and coarse grained quartzite, and maximum clast sizes of 30cm were recorded within one of the agglomerates on Naob 69. The matrices of the agglomerates consists of pyroxene-, hornblende- and feldspar-bearing, banded, amygdaloidal meta-basalts which also show epidote alteration.

Saussuritization within the meta-basalts has not been complete and pods of fresh basalt varying in size from a few centimetres to a few metres



Plate 1. Amygdaloidal meta-basalt showing a single pillow structure, Naob 69 (Folder 1, H4).



Plate 2. Quartz and epidote filled amygdales in meta-basalt on Naob 69 (Folder 1, H4).



Plate 3. Rotated garnet boudins in skarn within meta-basalts on Naob 69 (Folder 1, C3).

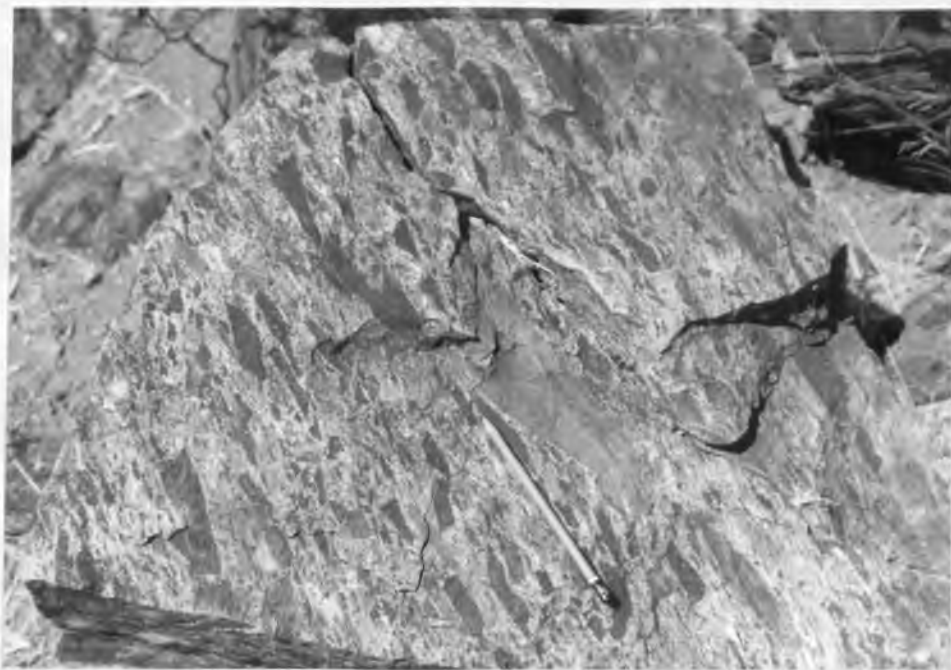


Plate 4. Agglomerate showing elongated, angular clasts which parallel the penetrative fabric, Naob 69 (Folder 1, H5).

may be found throughout most of its outcrop. The fresh basalt consists of a recrystallized mosaic of untwinned plagioclase, low Fe diopside-salite and hornblende with minor interstitial sphene, and large euhedral opaque Fe-oxide grains. Triple points are commonly developed between the three main rock forming minerals, whilst occasionally the diopside-salite show excellent poikiloblastic textures. Sphene occurs as interstitial grains or as metamorphic reaction rims around the Fe-oxides, whilst the accessory minerals may be present in the form of metamorphic interstitial, prismatic muscovite or rutile. Metamorphic recrystallization has resulted in the development of the hornblende at the expense of the diopside-salite and it is probable that little or no hornblende was present within the original basalt prior to metamorphism.

(vi) Sulphide mineralization

Copper mineralization is widespread within the metasedimentary, volcanic and pyroclastic sequences of the pre-Damaran rocks, and considerable quantities of ore were mined from the Henderson, Ubib and Abbisch River mines, probably late in the eighteenth century. The location of the abandoned mines, as well as exploration pits and copper showings are displayed on the simplified geological map (Fig. 3).

The three mines named above all occur within metasedimentary sequences of the pre-Damaran rocks. At the Henderson mine (Folder 1, A5) disseminated chalcopryrite and bornite are present within a band of calc silicate 1-2m in thickness, whilst at the Ubib mine (Folder 1, G1) chalcopryrite is present in quartz veins in a biotite- and sillimanite-bearing schist. At the third mine in the Abbisch River (Folder 1, S11) chalcopryrite occurs as disseminations within biotite- and pyroxene-bearing schists and as joint fillings within biotite- and sillimanite-bearing schists. The former consist of a recrystallized mosaic of quartz,

accessory Fe-oxide, apatite and sulphide with interlocking prismatic biotite and poikilitic tremolite, which are overgrown by radiating needles of enstatite.

Within the meta-basalt sequence chalcopyrite occurs as very minor disseminations within the basalts themselves, and also as minor quantities of massive ore associated with garnet-, epidote- and magnetite-bearing skarns. The two best developed occurrences of mineralized skarn within the meta-basalt unit are marked on Folder 1 (F2 and H4) by abandoned exploration pits.

(vii) Geochemistry of the basalts

An attempt has been made to classify the Abbabis basalts, define their magmatic affinity, and reconstruct the tectonic setting of the magmatic events associated with the deposition of the shallow water clastic and carbonate sequences of the Abbabis Formation. To achieve these aims, twelve samples of basalt were selected from various outcrops of the meta-basalt units (Fig. 3). Eight samples were taken from the main unit on Naob 69 and Ubib 76, one sample was selected from a narrow unit of basalt within the biotite schists on Naob 69, and a further three were taken from the narrow bands on Tsawisis Suid 95. All the samples were free of epidotization and saussuritization, and each weighed approximately 3kg before crushing. The mobility of many major and trace elements during metamorphism and secondary alteration processes must be emphasized however, and although these basalts appear to be unaltered petrologically, the conclusions that follow must be viewed with extreme caution.

The rocks were analysed by X-ray fluorescence spectrometry (X.R.F.) for the major elements as well as nine trace elements, and the major and trace element chemistry of the twelve Abbabis basalts are shown in Tables

2 and 3 respectively. The laboratory procedures and standard analytical conditions used during the X.R.F. analysis are given in Appendix 1.

(vii) A. Major element chemistry

The Abbabis basalts range from basalt to andesite in composition and they are characterized by a low titanium content ($\text{TiO}_2 < 1.2\%$), as well as a low alkali nature ($\text{Na}_2\text{O} + \text{K}_2\text{O} < 2.7\%$). Most basalts belong to one of two major groups, viz., the alkalic and the sub-alkalic (or non-alkalic) basaltic rocks, and the silica vs potash diagram may be used to distinguish between them (Middlemost, 1975). The Abbabis basalts are plotted on such a diagram in Fig. 5 and they fall well within the sub-alkalic fields. Middlemost (1975) has further subdivided the sub-alkalic rocks into tholeiites and high-alumina basalts by plotting alumina vs the alkalic index (A.I.), defined as $(\text{Na}_2\text{O} + \text{K}_2\text{O})/(\text{SiO}_2 - 43) \times 0.17$. All but one of the Abbabis basalts display a tholeiitic character when plotted on the alumina vs alkali index diagram (Fig. 6). To confirm the tholeiitic nature of the suite the samples have been plotted on the A.F.M. diagram (Fig. 7). They fall along a tholeiitic trend which displays Fe enrichment concomitant with differentiation along a line parallel to the F.M. axis. The suite follows a similar trend to the Hawaiian tholeiites (Macdonald and Katsura, 1964), as well as the Thingmuli tholeiites of the Tertiary flood basalt sequence from eastern Iceland (Carmichael, 1964).

Low Ti and low alkalis characterize all of the Abbabis basalts, but some of the samples display low $\text{FeO}/(\text{FeO} + \text{MgO})$ ratios, moderately

Table 2. Major element chemistry of the Abbabis Basalts

	<u>434</u>	<u>437</u>	<u>540</u>	<u>431</u>	<u>637</u>	<u>424</u>	<u>416</u>	<u>422</u>	<u>490</u>	<u>409</u>	<u>470</u>	<u>663</u>
Fe_2O_3 (t) = total Fe as Fe_2O_3												
Alkali Index (A.I.) = $(\text{Na}_2\text{O} + \text{K}_2\text{O})/(\text{SiO}_2 - 43) \times 0.17$												
SiO_2	51.70	48.79	48.41	46.84	52.74	50.88	53.27	51.81	61.36	52.77	53.66	48.78
TiO_2	0.98	0.51	1.17	0.37	0.62	0.91	0.78	0.66	0.82	0.75	0.96	0.33
Al_2O_3	15.24	8.20	16.95	6.67	8.77	14.63	8.74	12.73	13.37	13.79	11.72	8.36
Fe_2O_3 (t)	11.08	9.88	13.70	17.64	10.36	11.74	11.71	10.99	10.26	11.05	11.68	11.59
MnO	0.17	0.35	0.16	0.13	0.32	0.18	0.17	0.16	0.09	0.14	0.15	0.24
MgO	4.23	15.85	4.96	18.11	18.69	4.64	9.36	6.55	3.09	4.94	5.14	14.80
CaO	14.16	12.54	12.49	8.22	5.96	15.89	14.77	15.18	9.06	14.88	14.79	12.83
K_2O	0.36	0.42	0.68	0.06	1.10	0.18	0.12	0.14	0.43	0.29	0.40	0.52
P_2O_5	0.20	0.15	0.23	0.16	0.13	0.21	0.21	0.18	0.17	0.18	0.19	0.18
Na_2O	2.27	1.16	1.75	1.51	0.98	1.78	1.21	1.80	1.58	1.31	1.29	1.60
L.O.I.	0.00	0.08	0.00	3.83	1.08	0.00	0.00	0.08	0.00	0.00	0.00	1.83
Total	100.39	97.85	100.50	99.71	99.67	101.04	100.34	100.20	100.23	100.10	99.98	99.23
A.I.	1.78	1.61	2.64	2.41	1.26	1.46	0.76	1.29	0.64	0.96	0.93	2.16

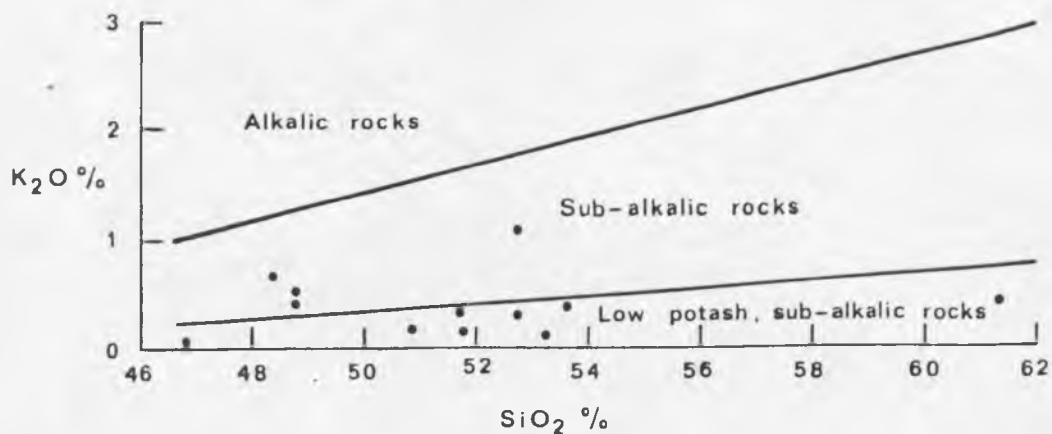


Fig. 5. K_2O vs SiO_2 diagram, illustrating the sub-alkalic nature of the Abbabis basalt suite. Boundaries after Middlemost (1975).

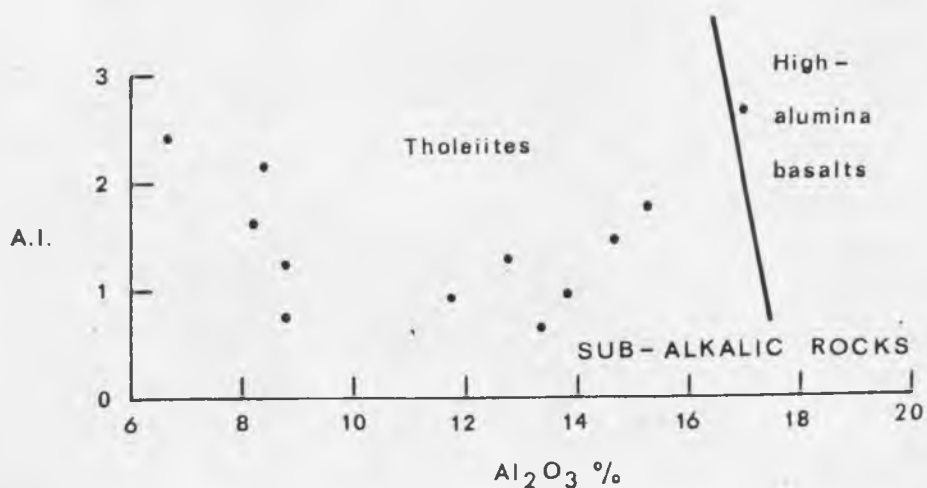


Fig. 6. Alkali index (A.I.) vs alumina diagram, illustrating the tholeiitic nature of the Abbabis basalt suite. $A.I. = (Na_2O + K_2O)/(SiO_2 - 43) \times 0.17$. Boundary after Middlemost (1975).

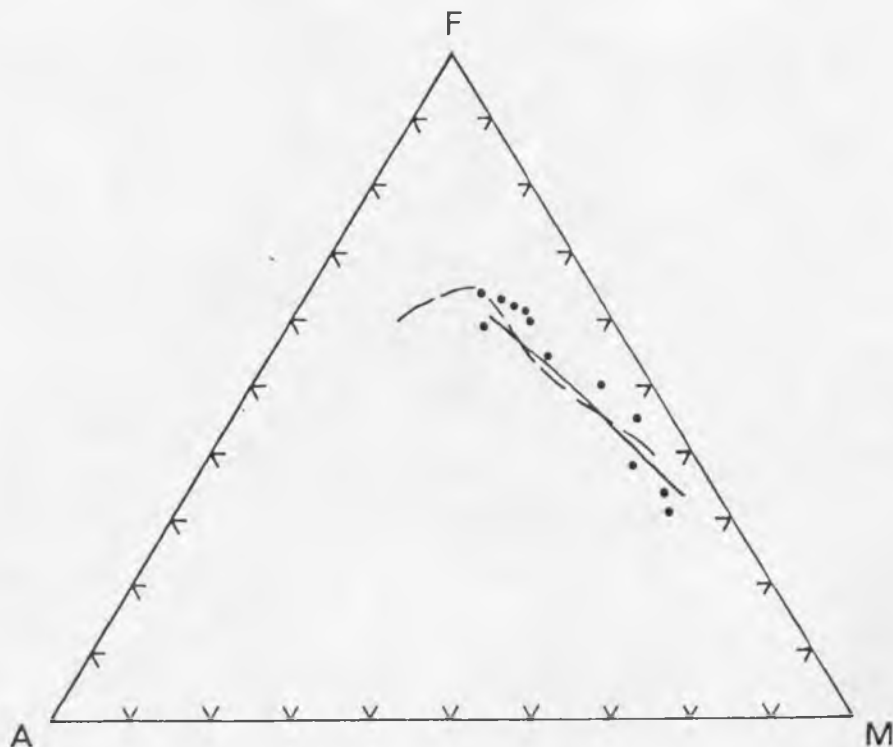


Fig. 7. A.F.M. diagram of the Abbabis basalt suite. Dashed line is the Thingmuli tholeiitic trend after Carmichael (1964). Full line is the Hawaiian tholeiitic trend after Macdonald and Katsura (1964).

low Al_2O_3 and high MgO . These chemical features are characteristic of komatiites (Viljoen and Viljoen, 1969; Arndt et al., 1977), and an attempt has been made to differentiate the Abbabis basalts which display a tholeiitic affinity from those which show a komatiitic one. Komatiites fall well within fields normally assigned to tholeiitic magmas on the alkalis vs silica plot and the A.F.M. diagram, and Arndt et al. (1977) suggest use of the $\text{FeO}/(\text{FeO} + \text{MgO})$ vs Al_2O_3 diagram is one of the most reliable means of distinguishing between the two magma types. A comparison of the Abbabis basalts (Fig. 8) with the komatiites and tholeiites of Munro Township, NE Ontario (Arndt et al., 1977), indicates certain samples show an affinity towards a komatiitic chemistry

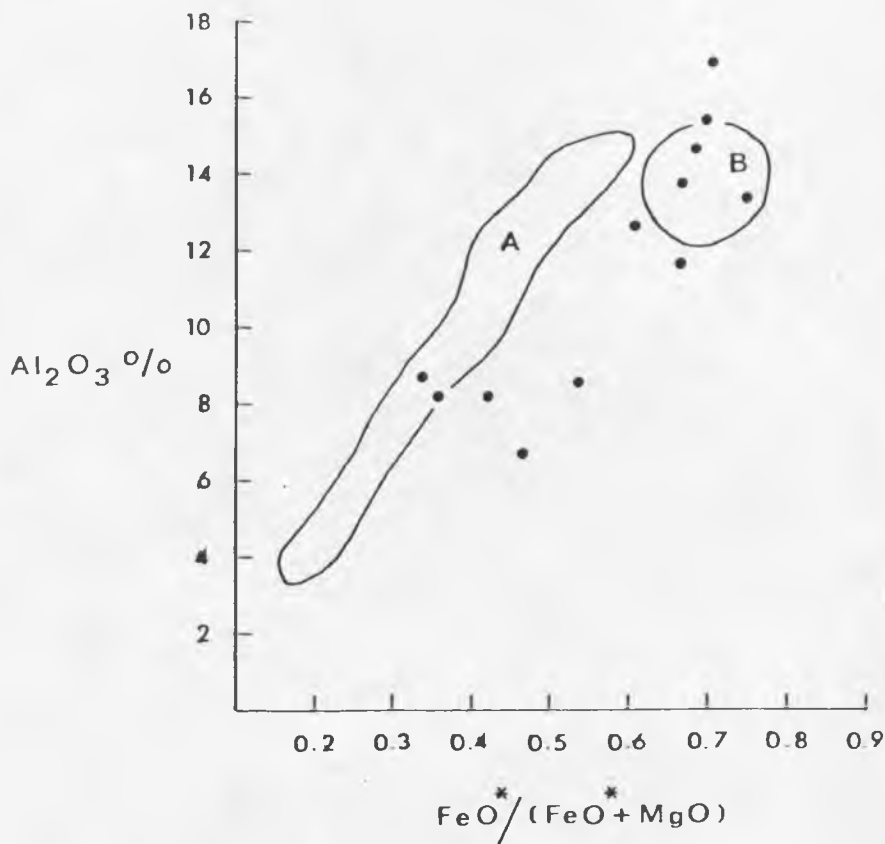


Fig. 8. Al_2O_3 vs $\text{FeO}/(\text{FeO} + \text{MgO})$ diagram of the Abbabis basalt suite. Fields A and B are komatiitic and tholeiitic lavas, respectively from Munro Township, N.E. Ontario (after Arndt et al., 1977).
 FeO^* = total Fe as FeO.

whilst others shown an affinity towards a tholeiitic one.

In an attempt to define the trend of differentiation of the magma the oxides were plotted against SiO_2 and MgO , but no correlations were apparent. The solidification index ($\text{MgO} \times 100 / \text{MgO} + \text{Fe}_2\text{O}_3 + \text{K}_2\text{O} + \text{Na}_2\text{O}$) of Kuno (1968) has been plotted against silica, titanium and iron in an attempt to confirm the affinity of the magma. Between certain levels of the solidification index these elements show specific trends which are characteristic of certain magmatic environments. No trends were detected however, and this may be an indication of the extent of alteration these basalts underwent during the Damaran metamorphism.

(vii) B. Trace element chemistry

The trace element chemistry of the Abbabis basalts (Table 3), is characterized by low Y values, extremely variable Rb and Sr values, as well as anomalous concentrations of Cr and Ni. The high Cr and Ni values provide further evidence for the komatiitic affinity of some of the Abbabis basalts.

It has become customary since the work of Cann (1970), Pearce and Cann (1971 and 1973), Floyd and Winchester (1975), Pearce (1975), Pearce et al. (1975) and Pearce and Norry (1979) to predict the geotectonic setting of basalt suites on the basis of the geochemistry of various trace elements known to be insensitive to the processes of alteration during metamorphism. Floyd and Winchester (1975) have used the elements TiO_2 , P_2O_5 , Zr, Y and Nb to discriminate between tholeiitic and alkalic basalts of oceanic and continental affinity. TiO_2 has been plotted against Zr for the Abbabis suite (Fig. 9) and the samples fall within the field occupied by continental and oceanic tholeiitic basalts. The Abbabis suite display a similar trend on the TiO_2 vs Zr diagram to the Ferrar tholeiites (Gunn, 1966) as well as the Karroo tholeiites (Cox and Hornung, 1966).

Pearce and Norry (1979) have used the Zr/Y vs Zr diagram to distinguish basalts from the three main tectonic settings. When the Abbabis basalts are plotted on this diagram (Fig. 10) the suite displays similar Zr/Y values to the 'within plate' basalts (ocean island or continental basalts), but they display slightly lower Zr values, resulting in the majority of Abbabis samples falling just to the left of the field occupied by 'within plate' basalts.

Pearce and Cann (1973) have used the TiO_2 -Zr-Y ternary diagram to distinguish 'within plate' basalts from ocean floor basalts, and low-

Table 3. Trace element chemistry of the Abbabis basalts (p.p.m.)

Cr	<u>434</u>	<u>437</u>	<u>540</u>	<u>431</u>	<u>637</u>	<u>424</u>	<u>416</u>	<u>422</u>	<u>490</u>	<u>409</u>	<u>470</u>	<u>663</u>
	68	2475	80	4270	1709	49	319	208	48	202	64	60
Co	23	62	51	92	56	24	45	31	37	25	40	42
Ni	36	779	74	815	216	33	80	81	52	57	95	38
Zn	40	88	49	92	7	37	71	43	27	28	57	9
Rb	14	9	18	3	88	12	2	6	7	18	4	21
Sr	331	15	263	3	30	314	261	194	270	276	392	12
Y	20	15	22	4	8	23	11	17	24	19	18	18
Zr	109	58	126	47	63	123	106	72	99	79	115	117
Ba	101	4	399	15	111	68	5	16	289	10	111	62
Zr/Y	5.5	3.9	5.7	11.8	7.9	5.4	9.6	4.2	4.1	4.2	6.4	6.5
K/Rb	257	467	378	200	125	150	600	233	614	161	1000	248

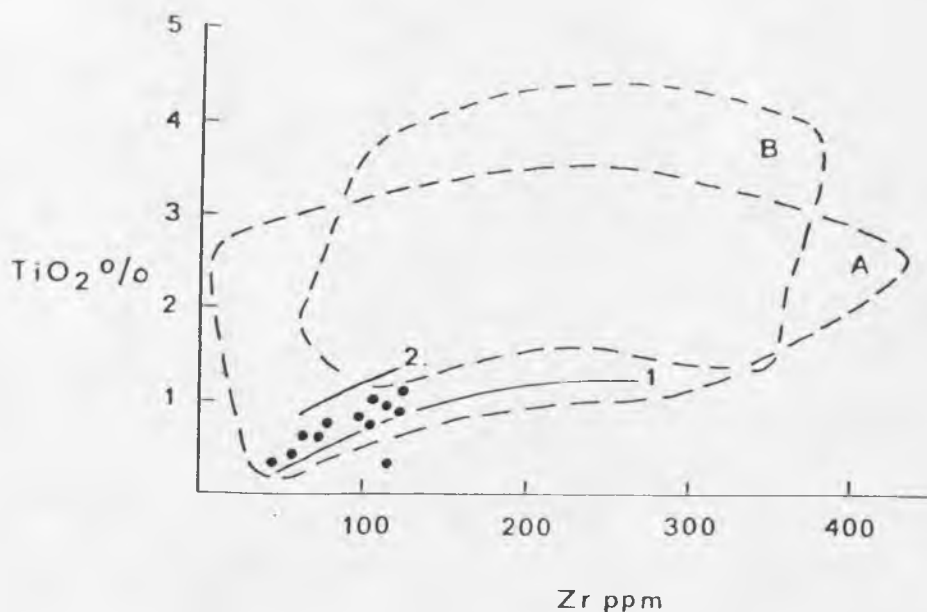


Fig. 9. TiO_2 vs Zr diagram of the Abbabis basalt suite. Fields A and B are continental and oceanic tholeiitic basalts, and continental and oceanic alkali basalts, respectively, after Floyd and Winchester (1975). Trend 1 = Ferrar tholeiites after Gunn (1966). Trend 2 = Karroo tholeiites after Cox and Hornung (1966).

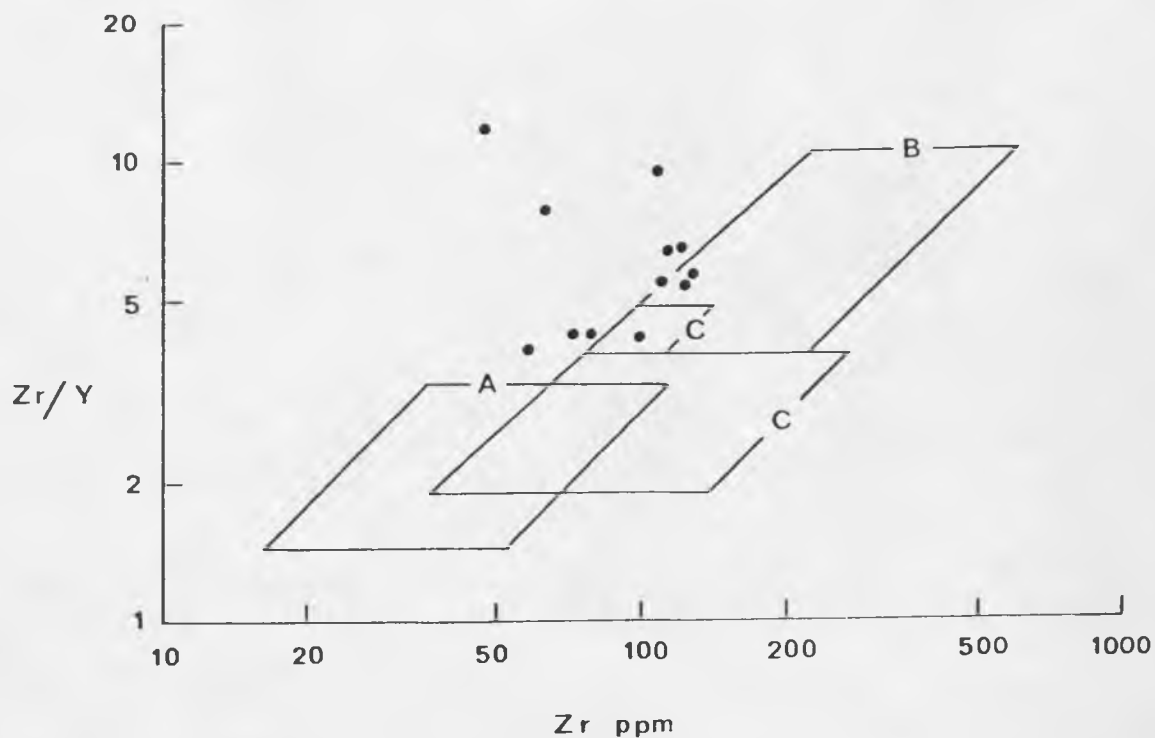


Fig. 10. The Abbabis basalt suite plotted on the Zr/Y vs Zr diagram of Pearce and Norry (1979). Island arc basalts plot in field A; within plate basalts plot in field B; and mid-ocean ridge basalts plot in fields C.

potassium tholeiites and calc-alkali basalts of volcanic arcs. When the Abbabis basalts are plotted on this diagram (Fig. 11) the suite falls in the field occupied by 'within plate' basalts.

II.3. The gneisses of the Abbabis Formation

The Abbabis gneisses clearly post-date the metasedimentary and meta-

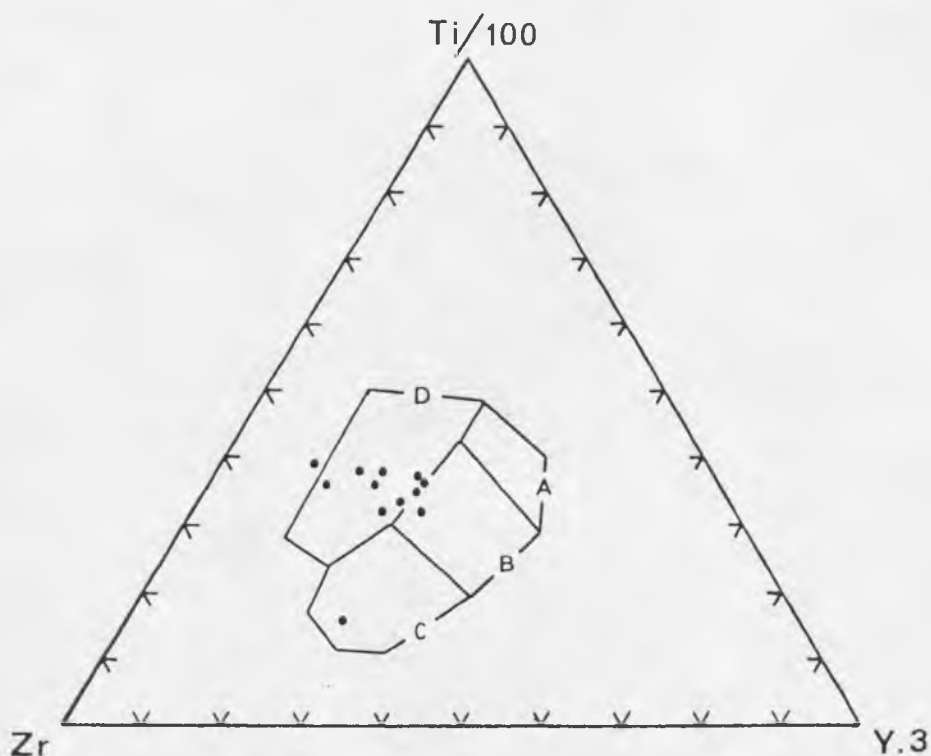


Fig. 11. The Abbabis basalt suite plotted on the TiO_2 -Zr-Y diagram of Pearce and Cann (1973). 'Within plate' basalts fall in field D; ocean floor basalts fall in field B; low potassium tholeiites fall in fields A and B; calc-alkali basalts fall in fields C and B.

volcanic sequences of the Abbabis Formation, and show a wide range in textural, mineralogical and chemical types. The commoner ones are muscovite-bearing, leucocratic granite gneisses and augen gneisses which may be divided into a more abundant muscovite-bearing granitic variety, and a less abundant biotite-bearing dioritic variety. A further granodioritic gneiss was mapped, and is shown separately on the geological map (Folder 1) because it appears to pre-date the other gneisses described above.

Smith (1965) has described what he considers to be a distinct unconformity between a biotite-sillimanite gneiss of the metasedimentary sequence of the Abbabis Formation and an Abbabis gneiss on Tsawisis 16 immediately N. of the Klein Chuos Mountain (Folder 1, P11). He states "the biotite-sillimanite gneiss forms a horizontal capping to a small flat-topped hill composed chiefly of augen gneiss exhibiting a vertical foliation". The biotite-sillimanite gneiss which outcrops at the top of the hill also contains a vertical foliation however, and is in vertical contact with Abbabis gneiss on the extreme N.W. and S.E. edges of the hill top. On the S.W. end of the hill the vertically foliated biotite-sillimanite gneisses continue to the S.W. for over 3km. The flat topped nature of the hill, which led Smith (1965) to believe the biotite-sillimanite gneiss was horizontally disposed is in fact caused by the hill having once been capped by a Karroo dolerite sill. The sill has now been almost totally removed by erosion and only large, rounded boulders of extremely tough dolerite are to be found covering parts of the hill top.

Two augen gneisses from the farm Abbabis 70 which lies a few kilometres to the E. of the area investigated gave a U-Pb age of $1925 \pm \begin{matrix} 330 \\ - 280 \end{matrix}$ Ma (Jacob et al., 1978). The age falls within error of U-Pb ages of 1730 ± 30 Ma

and 1870 ± 30 Ma (Burger et al., 1976) for the Franzfontein granite (Fig. 1), and has been used by Jacob et al. (1978) to suggest continuity between the Franzfontein and Abbabis basements, below the Damaran metasedimentary cover.

(i) The granodioritic gneiss

The gneiss outcrops over a small area to the N.E. and S.W. of the Usakos-Nordenburg road, as well as to a limited extent in the S. on Tsawisis Suid 95 (Folder 1, S11). It is typically a fine to medium grained, biotite-bearing granodioritic gneiss which contains narrow dykes of biotite-bearing, leucocratic aplite. The gneiss is clearly intrusive into the metasediments and metavolcanics of the Abbabis Formation and on Ubib 76 (Folder 1, I6), xenoliths of quartzite, fine grained schist, amphibolite and pyroxenite are to be seen.

The granodioritic gneiss consists of coarse grained zones of strained quartz and feldspar which are set in a fine grained, recrystallized mosaic of quartz and feldspar with minor biotite and symplectite, and accessory Fe-oxide and zircon. The feldspars which consist of perthite, orthoclase and plagioclase, show partial alteration to sericite and muscovite. The biotite which is variable in content forms grains which parallel the fabric, and alteration to chlorite and muscovite is commonly complete. The Fe-oxide is associated with the alteration products of the biotite, whilst the zircon forms subhedral inclusions mainly within the feldspars.

(ii) The leucocratic gneisses and augen gneisses

The leucocratic gneisses and augen gneisses outcrop over a wide area throughout that part of the basement inlier investigated, but they could not be differentiated on the geological map due to the scale

of mapping. The gneisses are clearly intrusive into the metasediments and metavolcanics of the Abbabis Formation, and xenoliths of the latter within the gneisses are common.

The biotite-bearing dioritic augen gneiss and the leucocratic gneiss are intimately associated near the abandoned copper mine in the Abbisch River (Folder 1, S11), where the former displays excellent intrusive relationships with the latter. On Naob 69 (Folder 1, G5) however, two dykes of leucocratic gneiss just over 1m in thickness, are intrusive into the biotite-bearing dioritic augen gneiss, and because of their intimate association with the muscovite-bearing granitic augen gneiss, the three granitoids are considered to be synchronous. They do however post-date the granodioritic gneiss described above. On Ubib 76, about 30m N.E. of the Usakos-Nordenburg road (Folder 1, I6), a dyke of leucocratic gneiss is intrusive into the granodioritic gneiss. The dyke is 3m wide, has sharp contacts, and contains xenoliths of the granodioritic gneiss. Very minor copper oxide deposits are present within the dyke near its south-western end.

The leucocratic gneiss is a fine to coarse grained, muscovite-bearing leucocratic rock which may contain metamorphic segregations of biotite, knots of sillimanite, poikiloblasts of muscovite or ilmenite- and magnetite-bearing pegmatite. A few small outcrops on Tsawisis Suid (Folder 1, M and N 10), contain xenoliths of calc silicate, and here the ferromagnesian minerals include diopside and garnet. The gneiss consists of a partially recrystallized mosaic of quartz, perthite and microcline with randomly oriented, interstitial, metamorphic biotite and knots consisting of interlocking, radiating sillimanite and muscovite. The feldspars show slight alteration to sericite, whilst the biotite shows

slight alteration to muscovite, haematite and chlorite. The accessory minerals include anhedral zircon, apatite and opaque Fe-oxide.

The granitic augen gneiss is a medium to coarse grained, muscovite-bearing rock containing K-feldspar phenocrysts up to 3cm across. Biotite and tourmaline may occur in minor amounts, whilst muscovite- and biotite-bearing pegmatite is common. The body of gneiss on Tsawisis Suid (Folder 1, S10) contains metamorphic sillimanite and magnetite. The gneiss consists of a recrystallized groundmass of quartz, microcline, orthoclase and plagioclase with minor chloritized biotite and Fe-oxide which form trains which define linear fabrics, and large muscovite poikiloblasts which post-date the fabric. Accessory minerals include apatite and anhedral zircon, the latter being present in association with primary Fe-oxide as well as inclusions within quartz.

The dioritic augen gneiss is a medium to coarse grained biotite-bearing rock containing augen of quartz and plagioclase. Both ilmenite and magnetite may be locally abundant, especially within the biotite-bearing pegmatite. The gneiss consists of a recrystallized mosaic of quartz, untwinned plagioclase and orthoclase with minor biotite and accessory Fe-oxide, zircon and apatite. The biotite which wraps around the augen structures, shows partial alteration to chlorite and muscovite.

(iii) Geochemistry of the Abbabis gneisses

In an attempt to characterize the various gneisses recognized within the area investigated, four samples of gneiss were analysed by X.R.F. for the major elements (Table 4). The four samples, each weighing approximately 10kg were collected from each of the four main gneiss types recognized, viz., muscovite-bearing granitic augen gneiss;

Table 4. Major element chemistry of the Abbabis gneisses

$$\text{Fe}_2\text{O}_3 \text{ (t)} = \text{total Fe as Fe}_2\text{O}_3$$

	<u>Al</u>	<u>le</u>	<u>qs ll</u>	<u>au</u>
SiO ₂	77.50	78.55	69.23	55.24
TiO ₂	0.10	0.07	0.42	1.36
Al ₂ O ₃	11.31	11.13	15.04	14.91
Fe ₂ O ₃ (t)	1.40	0.90	4.18	11.09
MnO	0.01	0.01	0.07	0.11
MgO	0.35	0.38	1.35	3.67
CaO	0.15	1.03	3.27	11.31
K ₂ O	5.59	5.22	2.81	0.36
P ₂ O ₅	0.12	0.09	0.12	0.18
Na ₂ O	2.85	2.40	3.89	1.35
L.O.I.	1.33	2.17	1.33	1.00
Total	99.38	99.78	100.38	99.58

- Al - Muscovite-bearing granitic augen gneiss
 le - Leucocratic gneiss
 qs ll - Granodioritic gneiss
 au - Biotite-bearing dioritic augen gneiss

leucocratic gneiss; granodioritic gneiss, and biotite-bearing dioritic augen gneiss. The location of the samples are shown on the simplified geological map (Fig. 3).

The samples have been plotted on the A.F.M. diagram (Fig. 12), which clearly displays the dioritic and granodioritic nature of the dioritic augen gneiss (sample au) and the granodioritic gneiss (sample qs 11), respectively. The granitic augen gneiss (sample A1) and the leucocratic gneiss (sample le) fall within the alkali-rich corner of the diagram occupied by alkali-rich granites. The last two rocks as well as the granodiorite fall along a typical calc-alkaline trend (Carmichael et al., 1974), whilst the dioritic augen gneiss falls close to a moderately fractionated portion of the Skaergaard trend (Wager, 1960). However, it is not clear whether the dioritic augen gneiss is related to a Skaergaard type trend or to an extreme end member of the calc-alkaline trend, and only further analysis of a suite of these rocks would solve this problem.

II.4. The amphibolite dykes

The amphibolite dykes post-date both the metasedimentary and metavolcanic sequences of the Abbabis Formation and the Abbabis gneisses. Normally they pre-date the rocks of the Damara Sequence, but locally as in the Skeleton Gorge, N. of the Swakop River in the Namib Desert Park remnants of amphibolite dykes can be seen within the lowest formation of the Damara Sequence.

Only three small dykes of amphibolite have been located within the portion of the Abbabis inlier investigated, each less than 1m in thickness, and only a few metres in length. The first is situated within biotite schist of the Abbabis Formation a few metres to the W. of the Naob River,

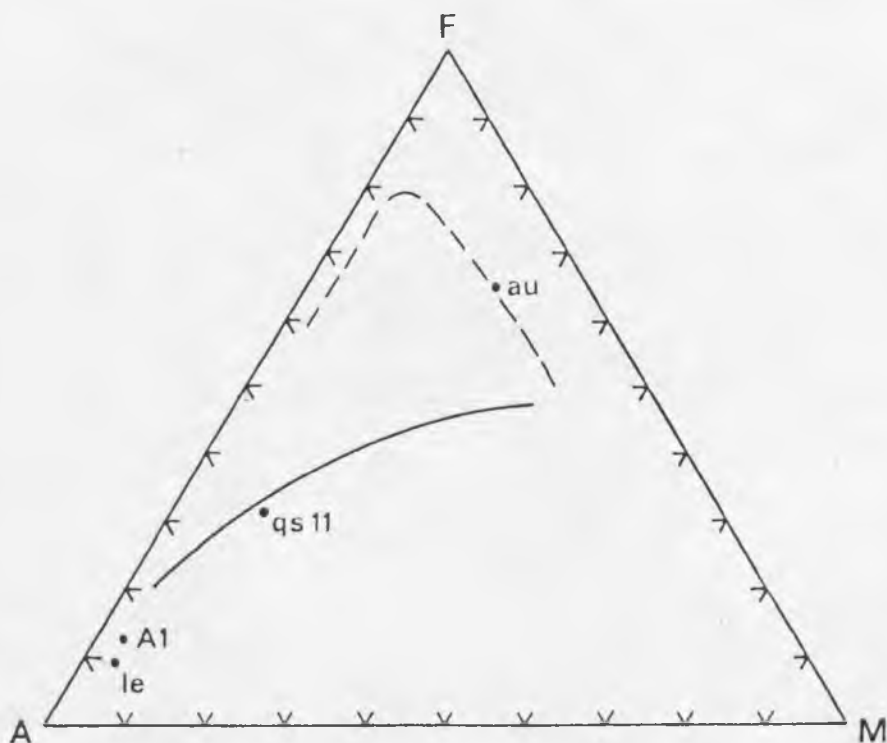


Fig. 12. A.F.M. diagram of the Abbabis gneisses. Solid line is a typical calc-alkaline trend from the California batholith (Carmichael, 1974). Dashed line is the Skaergaard trend (Wager, 1960).

and just S. of the contact with the overlying rocks of the Damara Sequence on Naob 69 (Folder 1, B7). The second occurs as a boudinaged body also within biotite schist in the river bed N.W. of the Naob farmhouse (Folder 1, D8), whilst the third transects a well bedded quartzite unit a few metres N.E. of the Usakos-Nordenburg road (Folder 1, J5).

The amphibolites consist of a recrystallized aggregate of poikilitic hornblende, zoned microcline and sericitized feldspar with minor biotite, sphene and opaque Fe-oxide and accessory, anhedral, interstitial zircon. The high ferric Fe biotite shows slight chloritization, whilst the hornblende is occasionally epidotized. Sphene occurs as small anhedral grains which are commonly clustered and associated with the Fe-oxide.

II.5 Conclusions

The pre-Dambaran rocks may be divided on older sequence of metasedimentary, metavolcanic and pyroclastic rocks of the Abbabis Formation and a younger series of Abbabis ortho-gneisses.

The shallow water clastic and carbonate rocks of the metasedimentary sequence are associated with extensive meta-basaltic and agglomeratic units. The largest meta-basalt reaches a maximum thickness of approximately 1km, and displays amygdaloidal textures and pillow structures.

The Abbabis basalts, which range from basalt to andesite in composition, are characterized by low Ti and Y values and a low alkali nature. These chemical features are diagnostic of continental basalts of a tholeiitic affinity. A few of the Abbabis basalts however, also display high MgO, Cr and Ni, moderately low Al_2O_3 and low $FeO/(FeO + MgO)$ and these chemical features characterize basalts of a komatiitic affinity.

The Abbabis gneisses exhibit a range in chemistry from diorites, through granodiorites to alkali rich granites.

Many of the basement rocks have undergone alteration effects including: sericitization or calcitization of feldspar; chloritization, muscovitization or haematization of biotite, and saussuritization of hornblende or feldspar. Amphibolitization and saussuritization is widespread within the metabasalts, and the alteration is considered to have taken place during the Dambaran orogeny.

CHAPTER III

THE GEOLOGY OF THE DAMARA SEQUENCE

III.1. Introduction

Detailed accounts of the geology of the Damara Sequence from various parts of the central belt of the Damaran orogen have been given by Gevers (1931), Smith (1965), Martin (1965), Nash (1971), Jacob (1974a), Barnes (1981) and Downing (in prep). The following discussion is concerned mainly with the Damara Sequence in those areas of the central belt which have been investigated due to the presence of radioactive Damaran granitoids. These areas include parts of the farms Goanikontes, Valencia 122, Namibfontein 91, Stinkbank 62, Lukasbank 63 and Otjua 37, and the locations of the areas investigated are shown on the simplified geological map of the Damaran belt (Fig. 2). The stratigraphic names used in the discussion follow those proposed by the South African Committee for Stratigraphy (S.A.C.S., 1980), and are largely based upon those established by Smith (1965) and Jacob (1974a). Each lithostratigraphic successions is shown for comparison in Table 5.

The oldest metasediments of the Damara Sequence are coarse, probably fluviatile clastics of the Etusis Formation, conformably overlain by interbedded gneisses, schists and calc silicates of the Khan Formation which are considered by Smith (1965) to represent calcareous, feldspathic sandstones deposited in fairly shallow water basins. Both are thought to be coeval with a suite of potassic lavas known as the Naauwpoort volcanics, as well as associated syenites and carbonatites exposed along the northern margin of the geosyncline.

Table 5. The lithostratigraphy of the Damara Sequence in the central portion of the orogen as proposed by Smith (1965), Jacob (1974a), Jacob (1974a) and SACS (1980)

SMITH (1965)		JACOB (1974a)			SACS (1980)			Maximum thickness (m)
Series	Stage	Formation	Group	Subgroup	Formation	Lithology		
DAMARA SYSTEM	Khomas	Witpoort in west	SWAKOP	Khomas	Kuiseb	Biotite-rich quartzofeldspathic schist, biotite-garnet-cordierite schist, minor amphibole schist, quartzite, calc-silicate rock and marble; basal graphitic schist with calc-silicate lenses (Tinkas Member)	3,000	
		Tinkas in east			Karibib	Marble, biotite schist, quartz schist, calc-silicate rock.	700	
	Hakos	Upper	Tinkas in east and Husab in west	Ugab	Chuoss	Mixtite, pebble- and boulder-bearing schist, minor quartzite	700	
		Middle or Chuoss	Chuoss		DISCORDANCE	Rössing	Very variable: marble, quartzite, conglomerate, biotite schist, biotite-cordierite schist and gneiss, aluminous gneiss, biotite-hornblende schist, calc-silicate rock.	200
Lower	Rössing							
UNCONFORMITY OR CONFORMABLE TRANSITION								
NOSIB FORMATION	Upper	Khan	NOSIB		Khan	Pyroxene-amphibole feldspathic quartzite, amphibole-pyroxene gneiss, amphibole and biotite schist.	1,100	
	Lower	Etusia			Etusia	Pinkish well-bedded feldspathic quartzite, arkose, conglomerate, quartzofeldspathic gneiss; minor biotite schist, marble, amphibolite, metarhyolite and calc-silicate rock	3,500	

There is either an unconformity or a conformable transition between the rocks of the Etusis and Khan Formations (Nosib Group) and the overlying formations (Swakop Group). The base of the latter represents the start of the geosynclinal succession, and consists of a variable sequence of carbonates, quartzites, conglomerates and pelites (Rössing Formation). This passes up into a mixtite (Chuos Formation), followed by a dominantly calcareous succession (Karibib Formation), then by a monotonous series of biotite-bearing schists (Kuseb Formation). Within the latter there are occasional sulphide-bearing orth-amphibolites, the best known being the Matchless belt (Fig. 1), which although often only a few metres thick, has been traced for over 300km along strike. Several authors have suggested that it may represent a fragment of ocean crust emplaced tectonically within the schists of the Kuseb Formation (Hartnady 1975, 1979; Burke et al., 1977).

III.2. The Damara Sequence

(i) The Etusis Formation

The Etusis Formation represents the base of the Damara Sequence and consists mainly of quartzites which vary in their texture and mineralogy, but which are normally coarse grained, red and slightly feldspathic. The formation was deposited on an eroded basement surface in local basins of variable depth, and its thickness in the central part of the belt varies from less than 40m to over 3500m (Smith, 1965). On Otjua 37 the quartzites are well exposed in the core of a dome structure. Part of the farm has been mapped to a scale of approximately 1:25,000, and the geology is shown in Folder 2.

The quartzites on Otjua 37 consist of a recrystallized mosaic of

quartz, sericitized microcline and plagioclase, with minor interstitial muscovitized and chloritized biotite and accessory anhedral Fe-oxide, sphene and zircon. Bands of calc silicate up to a few metres in thickness may be present within the quartzites. These consist of a fine grained recrystallized mass of hornblende and diopside with minor quartz, sphene, plagioclase, orthoclase and Fe-oxide and accessory rutile. The hornblende shows slight alteration to calcite, epidote and haematite, whilst the diopside occasionally displays alteration to hornblende. Both minerals are concentrated in bands a few millimetres in thickness which probably reflects a combination of metamorphic segregation and an original fine grained sedimentary banding.

In the vicinity of the Khan gorge on Namibfontein 91 and Wolfkoppe 105, some units of the Etusis quartzite are weakly radioactive. The coarse grained quartzites contain metamorphic sillimanite and muscovite, and consist of a recrystallized mosaic of quartz, sericitized microcline, plagioclase and orthoclase with minor interstitial biotite and Fe-oxide, and accessory monazite, zircon and apatite. The radioactivity is caused by the accessory monazite grains which contain Th. The grains occur interstitially or as inclusions in quartz and feldspar, and they reach a maximum size of about 0.2mm. The Th-bearing monazites were detected on the electron microprobe, and a back scattered electron image (B.E.I.) of a monazite grain associated with apatite is shown in Plate 5A. Brightness of a particular mineral on a B.E.I. is dependent upon the atomic number of the elements present, the higher the atomic number the brighter the image, and therefore minerals containing U or Th will be significantly brighter than minerals which do not contain these elements. Consequently the Th-bearing monazite grain shown on the B.E.I. in Plate 5A is relatively brighter than the apatite, quartz and feldspar

which surround it. The X-ray distribution maps of Th, P and Ca (Plate 5; B, C and D respectively) illustrate the distribution of these elements within the individual mineral phases, but the relative spot density cannot be compared in terms of relative composition because the X-ray maps are taken at different scan speeds.

The Etusis quartzites are normally massive and occasionally display large scale trough X-stratification. Conglomerates and grits may also be present locally, as on the Langer Heinrich Mountain in the Namib Desert Park. Here the updomed quartzites contain fluvial channel-type conglomerates measuring a metre or two in thickness and a few metres in width. Some of the conglomerates contain pebbles of smoky quartz within a fine grained, clear, quartzitic matrix, indicating that the radioactive damage which effected the smoky quartz pebbles occurred prior to the deposition of the conglomerate (Downing, in prep.). The pebbles are likely to have been derived from a strongly radioactive pre-Damara granitoid.

(ii) The Khan Formation

The Khan Formation conformably overlies the Etusis, the gradational contact being well exposed E. of the confluence of the Khan and Swakop Rivers. The upper contact of the Khan is discordant with the overlying Rössing Formation at Valencia 122, where amphibole and pyroxene bearing gneisses of the Khan pass abruptly into quartzites and schists of the Rössing Formation (Folder 4). On parts of Goanikontes however the Khan is transitional with the Chuos Formation, where boudinaged calc silicate bands within the biotite schists of the Khan gradually decrease in number as the matrix supported conglomerates of the Chuos increase. Part of the Goanikontes area immediately to the W. of the

confluence between the Khan and Swakop Rivers has been mapped to a scale of approximately 1:25,000 and the geology is shown on Folder 3. The gradational contact between the Khan and Chuos Formations described above is exposed over a strike length of about 4.5km (Folder 3, J12 to P5).

In the area around the Khan and Swakop Rivers Smith (1965) separated the rocks of the Khan Formation into an amphibolite facies and a calc granulite facies. He described the former as very fine grained granular rocks consisting of quartz and hornblende with subordinate plagioclase and accessory biotite, chlorite, sphene, zircon, scapolite and apatite, and the latter as typically greyish-green pyroxene- and amphibole-bearing feldspathic quartzites with minor epidote, biotite, garnet and scapolite and accessory zircon, sphene, Fe-oxide and apatite.

Stratiform copper deposits are present within the upper part of the Khan Formation, just below its contact with the Karibib Formation in the areas of the Ida and Husab domes in the Namib Desert Park. They are best developed at the abandoned Ida mine on the Ida dome, where disseminated chalcopyrite and copper oxide are present within biotite schist and calc silicate. Damaran pegmatites which have invaded this particular sequence have mobilized some of the disseminated copper within the metasediments.

(iii) The Rössing Formation

The Rössing Formation is characterized by its dramatic spatial variations in lithology and thickness, and is well developed on parts of Goanikontes, Valencia 122 and Namibfontein 91. The formation is typically developed at Valencia 122 where a variable sequence of quartzite, schist, marble and calc silicate is exposed. The N.W. part of Valencia 122 has been mapped to a scale of approximately 1:10,000 and the

geology is shown on Folder 4. The area mapped lies on the N.W. limb of a major N.E. striking synform which passes through Valencia 122 (Fig. 2).

The quartzites on Valencia 122 may be medium to coarse grained, red, feldspathic and biotite-bearing as in the case of the basal quartzite which reaches a maximum thickness of a few metres (Folder 4, R5). They may also be fine grained and mineralogically immature, consisting of a recrystallized mosaic of quartz, plagioclase, slightly epidotized diopside, garnet and orthoclase with minor sphene and Fe-oxide. Matrix supported, oligomictic conglomerates containing quartzite pebbles in a quartzitic matrix are also to be found locally (Folder 4, G5).

The schists represent the dominant rock type within the succession and may contain diopside, garnet, biotite, sillimanite and magnetite as well as minor sericitized and haematized feldspar, and accessory amounts of interstitial, rounded zircon. The calc silicates which may contain the same metamorphic minerals as the schists, are subordinate to the marbles and usually occur intercalated within them.

The base of the Rössing Formation at Valencia 122 has been taken as the lowest quartzite; whilst the top has been taken as the marble or schist which occurs directly below the Chuos mixtite in the N.E., and as the highest quartzite in the S.W. The formation thins from approximately 115m in the N.E. (Folder 4, P5) where the quartzites are thick and more predominant to approximately 70m in the S.W. (Folder 4, E3).

A typical sequence of rocks from the Rössing Formation is also exposed on Namibfontein 91, S. of the Ebony siding. Parts of the farms Namibfontein 91, Stinkbank 62 and Lukasbank 63 have been mapped to a scale of 1:50,000 and the geology is shown on Folder 5. The Rössing

sequence youngs to the S.E., but has been swamped by Damaran granitoids and an estimation of the total thickness of the formation is impossible.

Two well developed marble horizons are present within the Rössing Formation on Namibfontein 91. Each has a maximum thickness of a few tens of metres, although the lower one which was mapped by Smith (1966) as Karibib marble, is the thicker of the two. Along the lower contact of the upper marble unit a zone of diopside bearing wollastonite is developed. The wollastonite is red in places probably the result of the replacement of Ca by Mn (Folder 5, C3 - marked by the occurrence of an abandoned exploration pit). The marbles are separated by a sequence of calc silicates, schists and mineralogically immature quartzites which occur as xenoliths within a series of lit-par-lit intrusions of Damaran granitoid. Locally the schists show signs of magmatization, especially in the gorge S.E. of the Namibfontein farmhouse (Folder 5, E8), where zones of leucosome have developed along planes which parallel the regional fabric.

In the Goanikontes area the base of the Rössing Formation is not exposed within the area investigated, but the top displays both sharp and gradational contacts with the overlying Chuos Formation. North of the Swakop River (Folder 3, I-J5) quartzites, conglomerates, marbles and diopside- and magnetite-bearing schists of the Rössing Formation are gradational with mixtites of the Chuos Formation, whilst S. of the river (Folder 3, K7 and G6) marble and garnet-biotite schist are in sharp contact with the Chuos mixtite.

The schists within the Rössing Formation on Goanikontes may contain metamorphic assemblages of garnet, biotite and orthoclase, or orthoclase, biotite and sillimanite. The biotite grains parallel the main penetrative fabric and show slight chloritization and sericitization, whilst the

orthoclase forms flattened poikiloblasts which commonly contain bundles of sillimanite needles. The garnet, which also pre-dates the main fabric forming event, forms large idioblastic porphyroblasts, whilst the magnetite is post-tectonic and occurs as large euhedral poikiloblasts which are commonly rimmed by chlorite and sericite. Minor constituents include epidote and muscovite after biotite, sericitized and calcitized feldspar and symplectite, and the accessories consist of rounded, interstitial zircon and apatite, and interstitial, subhedral monazite.

Stratiform copper deposits are well developed within the Rössing Formation on Valencia 122 and Namibfontein 91. On the former they are best developed in the vicinity of the abandoned Kainkagchas copper mine (Folder 4, P6), where the cupriferous horizons reach a maximum thickness of about 10m. Here the mineralization occurs predominantly in garnet-, diopside-, tremolite- and sphene-bearing calc silicates, and to a lesser extent within the intervening biotite schists. Smith (1965) has detailed the exploration activities performed by Tsumeb Corp. Ltd., and states that the deposit is unlikely to be of economic value. The ore minerals which include bornite, chalcocite and chalcopyrite occur as anhedral, intergranular grains or as lenticular inclusions along tremolite cleavage planes.

The main copper mineralization at Valencia extends over a strike length of approximately 700m, but copper-bearing rocks have been observed over a total strike length of about 2.5km. Approximately 1800m S.W. of the Kainkagchas mine (Folder 4, G5) copper oxides are present within an oligomictic conglomerate, and they also occur within a quartzite at the top of the Rössing sequence over 2km S.W. of the mine (Folder 4, E4).

Minor copper showings are present throughout the Rössing Formation on Namibfontein 91. In the area mapped copper oxides are developed in xenoliths of biotite schist within a Damaran granitoid. The xenoliths, which measure only a few metres across, are situated just below the upper marble band and occur on both sides of the road running from the Ebony siding to the Namibfontein farmhouse (Folder 5, E6 - marked by abandoned prospecting pits). Copper oxides are also developed on a bedding plane in the upper marble unit, W. of the farmhouse (Folder 5, C8).

Two further copper deposits are present in rocks of the Rössing Formation to the S. of the area mapped. The first is at the abandoned Ebony mine where copper oxides occur in a biotite schist some 2m in thickness and a few metres in strike length. Bornite was located within a narrow quartz vein cutting the schist unit near the main shaft.

Smith (1966) indicates the location of the mine but has mapped the rocks in its vicinity as Khan Formation. The second showing is situated about 4km S.W. of the Ebony mine, and consists of copper oxide and minor chalcopyrite grains in a biotite-bearing Damaran pegmatite intrusive into biotite- and hornblende-bearing schist.

(iv) The Chuos Formation

The Chuos Formation is very well developed in the Goanikontes area where thicknesses in excess of 400m are present along the N.W. limb of a major antiform (Folder 3, K9). The formation consists of a variable sequence of conglomerates and intercalated units of biotite-, diopside- and magnetite-bearing schist, mineralogically immature quartzite and marble. The quartzite and marble units reach maximum thicknesses of a few metres, and these thicker units are shown on

the geological map (Folder 5; L3, 4 and 5, G4).

The conglomerates are normally polymictic and matrix supported, and the deformed clasts may consist of gneiss, vein quartz, quartzite and schist. The sorting is extremely variable and conglomeratic units are commonly interbedded with schistose units which are almost devoid of clasts (Plate 6). North of the Swakop River near the base of the Chuos sequence (Folder 3, L3) lenses of conglomerate measuring a few metres in width and a few tens of centimetres in thickness occur within a diopside- and magnetite-bearing schist, indicative of deposition within channel deposits. The matrix of the conglomerates consists of a recrystallized mosaic of quartz and slightly sericitized feldspar with minor weakly chloritized biotite, poikiloblastic muscovitized and calcitized tremolite, Fe-oxide, rutile and sphene, and accessory zircon and apatite.

Within the mapped area of Valencia 122 the Chuos Formation displays a maximum thickness of approximately 40m, about 500m S.W. of the Kainkagchas copper mine (Folder 4, N5) but it disappears along strike to the S.W. within about 1km. The sequence does not display lithological variations as it does on Goanikontes but consists of a well sorted polymictic conglomerate containing angular to rounded clasts within a biotite- and garnet-bearing schistose matrix. The clasts reach a maximum size of about 10cm and consist of fine to coarse grained quartzite, vein quartz, calc silicate, coarse grained biotite- and muscovite-bearing granite and pegmatite, and biotite- and garnet-bearing schist.

On the S.E. limb of the major synform on Valencia 122 (Fig. 2) beyond the mapped area the Chuos Formation reaches a maximum thickness of approximately 160m, and may be divided into three units. The upper

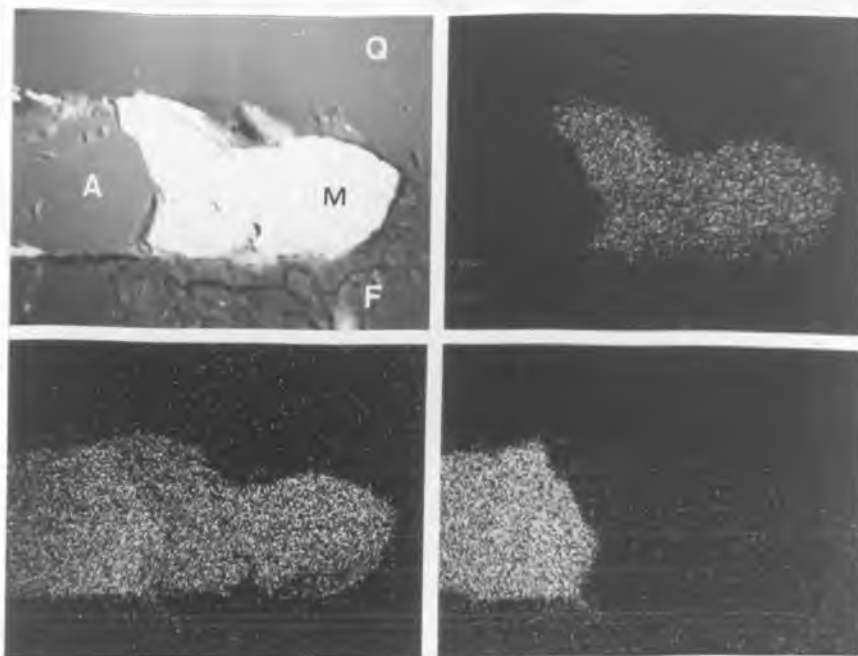


Plate 5. A = Back scattered electron image of monazite (M) associated with apatite (A) in a quartzite from Wolfkoppe 105. Q = quartz, F = feldspar. B, C and D are X-ray distribution maps of Th, P and Ca respectively, (x 400).



Plate 6. Interbedded, variably sorted conglomerates and schists of the Chuos Formation at Goanikontes (Folder 3, G6).

and lower units consist of conglomerates containing angular to rounded clasts of quartzite, biotite schist and vein quartz in a biotite-, muscovite- and diopside-bearing quartzitic matrix. The middle unit however, consists of a conglomerate containing similar clasts in a biotite- and muscovite-bearing schistose matrix.

The very wide distribution and local thick accumulations of the mixtite in the Damaran belt led Gevers (1931) to conclude that it had a glacial origin, and that the duration and extent of the ice-sheet were considerable. Smith (1965) held the same view, but Martin (1965) suggested that much of the formation is glacial-marine in origin rather than a moraine deposit. Martin (1979, pers. comm.) considers that all the mixtites in the Damaran belt cannot be the result of a single large scale glacial event, but they are more likely to be the result of local glacial events if a glacial origin is to be accepted.

(v) The Karibib Formation

The Karibib Formation is well developed on Valencia 122 where it consists of a sequence of marbles, calc silicates and schists, and maintains an approximate thickness of 200m throughout the area mapped. The base of the formation is taken as the contact with the Chuos Formation in the N.E., and with the upper quartzite of the Rössing Formation in the S.W.

The upper part of the Karibib Formation is gradational with the overlying Kuiseb Formation, and the top has been taken approximately 60 to 100m above the uppermost marble unit, where the biotite-bearing schists become coarser grained and poikiloblastic orthoclase appears. The contact is prominent on the aerial photographs of the area, due to the darker tones associated with the biotite- and orthoclase-bearing schists

of the stratigraphically overlying Kuiseb Formation.

The marble units within the Karibib Formation are characteristically thicker and more pure than those within the Rössing Formation and single beds reach maximum thicknesses of approximately 40m on Valencia 122. The calc silicates consist of a recrystallized mosaic of quartz, sericitized feldspar, diopside and biotite with minor sphene and Fe-oxide. The high Ti biotite commonly displays almost complete alteration to chlorite, whilst the diopside shows alteration to hornblende and epidote. The sphene is present as typical rhombs, or as reaction rims around the Fe-oxide which is normally very irregular in shape.

On Stinkbank 62 marbles and calc silicates of the Karibib Formation are well developed, but the sequence has been swamped by Damaran granitoids and the original thickness is impossible to estimate. The S.W. trending belt of granites containing xenoliths of Karibib rocks, (Folder 5, Q2 to N9) is about 1.5km wide and the xenoliths reach a maximum thickness of about 300m. Minor isoclinal fold structures are commonly developed within the marbles however, and the sequence has probably undergone a considerable amount of tectonic thickening. Diopside, tremolite, wollastonite and vesuvianite are present within the marbles and calc silicates. The wollastonite often occurs as radiating bundles within 1-5cm thick bands.

Stratiform Cu-Pb-Zn deposits are present in the Karibib Formation at the abandoned Usakos mines S.E. of Usakos, and at the Namib mines W. of Rössing. At the former, disseminated galena, sphalerite, pyrite and chalcopyrite are present within a sillimanite- and wollastonite-bearing marble unit. The ore horizon reaches a maximum thickness of about 2m and extends intermittently along strike for over 1km. Smith (1965) has detailed the mining activities which were performed during the life

of the mine. At the Namib mines disseminated galena and minor chalcopyrite occur in a pure white marble of the Karibib sequence.

(vi) The Kuiseb Formation

The Kuiseb Formation is well developed on Valencia 122 where it forms the core of the major N.E. trending synform which passes through the farm. The formation consists of a thick sequence of biotite- and orthoclase-bearing schists, with thin intercalations of biotite- and muscovite-bearing schist and calc silicate near the base. The former comprises orthoclase poikiloblasts and biotite prisms in a recrystallized mosaic of polygonal quartz, orthoclase and plagioclase with minor Fe-oxide and accessory, interstitial zircon and monazite. The orthoclase poikiloblasts reach a maximum size of 6mm across, show partial alteration to sericite along the rims, and may easily be confused with garnet on the weathered surface. The high Ti biotite prisms wrap around the orthoclase poikiloblasts, and both minerals pre-date the main fabric forming event.

Though the Kuiseb Formation is well developed on the S. of Stinkbank 62 (Smith, 1966), in the area mapped it forms very limited outcrops. A narrow sequence of biotite- and staurolite-bearing schists separate a post-tectonic Damaran granitoid to the N.W. from a composite pluton of older granitoids to the S.E. (Folder 5, Q6 to Q9). The only other occurrences of rocks belonging to the Kuiseb Formation occur as biotite-bearing schist, fine grained mineralogically immature quartzite and calc silicate xenoliths within the composite pluton in the S.E. of the area mapped (Folder 5, S10). The schists consist of recrystallized quartz, microcline and orthoclase with abundant prismatic biotite and accessory Fe-oxide and zircon. The high Ti biotite prisms which contain

abundant inclusions of zircon with large pleochroic haloes, pre-date the main fabric forming event. Staurolite may be present within the biotite schists as a minor constituent in the form of euhedral to anhedral, interstitial grains.

Smith (1965) considers the thick and uniform distribution of the Kuiseb schists represent deposition at an intermediate depth-zone in a distal environment, and Martin (1965) believes the rocks must originally have been typical eugeosynclinal assemblages of illite-bearing shale, arenaceous shale and greywacke.

The Kuiseb Formation exhibits a sedimentological facies change in the Otjua area where a characteristic sequence of the Tinkas Member overlies the quartzites of the Etusis Formation. Here the sequence consists of alternating bands of biotite- and garnet-bearing schist and garnet- and diopside-bearing calc silicate. Within this alternating sequence, intercalations of diopside- and wollastonite-bearing marble reach maximum thicknesses of approximately 80m. The Tinkas Member is considered by Martin (1979, pers. comm.) to represent a typical calc-arenite turbidite sequence, and the thick marble units present on Otjua indicate that the deposition of the turbidite sequence was interrupted by periods of quiescence characterized by negligible clastic input.

Copper mineralization is present within calc silicates of the Tinkas Member at the abandoned Gamikaubmund mine on Ukuib 84, as well as within calc silicate xenoliths in Damaran diorites at the abandoned Pot mine on Palmental 86. At the former, mineralized calc silicate units reach maximum thicknesses of about 15m, and contain disseminations of chalcopyrite and bornite. Damaran granodiorites which have invaded the sequence in the vicinity of the mineralized

zones have mobilized some of the copper. At the Pot mine the copper mineralization is again associated with a calc silicate sequence which occurs as a xenolith within a Damaran diorite. The xenolith measures a few metres in width and extends along strike for about 200m. The copper appears to have been mobilized by the diorite and is preferentially concentrated along the diorite-calc silicate contact. Other small xenoliths of calc silicate containing disseminated chalcopyrite are present within the Damaran granitoids which invade the Tinkas sequence on the Otjimbingwe Reserve 104.

III.3. Conclusions

Fluviatile clastics of the Etusis Formation followed by shallow-water calcareous, feldspathic sandstones of the Khan Formation represent the Nosib Group which constitutes the base of the Damara Sequence. This is overlain by the Swakop Group which represents a typical geosynclinal sequence starting with carbonates, quartzites, conglomerates and pelites (Rössing Formation), followed by mixtites (Chuos Formation) and a dominantly calcareous succession (Karibib Formation), and ending with a monotonous series of biotite-bearing schists (Kuseb Formation).

Weakly radioactive quartzites are present within the Etusis Formation in the vicinity of the Khan gorge on Namibfontein 91. The radioactivity is caused by the presence of Th-bearing monazite grains which occur interstitially or as inclusions in quartz and feldspar.

Smoky quartz pebbles which are probably derived from a strongly radioactive pre-Damaran granitoid are present within fluviatile

channel-type conglomerates within the Etusis quartzite on the Langer Heinrich Mountain.

Stratiform copper deposits are present at the top of the Khan Formation, and at various levels within the Rössing Formation and the Tinkas Member, in certain areas of the Damaran belt. The disseminated ore minerals which may include chalcopyrite, bornite and chalcocite occur preferentially within calc silicate units. Locally the copper has been partially mobilized by Damaran granitoids which invade the mineralized sequences.

Many of the metasediments of the Damara Sequence display alteration effects including sericitization of feldspar; calcitization or haematization of feldspar or hornblende, and saussuritization of biotite, hornblende or diopside. The alteration effects are very similar to those observed within the basement rocks, and it is likely that both are the result of the migration of fluids during the final stages of the Damaran metamorphism.

CHAPTER IV

THE GEOLOGY OF THE DAMARAN INTRUSIVES

IV.1. Introduction

Damaran intrusives from different parts of the central belt of the orogen have been described by Smith (1965), Martin (1965), Nash (1971), Faupel (1973), Jacob (1974a), Hoffman (1976), Kröner and Hawkesworth (1977), Berning et al. (1976), Toens et al. (1979), Cuney (1980) and Marlow (1981). Smith (1965) considered that 70% of the intrusives within the central belt were formed syn-tectonically by granitisation and magmatic assimilation, and that the rest were intruded at a late- to post-tectonic stage mainly as coarse grained leucocratic granites and pegmatites. Smith (1965) also established a subdivision of the syn-tectonic intrusives into red gneissic granite and grey biotite-rich gneiss and granite. He considered the former to be confined to antiformal structures below the stratigraphic level of the Karibib Formation, and the latter to be confined to synformal structures above the level of the Karibib Formation.

Smith's (1965) subdivision of the Damaran intrusives has been rejected for two reasons. Firstly, granitoids mineralogically identical to those within syn-tectonic suites are present as post-tectonic granitoids, and secondly there is not a total stratigraphic control on the location of the red gneissic granites and grey biotite-rich gneisses. A new subdivision of the Damaran granitoids is suggested, into Salem type granites, red granites, leucogranites and alaskites. This fourfold classification is necessarily a broad one, and is based mainly upon mineralogy. It does not endeavour to include every single intrusive

within the central belt, but merely to classify the major granite types which dominate the region.

The Salem type granites and red granites are syn- to post-tectonic in nature, whilst the leucogranites and alaskites are late- to post-tectonic. North of the Okahandja Lineament Zone (Miller, 1980, Downing and Coward, 1981), Salem type granites, red granites and alaskites predominate, whereas within and to the S. of this zone leucogranites prevail.

IV.2. The Salem type granites

The term "Salem granite", as pointed out by Blaxland et al. (1979), encompasses a suite of different generations of granodiorites, granites and adamellites, the type example occurring in the Swakop River on the farm Salem 102. Field relationships and age determinations (Kröner, 1981) indicate the earlier Salem granites tend to be more dioritic in composition, as on Palmental 86; whilst a general sequence from non-porphyrific, through porphyritic to leucocratic can be found in many areas. This sequence corresponds to Jacob's (1974a) threefold subdivision of the Salem granites in the lower Swakop River into non-porphyrific gneissic granite, porphyritic biotite granite and leucogranite.

The Salem granites consist essentially of quartz, K-feldspar, plagioclase, biotite and Fe-oxide. Symplectite is commonly present in the form of quartz blebs in plagioclase and orthoclase, and on Goas 79 the porphyritic Salem granite displays spectacular bundles of symplectite up to 4mm across. Hornblende may occur, especially in the more granodioritic varieties, where it can be the only ferromagnesian

mineral present. The accessories include euhedral to anhedral zircon which may be zoned as well as anhedral apatite, monazite and sphene. Alteration products include sericite after feldspar, muscovite and chlorite after biotite, calcite after hornblende, leucoxene after sphene and hornblende and haematite after magnetite.

Within the porphyritic varieties of the Salem granite the phenocrysts, which commonly exceed 3cm in length, consist of perthite or K-feldspar, and any of the feldspars may display zoning. The chemistry of the biotite as defined by the pleochroic scheme is variable, as is the development of pleochroic haloes around zircon inclusions. Metamorphic garnet may be present locally in the leucocratic facies of the Salem granite, as in the Swakop River between the Rote Adlerkuppe and the Witpoortberge. The characteristic mineralogical features of the Salem granites are summarised in Table 6.

The Salem granites are typically batholithic in form, and were considered by Smith (1965), Miller (1973), Jacob (1974a) and Hoffmann (1976) to be confined to synclinal structures within the Kuiseb Formation, and to have originated by granitisation or magmatic assimilation of the Kuiseb rocks. Sharp contacts between the various Salem granites and metasediments predominate, however, (Plate 7) and locally the granites occur well below the level of the Karibib Sequence. In the Onanis River, S.E. of Salem 102 foliated, porphyritic Salem granite is intrusive into both Etusis quartzite and basement augen gneiss, and in the Swakop River just W. of the Klein Gawib River as well as in the Skeleton Gorge, porphyritic Salem granite is in sharp contact with Etusis quartzite. Flow banding and biotite-bearing pegmatites are characteristic of the Salem granite, and xenoliths of

Table 6. Characteristic mineralogical features of the Damaran intrusives

Mineralogical Constituents	Salem	Red	Alaskites
	Granites	Granites	Leucocranites
MAJOR	Quartz, K-feldspar, plagioclase, biotite, Fe-oxide. ± myrmekite, hornblende	Quartz, microcline, perthite, plagioclase, biotite	Quartz, perthite, microcline, orthoclase, plagioclase (An 0-20, Jacob, 1974a).
MINOR	± sphene	± Fe-oxide, sphene, muscovite, hornblende, myrmekite, riebeckite	Biotite ± symplectite
ACCESSORY	zircon, apatite, monazite + sphene (more abundant when present in association with hornblende).	zircon, monazite, apatite, rutile. ± uraninite.	zircon, sphene, monazite, Fe-oxide sulphide, apatite, rutile. ± Uraninite, betafite.
METAMORPHIC	± Garnet in leucocratic types	± garnet, sillimanite, anthophyllite, muscovite	± biotite, garnet, sillimanite
COMMON SECONDARY	sericite after feldspar, muscovite + chlorite after biotite, haematite + limonite after Fe-oxide, calcite after hornblende, leucoxene after sphene + hornblende	sericite + muscovite + calcite + haematite + epidote after feldspar, chlorite + muscovite after biotite	sericite + muscovite + calcite after feldspar, chlorite + calcite + muscovite after biotite.
CHARACTERISTIC FEATURES	Perthite or K-feldspar phenocrysts. ± Biotite bearing pegmatite.	Microcline commonly very abundant. Zoned feldspars Non-sericitized feldspar rims	Quartz-feldspar + quartz-tourmaline graphic intergrowths

biotite schist and quartzite displaying sharp contacts with their host are commonly developed (Plate 7).

On Naob 69 (Folder 1, E3) a plug like body of Salem diorite measuring about 200m in diameter, and roughly circular in outcrop, is intrusive into basement augen gneiss. The diorite is medium to coarse grained and is associated with a hornblende- and ilmenite-bearing pegmatite. It outcrops either side of a tributary of the Naob River, and on the S. side it displays a strong fabric which is conformable with the margin of the body, as well as the regional tectonic fabric in the basement augen gneiss to the S.E. It is uncertain whether this fabric is tectonic or igneous in nature. The absence of tectonic fabrics elsewhere in the body, and the conformability of the fabric with the contact would suggest an igneous origin however.

The diorites consist of large anti-perthite phenocrysts and metamorphic aggregates of hornblende, sphene, ilmenite, phlogopite and allanite, set in a recrystallized polygonal groundmass of quartz, orthoclase and subordinate plagioclase with accessory, interstitial zircon, rutile, apatite and ilmenite. The feldspars are slightly sericitized, whilst the hornblende shows partial alteration to calcite, muscovite and chlorite, and the metamorphic phlogopite is slightly altered to chlorite and epidote.

IV.3. The red granites

The red granites are characterized by small amounts of ferromagnesian minerals, as well as large amounts of K-feldspar. Mineralogically they consist of quartz, microcline, perthite, plagioclase, biotite and opaque Fe-oxide. Muscovite may be present

but is always subordinate to biotite, and symplectic intergrowths between quartz and plagioclase, and quartz and microcline are occasionally observed. Primary amphibole occurs in the form of either hornblende or riebeckite in the foliated red granite dykes E. of the Audawip River on the Otjimbingwe Reserve 104; whilst metamorphic amphibole is present in the form of anthophyllite in the post-tectonic red granite on Lukasbank 63 (Folder 5).

Sphene is present in the hornblende-bearing red granites as a minor constituent, and garnet, a metamorphic mineral normally absent in the red granites, has been observed in a foliated red granite in the Onanis River. Metamorphic sillimanite occurs in the post-tectonic red granite on Namibfontein 91 and Lukasbank 63 (Folder 5).

The accessory minerals comprise euhedral to anhedral zircon, both as interstitial grains and as inclusions; euhedral to subhedral zoned monazite which reaches a maximum grain size of 0.5mm in the red granite on Namibfontein 91; as well as apatite and rutile. The alteration products include sericite, muscovite and calcite after feldspar, and chlorite and muscovite after biotite. Among the essential constituents microcline is commonly very abundant and may be zoned, whilst biotite shows a large compositional range. Opaque Fe-oxide, normally present as a minor constituent rather than an accessory, reaches a grain size of 0.5cm in the red granite dykes on the Otjimbingwe Reserve 104. The mineralogical characteristics of the red granites are shown in Table 6.

Smith (1965) considered the red gneissic granites around the Khan and Swakop Rivers to be confined to anticlinal and domal structures, below the level of the Karibib marble, and to have been derived by anatexis of rocks below this stratigraphic level. Jacob (1974a) termed the same

rocks in the lower Swakop River "red granite gneisses", and regarded them as anatectic products of the basement and Etusis Formation; whilst Hoffmann (1976) concluded that the red granites are most likely to have originated by partial melting of the Etusis and Khan Formations.

The red granites display a wide range in their mode of intrusion. Dykes are common on the Otjimbingwe Reserve 104, Abbabis 70, Habis 71, Otjua 37, Horebis Sud 108 and in the Ozomband River area (Plate 8). The dykes on the Otjimbingwe Reserve 104 are fine to medium grained and porphyritic, and they show a well developed foliation defined by the feldspar phenocrysts, which can be up to 1cm in length. The larger dykes, which show maximum thicknesses of a few metres, may contain veins of fine grained, leucocratic red granite which probably represents an aplitic phase of the red granite intrusion. The dykes on Abbabis 70 and Habis 71 consist of fine grained, leucocratic red granite porphyries which contain a strong fabric. The phenocrysts consist of feldspar and subordinate quartz, and reach a maximum of 4mm across.

On Otjua 37 the south-western contact between a body of red granite and Salem granite occurs in the form of a vertical or sub-vertical dyke swarm (Folder 2; D7, 8 and 9). The red granite is clearly intrusive into the Salem granite, individual dykes varying in thickness from 1m to 10m. In the Achas River on Horebis Sud 108 post-tectonic red granite dykes intrude Etusis quartzite, foliated Salem granodiorite and foliated porphyritic Salem granite. The red granite is medium grained, equigranular and characteristically contains abundant magnetite porphyroblasts and red feldspar-bearing pegmatite.



Plate 7. Biotite schist xenolith displaying a sharp contact with foliated, porphyritic Salem granite in the Skeleton Gorge, N. of the Swakop River in the Namib Desert Park.



Plate 8. Biotite- and muscovite-bearing, flow banded red granite dykes and sheets intrude foliated, porphyritic Salem granite in the Ozomband River, W. of Okahandja.

To the S. of Okakoara 43, on the farms Ombujomenge 39 and Meyersrust 118 a larger red granite dome is present. The granite is medium to coarse grained, equigranular, muscovite- and biotite-bearing and post-tectonic in nature, and it contains muscovite-bearing pegmatite. On the extreme eastern side of Okongava East 72 the granite contains metamorphic garnet, whilst on the S.W. corner of Ombujomenge 39 it contains quartz-feldspar graphic intergrowths and tourmaline. The dome is directly overlain by Karibib marble, and has a well developed marginal foliation along its northern rim which varies between 100m and 500m in thickness. In the centre of the dome flow banding is developed, and locally a flow banded facies invades the equigranular facies.

On Otjua 37 post-tectonic red granites occur in the form of a stock measuring over 3km by 1.5km within the core of a dome of Etusis quartzite (Folder 2). The granite was previously mapped as early red gneissic granite (Smith, 1966), and was not differentiated from a porphyritic Salem granite which invades the quartzite mainly along its upper contact with the Tinkas Member (Folder 2). Where the red granite is in direct contact with the Salem granite the dyke swarms are developed (described above). Other small dyke and sheet-like bodies of red granite occur within the quartzites elsewhere in the dome.

The red granite on Otjua 37 is medium to coarse grained, leucocratic, normally equigranular and occasionally flow banded. It consists of quartz, microcline, plagioclase and orthoclase with minor biotite and accessory Fe-oxide, muscovite, rutile, monazite and zircon. Xenoliths of biotite schist and quartzite are very common, as are pegmatites containing muscovite, magnetite and biotite, and

To the S. of Okakoara 43, on the farms Ombujomenge 39 and Meyersrust 118 a larger red granite dome is present. The granite is medium to coarse grained, equigranular, muscovite- and biotite-bearing and post-tectonic in nature, and it contains muscovite-bearing pegmatite. On the extreme eastern side of Okongava East 72 the granite contains metamorphic garnet, whilst on the S.W. corner of Ombujomenge 39 it contains quartz-feldspar graphic intergrowths and tourmaline. The dome is directly overlain by Karibib marble, and has a well developed marginal foliation along its northern rim which varies between 100m and 500m in thickness. In the centre of the dome flow banding is developed, and locally a flow banded facies invades the equigranular facies.

On Otjua 37 post-tectonic red granites occur in the form of a stock measuring over 3km by 1.5km within the core of a dome of Etusis quartzite (Folder 2). The granite was previously mapped as early red gneissic granite (Smith, 1966), and was not differentiated from a porphyritic Salem granite which invades the quartzite mainly along its upper contact with the Tinkas Member (Folder 2). Where the red granite is in direct contact with the Salem granite the dyke swarms are developed (described above). Other small dyke and sheet-like bodies of red granite occur within the quartzites elsewhere in the dome.

The red granite on Otjua 37 is medium to coarse grained, leucocratic, normally equigranular and occasionally flow banded. It consists of quartz, microcline, plagioclase and orthoclase with minor biotite and accessory Fe-oxide, muscovite, rutile, monazite and zircon. Xenoliths of biotite schist and quartzite are very common, as are pegmatites containing muscovite, magnetite and biotite, and

quartz-feldspar graphic intergrowths. The granite appears to have partially mobilized the constituent xenoliths, as well as the country rock in its immediate vicinity. Biotite schist xenoliths show signs of partial melting, with the development of melt and restite bands, whilst quartzites occasionally display gradational and cusped contacts with the granite.

IV.4. The leucogranites

The leucogranites which are typified by the Donkerhuk and Bloedkoppie granites, are characterized by their leucocratic nature, their white to grey colour, and their predominantly late- to post-tectonic nature. Mineralogically they consist of quartz, K-feldspar, perthite, plagioclase, muscovite and opaque Fe-oxide. K-feldspar is normally the dominant feldspar present. Metamorphic garnet may be present in relatively large amounts, as in the medium grained, porphyritic facies of the Gawib granite in the Namib Desert Park; whilst biotite if present is normally subordinate to muscovite. Both hornblende and sphene may be present as in the Achas granite on Wilsonfontein 110. Symplectic intergrowths of quartz and K-feldspar are not infrequent, whilst tourmaline is present in the Bloedkoppie granite in the Namib Desert Park, Magnetite commonly occurs as a minor constituent, and on Kamandibmund 83 leucogranite dykes contain magnetite porphyroblasts up to 6mm across.

The accessory minerals may include euhedral to anhedral, zoned zircon; euhedral to subhedral monazite which reaches a maximum grain size of 0.1mm in the leucogranite on Stinkbank (Folder 5); apatite as in the Horebis granite on Modderfontein 131 and the Achas granite, and also opaque Fe-oxide. The zircons in the Donkerhuk granite

on the Otjimbingwe Reserve 104 appear to be of two generations, the first occurring as relatively large and often elongated grains in the groundmass, and the second being smaller, euhedral and occurring as inclusions in the biotite.

The phenocrysts in the porphyritic leucogranites normally consist of perthite or K-feldspar, but antiperthite has been observed in the Bloedkoppie granite. The feldspars are commonly sericitized and muscovitized, whilst the biotite shows partial alteration to chlorite and muscovite. A characteristic feature of many of the feldspars within the Damaran granitoids is the presence of non-sericitized albitic rims surrounding sericitized cores (Plate 9), which suggests the sericitic alteration pre-dates complete recrystallization. The characteristic mineralogical features of the leucogranites are summarised in Table 6.

Faupel (1973) considered that the Donkerhuk granite crystallized from a melt derived by anatexis of a geosynclinal sediment during tectonic processes and metamorphism. Jacob (1974a) however, proposed that the leucogranites in the lower Swakop River were probably derived from residual melts of earlier granites, the Bloedkoppie granite in particular being formed from a Salem residual melt.

The leucogranites have a variable mode of intrusion which is commonly batholithic, but may also be diapiric or in the form of large and small scale dykes and sills, or as plugs. The Donkerhuk and Bloedkoppie granites form large scale batholiths, whilst dykes of Bloedkoppie granite are commonly present within the Tinkas sequence on the periphery of the main intrusion (Plate 10). In the Klein Tinkas River the Bloedkoppie granite contains xenoliths of fine grained, foliated, porphyritic biotite granite, basement augen gneiss and Etusis quartzite.

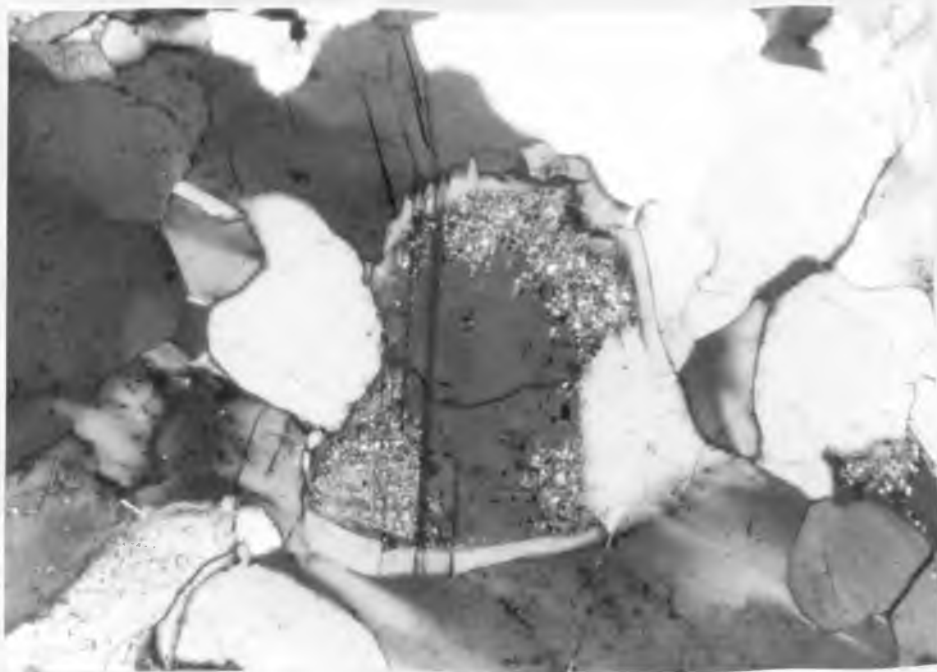


Plate 9. Photomicrograph of a leucogranite from Stinkbank 62, illustrating a non-sericitized albitic rim surrounding a sericitized plagioclase grain, (XN; x 100).



Plate 10. Bloedkoppie granite dyke with apophyse in biotite schist and calc silicate sequence of the Tinkas Member in the Namib Desert Park.

The leucogranites on Kamandibmund 83 occur in the form of dykes and small plugs, and they intrude Salem diorites and late pegmatites. On Palmental 86 and the Otjimbingwe Reserve 104 they invade the diorites as well as small gabbro stocks (Fig. 13). The leucogranite forming the Geisterberg on Consolidated Kaliombo 119 forms a post-tectonic body over 3km across within Kuiseb schists, whilst the leucogranite on Stinkbank 62 (Folder 5), forms post-tectonic intrusions in Karibib and Kuiseb rocks as well as early Salem granites.

Jacob (1974a) considers the Gawib granite in the Namib Desert Park to be a stock, but the granite shows many features characteristic of a high level, post-tectonic diapir. The early marginal granodioritic facies was located on both the eastern and western sides of the body, although the central porphyritic facies does occur in direct contact with the Tinkas sequence where the marginal granodiorite is absent. The non-porphyritic phase mentioned by Jacob (1974a), appears to form a core to the diapir, whilst his aplitic phase represents a late, leucocratic facies which occurs as dykes within the granodioritic and porphyritic facies.

Two varieties of leucogranite are present in the region of Ubib 76 and Tsawisis Suid 95 (Folder 1). The first occurs in the form of a large pluton mainly on Ubib 76, and it displays excellent intrusive relationships with most lithologies of the basement as well as a sequence of the Damaran metasedimentary cover. The leucogranite is medium to coarse grained and equigranular, and consists of quartz, plagioclase, perthite and subordinate orthoclase with minor biotite or muscovite, accessory Fe-oxide and metamorphic garnet. It contains a muscovite-, biotite- or magnetite-bearing pegmatite, and displays flow banding along its contact with the Etusis quartzite on Tsawisis

Suid 95 (Folder 1, R8). The second leucogranite post-dates the first and forms two relatively small lenticular bodies which occur along the contact between the earlier leucogranite and the basement rocks on Ubib 76 (Folder 1, H3), and Tsawisis Suid 95 (Folder 1, R9). The northern body was previously mapped as pegmatite (Smith, 1966). The age relationship between the two granites is well displayed at the southern body, where an E. to W. trending swarm of pegmatite dykes associated with the younger leucogranite intrude the earlier one (Folder 1, Q9). The rock is medium grained, equigranular and differs from the earlier leucogranite by its absence of garnet, and its presence of large metamorphic muscovite grains which commonly form reaction rims around the anhedral Fe-oxide grains.

IV.5. The alaskites

The alaskites are fine to coarse grained or pegmatitic granites, characterized by their extremely leucocratic nature, as well as their anastomosing and vein-like style of intrusion (Plate 11). They are hosts to the uranium mineralization at Rössing, and because of their economic importance have been the subject of discussion by Nash (1971), Jacob (1974b), Rogers et al. (1978), Corner and Henthorn (1978), Toens et al. (1979), Cuney (1980), Hawkesworth and Marlow (1981) and Marlow (1981).

Essentially the alaskites consist of quartz, feldspar and minor biotite. The feldspar may be perthite, microcline, orthoclase and plagioclase (An_{0-20} , Jacob, 1974a), although potash feldspars are dominant and any can display zoning. Accessory minerals include rounded to euhedral zircon, zoned sphene, monazite, opaque Fe-oxide, sulphides, apatite, fluorite and rutile. The alteration products

are chlorite, calcite and muscovite after biotite, and sericite, muscovite and calcite after feldspar.

Symplectitic intergrowths of quartz in plagioclase or orthoclase are commonly present within the alaskites, and occasionally zoned, whilst macroscopic quartz-feldspar graphic intergrowths are also common in some bodies. Biotite which normally occurs as a minor constituent or an accessory may form metamorphic clots or bundles up to a few centimetres across. Metamorphic garnet and sillimanite have been observed within the alaskite on Valencia 122, whilst on Wolfkoppe 105 tourmaline is relatively abundant. The characteristic mineralogical features of the alaskites are summarised in Table 6.

The alaskites are considered by Jacob (1974a) to have originated by anatexis of basement and Nosib rocks, whilst Berning et al. (1976) suggest they were derived by syntexis of basement rocks and the Etusis quartzite. The alaskites commonly display sharp contacts with the rocks they invade, but occasionally migmatitic rocks derived from both the basement and the Damaran metasedimentary cover cannot be distinguished from alaskites either in composition or texture, suggesting that some alaskites are in fact derived from migmatized basement, and that others are derived from migmatized cover.

In the Swakop River, S. of the Tsabichas River, migmatized basement is invaded by alaskites, some of which display sharp contacts, whilst others show diffuse ones. Three generations of alaskite can be seen in this vicinity; firstly as leucosome which parallels the deformed fabric within the migmatized basement; secondly as alaskite which encloses xenoliths of the migmatized basement, and thirdly as anastomosing alaskite veins which cut the alaskite-basement xenolith contacts (Plate 12).



Plate 11. Anastomosing veins of alaskite in biotite schists of the Etusis Formation in the Rössing dome.

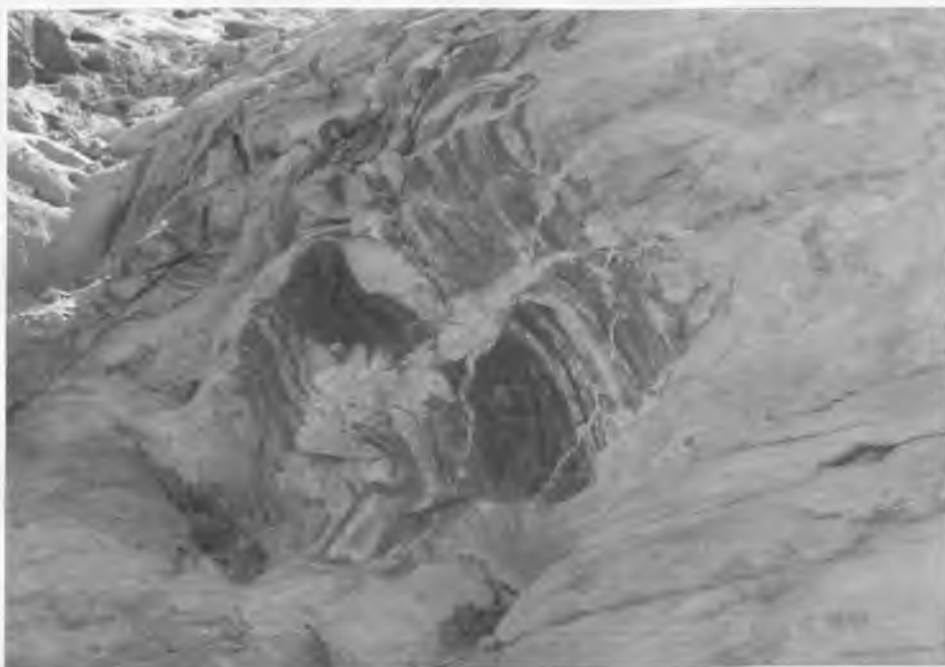


Plate 12. Migmatized basement xenolith included in alaskite which is cut by anastomosing alaskite veins, in the Swakop River S. of the Tsabichas River, (xenolith approximately 10m across).

On Namibfontein 91, Wolfkoppe 105 and Bergrus 94, S.E. of the Khan River, alaskites invade the Etusis quartzite in the form of dykes sheets and plugs. Migmatized zones of quartzite which resemble alaskite are locally developed on a small scale, but the larger bodies of alaskite all display sharp contacts with the quartzite.

IV.6. The gabbros

Gabbros of Damaran age occur locally within the central belt of the orogen, but they do not readily fall into the fourfold classification proposed for the Damaran intrusives and for this reason are discussed here separately. They occur in a number of areas within the central belt: firstly on Palmental 86 and the adjacent parts of the Otjimbingwe Reserve 104; secondly on Etusis 75 and the adjacent parts of Neikhoes 74 and Goas 79; thirdly as isolated outcrops on Neu Schwaben 73 and Okongava East 72, and finally on Stinkbank 62.

On Palmental 86 and the Otjimbingwe Reserve 104 coarse grained, equigranular gabbros occur as dykes, plugs and stocks within the Tinkas sequence and within foliated Salem diorites and granodiorites. The area in the vicinity of the gabbro outcrops has been mapped to a scale of 1:50,000, and the distribution of the gabbros is shown in Fig. 13. The gabbros contain inclusions of calc silicate, marble and biotite schist and display sharp contacts with the early Salem granitoids. The feldspar content within the gabbros is variable, and the plagioclase phenocrysts may reach a maximum size of 1cm in length.

In the Neikhoes 74 - Etusis 75 - Goas 79 area a pluton of Salem diorite is cut by a series of gabbroic ring dykes. The individual dykes extend for up to 1km in length and they occur within a zone of Salem diorite measuring about 5km in diameter. The distribution of the

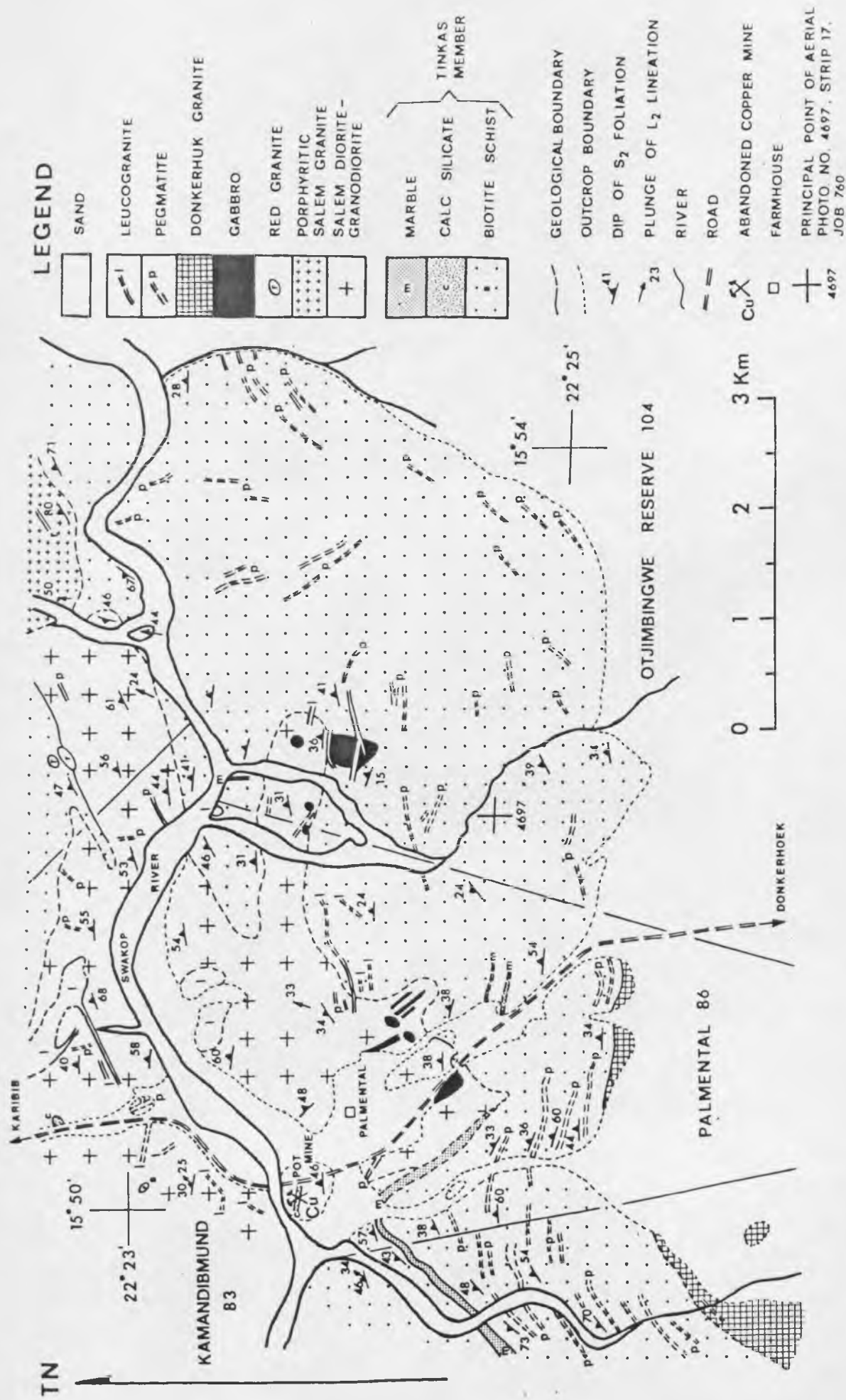


Fig. 13. Geological map of part of Palmental 86 and the Otjimbingwe Reserve 104, illustrating the distribution of gabbro outcrops.

ring dykes is shown on Smith's (1966) geological map.

On Neu Schwaben 73 in the vicinity of Henkert's tantalum prospect, equigranular sulphide-bearing gabbros intrude foliated Salem granites and biotite schists of the Kuiseb Formation. The gabbros contain metamorphic biotite, garnet and pyrite cubes up to 1cm across, as well as minor disseminations of chalcopyrite. The gabbros are cut by dykes of biotite-bearing, leucocratic granite and muscovite, tourmaline and columbite/tantalite-bearing pegmatite. On Okongava East 72 about 7km N.E. of the Henkert prospect, Smith (1965 and 1966) has mapped an isolated occurrence of gabbro which he considers is associated with mafic-rich portions of a quartz diorite intrusion.

On Stinkbank 62 an outcrop of gabbro is situated just over 1km S. of the farm road running from the Stinkbank siding to the Namibfontein farmhouse (Folder 5, H7). The body forms a prominent topographic high, measures some 150m across and has a circular outcrop pattern suggestive of a plug-like intrusion. A subsidiary outcrop measuring only a few metres across, and situated approximately 50m to the N.E. of the main intrusion may represent a satellite body. A few metres to the S. of the gabbro body, migmatized biotite schist of the Rössing sequence is exposed, whilst to the N.E. an equigranular red granite outcrops. The latter invades the Rössing sequence in this region in the form of lit-par-lit intrusions, but the age relationship between the red granite and the gabbro is unknown. However, a red pegmatite which is commonly associated with the red granite on Namibfontein 91 and Stinkbank 62, occurs as a N.W. trending dyke within the gabbro, suggesting the latter pre-dates the red granite.

The gabbro on Stinkbank 62 is coarse grained and equigranular, and

it consists of a recrystallized network of plagioclase, cummingtonite, diopside, phlogopite and Fe-oxide, with relict olivine grains displaying partial alteration to antigorite. Reaction rims around the olivines consist of an inner zone of diopside, surrounded by cummingtonite which commonly displays symplectic intergrowths with the diopside. The Fe-oxide occurs mainly in association with antigorite within cracks in the olivines, but also as anhedral grains associated with the metamorphic minerals.

Gevers (1931) considers the gabbros which form the ring dykes on and around Neikhoes 74 are genetically related to the diorites which they intrude, and Smith (1965) concluded that they may possibly have been formed at the same time as the Salem diorites. The similarity of the gabbros within the areas discussed points to a common origin, but those on Stinkbank 62 and Neu Schwaben 73 show no association with diorites, which mitigates against a genetic relationship between the gabbros and the diorites. Also, those on and around Palmental 86 are clearly much later in age than the early Salem diorites and granodiorites which display strong tectonic fabrics, and if they are associated with these rocks they should theoretically have been emplaced before them. Further work on the gabbros is required before a clear understanding is obtained of their origin and their genetic relations with the rocks they are associated with.

IV.7. Conclusions

A fourfold classification of the Damaran intrusives from the central belt of the orogen into syn- to post-tectonic Salem type granites and red granites, and late- to post-tectonic leucogranites and alaskites is proposed.

Sharp contacts between the various Salem granites and the metasediments of the Damara Sequence are predominant, and locally the Salem granites occur well below the stratigraphic level of the Karibib Formation, and it is considered they are derived from a source deeper than the Damara Sequence.

The alaskites commonly display sharp contacts with the rocks they invade, but occasionally migmatitic rocks derived from both the basement and the Damaran metasedimentary cover cannot be distinguished from alaskites either in composition or texture, suggesting that some alaskites are in fact derived from migmatized basement, and that others are derived from migmatized cover. Locally at least three generations of alaskite are present.

Many Damaran granitoids contain zoned feldspars with non-sericitized albitic rims surrounding sericitized cores, which suggests that the sericitization pre-dates complete recrystallization, and represents a deuteritic alteration. The sericitization is commonly associated with calcitization of feldspar or hornblende, chloritization and muscovitization of biotite and hornblende, saussuritization of phlogopite and haematization of magnetite. These alteration effects are very similar to those observed within the basement and metasedimentary cover rocks, and it is likely that these were coincident with the deuteritic alteration of the granitoids.

CHAPTER V
STRUCTURAL EVOLUTION

V.1. Introduction

A structural analysis has been made of the five areas which were mapped in detail, viz. the section across the Abbabis inlier (Folder 1); the area surrounding the mineralized alaskites on Goanikontes (Folder 3); the region in the vicinity of the mineralized alaskites on Valencia 122 (Folder 4); the parts of Stinkbank 62 and Namibfontein 91 containing radioactive granites (Folder 5); and the portion of Otjua 37 where mineralized red granites are exposed (Folder 2). Though there has been no previously published detailed work in these areas, the regional structural style of the central portion of the Damaran orogen is well displayed on the geological maps of Smith (1966) and Jacob (1974a). These authors mapped a series of N.E. to S.W. trending antiforms and synforms, and reported the presence of fold interference patterns in several localities. Recently, detailed structural analyses of specific regions of the central belt have been undertaken by Sawyer (1978), Haack et al. (1980), Barnes (1981) and Downing (in prep.), whilst regional studies across the belt have been made by Miller (1980) and Coward (1981a and b).

The aims of this study are to:

- A. Establish the various tectonic events in each area analysed, and attempt a correlation of these events across the central belt.
- B. Relate the individual mineralized and radioactive granites and alaskites to the tectonic events recognized.
- C. Establish what effect, if any, the various deformation events have on the localization of mineralized granitoids.

The structural data such as schistosity planes, lineations and fold hinges shown on the geological maps are presented here in the form of stereograms. Poles to linear and planar fabrics are plotted on equal-area projections and where measurements within a single stereogram exceed about 30, the poles have been contoured with the help of a Karlsbeck diagram (Ragan, 1973). The contour figures, which refer to percentages per one percent of the stereonet area, are given for each stereogram in Appendix 2.

V.2. Structural evolution of the Valencia area

The portion of Valencia 122 mapped (Folder 4) is situated on the north-western limb of a major synform which is shown on the simplified geological map of the Damaran belt (Fig. 2). Younging directions indicate that the synform, which faces to the N.W., is the correct way up and the axial plane dips by $60-70^{\circ}$ to the S.E. The strike of the strong penetrative fabric on Valencia parallels the axial trace of the major synform, and the fold and fabric development are considered to have formed during the same tectonic episode. However, this is not the first event to be recognized within the area, as orthoclase poikiloblasts in biotite schists of the Kuiseb Formation contain inclusions which define a relict fabric which is discordant to the main penetrative fabric in the schists (Plate 13). A sketch of the photomicrograph (Fig. 14) illustrates the relationship between the relict fabric, designated S_1 , defined by the small biotite inclusions in the orthoclase poikiloblast, and the later fabric which is S_2 , delineated by the larger biotite grains which wrap around the poikiloblast.

The strong S_2 schistosity within the Damaran metasediments normally parallels the bedding defined by marble bands in the Rössing and Karibib

Formations. Other F_2 deformation features which accompanied the development of the S_2 fabric include boudinage structures which have developed within the more competent units of the Damara Sequence and isoclinal folds and strong linear fabrics. The linear fabrics are defined by ferromagnesian minerals in the Damaran schists, deformed pebbles in conglomerates of the Chuos Formation and perthite phenocrysts in the Salem granites. The S_2 fabrics within the metasediments and Salem granites on Valencia 122 are shown on the simplified structural map (Fig. 15; stereograms 3 and 1 respectively), and the pole-maxima common to both stereograms indicates that the dominant S_2 schistosity plane dips steeply to the S.W. The poles to the extensional L_2 fabrics in the Salem granite (stereogram 2) form a well defined maximum which plunges at 40° towards 194° .

The regional trend of the S_2 fabric has been deformed by an F_3 event which has produced an antiform-synform pair along the N.W. limb of the major F_2 structure described above. The wavelength of the open F_3 structures is about 1.5km and the axial traces strike S.S.W. As well as the open F_3 fold structures there are minor tight to isoclinal F_3 folds in the Kuiseb schists. These plunge towards the S.S.W. and develop strong S_3 axial planar fabrics in their hinge zones (Plate 14). The poles to the S_2 schistosity planes (stereogram 3) define a π -axis which plunges at 50° towards 197° . The pole-maximum of the lineations measured within the metasediments (stereogram 4) is close to the π -axis defined by the S_2 π -pole circle, as well as the L_2 pole-maximum of lineations in the Salem granite, and it is uncertain whether the lineations in the metasediments are L_2 or L_3 . Possibly they are L_3 lineations, in which case the L_2 and L_3 fabrics are co-linear. The pole-maximum of the S_3 axial planar fabrics



Plate 13. Photomicrograph of an orthoclase poikiloblast in a biotite schist from the Kuiseb Formation on Valencia 122 (PPL; x50; Folder 4, G8).

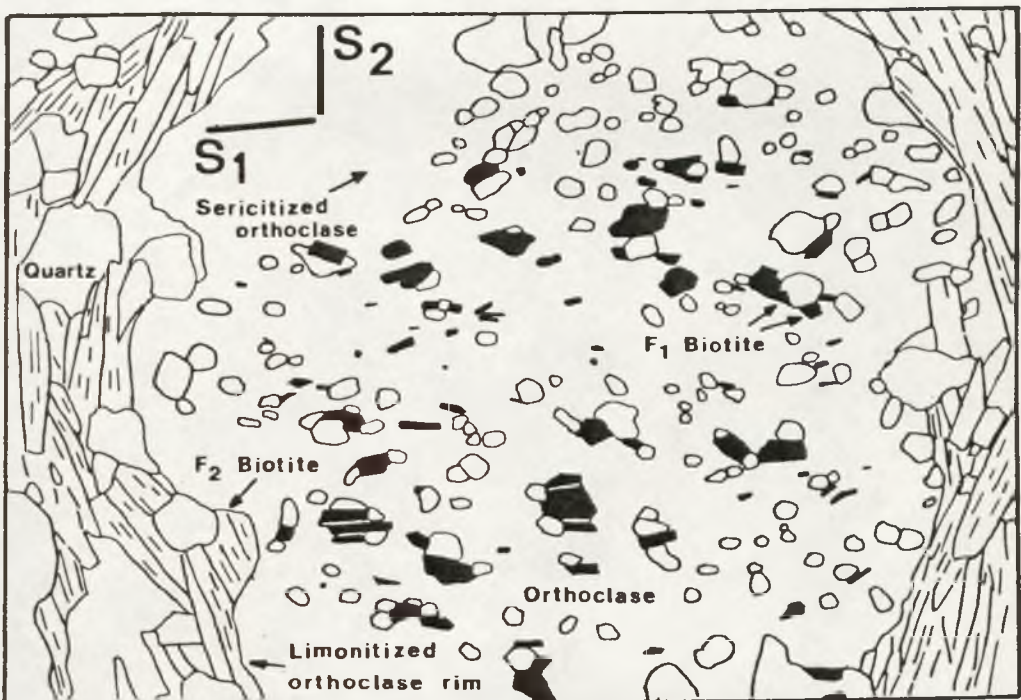
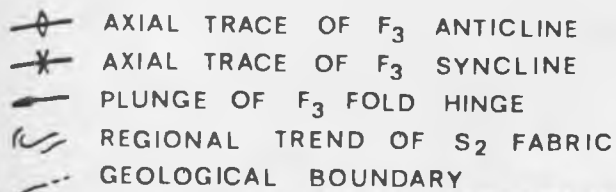
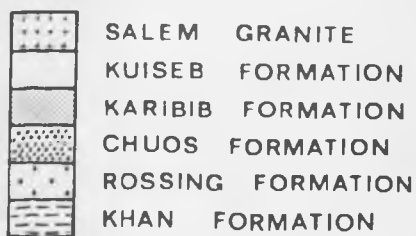


Fig. 14. Sketch of the photomicrograph shown in Plate 13, illustrating the relationship between the S_1 fabric defined by the small biotite inclusions within the orthoclase poikiloblast, and the S_2 fabric delineated by the larger biotite grains which wrap around the poikiloblast.

LEGEND



STEREOGRAMS

1. S₂ fabrics in Salem granite
2. L₂ fabrics in Salem granite
3. S₂ fabrics in metasediments
4. L₃ fabrics in metasediments
5. F₃ fabrics in Kuseb schists
6. F₃ fold hinges in Kuseb schists

0.0 0.2 0.4 0.6 Km

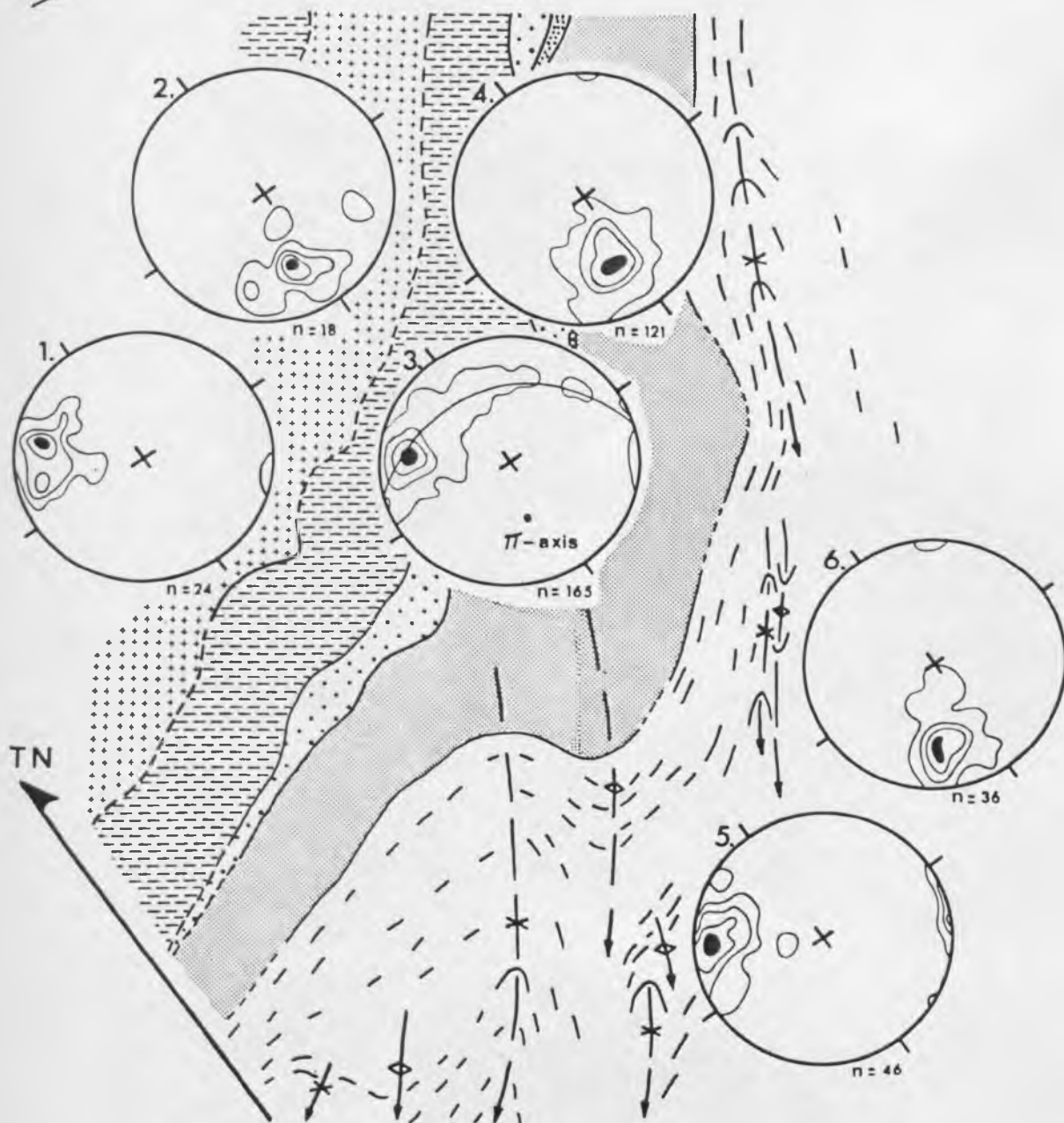



Fig. 15. Simplified structural map of part of Valencia 122. For detailed geology see Folder 4.

(stereogram 5) suggests that the axial planes of the open F_3 structures dip steeply to the S.E., and are locally co-planar with S_2 . The pole-maximum of the F_3 minor fold hinges (stereogram 6) indicates that the folds plunge at 32° towards 212° , close to the regional F_3 fold hinge defined by the π -axis to the S_2 fabrics.

As well as deforming the S_2 fabric in the Damaran metasediments the F_3 event has resulted in the deformation of pre- F_3 alaskites. Within the hinge zones of the minor isoclinal F_3 folds, alaskites which have invaded the Kuiseb schists display well developed parasitic folds. In the hinges parasitic 'M' folds have formed, whilst on the flanks parasitic 'S' and 'Z' folds are developed (Plate 15). Along the limbs of the minor isoclinal F_3 folds however, the alaskites which are more competent than the Kuiseb schists, are strongly boudinaged. The boudinaged nature of the pre- F_3 alaskites can be seen on a local scale (Plate 16) where individual boudins measure only a few centimetres in length, as well as on a regional scale (Folder 4; O-P, 7-8) where they measure up to 170m in length.

Post-tectonic alaskites clearly cut pre- F_3 boudinaged alaskites along the limbs of the minor F_3 folds in the Kuiseb schists (Folder 4; H and K8). Others display strongly folded veins and apophyses (Plate 17) which are considered to have formed in response to the emplacement of large volumes of nearby post-tectonic alaskite.

A number of deformed xenoliths within the Salem granite have been measured in an attempt to establish the strain which the granite underwent during the F_2 deformation. The biotite schist xenoliths which represent the strain markers are considered to be less competent than their quartzofeldspathic host, and will presumably give a maximum value for the strain



Plate 14. Sub-vertical axial planar S_3 fabrics intersecting folded S_2 fabrics in the hinge of a minor F_3 fold in the Kuiseb schists on Valencia 122 (Folder 4; E8).



Plate 15. Parasitic 'Z' folds developed in a pre- F_3 alaskite near the hinge zone of a minor isoclinal F_3 fold in the Kuiseb schists on Valencia 122 (Folder 4; F8).



Plate 16. Boudinaged pre- F_3 alaskites which have developed along the limb of a minor isoclinal F_3 fold in the Kuiseb schists on Valencia 122 (Folder 4; M8).



Plate 17. Ptygmatically folded veins and apophyses of post- F_3 alaskite in Khan metasediments on Valencia 122 (Folder 4; G3). The folds are considered to have formed in response to a stress system which developed during the emplacement of large volumes of post-tectonic alaskite.

ellipsoid. The xenoliths were measured near the upper contact of the Salem granite body with the Khan Formation (Folder 4; M4). Between 18 and 58 measurements were recorded within each principal plane, and the strain ellipsoid was determined by calculating the harmonic mean of the ratios measured. The harmonic mean (HM) is defined by Lisle (1977) as:

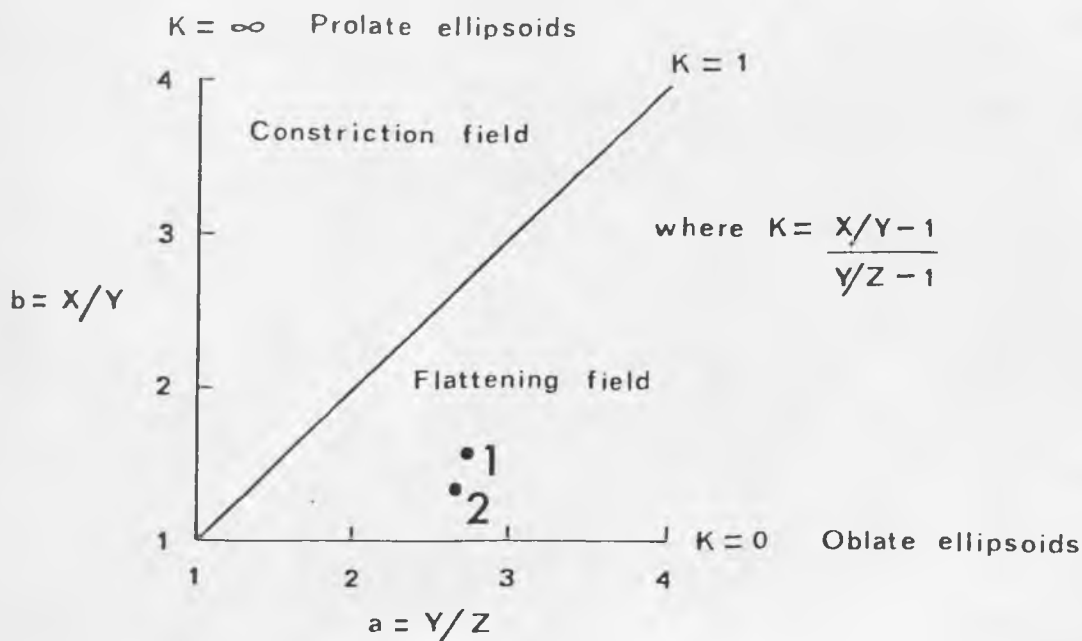
$$1/HM = 1/n (1/a_1 + 1/a_2 + 1/a_3 \dots\dots\dots 1/a_n)$$

A strain ellipsoid of 4.24 : 2.72 : 1 was obtained which falls well within the oblate field on the Flinn diagram (Fig. 16), indicating that the F₂ event resulted in the development of a strong flattening fabric in the Salem granites on Valencia 122.

The majority of alaskites on Valencia 122 are post-tectonic in nature, and the pre-F₃ alaskites are minor in number and restricted mainly to the Kuiseb Formation. Strongly mineralized alaskites appear to be concentrated within the Rössing and Karibib Formations in the core of the F₃ antiform (Folder 4; E-G, 5-6), and it is possible that the migration of alaskite to this part of the fold structure was influenced by the presence of a low-pressure regime within the fold core.

V.3. Structural evolution of the Goanikontes area

The mapped portion of Goanikontes (Folder 3) has been subdivided into five tectonic domains, and their distribution is shown on the simplified geological map (Fig. 17). Domain A consists of a N.E. trending antiform which is fault bounded to the N.W. It is underlain by quartzo-feldspathic Abbabis gneisses, and although exposures to the S. of the area mapped are very limited, aerial photographs indicate that the antiform closes just to the S. of square M15 on Folder 3. Domain B is characterized by a series of N.E. trending antiforms and synforms which are smaller in amplitude and



Rock type	Mean ratios						Flinn parameters		
	Y-Z	n	X-Z	n	X-Y	n	a	b	k
Salem granite	7.87	58	5.04	22	1.85	17	1.56	2.72	0.32
Etusis quartzite	5.53	38	4.13	54	1.54	32	1.34	1.54	0.63

Fig. 16. Flinn diagram displaying the strain states in (1) the Salem granite on Valencia 122 (strain ellipsoid = 4.24 : 2.72 : 1), and (2) the Etusis quartzite on Naob 69 (strain ellipsoid = 3.58 : 2.68 : 1).

tighter in style than the one in domain A. The nature of the fold structures along a N.W.-S.E. line across domains A and B is shown on profile A-B (Folder 3). Domain C consists of a refolded synform, the axis of which has been rotated from N.E. to S.E. Lineations in domain B plunge to the N.E., whilst those in domain C plunge to the S.W. Domains D and E represent small sub-areas of domain C, and consist of N.E. and S.E. trending antiforms, respectively.

Barnes and Downing (1979) consider that the area just to the E. of Goanikontes underwent two major nappe-forming events (F_1 and F_2), the first of which resulted in large scale repetitions and inversions of stratigraphy involving both the Abbabis basement and the Damaran cover. Stratigraphic inversions are not encountered in the area mapped, and the

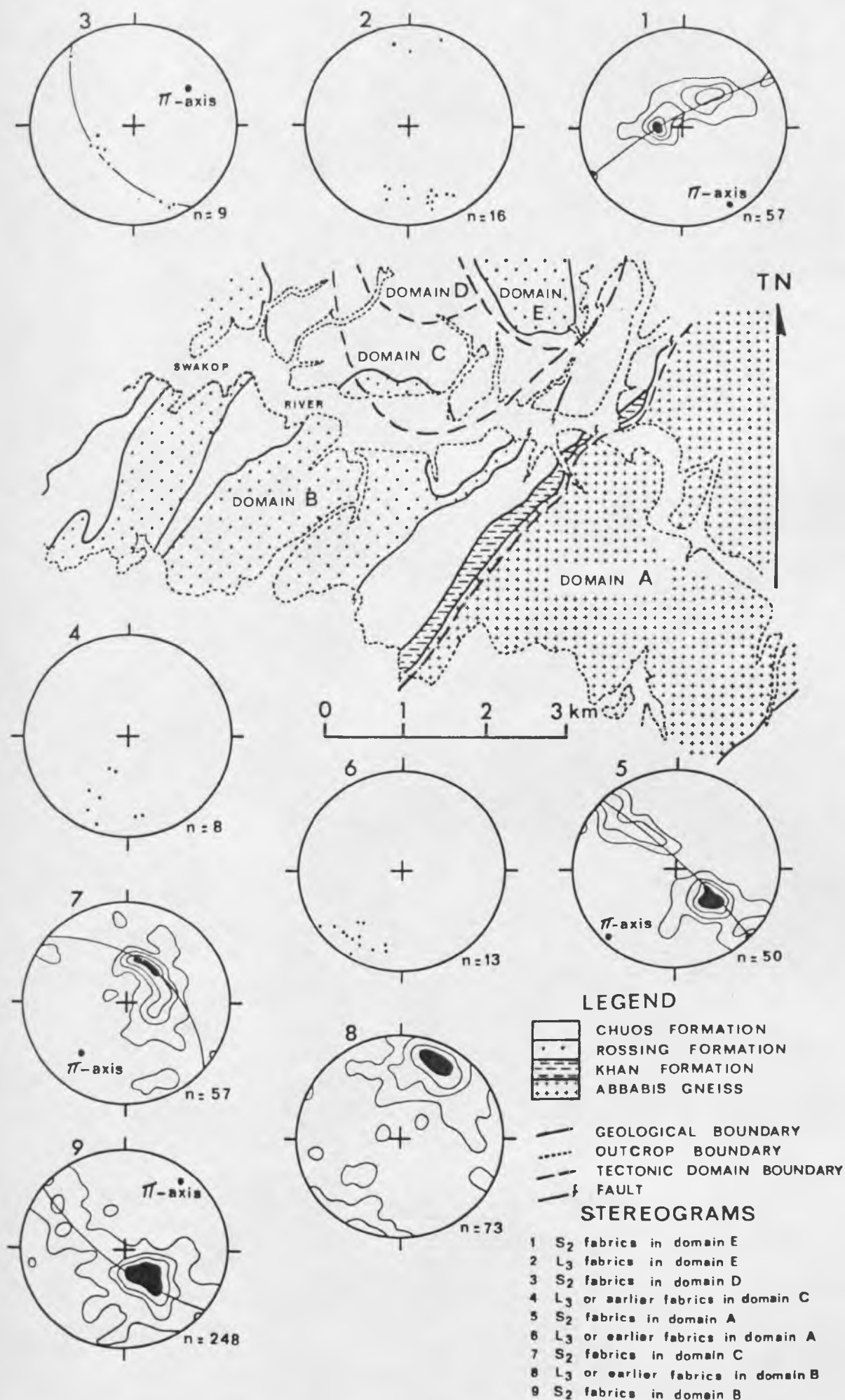


Fig. 17. Simplified geological map of the Goanikontes area showing the major tectonic domains.

earliest deformation recognized is associated with the F_2 event. This has resulted in the development of N.E.-striking isoclinal fold structures in domain B, strong penetrative fabrics, boudinage structures and thrust faults with fault traces striking to the N.E. The faults shown on profile A-B (Folder 3) have been steepened by F_3 or later events, but the original thrust planes were probably of a low angle. The fabrics on either side of the faults are parallel and conformable with the thrust planes. The overturned contact between the Abbabis gneisses and the Khan metasediments along the S.E. limb of the antiform in domain A may also be a fault contact. A narrow zone of quartzites measuring a few meters in thickness separates the quartzo-feldspathic gneisses from the Khan metasediments, but they are not considered to be Etusis in age, firstly because they are extremely limited in thickness, and secondly because similar rocks have been found incorporated within the Abbabis gneisses elsewhere in the antiform (e.g. Folder 3, P7). Immediately to the E. of this area the Etusis quartzite exceeds 1000m in thickness (Barnes, 1981) and it is not considered that local stratigraphic thinning would result in the observed thickness on Goanikontes.

The S_2 schistosity planes from each structural domain are represented as poles on the stereograms in Fig. 16. The S_2 poles from domain A (stereogram 5) fall along a π -pole circle which defines a π -axis (plunge 8° towards 224°) representing the fold hinge of the N.E. trending F_3 antiform. Similarly the S_2 fabrics from domains B, C, D and E define π -poles which represent the plunge of the F_3 fold hinges within each structural domain.

In domain B an F_3 and an F_4 deformation event has been recognized. The first resulted in the development of large and small scale recumbent

folds which verge to the N. These structures contain sub-horizontal fold hinges, and they are well displayed in the middle-distance of the photograph shown in Plate 18. The F_4 event gave rise to the widespread development of small scale open to isoclinal ptygmatic structures, which refold the F_3 structures. They are characterized by steeply plunging fold hinges which strike towards the N.N.E. (Plate 19). In domain C the F_3 or later deformation has resulted in the regional rotation of the isoclinal F_2 axial trace, and the open, asymmetric antiform in domain A is also regarded as an F_3 or later structure.

The lineations from each structural domain (excepting domain D) are represented as poles on stereograms in Fig. 17. The pole-maxima on each, fall in the same area of the net as the π -axis defined by the S_2 π -pole circle from the same structural domain. This suggests that the lineations are either L_3 lineations which parallel the F_3 fold hinges, or they are L_2 or earlier lineations which are co-linear with the F_3 fold hinge.

As on Valencia 122, at least two generations of alaskite have been recognized. On Goanikontes the majority of the alaskites post-date the F_4 deformation, but some bodies within domain B have been folded by the steeply plunging tight to isoclinal F_4 structures. Both ptygmatic folds and 'pinch and swell' structures are commonly developed in the post- F_4 alaskites. These structures are considered to have formed during the 'ballooning' of late domes, the ptygmatic folds being developed in the alaskites which transect the S_2 fabric, and the pinch and swell structures forming in those which parallel it. Alaskites displaying pinch and swell structures are occasionally seen folded around upright F_4 fold structures, indicating that the ballooning of the late domes was in



Plate 18. Recumbent F_3 folds in quartzites and schists of the Rössing Formation on Goanikontes. (Foreground J6 and middle-distance H6 on Folder 3).



Plate 19. Steeply plunging, open F_4 fold structure in schists of the Rössing Formation on Goanikontes (Folder 3, K7).

progress in the Goanikontes area prior to the F_4 event. Barnes and Downing (1979) have discussed the mechanism of dome formation in the area E. of Goanikontes, and they consider the domes in this region are synchronous with the F_3 deformation, and result by a combination of granite intrusion and crustal shortening.

The mineralized alaskites on Goanikontes are concentrated in a zone which parallels the southern and western flanks of the F_3 antiform in domain A. They are emplaced preferentially within the Khan Formation, and only occur to a limited extent in the Chuos Formation above, and in the basement gneisses below. It will be shown in Chapter VIII that these particular alaskites were derived from local Khan source rocks, and the presence of mineralized alaskites within rocks of the Khan Formation elsewhere in the orogen (e.g. Rössing and the Ida dome) certainly suggests that their emplacement is stratigraphically controlled. However, at Goanikontes the Khan sequence was folded around the N.E. trending F_3 antiform prior to the formation of the alaskites, and their emplacement was therefore both stratigraphically and structurally controlled.

V.4. Structural evolution of part of the Abbabis inlier

Although the lithological distribution of Abbabis rocks is pre-Damaran, the tectonic fabrics within the basement rocks appear to be related to the Damaran F_2 and F_3 events. Only in the area S. of the Klein Chuos Mountain (Folder 1; ST - 10, 11) does there appear to be any earlier fabrics, and these are represented by schistosity planes which could be either F_1 or pre-Damaran in age. The F_2 event has resulted in the development of strong penetrative fabrics in the basement rocks identical to those

produced in the Damaran cover, and the F_3 event has formed open folds which deform the F_2 fabrics on a regional scale. The section across the Abbabis inlier mapped (Folder 1) has been divided into five structural domains, and these are illustrated in Fig. 18. Domains A and E represent areas occupied by Damaran metasediments to the N. and S. of the inlier, respectively. Domain C covers the area of basement rocks which have been influenced by the F_2 event only, whilst domains B and D represent areas of the basement which were initially affected by F_2 structures, then subsequently reorientated by F_3 folds.

The distribution of S_2 schistosity planes, lineations and F_3 fold hinges within the cover rocks of the Etusis and Karibib Formations are shown on the stereograms in Fig. 18. The S_2 fabrics in domain E (stereogram 11) fall about a π -pole circle defining a π -axis which coincides with the majority of minor F_3 folds measured in the same area (stereogram 12). This indicates that the larger scale fold structures in the Etusis quartzites in domain E are also F_3 in age. The π -pole circle to the folded S_2 fabrics in domain B (stereogram 4) suggests that the N.E. striking S_2 fabrics in the basement rocks have been affected by the same F_3 event as the overlying cover rocks. The lineations and minor fold hinges in the basement rocks do not appear to be related to the F_3 structures, and they are probably F_2 or earlier in age. The recognition of F_2 and F_3 fabrics in both the basement and cover rocks, indicates that the unconformity separating the two sequences must have been subjected to the same deformation events. However, the juxtaposed fabrics within the basement and cover are clearly discordant in the region S.W. of the Gangamchab Mountain (Folder 1; AB - 3, 4), and this area represents a good example of the folding of an angular discordance (Ramsay, 1967).

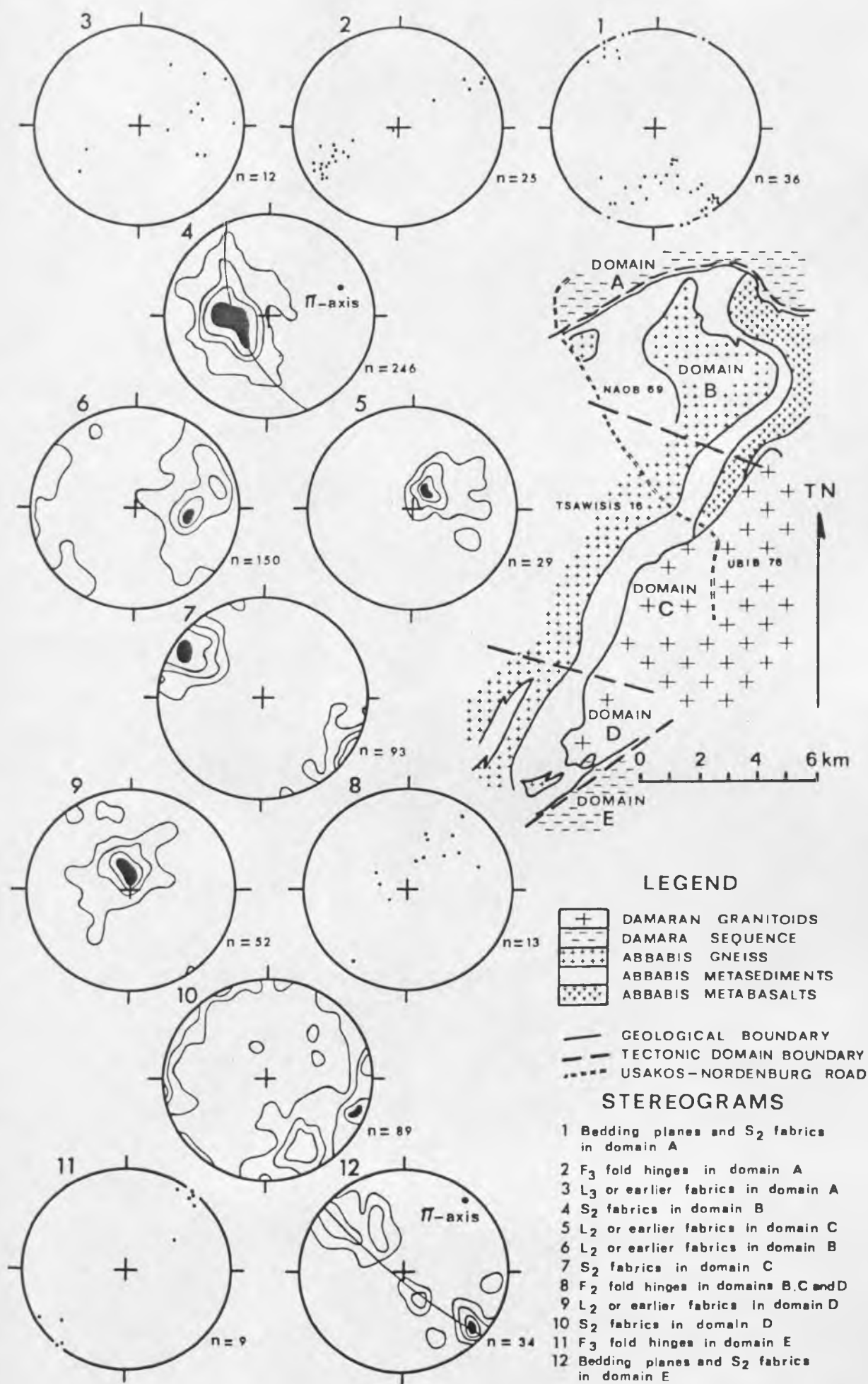


Fig. 18. Simplified geological map of part of the Abbabis inlier showing the major tectonic domains.

Within the ductile sequences of the Karibib Formation the F_2 event has resulted in the widespread formation of isoclinal folds with well developed axial planar fabrics (Plate 20). The same event has produced internal boudins in sillimanite-biotite schists of the Abbabis Formation (Plate 21). Internal boudinage within composite foliated rocks is considered by Cobbold et al.(1971) to form as a result of a compression normal to the foliation.

Strong, steeply plunging L_2 fabrics are developed in the meta-basalts in the core of the regional F_3 structure in domain B (Folder 1, C2 and 3). These lineations are commonly defined by boudinaged garnet 'cigars' (Plate 3) which have developed by extension and boudinage of garnet aggregates within skarns, and their subsequent filling of the boudin necks by quartzo-feldspathic material. The garnet boudins shown in Plate 3 were formed with their short axes parallel to the extension direction, and they show some rotation effects relative to this direction. The garnet cigars were probably spherical originally, and if they are restored to their prolate form prior to boudinage, they represent strain ellipsoids which indicate extensions of 10 to 1 or more.

In an attempt to make a crude estimation of the longitudinal strain these rocks have undergone during boudinage, the quadratic elongation was calculated for a number of boudinaged garnet cigars. The quadratic elongation λ is defined as

$$\lambda = (l_1 / l_0)^2 \quad \text{Ramsay (1967)}$$

where l_1 is the present length of the boudinaged garnet cigar and l_0 is its original length. λ varies between 1.4 and 3.0 with an average value of 2.1. These relatively low values suggest most of the extensional deformation resulted in the garnets being drawn out into the direction of maximum extension, and only during the final stages of deformation did



Plate 20. Isoclinal F_2 fold with a well developed axial planar fabric, within Karibib marble in the Naob River (Folder 1; B8). The pencil parallels the fold hinge.



Plate 21. Internal boudins in sillimanite-biotite schists of the Abbabis Formation in the Naob River on Naob 69 (Folder 1; C4).

they yield to boudinage.

An approximate estimate of the strain state within the cover rocks in domain A has been made by measuring a series of strain markers in the Etusis quartzite. Hornblende segregations were used as strain markers and their competency should be close to that of the quartzite, giving a true value for the strain ellipsoid. The analysis was performed just above the basement contact on Naob 69 (Folder 1; 2C) and between 32 and 54 measurements were recorded within each principal plane. A strain ellipsoid of 3.58 : 2.68 : 1 was calculated, which falls well within the flattening field on the Flinn diagram (Fig. 16), and close to the strain ellipsoid calculated for the pre- F_2 Salem granite on Valencia 122.

V.5. Structural evolution of the Stinkbank-Namibfontein area

The regional trend of the S_2 fabrics on Stinkbank 62 and Namibfontein 91, which is defined by xenoliths of metasediment in the various Damaran granitoids (Fig. 19), has been affected by open F_3 folding. Poles to bedding planes and S_2 fabrics on both Stinkbank 62 and Namibfontein 91 (stereograms 1, 2 and 7) indicate that the regional F_3 fold hinge has a shallow plunge towards the N.E. Minor F_3 fold hinges plunge in a similar manner (stereogram 6), and S_3 axial planar fabrics (stereogram 5) indicate the regional F_3 axial plane dips steeply to the S. The F_3 fold hinge is co-linear with strong L_2 fabrics measured within both the metasediments and the pre- F_2 Salem granites (stereograms 3 and 4 respectively).

There does not appear to be a structural control to the location of radiometric anomalies within any of the Damaran granitoids on Stinkbank 62 and Namibfontein 91. This is understandable however, because these anomalies are considered to have developed by secondary processes, (Chapter VI) and their location is likely to be controlled by the

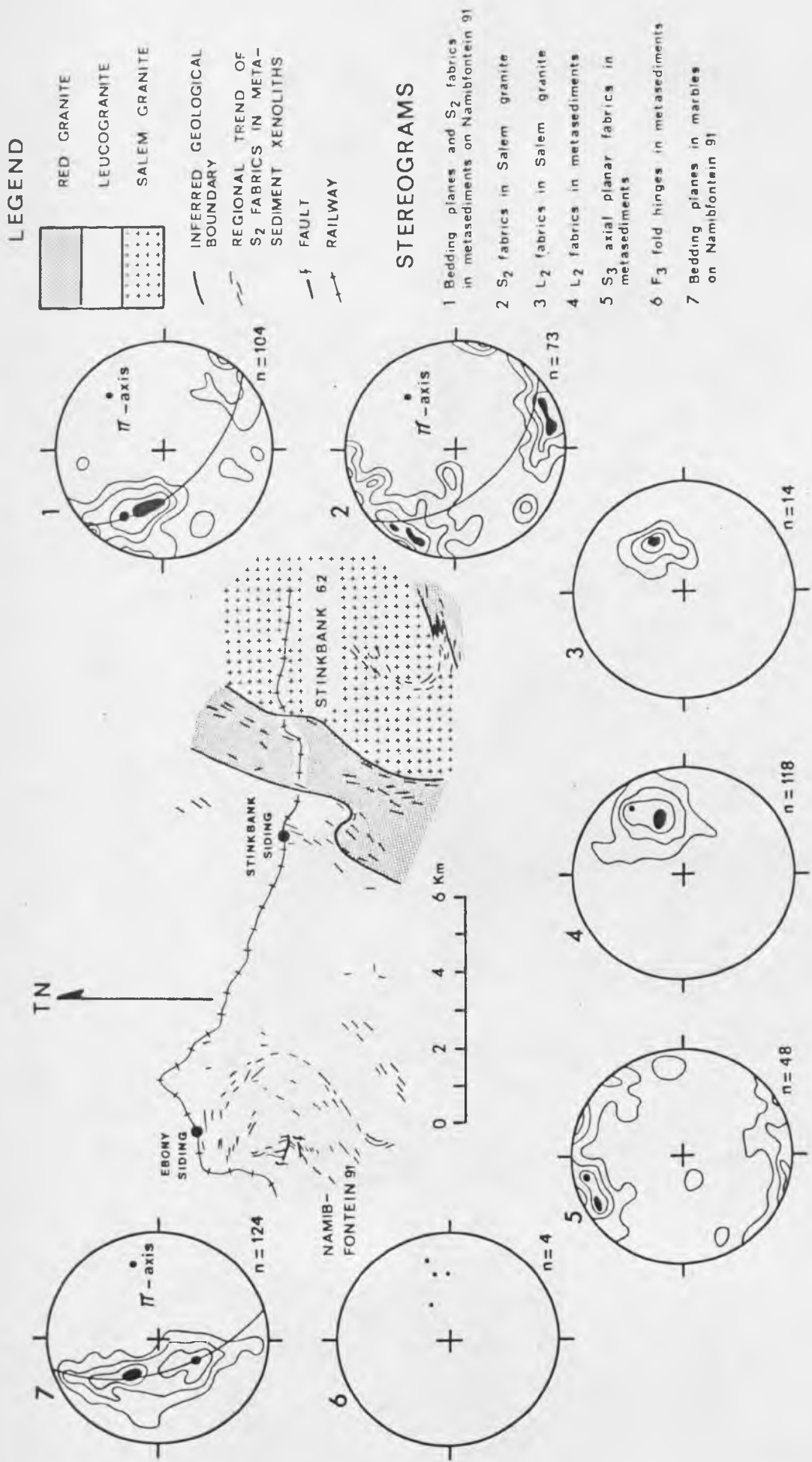


Fig. 19. Simplified geological map of the Stinkbank-Nambibfontein area showing the regional trend of the S₂ fabric defined by metasediment xenoliths in the Damaran intrusives.

migration of near-surface ground waters.

V.6. Structural evolution of the Otjua area

The portion of Otjua 37 mapped (Folder 2) represents only the N.W. portion of a heart shaped dome structure which measures about 13km across. Poles to bedding planes within the Etusis quartzites (Fig. 20, stereogram 3) suggest that the dome is slightly asymmetrical, the pole-maxima indicating a predominance of shallow to moderate dips to the N.E.

The domes within the central portion of the Damaran belt are considered to have developed between 500 and 460 Ma. by a process of intrusion, upward motion and ballooning of large masses of granite material (Barnes and Downing 1979; Coward 1981b; Coward 1981c; Kröner and Döpke, in press; Barnes, 1981). In an attempt to verify this in the Otjua area, strain markers have been measured within the Salem granites, which form a sheet between the underlying Etusis quartzite and the overlying Tinkas schists. The sheet was emplaced prior to the formation of the Otjua dome, and therefore the strain markers should record the deformation associated with dome formation. The strain markers, represented by fine grained quartzite and biotite schist xenoliths, appear to be oblate throughout the area investigated. Between 38 and 57 measurements of the major and minor axes of the xenoliths were recorded in the X-Z principal plane at 15 localities around the dome, and the structural measurements and average strain ratios are given in Table 7.

The finite strain recorded by the xenoliths is shown in Fig. 20 and it is clear that the xenoliths near the edge of the dome have suffered more deformation than those nearest the core. The actual strain ratios recorded have been plotted against the radial distance to

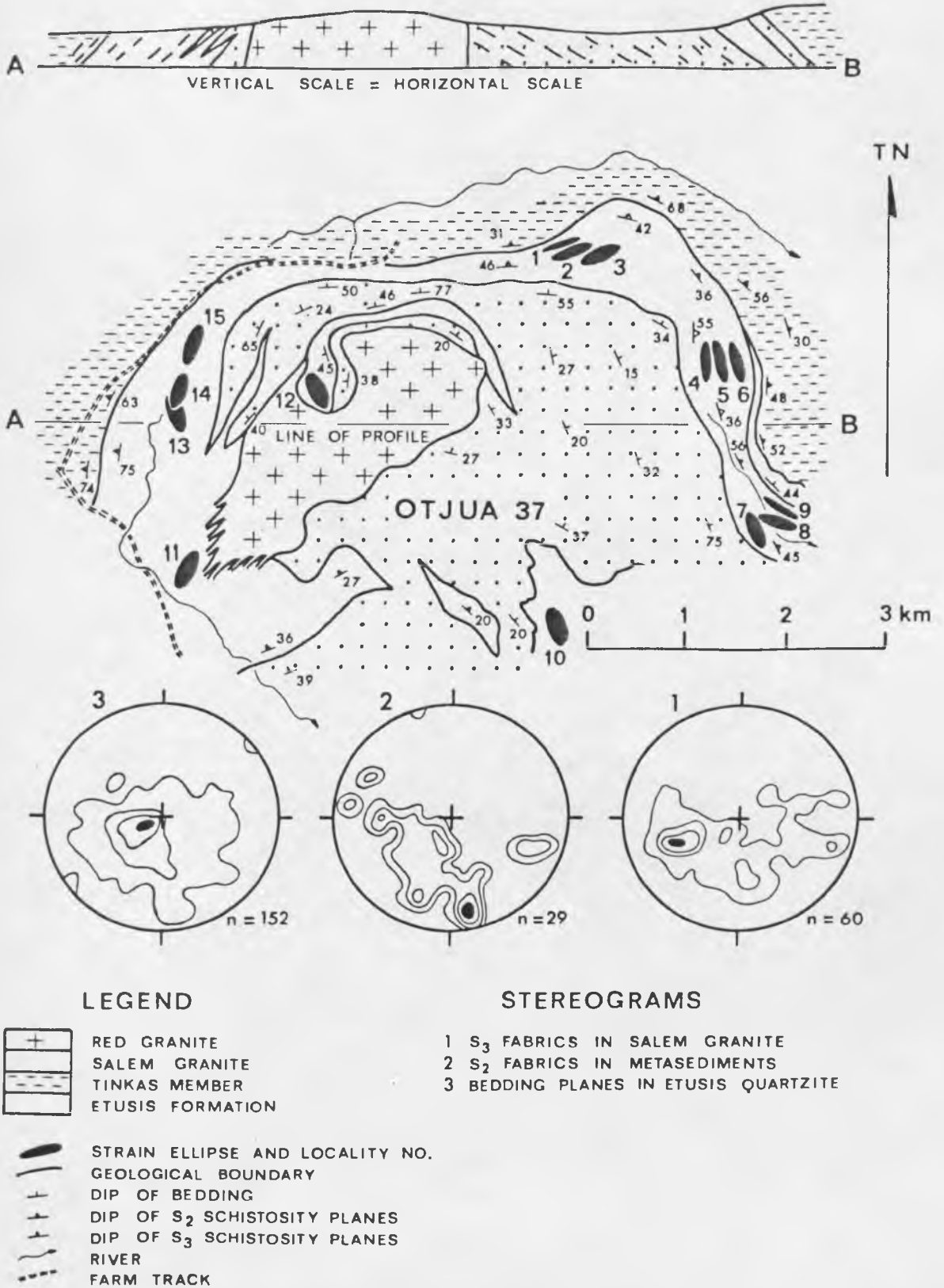


Fig. 20. Simplified geological map of the Otjua area illustrating the finite strain recorded by xenoliths in the Salem granites. Locality numbers of the strain ellipsoids refer to the strain data (Table 7), and the strain profile (Fig. 21). Long axes of strain ellipse drawn parallel to strike of S₃ planar fabric.

Table 7. Structural measurements and F_3 strain data recorded by xenoliths in the Salem granite on Otjua 37. Strain ellipse numbers refer to localities in Fig. 20.

<u>Strain ellipse no.</u>	<u>Strain ratio X/Z</u>	<u>n</u>	<u>S₃ schistosity</u>	
			<u>strike</u>	<u>dip</u>
1	26.4	42	075°	54° to N.
2	17.3	54	070°	43° to N.
3	10.6	57	080°	46° to N.
4	9.1	38	160°	55° to E.
5	9.2	54	175°	32° to E.
6	9.3	54	165°	50° to E.
7	7.5	38	065°	52° to N.W.
8	13.3	54	100°	37° to N.
9	19.8	54	121°	43° to N.E.
10	7.7	51	163°	38° to E.
11	4.6	52	020°	55° to E.
12	4.6	54	148°	58° to N.E.
13	4.3	54	165°	steep to W.
14	3.6	51	015°	72° to W
15	7.3	54	015°	72° to W

the rim of the dome, which has been taken as the contact between the Salem granite and the Tinkas Member (Fig. 21). The strain increases dramatically near the actual rim which is characteristic of the flattening deformation which occurs in the rim of a ballooning pluton (Holder, 1981). The S_3 planar fabrics in the Salem granites dip away from the centre of the dome by about 30 to 65°, and the attitudes of the flanks

of the dome are shown on the simplified cross-section in Fig. 20. Dixon (1975) has experimentally studied the distribution of strain within and around gravitationally produced diapiric structures, and he demonstrates that the greatest strain is a horizontal stretching above the diapir where maximum strain values of 60 : 1 may occur. The high values recorded in the Salem granites near the dome rim suggest that the present exposure level on Otjua 37 is close to the roof of the diapiric dome.

The emplacement of the mineralized red granite in the centre of the Otjua dome (Folder 2), is probably related to the uprise and ballooning of granitic material which is considered to have produced the dome; and the intrusive age of 516 ± 23 Ma for the Otjua red granite (Marlow, 1981) would represent a lower age limit for the development of domes in this portion of the Damaran belt. The indication that the present erosion surface is close to the roof of the diapiric dome, suggests that the exposed red granites represent the mineralized cupola of a larger body of red granite which underlies the Etusis quartzites in the core of the dome. The diapiric emplacement of granites in the Rum Jungle area of northern Australia is considered by Stephansson and Johnson (1976) to be a possible energy source to remobilize and concentrate uranium protore into structural traps, and the model appears to be very applicable to the Otjua mineralization.

V.7. Regional correlations

The relict S_1 fabrics observed within orthoclase poikiloblasts in the Kuiseb schists on Valencia 122 may correlate with the F_1 event of Coward (1981b) and Downing and Coward (1981) which is represented in some areas by early thrusts and folds which verge to the S.W. The strong S_2

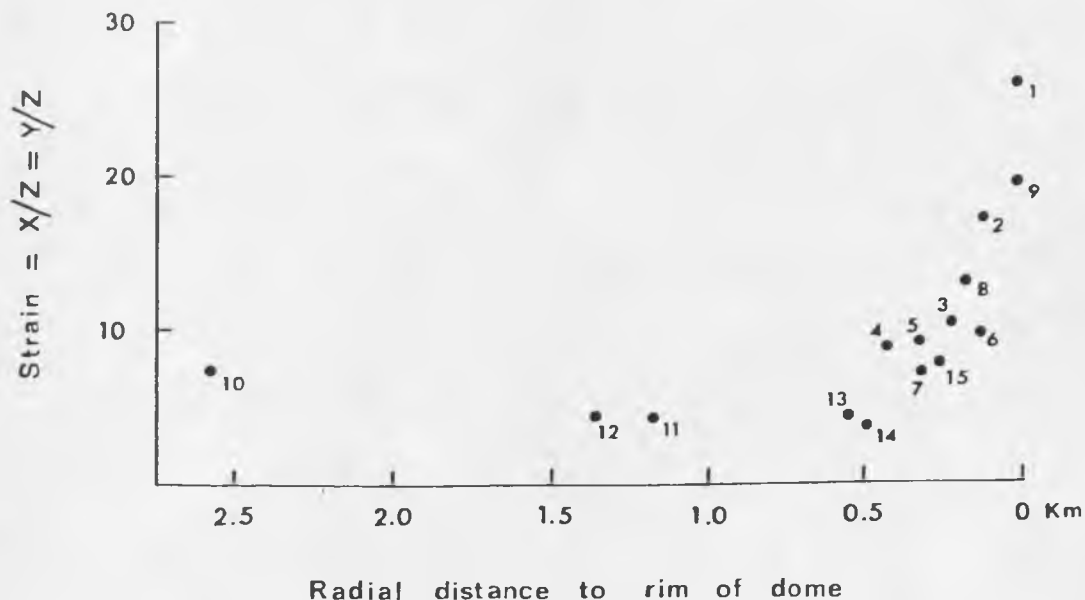


Fig. 21. Strain profile for the Otjua dome, recorded by xenoliths in the Salem granites. Numbers refer to locality of strain ellipse in Fig. 20.

and L_2 fabrics recognized throughout the belt can be correlated with the regional F_2 of Coward (1981b) which produced recumbent S.W.-verging sheath folds, and both are probably equivalent to the F_1 of Haack et al. (1980). It is this event which is primarily responsible for the dominant N.E.-trending fabric which characterizes the central portion of the Damaran orogen.

The F_3 and later events which have been recognized in various parts of the belt are not of the same tectonic style and they are probably not coeval. Dome formation appears to be related to diapirism and to the upward movement and subsequent ballooning of large volumes of granitic material. At Rössing the 458 ± 8 Ma. alaskites (Hawkesworth et al, 1981) post-date dome formation, whilst at the Ida dome the 542 ± 33 Ma. alaskites (Marlow, 1981) pre-date it, and on Otjua 37 the 516 ± 23 Ma. mineralized red granites (Marlow, 1981) appear to be directly associated with dome formation. This suggests that dome formation within the central portion of the Damaran belt occurs mainly between the interval 542 and 458 Ma.

IV.8. Conclusions

Pre- and post- F_3 alaskites are present on Valencia 122. The first have been involved in F_3 isoclinal folding, resulting in the formation of boudinage structures along the limbs of the F_3 folds, and parasitic folds in their hinges. The post- F_3 alaskites commonly display folded veins and apophyses which are considered to have formed in response to deformation resulting from the emplacement of large masses of the alaskite. Strongly mineralized post-tectonic alaskites are concentrated within the core of a major F_3 antiform, and it is possible that the migration of alaskite to this part of the fold structure was influenced by the presence of a low-pressure regime within the fold core.

At Goanikontes F_3 and F_4 fold structures are locally developed. The majority of the alaskites post-date the F_4 deformation, but some have been folded by the steeply plunging, tight to isoclinal F_4 structures. Post F_4 alaskites display ptygmatic folds and pinch and swell structures which are considered to have formed during the ballooning of late domes. The emplacement of the mineralized alaskites is both stratigraphically and structurally controlled, because firstly the alaskites occur predominantly within rocks of the Khan Formation, and secondly the Khan sequence was folded around a N.E. trending F_3 antiform prior to their emplacement.

The localization of radiometric anomalies within the Damaran intrusions on Stinkbank 62 and Namibfontein 91 is controlled by near-surface ground waters rather than any structural features of Damaran age.

The Otjua dome is considered to have developed by a diapiric process, involving the upward movement and subsequent ballooning of a large body of granitic material. The uraniferous red granites within the centre of the dome may represent the mineralized cupola of a larger body of granite which underlies the Etusis quartzite in the core of the dome.

CHAPTER VI

URANIUM MINERALIZATION IN THE DAMARAN BELT

VI.1. Introduction

Uranium minerals have been known to exist in the granites of the central belt of the Damaran orogen since the 1920's when davidite, a multiple oxide of Ti, Fe and U was found in the vicinity of the Rössing mine (Backström, 1970). It was not until the late 1950's however, that major exploration programmes were initiated, leading to the discovery of the world's largest, low grade, primary uranium deposit in the alaskites at Rössing. Other primary uranium mineralizations were subsequently found, but all the discoveries were restricted to the alaskites, and only secondary uranium minerals, mainly in the form of uranophane, were found within the other Damaran granitoids. Secondary uranium minerals have been reported within the metasediments of the Damara Sequence at Rössing (Berning et al., 1976), but the primary uranium minerals were considered to be restricted to the alaskite.

In an attempt to determine the source of the uranium mineralization within the alaskites, a number of localities were studied where the alaskites display relatively strong radiometric anomalies. Two of these areas, viz., Valencia 122 and Goanikontes were studied in detail and geological mapping was undertaken at scales of 1:10,000 (Folder 4), and 1:25,000 (Folder 3), respectively. As the radioactive anomalies are not restricted to areas invaded by alaskites, further anomalies were studied in regions dominated by other Damaran granitoids in an attempt to establish the cause of the radioactivity in these rocks.

Anomalies associated with the Salem granites were investigated on

Stinkbank 62, where a portion of the farm was mapped to a scale of 1:42,000 (Folder 5). Further anomalies associated with red granites were studied on Otjua 37 and Namibfontein 91, where geological mapping was undertaken at scales of 1:25,000 (Folder 2), and 1:42,000 (Folder 5), respectively. Finally a small anomaly associated with a leucogranite on Stinkbank 62 was examined, and mapped to a scale of 1:42,000 (Folder 5). The location of these areas within the central portion of the Damaran belt are shown in Fig. 2.

During the course of the investigation, uranium mineralization has been discovered within the pre-Damaran basement on Namibfontein 91; within the Damaran metasedimentary sequence at Rössing, on Wolfkoppe 105 and on Valencia 122; and also within the red granites on Otjua 37.

VI.2. Uranium in the pre-Damaran basement

Primary uranium mineralization has been located at the Breytenbach copper prospect on Namibfontein 91, on the N.E. side of a prominent koppie within a basement dome. The mineralized horizon lies a few hundred metres below the contact with the overlying Etusis Formation, in a sequence of metasediments and possible metavolcanics which have been intruded by narrow dykes of uraniferous alaskite. The area was originally mapped by Smith (1966) as red gneissic granite, and the location of the mineralization is shown on the simplified geological map (Fig. 22).

The mineralized zone occurs within a gossanous pyroxenite which maintains a thickness of about 2m over a strike length of a few tens of metres. The sequence dips to the N.E. by about 66° , and the gossan displays a weak radioactivity at the surface. The gossanous pyroxenite contains malachite and azurite at the surface, whilst the less altered pyroxenite

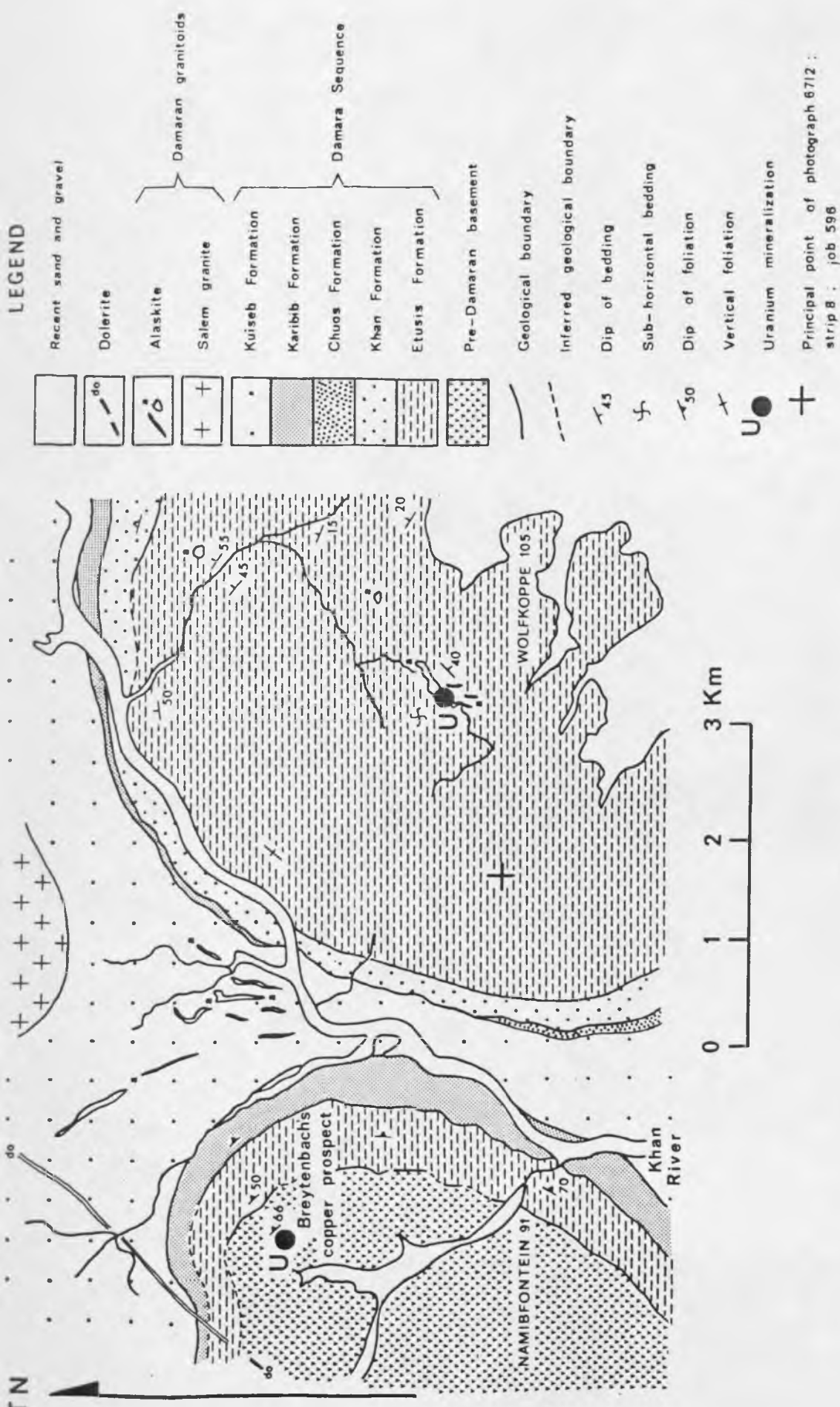


Fig. 22. Simplified geological map of the area bordering the Khan River on Namibfontein 91 and Wolfkoppe 105 (modified after Smith, 1966), showing the location of the uranium mineralization in the basement and the Etusis quartzite.

consists of a metamorphic aggregate of diopside, tremolite and magnetite, with minor chloritized muscovite and disseminated chalcopyrite. The diopside and tremolite form interlocking saussuritized laths which are intergrown with the magnetite which displays embayed grain boundaries. The uranium mineralization occurs in the form of uraninite inclusions within the magnetite (Plate 22). The inclusions are sub-rounded in shape, with indented grain boundaries, and they reach a maximum diameter of 20 μ .

The presence of the uraninite in the pyroxenite suggests that either the uraninite existed as an accessory constituent within the pyroxenite prior to metamorphism, or that it crystallized from available uranium in solution together with the diopside, tremolite and magnetite during the Damaran metamorphism. The latter is more likely since uraniferous alaskites have invaded the basement sequence on Namibfontein 91, and the uranium may have been partially mobilized after the intrusion, and migrated from the alaskite to the host rocks.

Weak ground radiometric anomalies have been located within sillimanite-biotite schists of the Abbabis Formation at the abandoned copper mine in the Abbisich River on Tsawisis Suid 95 (Folder 1, S11). The schists consist of bundles of sillimanite, prismatic biotite, poikilitic muscovite and acicular graphite in a fine grained recrystallized polygonal mosaic of quartz and feldspar. The radioactivity appears to be caused by the presence of Th-bearing monazite which occurs as symplectic intergrowths in feldspar. The bright areas on the back scattered electron image (B.E.I.) which represent the monazite (Plate 23A) clearly correspond with the distribution of Th shown on the X-ray map (Plate 23B). The Th is not uniformly distributed within the monazite however. The acicular graphite and prismatic biotite can also be seen on the B.E.I.

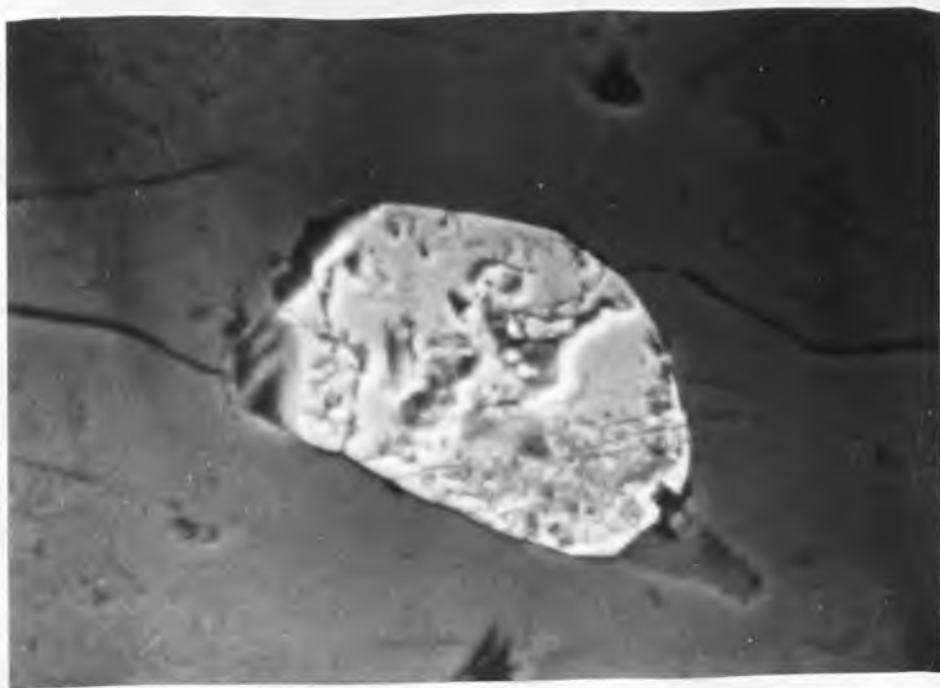


Plate 22. B.E.I. of a uraninite inclusion in magnetite within a pyroxenite from the Abbabis Formation on Namibfontein 91, (x 2750).

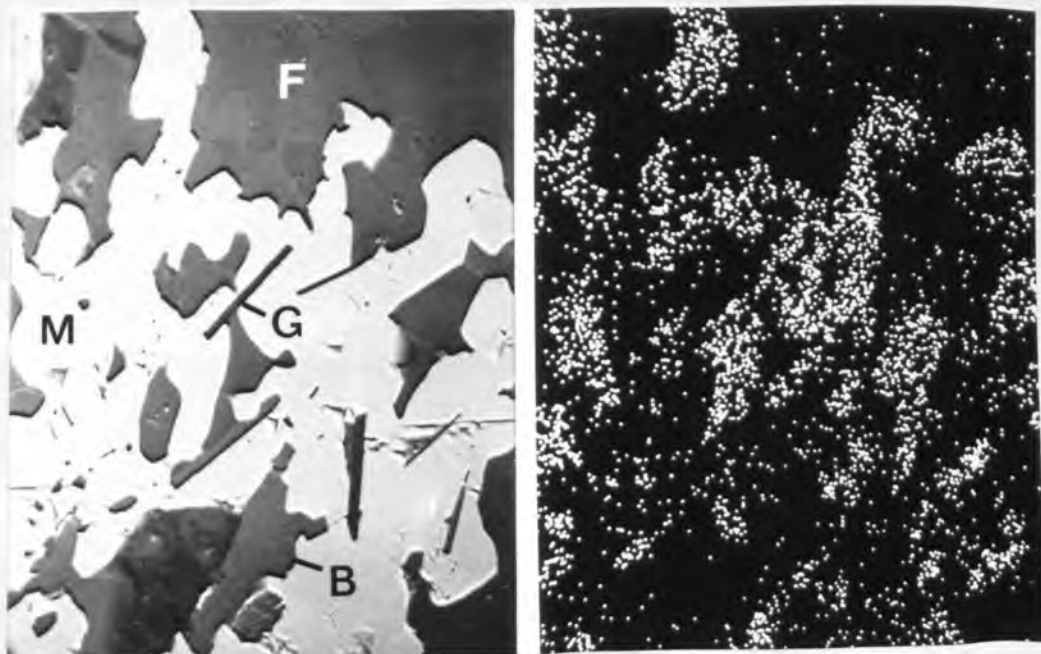


Plate 23. A = B.E.I. of a symplectitic intergrowth of monazite (M) and feldspar (F) in a sillimanite-biotite schist from the Abbabis Formation on Tsawisis Suid 95. B = biotite, G = graphite. Plate B = X-ray distribution map of Th. (x 2000).

VI.3. Uranium in the Damara Sequence

Secondary uranium minerals consisting mainly of beta-uranophane have been known to exist within the rocks of the Khan and Rössing Formations at the Rössing uranium mine since its early development, and they are thought to have been derived directly from the alteration of uraninite and betafite within juxtaposed alaskites (Berning et al., 1976). The complex multiple oxides of uranium such as betafite are relatively insoluble however (Klepper and Wyant, 1956), and it is likely that most of the secondary uranium minerals at Rössing are derived from the alteration of uraninite rather than betafite.

Primary uranium minerals or secondary uranium minerals derived from their alteration have been found within the metasediments of the Damara Sequence in both the Etosis and Rössing Formations. The mineralization in the former occurs on the northern part of Wolfkoppe 105, whilst that within the Rössing Formation is present at the Rössing mine, and near the abandoned Kainkagchas copper mine on Valencia 122.

VI.3. (i) Uranium in the Etosis Formation

The mineralized quartzites on Wolfkoppe 105 are located within the core of a domed structure and the position of the mineralization is shown on the simplified geological map (Fig. 22). The quartzite is red, fine to medium grained and carries metamorphic biotite and muscovite, and locally anastomosing veins of red migmatite have been developed within the rock. It has been invaded by radioactive alaskite which forms dykes and sills within the quartzite. The alaskites contain biotite, graphic intergrowths of quartz and tourmaline, and locally uranophane is present. The quartzites in the immediate vicinity of the mineralized alaskites may also contain uranophane.

The quartzite consists of partially recrystallized grains of strained quartz, microcline, orthoclase and subordinate plagioclase with minor interstitial Fe-oxide, biotite and muscovite. The accessory minerals are relatively abundant and consist of zircon and monazite which occur predominantly as inclusions within the quartz and feldspar grains, but also interstitially. The uranium mineralization occurs in the form of an unidentified uranyl silicate which is present as inclusions within the microcline. The inclusions reach a size of about $5\ \mu$ across, show indented grain boundaries (Plate 24A), have a pale-orange colour in plane polarized light and display extreme birefringence. They are surrounded by Fe-rims (Plate 24D) which have probably developed in the microcline host as a result of structural damage caused by the radioactive decay of U and Th, and the subsequent occupation of the damaged feldspar lattice by Fe. The inclusions appear to show a uniform distribution of both U and Th (Plate 24 B and C, respectively).

The polygonal nature of many of the quartz and feldspar grains indicates that the quartzite has undergone a considerable amount of recrystallization during the Damaran metamorphism. However, the microcline represents an original constituent of the metamorphosed sandstone, and the uranyl silicate inclusions must have been present within the microcline grains during deposition. The presence of the uranyl silicate inclusions therefore provides direct evidence of radioactive material, probably in the form of uraniferous, alkali-rich granitoids, within the pre-Damaran basement prior to its erosion, transportation and deposition within the lower part of the Damara Sequence.

Secondary uranium minerals are present within the Etusis quartzite on Otjua 37 in the immediate vicinity of the red granite body (Folder 2).

The uranium occurs in the form of uranophane along joint surfaces within the quartzite, as well as between the grain boundaries. Some of the quartzite xenoliths which have been incorporated within the red granite display stronger radioactive count rates than their host.

VI.3. (ii) Uranium in the Khan Formation

Secondary uranium minerals are present within the biotite-amphibole schist unit of the Khan Formation at the Rössing uranium mine. The local lithostratigraphic unit proposed by Berning et al. (1976) occurs at the top of the Khan Formation, and represents the lower part of the Damara Sequence at Rössing which has been invaded by uraniferous alaskite (Table 8).

Table 8. Lithostratigraphy of the Damara Sequence in the vicinity of the Rössing uranium mine, after Berning et al. (1976).

<u>Formation</u>	<u>Local Lithostratigraphic Units</u>	
Rössing	Feldspathic quartzite Upper biotite-cordierite gneiss Upper marble Conglomerate Lower biotite-cordierite gneiss Lower marble	} Stratigraphic position of uraniferous alaskite
Khan	Biotite-amphibole schist Upper pyroxene-hornblende gneiss Pyroxene-garnet gneiss/amphibolite	
Etusis	Lower pyroxene-hornblende gneiss Upper biotite gneiss Marker quartzite Lower biotite gneiss Feldspathic quartzite	

The schists of the biotite-amphibole schist unit at Rössing consist of a metamorphic aggregate of hornblende, biotite, feldspar, Fe-oxide, quartz and epidote. The secondary uranium minerals occur in the form of radiating bundles of uranophane needles which occupy interstices between

the quartz and feldspar grains (Plate 25). The individual uranophane needles are length slow, and they display pale yellow colours in plane polarized light and second order polarization colours.

VI.3. (iii) Uranium in the Rössing Formation

Primary uranium mineralization has been found within rocks of the lower biotite-cordierite gneiss unit of the Rössing Formation at the Rössing uranium mine (Table 8). The medium to coarse grained gneisses consist of a recrystallized mosaic of quartz, orthoclase and plagioclase with metamorphic prismatic biotite, minor Fe-oxide and muscovite, as well as accessory monazite, apatite and zircon. The monazite is the most abundant accessory constituent, forming rounded grains up to 0.1mm across. It occurs interstitially or as inclusions in feldspar and quartz, and the high Th content of some of the grains has resulted in structural damage within the lattice of the surrounding host mineral.

The primary uranium minerals include uraninite and betafite. The former occur as subhedral grains up to 0.1mm across as inclusions within chloritized and muscovitized biotite (Plate 26), or interstitially. The radioactive decay of the uraninite has resulted in the development of pleochroic haloes within biotite grains which host the uraninite (Plate 26). Where feldspar is in direct contact with uraninite, a zone of Fe enrichment may develop in the form of a rim around the uraninite (Plate 27). The uraninite is commonly associated with monazite, and may contain inclusions of the latter, or be intergrown with it (Plate 28). Some of the interstitial uraninite grains have been partially leached and the uranium has subsequently crystallized as uranophane along grain boundaries radiating away from the uraninite

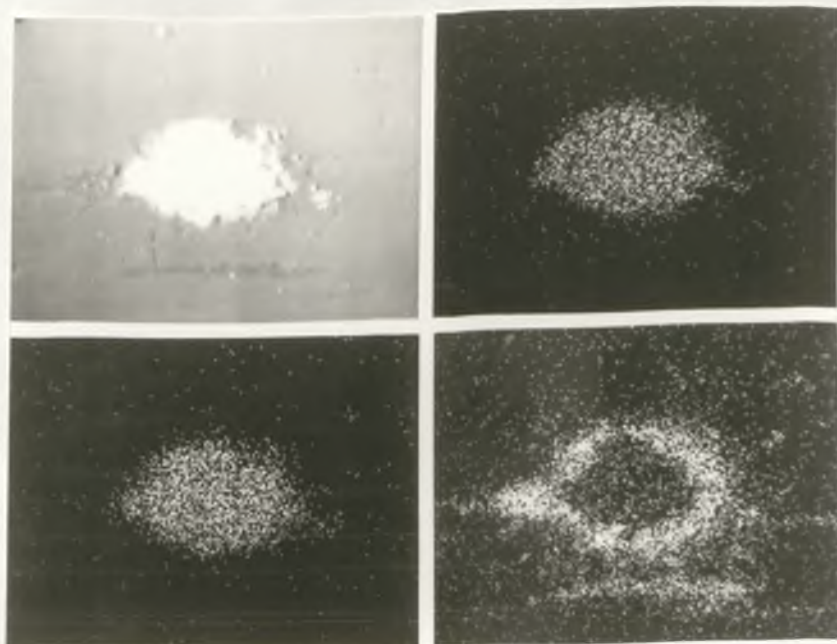


Plate 24. A = B.E.I. of a uranyl silicate inclusion in a microcline grain from an Etusis quartzite on Wolfkoppe 105. B, C and D are X-ray maps of U, Th and Fe respectively. (x 4000).

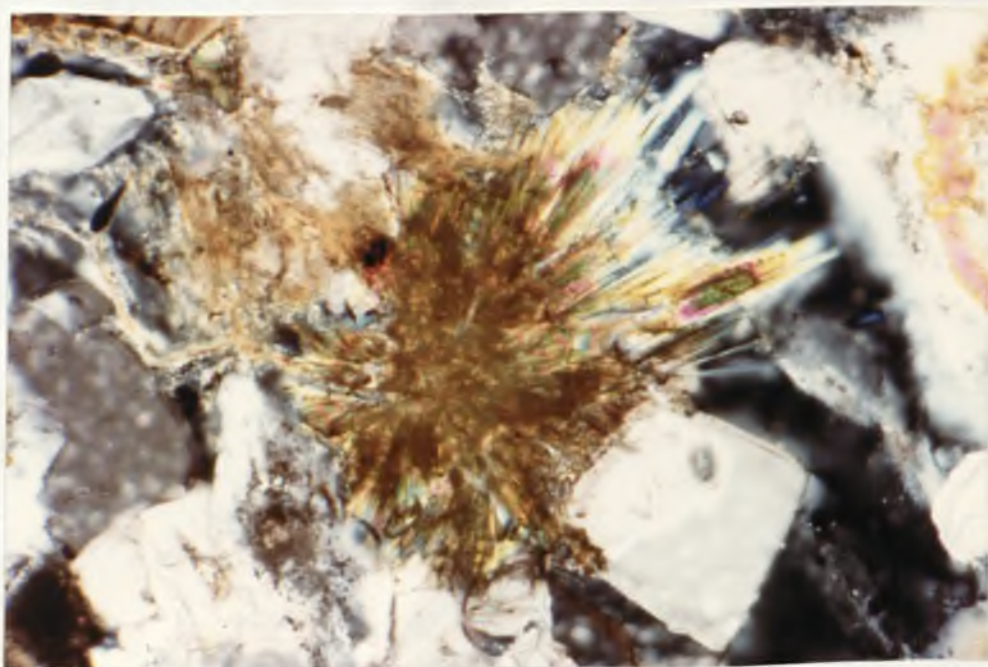


Plate 25. Photomicrograph of radiating bundle of uranophane needles in an interstice between quartz and feldspar in the biotite-amphibole schist unit of the Khan Formation at Rössing. (XN; x 200).

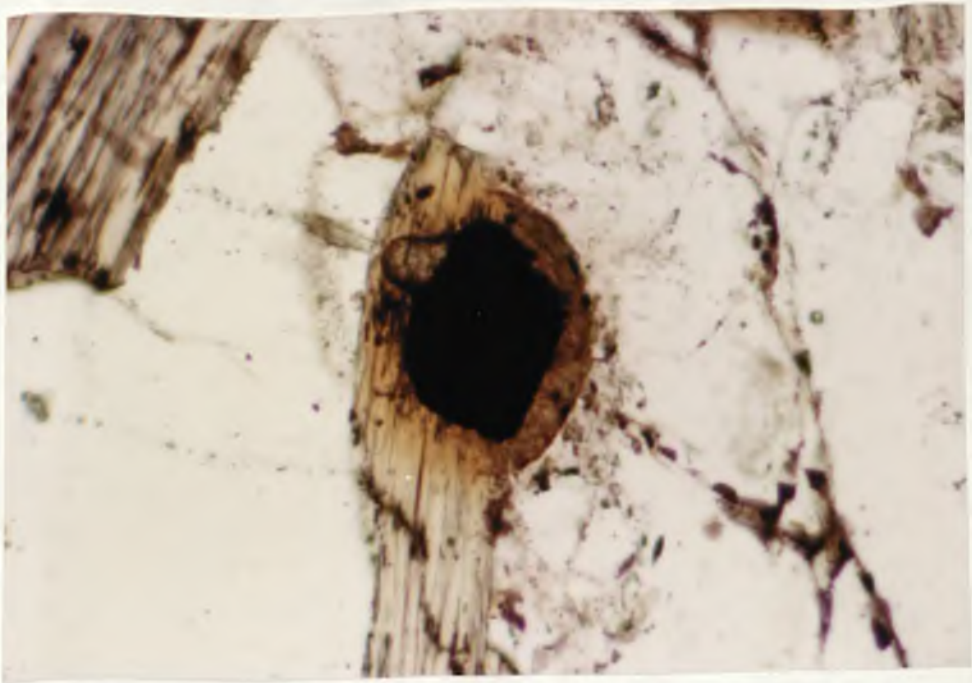


Plate 26. Photomicrograph of opaque uraninite inclusion in chloritized biotite from the lower biotite-cordierite gneiss unit of the Rössing Formation at Rössing. Note the pleochroic halo in the biotite and the small monazite grain included by the biotite to the left of the uraninite (PPL; x 300).

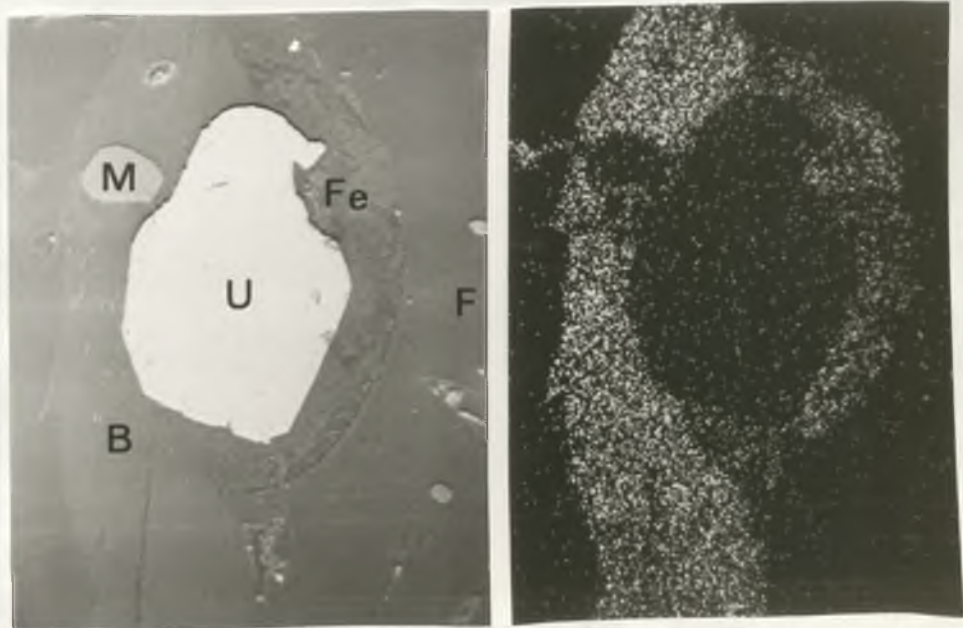


Plate 27. A = B.E.I. of uraninite (U) shown in Plate 26. M = monazite, B = biotite. Note the zone of Fe enrichment (Fe) within the feldspar (F) in direct contact with the uraninite. Plate B = X-ray distribution map of Fe (x 400).

(Plate 28). The betafite occurs as anhedral, interstitial grains up to 0.1mm across, which may be enclosed by narrow zones of haematized feldspar when included by the latter mineral.

Betafite has also been located within calc silicates of the Rössing Formation near the abandoned Kainkagchas copper mine on Valencia 122. The cupriferous calc silicates of the Rössing sequence described in section 2 (iii) of Chapter III, are weakly radioactive and the rocks showing the highest copper concentrations also display the highest radioactive count rates. The calc silicates exposed in the gorge 300m S.W. of the abandoned mine (Folder 4, 05), give count rates equal to those of the uraniferous alaskites which invade the upper part of the Rössing sequence a few metres to the E.

The radioactive calc silicates consist of a metamorphic aggregate of diopside, tremolite and phlogopite with minor sphene, Fe-oxide, quartz, betafite and apatite. The betafite may form anhedral inclusions within chloritized and calcitized phlogopite (Plate 29), or interlocking grains associated with sphene and phlogopite in metamorphic segregations up to 1cm across. The photomicrograph of the betafite inclusions (Plate 29) shows the pale brown colour of the isotopic mineral, and the typically cracked and indented nature of the grain.

The metamorphic minerals associated with the uraninite and betafite at Rössing and Valencia 122 appear to be post-tectonic in nature. Since some of the uraniferous alaskites at these two localities pre-date the final stages of tectonism, it is possible that the uranium was introduced into the metasediments of the Rössing Formation after the intrusion of the earlier uraniferous alaskites. It is also possible however, that the uranium is syngenetic and that it existed within the original sediments

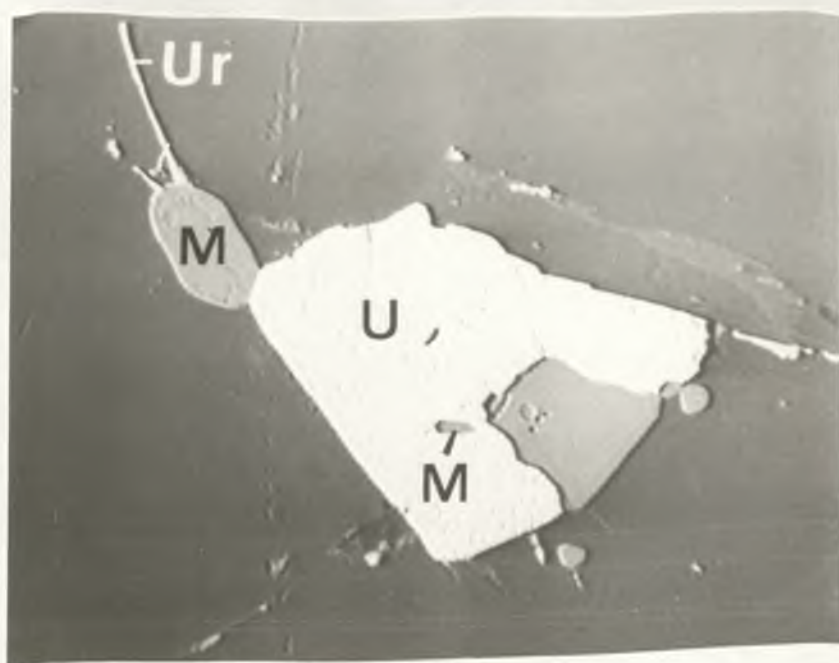


Plate 28. B.E.I. of uraninite (U) intergrown with monazite (M) at interstice between quartz grains from the lower biotite-cordierite gneiss unit of the Rössing Formation at Rössing. Note the uranophane (Ur) developed along the quartz grain boundaries, and the small lenticular monazite inclusion in the uraninite (x 500).

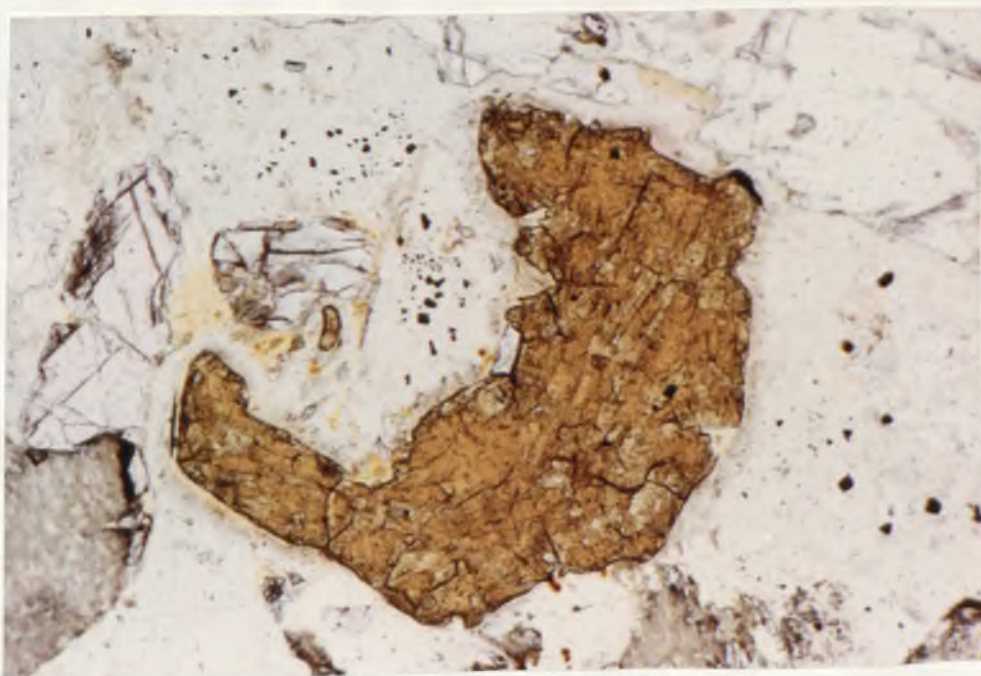


Plate 29. Photomicrograph of betafite included in chloritized and calcitized phlogopite in a calc silicate from the Rössing Formation on Valencia 122 (PPL; x 160).

prior to the emplacement of the uraniferous alaskites. The latter theory is preferred for two reasons. Firstly, the most radioactive calc silicates of the Rössing sequence on Valencia 122 represent the host rocks to the more strongly developed stratabound copper deposits; and secondly certain rocks within the Rössing sequence at Rössing contain an abundance of monazite grains which may have formed part of the same pre-Damaran radioactive source as the original uranium phases.

VI.4. Uranium in the Damaran Intrusives

The primary uranium mineralization in the alaskites at the Rössing uranium mine has been discussed by Berning et al. (1976), whilst Jacob (1974b) has detailed some radioactive anomalies associated with alaskites in the vicinity of the Ida dome. A comprehensive account of the uranium phases within the alaskites is lacking however, and no satisfactory explanation has been provided for the presence of radioactive anomalies associated with the other Damaran granitoids. The following section is aimed at :

- A) A discussion of some radiometric anomalies associated with the Salem granites and leucogranites, in an attempt to identify the primary cause of the radioactivity within these rocks.
- B) A discussion of some radiometric anomalies associated with the red granites, and a description of the primary and secondary uranium minerals found in the red granites on Otjua 37.
- C) A description of the uranium minerals identified within the alaskites from the Rössing mine, Valencia 122 and Goanikontes.

VI.4. (i) The radioactive Salem granites

A major airborne radiometric anomaly is present over some Salem granites on Stinkbank 62. The anomaly lies S.E. of the Stinkbank siding over pre-F₂ Salem granites which form an oval body measuring about 5km across (Folder 5). The granites are bounded to the S. and W. by biotite- and garnet-bearing schists of the Kuiseb Formation, and to the S.E. by post-tectonic leucogranites which clearly intrude the Salem granites.

The granites may be divided into an early biotite-rich facies, and a later leucocratic facies, both of which contain a strong F₂ fabric defined by perthite phenocrysts and prismatic biotite grains. The latter is intrusive into the former as dykes, sheets and small plutons. The early biotite-rich facies is typical of many coarse grained strongly porphyritic Salem granites throughout the Damaran belt, but is characterized on Stinkbank 62 by the presence of graphic quartz-tourmaline intergrowths as well as biotite-bearing aplites and pegmatites, the latter being especially well developed within the Kuiseb schists along the western contact of the granite (Folder 5, 09). The granite consists of perthite phenocrysts up to 4cm in length within a groundmass of quartz, plagioclase, biotite and minor orthoclase, with metamorphic biotite and accessory Fe-oxide, zircon and apatite.

The leucocratic facies of the Salem granite consists of a coarse grained porphyritic rock which contains perthite phenocrysts which are normally smaller and less frequent than those of the earlier biotite-rich facies. The graphic quartz-tourmaline intergrowths are also present, whilst porphyroblasts of garnet up to 1cm across may occur locally. The granite is characterized by the presence of composite aplite-pegmatite dykes, which carry metamorphic garnet and tourmaline,

and measure up to a metre or two in thickness. The mineralogy of the leucocratic facies is essentially the same as that of the biotite-rich facies, with the exception that monazite is present as an abundant accessory constituent in the former.

Two strong ground radiometric anomalies occur within the Salem granites, the first being associated with a major development of the composite aplite-pegmatite dykes, and the second with the coarse grained leucocratic facies. The first anomaly, situated just N.E. of a tall koppie, about 1km S. of the railway line (Folder 5, Q6), has been drilled by a mining company. The second lies within a pluton of the leucocratic facies (Folder 5, T9), which measures about 3km x 1km. At both localities secondary uranium minerals mainly in the form of uranophane are commonly developed along exfoliation, fracture and cleavage planes within the granite.

Samples of the more strongly radioactive granite from the second anomaly have been investigated on the electron microprobe, and they have been found to contain an abundance of Th- and U-bearing phosphates. These phosphates measure up to 0.1mm across, and occur interstitially commonly in association with Fe-oxide, or as inclusions. Some of the grains display strongly developed radial cracks (Plate 30) which have probably formed in response to differential expansion which is assumed by Stackelberg and Rottenbach (1940) to accompany the process of metamictization. The host grains to the phosphate inclusions have also suffered structural damage in the immediate vicinity of the inclusion (Plate 31A). The damaged lattices have subsequently been filled by Al (Plate 31D), as well as minor Fe and traces of K and Ca. U and Th have migrated from the phosphate to the damaged lattice in the host (Plate 31B and C), and the bright images around the host (Plate 31A) represent secondary U and Th phases which appear to be migrating from the monazite

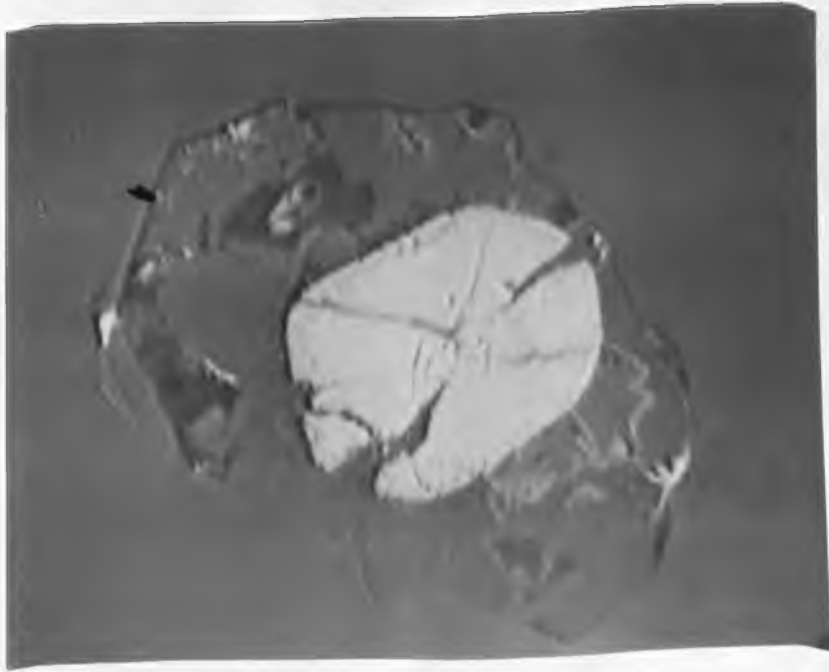


Plate 30. B.E.I. of a U- and Th-bearing phosphate with strongly developed radial cracks which have probably formed in response to differential expansion which is assumed to accompany the process of metamictization. Inclusion in quartz within leucocratic facies of the Salem granite on Stinkbank 62 (x 400).

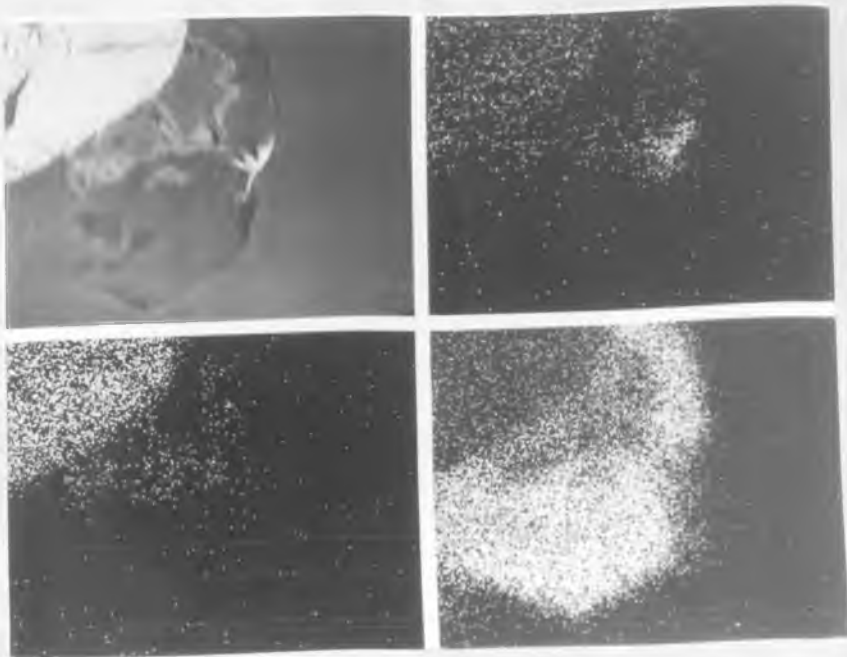


Plate 31. A = B.E.I. of the bottom-right portion of Plate 30. B, C and D are X-ray distribution maps of U, Th and Al respectively (x 400).

grain via the radial cracks.

The uranophane and other secondary uranium minerals which are concentrated near the surface of some Salem granites have produced major airborne and ground radiometric anomalies. The primary cause of the radioactivity however is considered to be the abundance of the U- and Th-bearing phosphate. The U and Th of the phosphate have migrated during the process of metamictization, and secondary U and Th phases have developed within alteration zones in silicates that host the phosphate inclusions. The U and Th in these secondary phases have been tapped by ground water solutions, and surface enrichment processes have concentrated the elements in the near surface environment, resulting in the development of uranophane and related minerals at the surface.

Rocks of a similar nature to the leucocratic facies of the Salem granite on Stinkbank 62 are present in the Namib Desert Park, within the area covered by the government survey sheets 2315 AC and AD. The granites in this vicinity invade calc silicates and biotite schists of the Tinkas Member, and locally they display strong ground radiometric anomalies. Further anomalies within leucocratic suites of the Salem granite have been reported by Jacob (1974b) from Jakkalswater 13, Modderfontein 131 and Geluk 116. Surface enrichment by secondary processes has undoubtedly had a major role to play in the development of these anomalies, but the primary uranium, like that in the Salem granites on Stinkbank 62, is considered to have originally been held in the lattice of U- and Th-bearing accessory constituents, and to have migrated from these minerals during the process of metamictization.

VI.4. (ii) The radioactive red granites

Jacob (1974b) has previously noted the correspondence between airborne radiometric anomalies and a group of granite rocks and

gneisses which he designated red granite gneisses, and he considers that a relationship exists between the radioactivity and their biotite content. He also points out that much of the radioactivity within the more radioactive red granite gneiss may be due to the presence of monazite. Two airborne anomalies associated with red granites have been investigated in an attempt to establish the origin of the radioactivity. The first anomaly is situated on Namibfontein 91, and the second is on Otjua 37.

The Namibfontein anomaly corresponds to the outcrop of a post-tectonic red granite which occurs in the form of a lit-par-lit intrusion in the Rössing metasedimentary sequence S. of the Ebony siding. A number of ground radiometric anomalies were located and drilled by the mining company investigating the area, and the distribution of secondary uranium minerals in the red granites is shown on the geological map (Folder 5, D6, C7 and D7). Uranophane has developed within joints, cracks and cleavage planes on the exfoliation domes exposed in the areas where the strongest anomalies are located.

The radioactive granite consists of quartz, microcline, plagioclase, orthoclase and biotite with accessory Fe-oxide, monazite and zircon. Red pegmatite is commonly developed but it is less radioactive than the host granite. A number of samples of the granite were investigated on the electron microprobe, and the accessory monazite was found to contain relatively large amounts of Th. The euhedral to rounded grains which reach a maximum size of 0.5mm across contain major amounts of P, Ce and La, but U was not observed within any of the grains investigated.

The radioactivity in the red granites on Namibfontein 91 appears to be caused by the presence of the Th bearing monazite, but the source of the uranium which has been concentrated in the near surface environment

in the form of uranophane remains an enigma. Similar radioactive red granites to those on Namibfontein 91 also occur on Lukasbank 63, and about 650m S.W. of the Lukasbank farmhouse (Folder 5, 01) a mining company has drilled another strong ground radiometric anomaly.

The airborne anomaly on Otjua 37 lies over the N.W. portion of a post-tectonic intrusion of Salem granite which occupies part of a dome structure, the core of which is dominated by quartzites of the Etusis Formation, and the flanks by schists and marbles of the Tinkas Member. The gently dipping quartzites within the core of the dome have been intruded by a stock of red granite which has been described in section 3 of Chapter IV. It is the red granite which causes the anomaly on Otjua 37, and three distinct ground radiometric anomalies were located and drilled by a mining company (Folder 2; E7, F6 and H6). The radioactivity at depth was found to be much less than that recorded at the surface, and surface enrichment by secondary processes was considered to be a dominant factor in the development of the anomalies.

At the N.W. ground radiometric anomaly (Folder 2, E6) zones of strong radioactivity occur along certain red granite-Salem granite contacts, as well as within some red granite pegmatites, and these features are likely to be associated with the intrusion and subsequent crystallization of the red granite magma. Radioactive samples of red granite were collected from this area and investigated on the electron microprobe, and uranium minerals were found in the form of uraninite, thorogummite and an unidentified uranyl silicate. The minerals are physically too small to extract from the rock and spectrographic data is therefore unavailable.

The uraninite grains measure up to 40 μ , whilst the uranyl silicate and thorogummite grains measure up to 0.2mm. The former are present in

the form of euhedral grains which occur interstitially in association with zircon. The uranyl silicate and thorogummite may be euhedral or irregular in shape, and they occur interstitially or as inclusions in quartz, feldspar and Fe-oxide. The euhedral uranyl silicate grain shown in Plate 32 displays a pale yellow colour in plane polarized light, a weakly developed parting, aggregate polarization and a haematite rim measuring 20μ in thickness. The uranyl silicate may be intimately associated with monazite and zircon, and the intergrowth shown on the B.E.I. in Plate 33 suggests that pressure solution has affected the grain boundaries between these three minerals. Pressure solution appears to have had the effect of an inward migration of zircon and uranyl silicate at the expense of the softer monazite.

The intimate association between the secondary U phases and the accessory minerals is illustrated in Plates 34 and 35, where euhedral uranyl silicate is intergrown with euhedral monazite which includes zircon. Due to the high magnification of the photomicrograph the grain boundaries between the three minerals are indistinct, but the extreme polarization of the uranyl silicate is well displayed, as is the haematite which forms a rim around the intergrowth. The grain boundaries are better exposed on the B.E.I. of the intergrowth (Plate 35A), where the brighter image corresponds to the euhedral uranyl silicate, and the darker images in the monazite grain correspond to the zircon inclusions. The X-ray distribution maps of U, P and Zr (Plate 35B, C and D respectively) reveal the location of the uranyl silicate, monazite and zircon respectively. The U X-ray map displays the uniform distribution of this element within the uranyl silicate, and it also indicates that the U counts within the monazite are above those of background. The P distribution map shows a

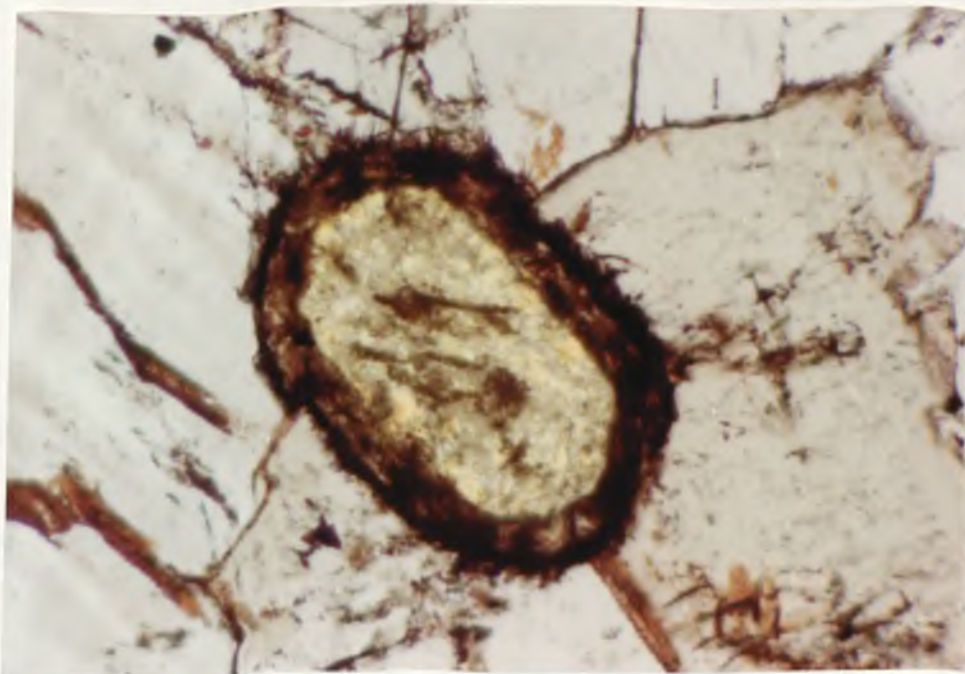


Plate 32. Photomicrograph of euhedral uranyl silicate in red granite from Otjua 37. Note the weak parting within the uranyl silicate and the haematite rim. (PPL; x 275).

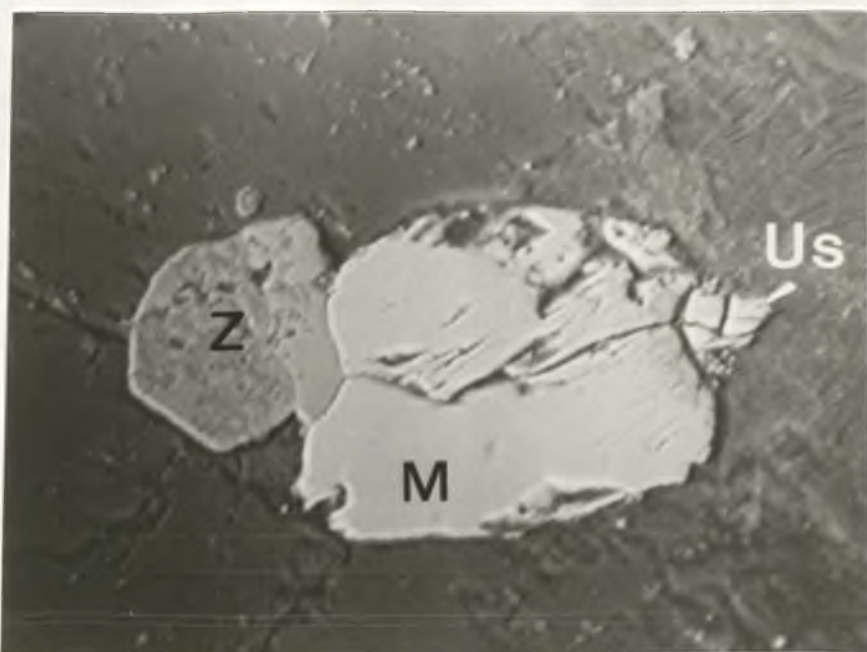


Plate 33. B.E.I. of an intergrowth of zircon (Z), monazite (M) and uranyl silicate (Us) in red granite from Otjua. Note the affects of pressure solution along the contacts between the grains, (x 1200).

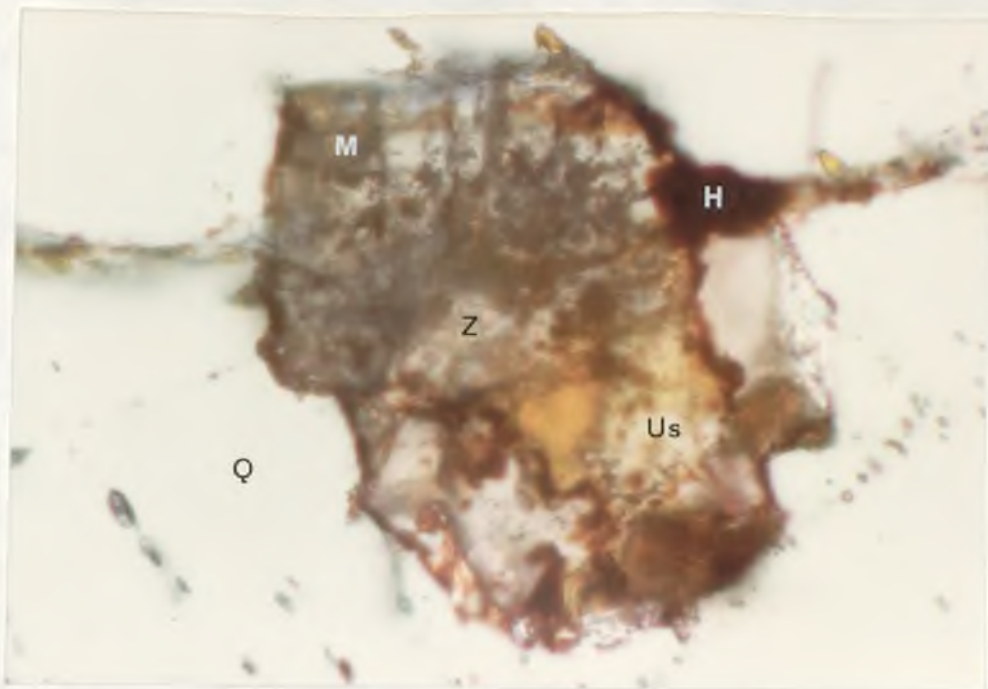


Plate 34. Photomicrograph of an intergrowth between uranyl silicate (Us), monazite (M) and zircon (Z), included in quartz (Q) from a red granite on Otjua 37. Note the haematite (H) rim (XN; x 900).

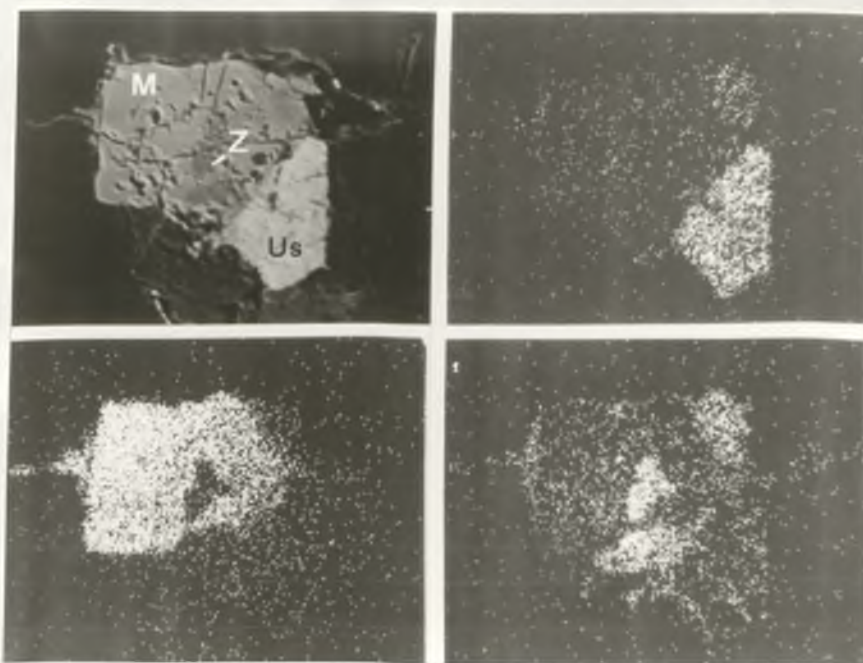


Plate 35. A = B.E.I. of intergrowth shown in Plate 34. Us = Uranyl silicate, M = monazite, Z = zircon. B, C and D are X-ray distribution maps of U, P and Zr respectively. (x 300).

migration of P along the crack within the quartz host which is depicted on the photomicrograph. The X-ray distribution map of Zr indicates that this element is also present in minor amounts in the monazite and the uranyl silicate, but it does not appear to show an even distribution within these minerals.

The euhedral nature of many of the uranyl silicate grains in the red granite, as well as their intimate association with monazite and zircon indicates they represent secondary alteration products of primary uraninite. The thorogummite is probably an alteration product of primary thorite, and it is considered that uraninite and thorite crystallized from a magma enriched in U and P together with the accessory constituents. The presence of uranyl silicate inclusions within the major constituents such as quartz and feldspar, suggests the uraninite may have been a relatively early-formed mineral.

VI.4. (iii) The radioactive leucogranites

A number of ground radiometric anomalies have been recorded over the Bloedkoppe granite, and although the granite is not of economic importance in itself, it is generally agreed that it represents the protore of the secondary uranium mineralization in the gravels which are situated downstream of the granite (Jacob, 1974b). Anomalous leucogranites are also exposed on Stinkbank 62, where a ground radiometric anomaly has been drilled by a mining company. The anomaly is situated just S. of the railway line and about 25km E. of the Stinkbank siding (Folder 5, 05).

The leucogranite on Stinkbank 62 occurs at the stratigraphic level of the Karibib Formation, and it incorporates large xenoliths of marble and calc silicate up to 1km in strike length and a few hundred metres

in thickness. The granite consists of orthoclase, quartz and plagioclase with minor biotite, microcline, symplectite and muscovite, and accessory zircon, Fe-oxide, monazite and apatite. Orthoclase may be present in the form of phenocrysts which are commonly strongly aligned within a flow fabric, whilst garnet- and muscovite-bearing pegmatite and aplite dykes, and quartz-tourmaline graphic granites are developed locally. The subhedral monazites are extremely abundant in the more radioactive samples, reaching a maximum size of 0.1mm across. Uranophane is developed over parts of the exfoliated domes of the leucogranite which reveal the higher radioactive count rates.

Samples of the radioactive leucogranite have been investigated on the electron microprobe and the monazites contain traceable amounts of Th, but U was absent within all the monazites observed. The radioactivity within the leucogranites appears to be caused by the abundance of Th bearing monazite, but the source of the uranium which now exists in the form of secondary uranophane at the surface remains unsolved.

IV. 4. (iv) The radioactive alaskites

The regional distribution of mineralized alaskites in the central belt of the orogen seems to be random, but there does appear to be a stratigraphic control to the mineralization. Jacob (1974b) has described the occurrence of mineralized alaskites at the Khan-Karibib contact over a strike length of some 9km in the vicinity of the Ida and Husab domes, and the mineralized alaskites at Rössing appear to be restricted to the Upper Khan and Lower Rössing Formations (Berning et al., 1976). Further stratigraphic control seems to pertain at Goanikontes

where mineralized alaskites are most strongly developed within the Upper Khan, and also at Valencia 122 where the largest development of radioactive alaskite occurs between the Rössing and Karibib Formations. It is significant that mineralized alaskites have invaded metasediments containing stratabound copper deposits at Valencia 122 and in the Husab-Ida region.

A number of samples of radioactive alaskite have been investigated in an attempt to identify the primary uranium constituents, as well as the secondary uranium minerals which have developed directly from them. The samples were collected from the Rössing open pit; a blasting site near the upper contact of the Khan Formation on Goanikontes (Folder 3, M8), and from drill core obtained from the mining company exploring Valencia 122.

Due to the minute size of most of the uranium phases as well as their commonly non-crystalline metamict state, spectrographic analysis was not undertaken, and the alaskites were simply investigated with the optical microscope and the electron microprobe. The primary uranium minerals identified include uraninite, betafite and metamict thorite. The metamict thorite has not previously been recorded within the alaskites. The physical and optical characteristics of these minerals are shown in Table 9.

A. The primary uranium minerals in the alaskites

The dominant primary uranium phase at Rössing and Valencia 122 is uraninite, whereas on Goanikontes it is betafite. Although uraninite has been reported within the alaskites from Goanikontes (Valois and Walgenwitz, 1979; Brigueu et al., 1980), it was not identified within any of the samples investigated from this locality. The uraninite occurs

Table 9. Physical and optical characteristics of the primary and secondary uranium minerals identified in the alaskites.

MINERAL	COLOUR IN PLANE POLARIZED LIGHT	POLARIZATION COLOURS	HABIT	MINERAL ASSOCIATION	ALTERATION RIM	CHARACTERISTICS	SIZE RANGE	OCCURRENCE
Uraninite	Opaque	Opaque	Interstitial and euhedral inclusions in quartz, feldspar and biotite.	Biotite and accessory zircon, monazite and Fe-oxide	Haematite, calcite, chlorite, muscovite and uranophane	Euhedral, occasionally twinned zircon inclusions	A few microns up to 0.3mm	Rössing and Valencia 122
Betafite	Various shades of yellow and orange, commonly canary-yellow	Pseudo-isotropic, (dark olive-green when light intensity is increased)	Interstitial and irregular to sub-rounded inclusions in quartz and feldspar	Accessory magnetite	Secondary pyrochlore rims developed at the deuteric stage	Commonly strongly zoned. Irregular or radial cracks. Silicate inclusions	A few microns up to 0.1mm	Rössing and Goanikontes
Thorite (metamict)	Pale-yellow to pale-brown	Isotropic	Euhedral inclusion in perthite	Accessory monazite and zircon	None	Intergrown with zircon	0.1mm to 0.3mm	Rössing and Valencia 122
Uranyl silicate	Pale-yellow	Isotropic or aggregate polarization	Euhedral or anhedral inclusions, or discrete rims around uraninite	Uraninite and zircon	Uranophane	Euhedral	Grains up to 0.1mm, or rims up to 50 μ in width	Rössing and Valencia 122
Thoroniumite, calcliothorite and ferrothorite	Various shades of brown	Isotropic or displays aggregate polarization	Inclusions in quartz, feldspar or biotite.	Accessory monazite and zircon	Haematite and calcite	Wide range in composition Internal composition of U, Th, Ca and Si extremely variable	A few microns up to 0.3mm	Rössing, Valencia 122 and Goanikontes
Uranophane	Various shades of pale-yellow	Second order	Aggregates of needles in cracks or along grain boundaries	Calcite, muscovite and haematite	---	Commonly rims the other uranium phases	Berning et al. (1976) report individual crystals up to 0.75 x 0.3mm	Rössing, Valencia 122 and Goanikontes

interstitially or as euhedral inclusions in quartz, feldspar and biotite, commonly in association with zircon, monazite or Fe-oxide. A typical cluster of opaque uraninite and zircon inclusions in quartz is shown in the photomicrograph in Plate 36. The association with biotite reported by Berning et al. (1976) is typical of that shown in the photomicrograph, where the uraninite has crystallized near the edge of a biotite grain. The euhedral nature of these grains is illustrated better on the B.E.I. (Plate 37), which also displays the development of chlorite and uranophane in a rim around the uraninite. The uraninite grains, which are commonly twinned, may be surrounded by secondary rims containing calcite, muscovite and haematite as well as chlorite and uranophane. The uraninites at Rössing range in size from a few microns up to 0.3mm (Berning et al., 1976), and those from Valencia 122 appear to have a similar size range.

The betafite identified in the Rössing and Goanikontes alaskites is commonly irregular to sub-rounded and occurs interstitially or as inclusions in quartz and feldspar. The mineral was originally identified by Berning et al. (1976) in the Rössing alaskite, but it is not of economic importance because of its refractory chemical nature. It displays a variety of shades of yellow and orange in plane polarized light, but the dominant colour is a pale canary-yellow. The betafites observed range in size from a few microns up to 0.1mm. They may show an association with magnetite, and they commonly exhibit a well developed zonation (Plates 38 and 39), which is principally caused by a variation in the elements Si, Ca and U.

The betafite inclusion shown on the B.E.I. in Plate 39A displays a very complicated zonation, and the convoluted nature of some of the zones suggest the zonation may be caused by a secondary alteration rather

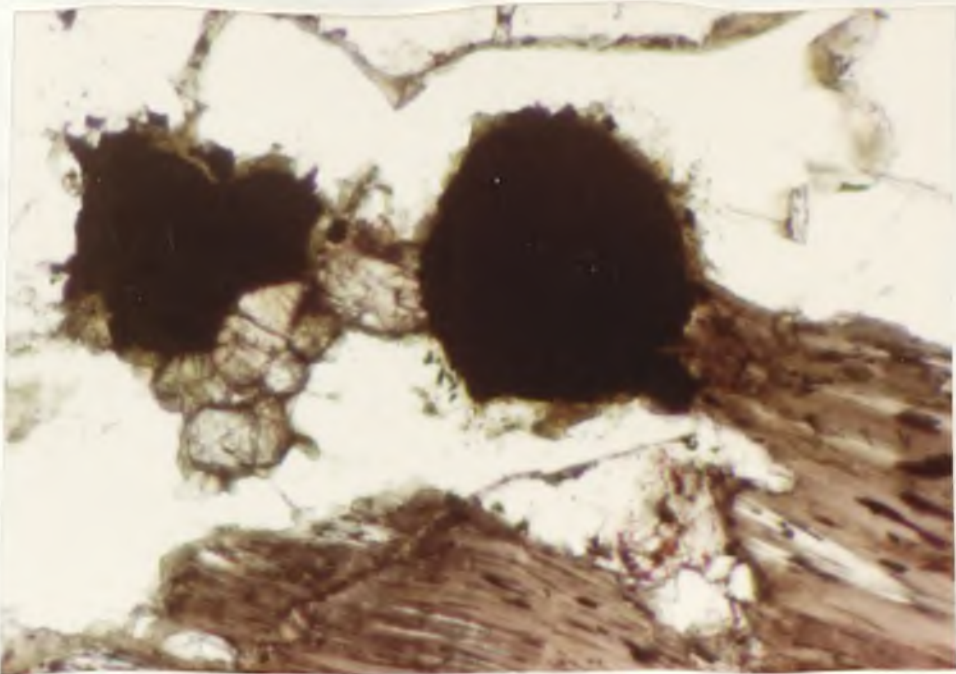


Plate 36. Photomicrograph of a cluster of uraninite and zircon inclusions in a quartz grain in contact with chloritized and muscovitized biotite in a Rössing alaskite (PPL; x 300).

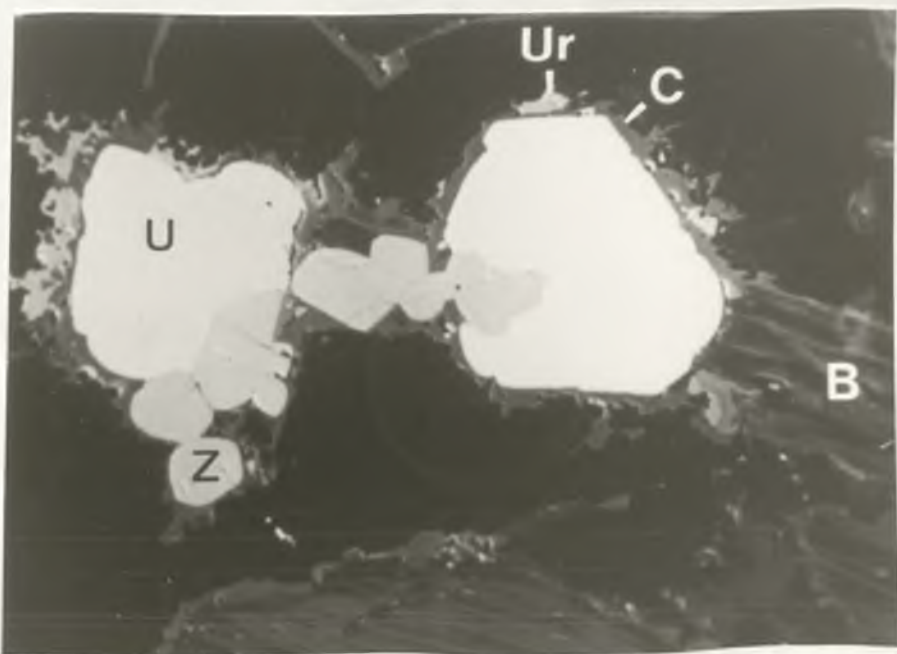


Plate 37. B.E.I. of the cluster of grains shown in Plate 36. U = uraninite, Z = zircon, B = biotite. Note the chlorite (C) and uranophane (Ur) which rim the uraninites, (x 300).

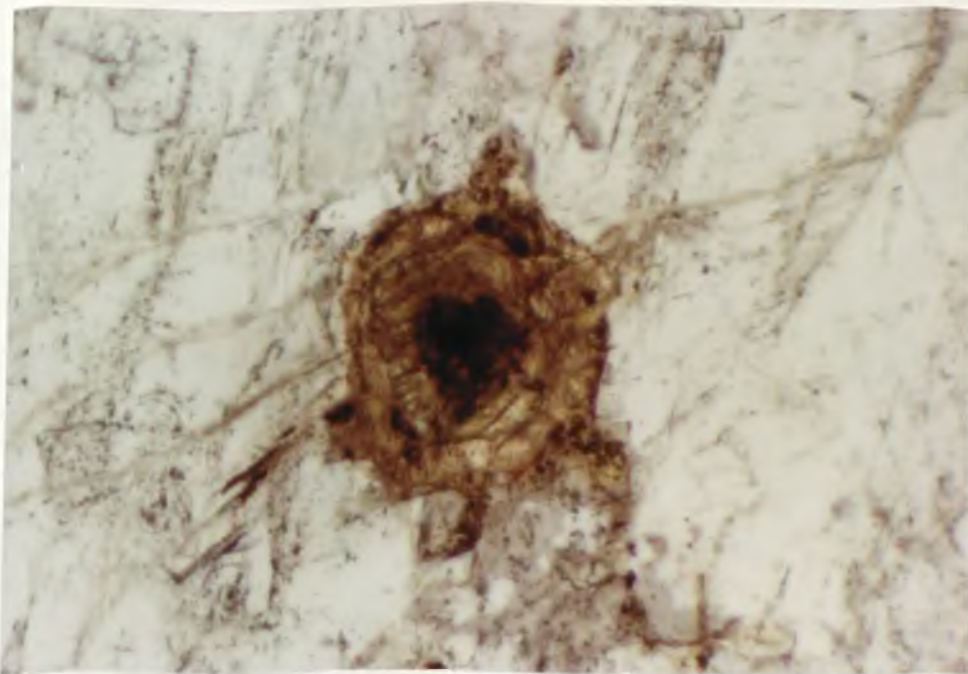


Plate 38. Photomicrograph of a zoned betafite inclusion in perthite from a Rössing alaskite, (PPL; x 300).

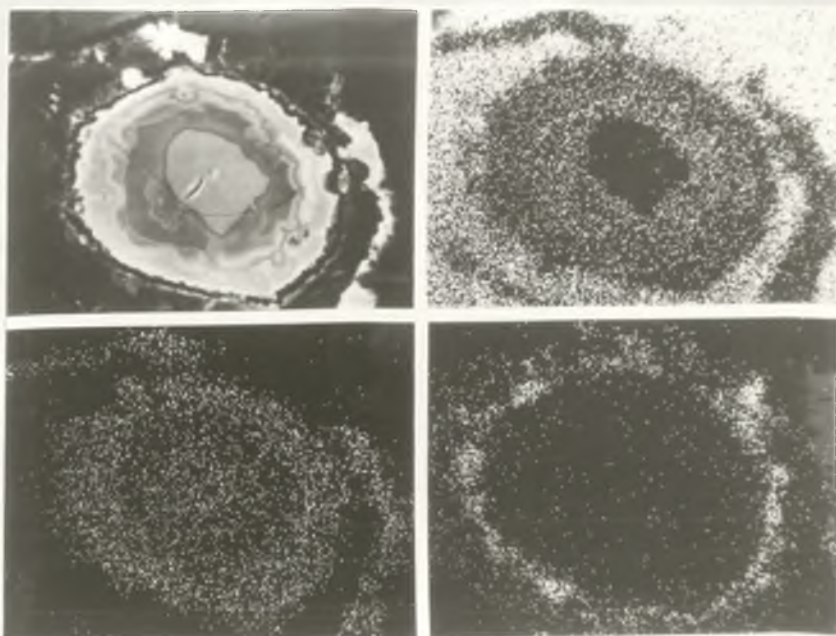


Plate 39. A = B.E.I. of a zoned betafite inclusion in quartz from an alaskite on Goanikontes. B, C and D are X-ray distribution maps of Si, U and Fe respectively, (x 1500).

than being a primary feature. The zonation in this particular grain is caused by a variation in the Si content, and to a lesser extent by a variation in the U content (Plate 39B and C). The Si is absent in the core of the grain and depleted at the rim, and is concentrated mainly in the intermediate zone between the two. The U shows an inverse relationship with the Si, being concentrated mainly in the core and the rim. The betafite inclusion is surrounded by a zone of haematite, which is indicated by the distribution of Fe on the X-ray map (Plate 39D). This zone is surrounded in part by a rim of uranophane which forms a bright image on the B.E.I. The U X-ray map suggests that the concentration of U in the uranophane is similar to that within the rim of the betafite.

The betafite is pseudo-isotropic under crossed nicols, and displays a dark olive-green colour when the light intensity is increased (Plate 40). The grains normally display a network of internal cracks, which may be dense and irregular, or well defined and radial in nature. The radial cracks in the betafite inclusion shown on the B.E.I. in Plate 41 clearly developed later than the zonation. These radial cracks probably formed during differential expansion which is presumed to accompany the transformation of a mineral to the metamict state. The brighter secondary betafite rim shown on the B.E.I., which contains tongues which penetrate the quartz host, has similar optical properties to the primary betafite within, and is considered to have developed during a deuteric stage of alteration prior to the metamictization. The zonation of the betafite appears to have been caused by the development of the secondary rim which has depleted the betafite in U in the zone immediately adjacent to the rim (Plate 41).

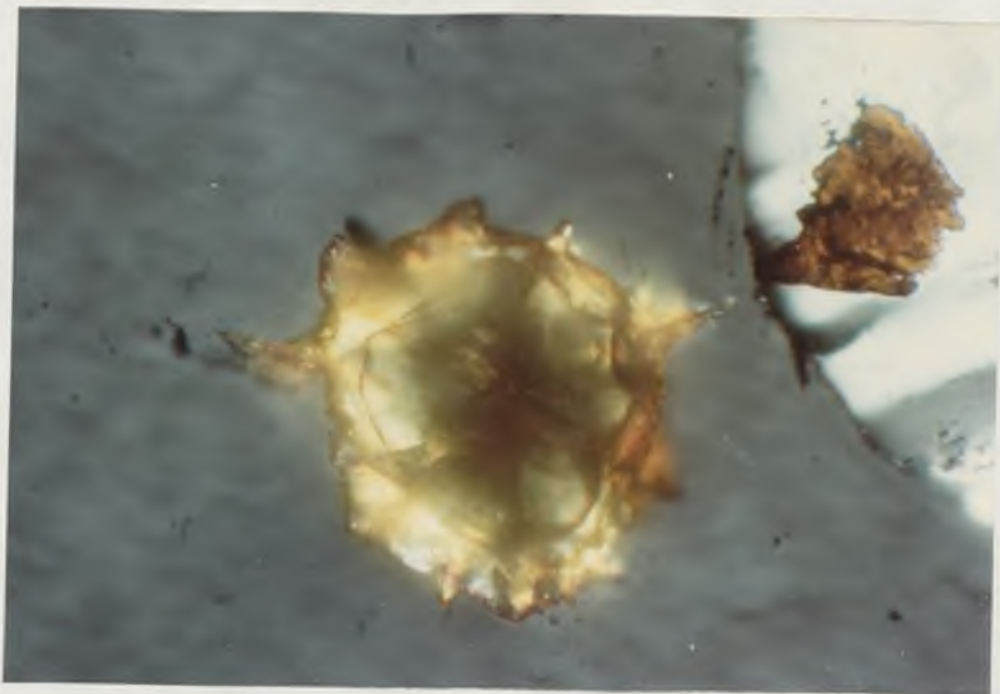


Plate 40. Photomicrograph of a betafite inclusion in quartz within an alaskite from Goanikontes, (XN; x 350).

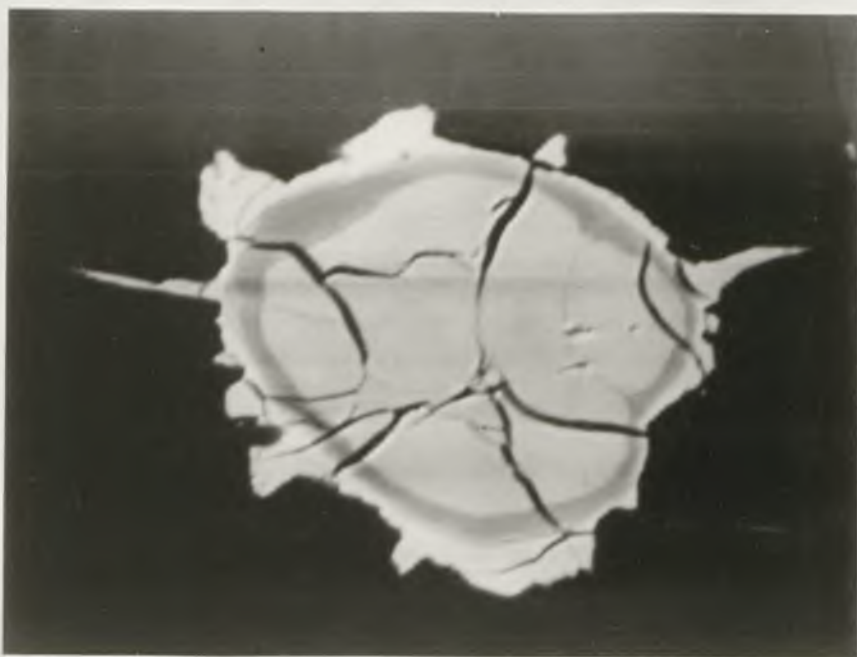


Plate 41. B.E.I. of the betafite inclusion shown in Plate 40. Note the zonation and the well developed radial cracks (x 750).

Metamict thorite has been identified in the Rössing and Valencia alaskites in the form of euhedral inclusions in quartz and feldspar. The inclusion shown in the photomicrograph (Plate 42) is intimately associated with monazite and zircon, and the latter mineral has intergrown with the thorite. It has a pale yellow to brown colour in plane polarized light, is isotropic, and varies in size from 0.1mm to 0.3mm across.

The uraninite, betafite and thorite are considered to be primary constituents of the alaskite, because of their intimate association with the other accessory minerals as well as their presence as inclusions within the major constituents. They are thought to have crystallized from a magma enriched in U and Th, and their abundance as small inclusions within the major constituents of the alaskite suggests that they may be relatively early-formed minerals.

B. The secondary uranium minerals in the alaskites

The secondary uranium minerals found within the alaskites include an unidentified uranyl silicate, thorogummite, calciothorite, ferrothorite and uranophane. The uranyl silicate is an alteration product of the uraninite, whilst the thorogummite, calciothorite and ferrothorite are alteration products of thorite. Uranophane may develop as an alteration product of any of the other primary or secondary uranium phases. The physical and optical characteristics of these minerals are listed in Table 9.

A uranyl silicate has been identified in the alaskites from Rössing and Valencia 122. The mineral occurs as rounded inclusions in quartz, commonly in association with zircon (Plate 44), or as partial alteration products of uraninite (Plate 43). Individual grains may be up to 0.1mm across, whilst discrete rims around

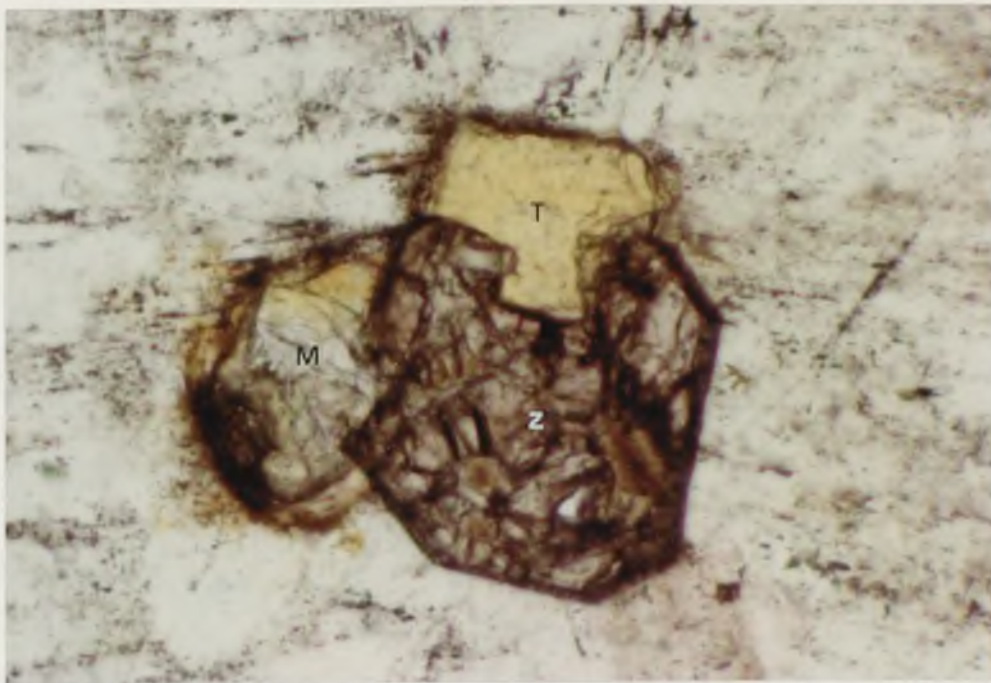


Plate 42. Photomicrograph of metamict thorite (T) inclusion associated with euhedral zircon (Z) and rounded monazite (M) in sericitized perthite from a Rössing alaskite (PPL; x 300).

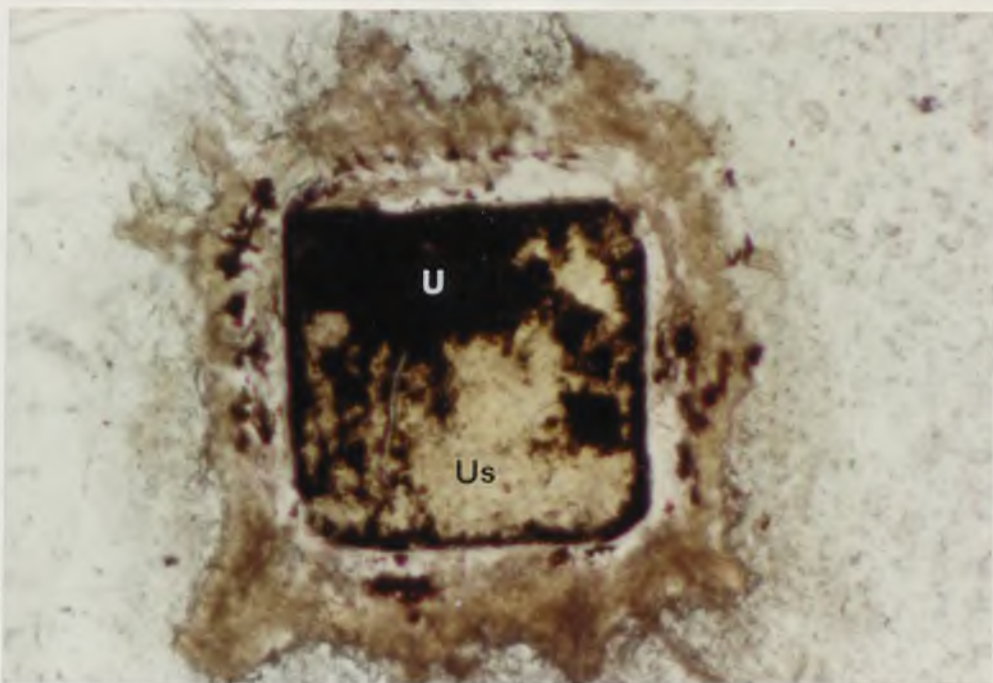


Plate 43. Photomicrograph of a uraninite (U) inclusion in orthoclase showing partial alteration to uranyl silicates (Us), in a Rössing alaskite (PPL; x 225).

uraninite grains range between a few microns and 50 μ in width. The uranyl silicate is pale-yellow in colour in plane polarized light, and is either isotropic or it displays aggregate polarization.

The photomicrograph in Plate 43 shows a euhedral uraninite inclusion in sericitized orthoclase which displays partial alteration to uranyl silicate. The latter has a pale-yellow colour in plane polarized light, and is isotropic. The altered uraninite is surrounded by a rim of calcite, muscovite, haematite and uranophane. The uraninite alteration is considered to have taken place during a deuteritic stage of alteration. It is not known when the uranophane around this particular grain developed, but its association with minerals such as calcite, muscovite and haematite indicates that it was also formed during the deuteritic stage.

The inclusion shown on the photomicrograph (Plate 45) is intergrown with a cluster of zircon grains, and the contact between the two grains on the B.E.I. (Plate 45A) suggests that pressure solution has resulted in the migration of the harder zircon into the softer uranyl silicate. Uranophane has developed in a rim around the inclusion, and within a crack in the quartz host. The X-ray distribution map of U (Plate 45B) indicates that the U content of the uranophane is greater than that of the uranyl silicate, whilst that of Th (Plate 45C) indicates an even distribution of Th within the uranyl silicate but a total absence in the uranophane. The Ca distribution map (Plate 45D) suggests an even distribution of Ca in the uranyl silicate, and possibly a slightly elevated Ca content in the uranophane.

The thorogummite, calcliothorite and ferrothorite which occur as pseudomorphs after thorite, are present as anhedral to euhedral inclusions in quartz, feldspar and biotite. They have been identified

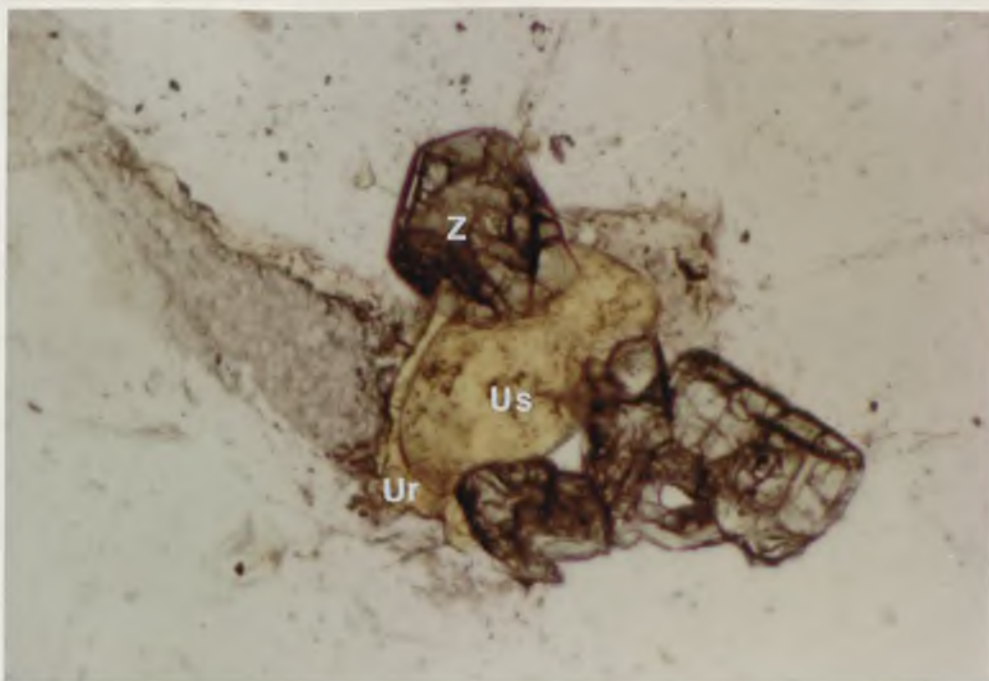


Plate 44. Photomicrograph of uranyl silicate (Us) associated with zircon (Z) as inclusions in quartz from a Rössing alaskite. Note the uranophane (Ur) rimming the uranyl silicate (PPL; x 300).

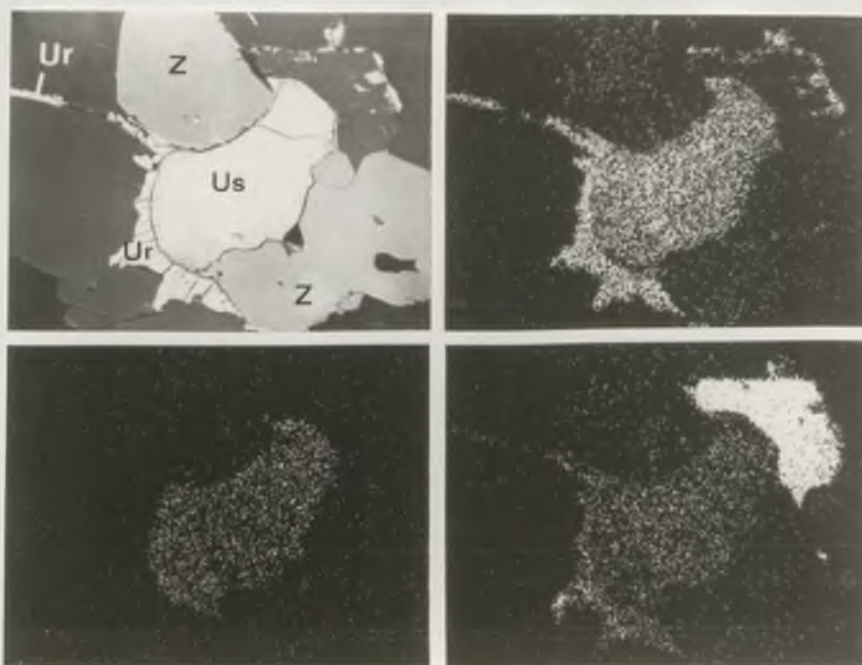


Plate 45. A = B.E.I. of uranyl silicate (Us) and zircon (Z) inclusions shown in Plate 44. Note the development of uranophane (Ur) in the crack within the quartz host. B, C and D are X-ray distribution maps of U, Th and Ca respectively, (x 225).

within the alaskites from Rössing, Valencia 122 and Goanikontes, and they show a range in size from a few microns up to 0.3mm. Like the uraninite they are commonly associated with monazite and zircon, and alteration rims containing haematite and calcite are normally present. The minerals display a variety of shades of brown in plane polarized light (Plate 46), and under crossed nicols they may be isotropic or display aggregate polarization (Plate 48).

The thorogummite shows a wide range in composition from Ca rich calcliothorites to Fe rich ferrothorites. The internal composition of some grains is extremely variable, but it is uncertain whether this is a primary feature of the original thorite grain, or a secondary feature related to the hydration of the thorium silicate. In Plate 47A a B.E.I. of the thorogummite grain shown in Plate 46 indicates the presence of inclusions. X-ray distribution maps of the same grain (Plate 47B, C and D) show how the elements Th, Ca and Si may vary within a single grain. The Th map indicates that the thorogummite may be enriched in Th along its rim, whilst the Ca and Si maps suggest a very irregular distribution of these two elements. There does however, appear to be an inverse relationship between the distribution of Ca and that of Si.

Part of the thorogummite grain shown on the photomicrograph in Plate 48 is enlarged in Plate 49 as a B.E.I. X-ray maps of the enlarged region indicate a peculiar variability exists in the distribution of the elements U, Ca and Th. The Ca shows a similar distribution to that of U, with the exception that it is concentrated within the internal crack seen on the B.E.I. The distribution of Th however, shows a strong inverse relationship with that of U.

The uranophane may occur as aggregates of needles around most of

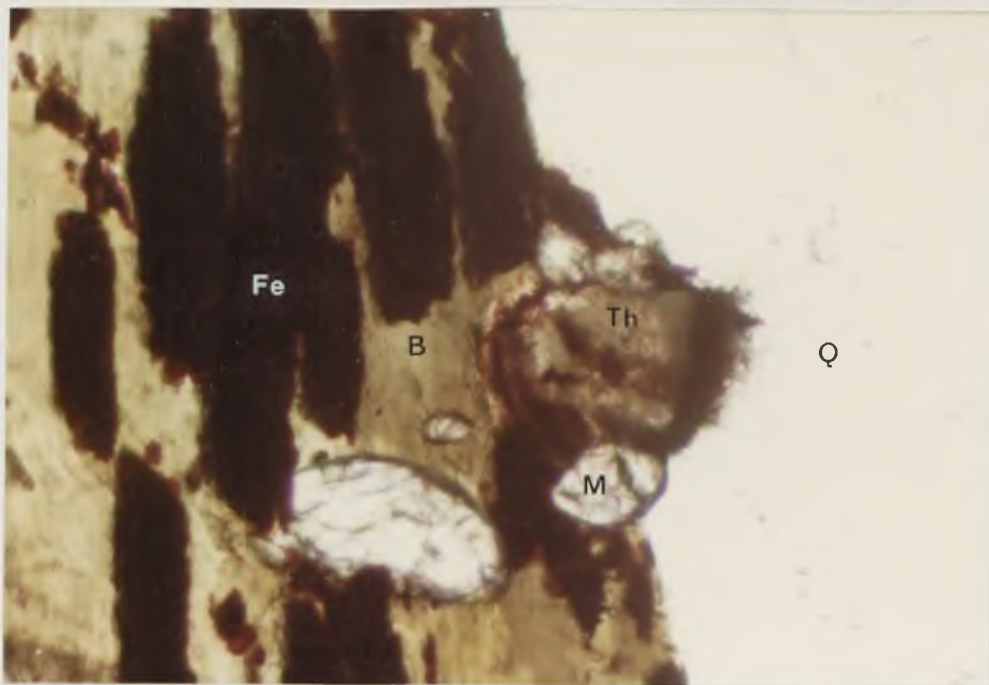


Plate 46. Photomicrograph of thorogummite (Th) grain at quartz (Q)-chloritized biotite (B) grain boundary, from a Goanikontes alaskite. Note the association with monazite (M). Fe = Fe-oxide, (PPL; x 250).

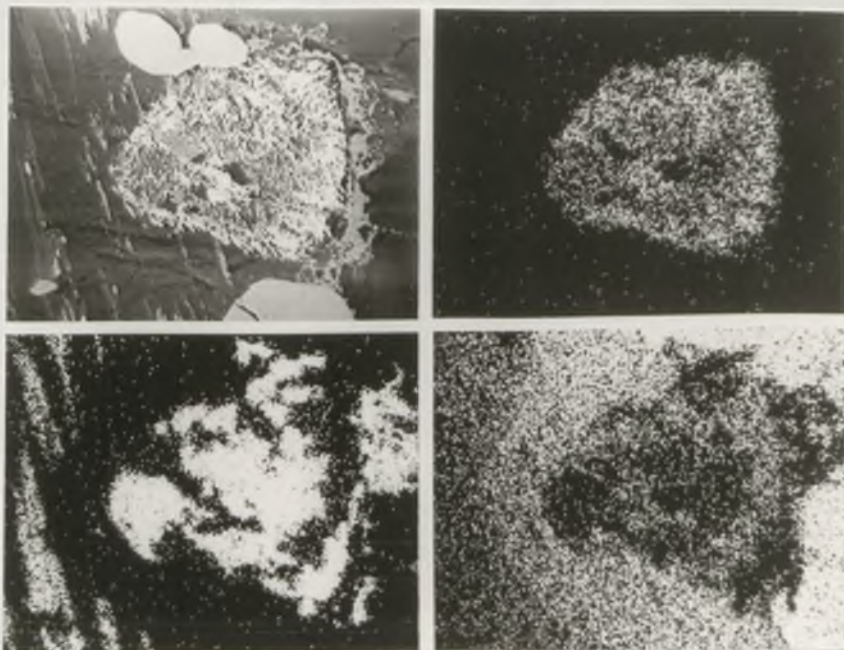


Plate 47. A = B.E.I. of the thorogummite grain shown in Plate 46. B, C and D are X-ray distribution maps of Th, Ca and Si respectively. Note the inverse relationship shown by the distribution of Ca and Si (x 320).

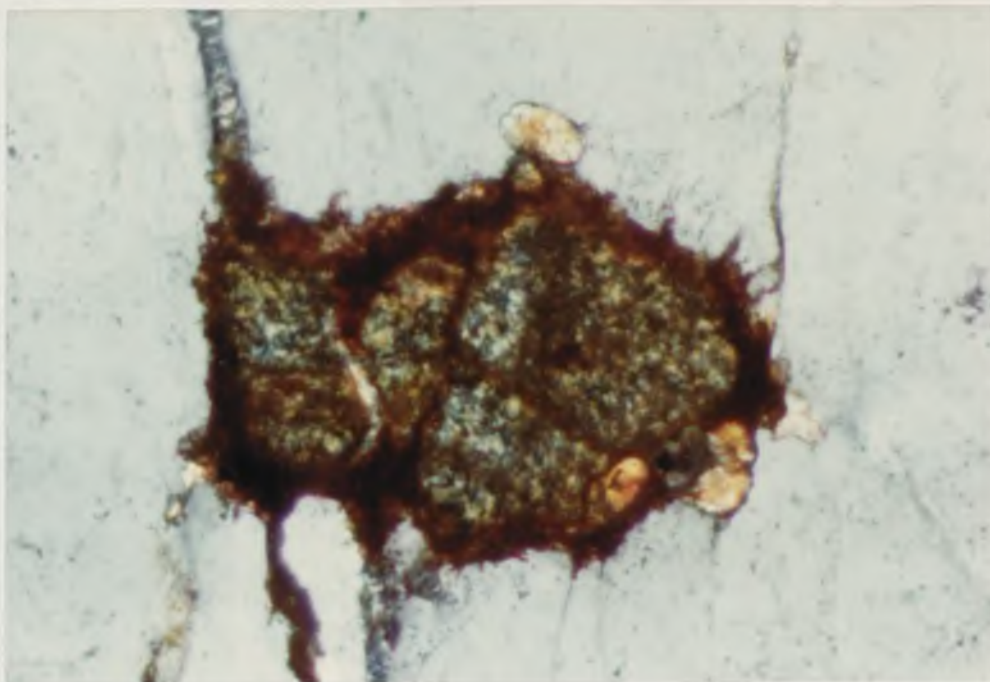


Plate 48. Photomicrograph of a thorogummite inclusion associated with small monazite grains in quartz, from a Rössing alaskite. Note the aggregate polarization and the haematite rim, (XN; x 250).

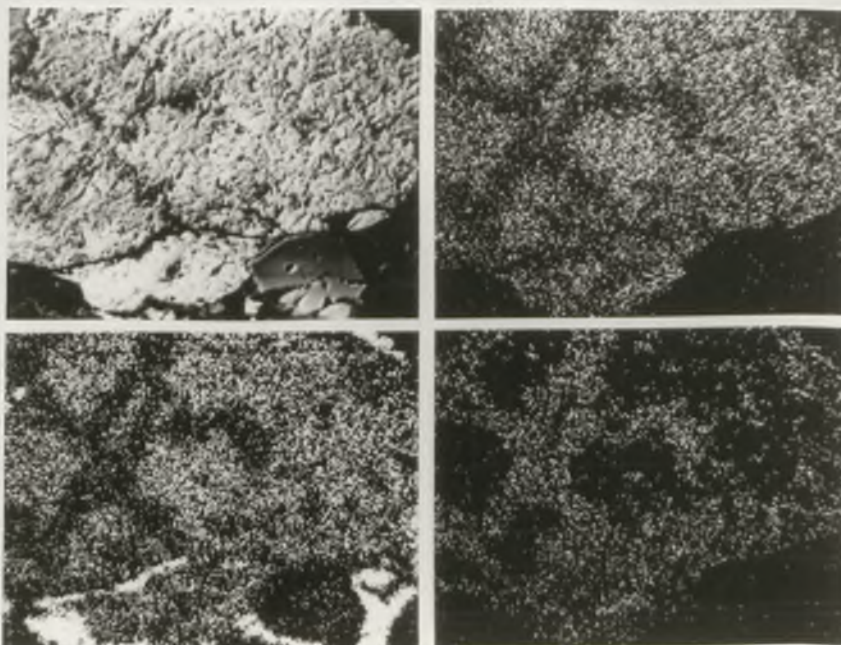


Plate 49. A = B.E.I. of part of the thorogummite grain shown in Plate 48. B, C and D are X-ray distribution maps of U, Ca and Th respectively. Note the inverse relationship shown by the distribution of U and Th. (x 340).

the primary and secondary uranium minerals described above, as well as within cracks and along grain boundaries of the major constituents of the alaskite. The optical properties of the uranophane are identical to those described in Section 3 (ii), for the uranophane situated within the metasediments of the Khan Formation.

The secondary uranium minerals in the alaskites are considered to have developed during two periods; firstly, during a deuteric alteration, and secondly during a recent stage of surface enrichment and secondary alterations. The extent to which the various secondary minerals developed during each alteration is unknown. It is likely however, that many of the secondary uranium phases have developed during the deuteric stage because they are commonly associated with other secondary minerals such as muscovite, chlorite, calcite and haematite which have been recognized as deuteric minerals. The secondary betafite rims pre-date metamictization and must certainly be associated with the earlier alteration. During the recent period of surface enrichment and secondary alteration the dominant minerals to form are those such as uranophane which commonly show no associations with primary uranium phases. These minerals are considered to have developed by a process of ground water interaction with existing primary and secondary uranium minerals, removal of the uranyl ion in solution and subsequent precipitation in the near-surface environment in available cracks, interstices and pore spaces.

IV.6. Conclusions

Primary uranium mineralization has been located within the basement at the Breytenbach copper prospect on Namibfontein 91. The mineralization occurs in the form of uraninite inclusions in magnetite grains within weakly radioactive pyroxenite which contains disseminated chalcopyrite. The

uraninite probably crystallized from uraniferous solutions derived by the partial mobilization of uranium in juxtaposed radioactive alaskites.

Uranium minerals have been found in the Etusis quartzites on Wolfkoppe 105 in the vicinity of radioactive alaskites. The minerals occur in the form of uranyl silicate inclusions in microcline grains which represent original detrital constituents of the metasediment. The presence of this uranium phase provides direct evidence of radioactive material within the pre-Damaran basement prior to its erosion, transportation and deposition within the Etusis Formation.

Primary uranium minerals have been found within metasediments of the Rössing Formation at Rössing and Valencia 122. The mineralization occurs in the form of uraninite and betafite within calc silicates at Valencia, and schists of the lower biotite-cordierite gneiss unit at Rössing. The uranium is considered to be syngenetic, and to have recrystallized during the Damaran metamorphism prior to the emplacement of the uraniferous alaskites at Rössing and Valencia 122.

The most radioactive calc silicates of the Rössing sequence on Valencia 122 represent the host rocks to the more strongly developed stratabound copper deposits.

The primary cause of the radioactivity displayed by the leucocratic varieties of the Salem granite is considered to be the abundance of U- and Th-bearing phosphate. The U and Th in the phosphate has migrated during the process of metamictization, and secondary U and Th phases have developed within alteration zones in silicates that host the

phosphates. The U and Th in these secondary phases have been trapped by ground water solutions, and surface enrichment processes have concentrated these elements in the near-surface environment resulting in the development of secondary uranium minerals such as uranophane.

Uranium minerals have been found within a radioactive red granite on Otjua 37. The minerals identified include uraninite, thorogummite and an unidentified uranyl silicate. The last two minerals may occur as euhedral inclusions in association with monazite and zircon and they are thought to represent alteration products of thorite and uraninite respectively. The primary uranium minerals are considered to have crystallized from a magma enriched in U and Th, possibly as relatively early-formed minerals.

There appears to be a stratigraphic control on the location of mineralized alaskites in certain areas of the belt. There is also an association between the presence of stratabound copper deposits and mineralized alaskites.

Primary uranium minerals identified within the alaskite include uraninite, betafite and metamict thorite. They are considered to be primary in nature because of their intimate association with the other accessory minerals as well as their presence as inclusions within the major constituents. Like the primary phases in the red granites they are thought to have crystallized from a melt enriched in U and Th.

The betafite in the alaskites is characteristically zoned, a feature which appears to have developed during a deuteritic stage of

alteration. The zonation is mainly caused by an internal variation in Si, Ca and U, and the distribution of Si and U is inversely related in some grains. The characteristic radial cracks are considered to have developed in response to differential expansion which is presumed to accompany the transformation of the mineral to the metamict state.

Secondary uranium minerals found within the alaskite include an unidentified uranyl silicate, thorogummite, calciothorite, ferrothorite and uranophane. These minerals are considered to have developed during two periods; firstly, during a deuteritic alteration, and secondly during a recent stage of surface enrichment and secondary alteration. Minerals have formed during the latter stage by a process of ground water interaction with existing primary and secondary uranium minerals, removal of the uranyl ion in solution and subsequent precipitation in the near surface environment in available cracks, interstices and pore spaces.

The thorogummites commonly display a peculiar internal variability in the distribution of the elements U, Th, Ca and Si. The U can be inversely related to the Th, whilst the Si can be inversely related to the Ca. This chemical variability may in part be related to the alteration of thorite to thorogummite.

CHAPTER VII

CHEMISTRY OF THE URANIUM MINERALS

VII.1. Introduction

Many of the uranium minerals within the uraniferous rocks from the Damaran belt display similar optical features (Table 9), and in the absence of spectrographic data it was necessary to obtain a first approximation of the chemistry before a specific mineral identification could be made. The minerals were analysed with the Jeol JXA 50A wavelength dispersive electron probe microanalyzer at Leeds, using an accelerating voltage of 20 kV, a specimen current of 3×10^{-8} amps, and a count time of 40 seconds per element. The programme "FRAME" (Yakowitz et al., 1973) was used for the Z.A.F. correction.

A total of 72 partial analysis have been obtained on various uranium phases including uraninite, betafite, metamict thorite, uranyl silicate, thorogummite and uranophane. The partial analyses are tabulated in Appendix 3. The low totals in some of the analyses may be due to the presence of rare earth elements (R.E.E.) and water which could not be analysed. Frondel (1958) quotes uraninite analyses from pegmatites with up to 11% total R.E.E. and he states that uraninite in pegmatite typically contains considerable amounts of R.E.E. in solid solution. Likewise Bjørlykke (1931) quotes concentrations of up to 3.9% Y in betafites from Tangen in Norway, whilst Hogarth (1961) cites concentrations of up to 2.2% Ce in betafites from Canada. Water may also be present as an essential constituent of betafite and the secondary uranium phases. For instance, Bjørlykke (1931) quotes figures of over 13% H₂O in betafite, whilst Frondel (1958)

cites analyses of thorogummite with up to 10% H₂O, and of uranophane with up to 13% H₂O. Because the R.E.E. and water were not analysed there will be an inbuilt error in the corrected weight per cent, and therefore the partial analyses should be considered as first approximations only, and have consequently been quoted to one decimal place (Appendix 3).

VII.2. Uraninite

Twenty three partial analyses of uraninite have been obtained from various mineralizations within the belt, including thirteen analyses from the Rössing alaskites, four from the Valencia alaskites, four from the lower biotite-cordierite gneiss unit of the Rössing Formation at Rössing, and single analyses from the red granite on Otjua 37 and the basement on Namibfontein 91. The partial analyses are given in Appendix 3A.

The uraninites have been plotted on a U-Th-Pb triangular diagram (Fig. 23) on which fields are drawn around the uraninites from the Rössing alaskites (field 1), those from the Valencia alaskites (field 2), and those from the Rössing schists (field 3). The Rössing uraninites appear to show a larger variation in U, Th and Pb than the other groups, but this may merely be due to the larger number of samples analysed from this locality. The majority of the analyses fall within a fairly restricted field, and there does not appear to be any significant differences in the absolute amounts of U, Th and Pb in the various uraninites, with the exception of that from the basement on Namibfontein 91 which shows lower Th. The basement uraninite also displays relatively high Fe₂O₃ which may indicate that the mineral is slightly altered.

The U/Th ratios of the uraninites tabulated in Appendix 3A show slight differences from one locality to the next. The Rössing alaskites display

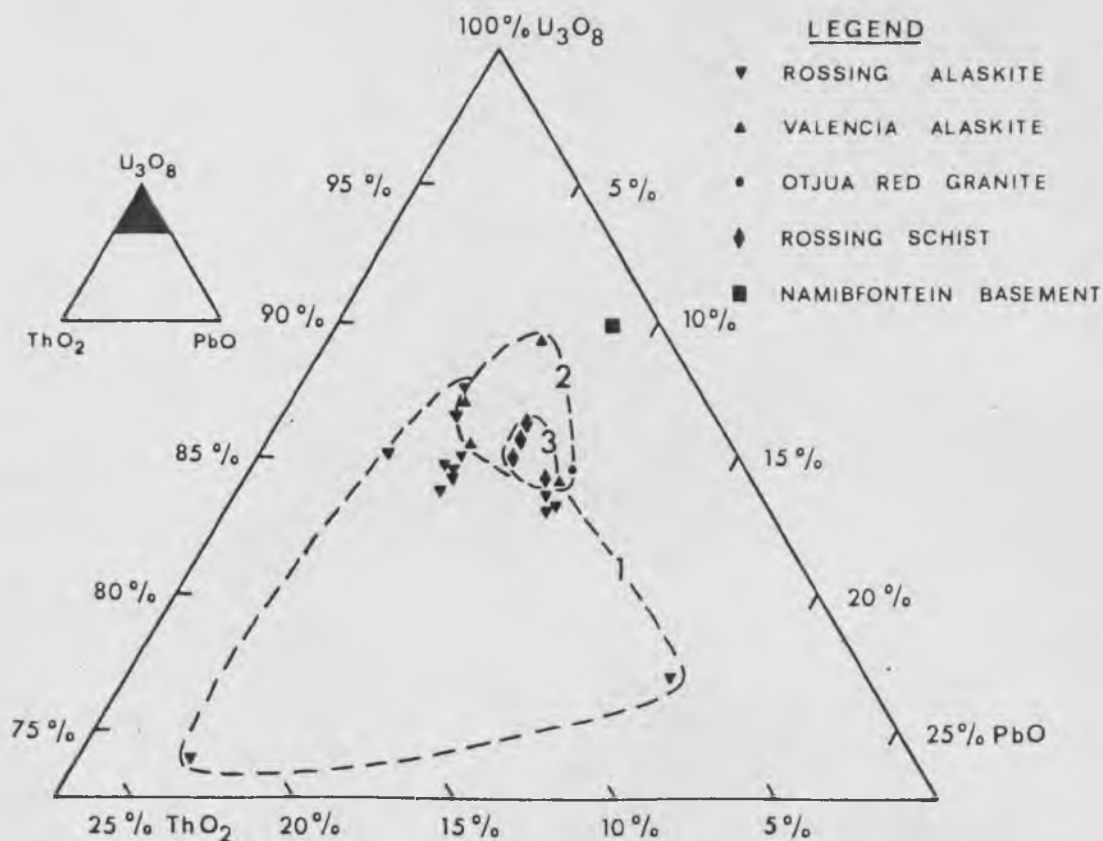


Fig. 23. U-Th-Pb triangular diagram of the uraninites. Fields 1 and 2 enclose uraninites from the Rössing and Valencia alaskites respectively; field 3 encloses uraninites from the biotite-cordierite gneiss unit of the Rössing Formation at Rössing.

the lowest U/Th ratios, having a range between 3.1 and 12.9. Berning et al. (1976) quote a U/Th ratio of 13.05 for a purified uraninite concentrate from the Rössing alaskite. The Valencia alaskites show a higher range between 10.5 and 22.9, and the single analysis of uraninite from the Otjua red granite gives a ratio of 15.7. The U/Th ratios of the uraninites in the Rössing schists are higher than those within the Rössing alaskites, and the ratio of 64.6 calculated for the basement uraninite is well above the others.

The U/Th ratios suggest that the mineralized alaskites and red granites crystallized from magmas which may have had significantly different U/Th ratios. Also the higher range of U/Th ratios displayed by the uraninites in the Rössing schists relative to the Rössing alaskites

suggests that these minerals crystallized from different melts. This is consistent with the theory that U was present within metasediments of the Rössing Formation at Rössing and Valencia 122, prior to the emplacement of the uraniferous alaskites.

The minor amounts of Th and Zr present within the uraninites are considered by Frondel (1958) to be held in solid solution, whilst the Pb is taken into solid solution during the continuous decay of U and Th. The nature in which small quantities of Si, Ti, K, Fe and Al are held within the mineral is uncertain however. Frondel (1958) indicates that those elements have not been shown to be part of the uraninite composition, and he considers they are probably due to the presence of microscopic inclusions, or the admixture of other material within the uraninite. In contrast, Snelling (1980) suggests the minerals Ca, Si, Fe and Mn may substitute in the UO_2 lattice, because of the homogeneous distribution of these elements in uraninites from Koongarra in Australia.

VII.3. Betafite

Seventeen partial analyses of betafite from the Damaran metasediments and alaskites are tabulated in Appendix 3B. The analyses include seven betafites from the Goanikontes alaskite, three from the Rössing alaskite, six from the calc silicates in the Rössing Formation at Valencia, and a single analysis from the lower biotite-cordierite gneiss unit of the Rössing Formation at Rössing.

The betafites have been plotted on a U-Ti-(Nb + Ta) triangular diagram (Fig. 24) on which fields are drawn around the alaskitic betafites (field 1) and the metasedimentary betafites (field 2). These fields are clearly separated, the metasedimentary betafites showing higher Ti values than the alaskitic ones. The betafites from the different alaskites

can not be distinguished but those in the calc silicates from Valencia 122 show higher U values and lower (Nb + Ta) values than the betafite from the Rössing schist.

The betafites have also been plotted on a Nb-Ta-W triangular diagram (Fig. 25) on which fields are drawn around those from the Goanikontes alaskites (field 1) and those from the Valencia meta-sediments (field 2). The betafites from the four environments clearly fall in separate fields in Fig. 25, those from the Rössing alaskites showing higher Ta and W, and lower Nb than the single analysis from the Rössing schist. Although the data is limited in terms of the number of analyses obtained, it suggests that differences existed within the various melts from which the betafites crystallized.

The U/Th ratios of the betafites shown in Appendix 3B are extremely variable, ranging from 11 to 177 in the Goanikontes alaskites. The lowest ratio of 6.2 calculated for the Rössing schist is significantly lower than the range of 41 to 55 obtained for the Rössing alaskites. The Nb/Ta ratios (Appendix 3B) are less variable, but again the greatest range of 1.7 to 6.7 is shown by the Goanikontes alaskites. The highest ratio of 10.3 calculated for the Rössing schist is once more significantly different from the range of 7.0 to 7.1 obtained for the Rössing alaskites. These ratios may indicate that slight differences existed within the original liquids from which the betafites crystallized. However, the very limited number of samples analysed precludes any definite statements in this respect.

In an attempt to establish the amount of internal variations in chemistry shown by the betafites, a single grain was analysed in four separate places. The zoned grain is shown on the B.E.I. in Plate 50A and it consists of a core which is enriched in Ca and depleted in Si

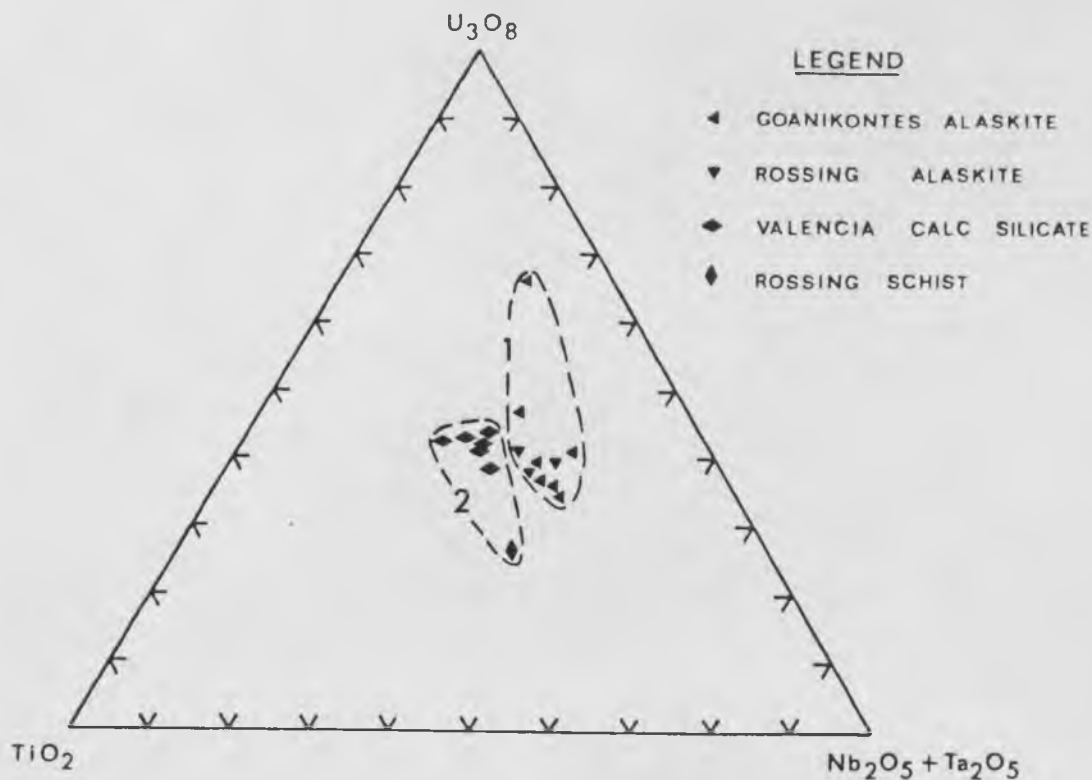


Fig. 24. U-Ti-(Nb + Ta) triangular diagram of the betafites. Field 1 encloses betafites in alaskites, whilst field 2 encloses those in metasediments.

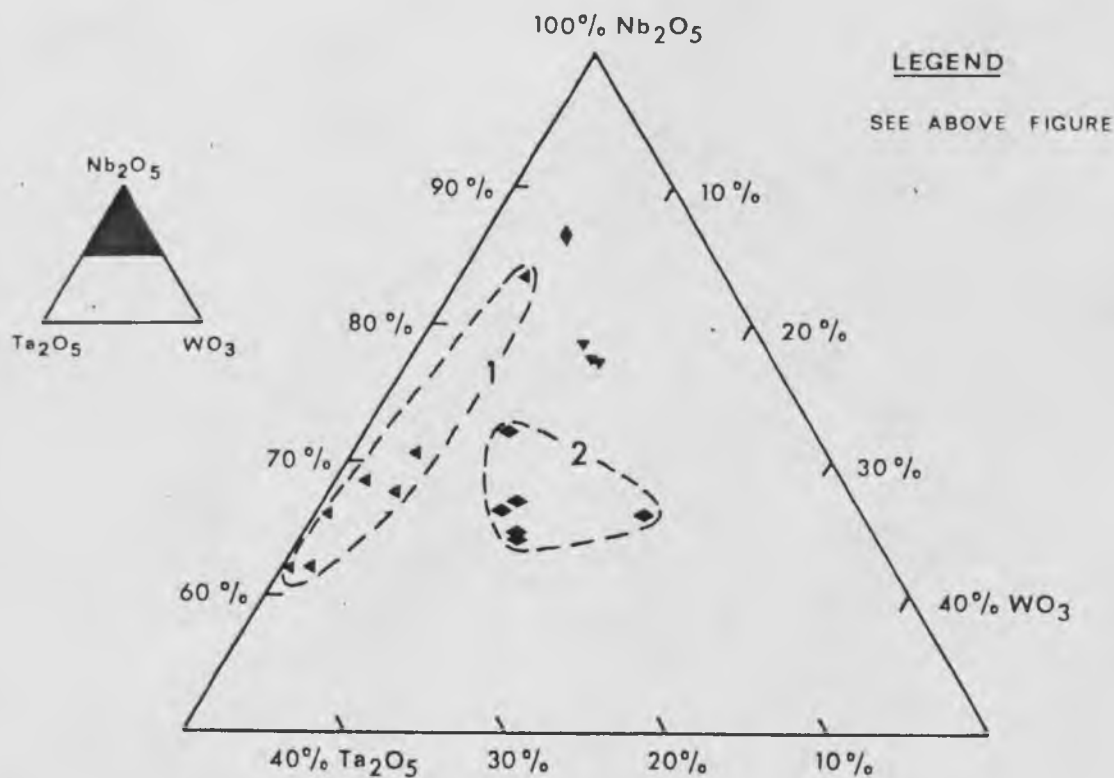


Fig. 25. Nb-Ta-W triangular diagram of the betafites. Field 1 encloses betafites from the Goanikontes alaskite, whilst field 2 encloses those from the Rössing Formation at Valencia.

(Plate 50, D and C respectively), and a zoned rim which appears to be depleted in U along its inner edge, due possibly to secondary enrichment at the extreme rim. The position of the spots probed are shown on the B.E.I., and the partial analyses are given in Table 10. The core of the grain is clearly enriched in Ca and U, and depleted in Si relative to the rim. There also appears to be a slight enrichment, in the elements Ti, Fe, Nb and W, and a concomitant depletion in Th in the core relative to the rim.

There is a certain amount of confusion in the literature with regard to the distinction between betafite and uranoan pyrochlore, and Frondel (1958) considers the minerals in some reported localities may have been confused. Hogarth (1961) defines betafite as a mineral with the pyrochlore structure and high U and Nb contents, and his frequency diagrams suggest a natural division of the two minerals at 15% U. Uranium and Nb are major constituents of the Namibian betafites showing ranges of 18 to 53% and 14 to 27% respectively, and they have been named betafite for this reason. The minor amounts of Ca, Ta and Ti within the Namibian betafites are present as essential constituents, whilst Pb and Th are considered by Frondel (1958) to occur within betafite in substitution for U and Ca. Hogarth (1961) is of the opinion that if water is present it occurs in open spaces, loosely held by bonds that have been disrupted through radioactive bombardment.

VII.4. Metamict thorite

Two partial analyses of metamict thorite are shown in Appendix 3C. One is from a Rössing alaskite shown in Plate 42, and the other is from a Valencia alaskite. The mineral is characterized by high Th and low U, but minor amounts of Si, Ca and radiogenic Pb are also present. The

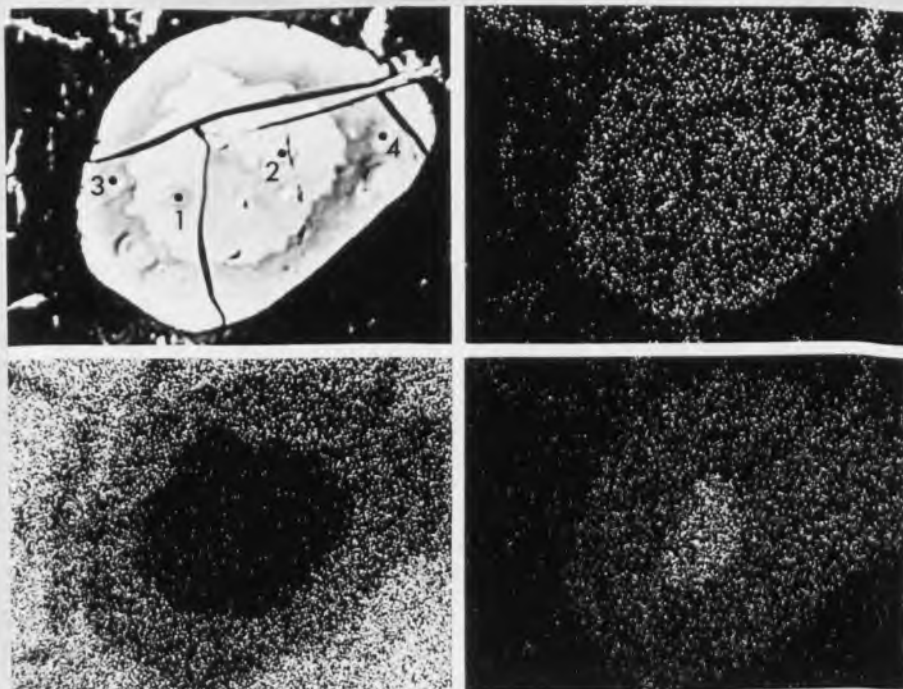


Plate 50. A = B.E.I. of a zoned betafite in a Goanikontes alaskite, showing the location of analyses given in Table 10. B, C and D are X-ray distribution maps of U, Si and Ca respectively, (x 500).

TABLE 10. Partial analyses of a single grain of betafite (sample G7 F) showing a well developed zonation. Location of spots within the zoned grain are shown on the B.E.I. in Plate 50A.

$\text{Fe}_2\text{O}_3(t)$ = total Fe as Fe_2O_3

	<u>Spot 1</u>	<u>Spot 2</u>	<u>Spot 3</u>	<u>Spot 4</u>
ThO_2	1.7	2.0	2.3	2.6
U_3O_8	28.9	28.4	25.0	27.9
CaO	13.0	12.7	5.1	5.1
TiO_2	17.4	17.5	15.3	11.5
$\text{Fe}_2\text{O}_3(t)$	1.4	1.3	0.7	0.7
Al_2O_3	0.1	0.1	0.3	0.3
SiO_2	0.0	0.0	9.0	12.0
Nb_2O_5	24.1	23.3	21.1	17.8
Ta_2O_5	10.0	8.4	10.6	10.8
WO_3	1.5	1.3	0.2	0.1
Total	98.1	95.0	89.6	88.8

thorites are plotted on a U-Th-Si triangular diagram (Fig. 26, open symbols), next to secondary thorogummites derived by alteration of primary thorite.

VII.5. Uranyl silicate

Thirteen partial analyses of an unidentified uranyl silicate are shown in Appendix 3D. These include five analyses from the Rössing alaskite, three from the Valencia alaskite and five from the Otjua red granite. The mineral consists of major amounts of U, Th and Si and minor amounts of Ca, Pb and Zr. The analyses are plotted on the U-Th-Si triangular diagram (Fig. 26) adjacent to analyses of the thorogummites. They display a wide range in U and Th values but the Si content falls within a restricted range of 10 to 20%.

The euhedral uraninite inclusion shown in Plate 43 which displays partial alteration to uranyl silicate, has been examined in an attempt to establish the chemical changes which take place during the alteration of uraninite to uranyl silicate. The grain was analysed in three places, firstly within an unaltered part of the uraninite, secondly at the boundary between the unaltered uraninite and the secondary uranyl silicate, and lastly within a portion of the uranyl silicate itself. These positions are marked 1, 2 and 3 respectively on Fig. 27 which shows the distribution of uraninite and uranyl silicate in the inclusion displayed in the photomicrograph in Plate 43. The three partial analyses are given in Table 11, and their positions on the U-Th-Si triangular diagram (Fig. 26) are marked by the numbers 1, 2 and 3. The path of alteration from uraninite to uranyl silicate, defined by arrows on the triangular diagram is characterized by an increase in Si and Ca, and a decrease in U and Pb.

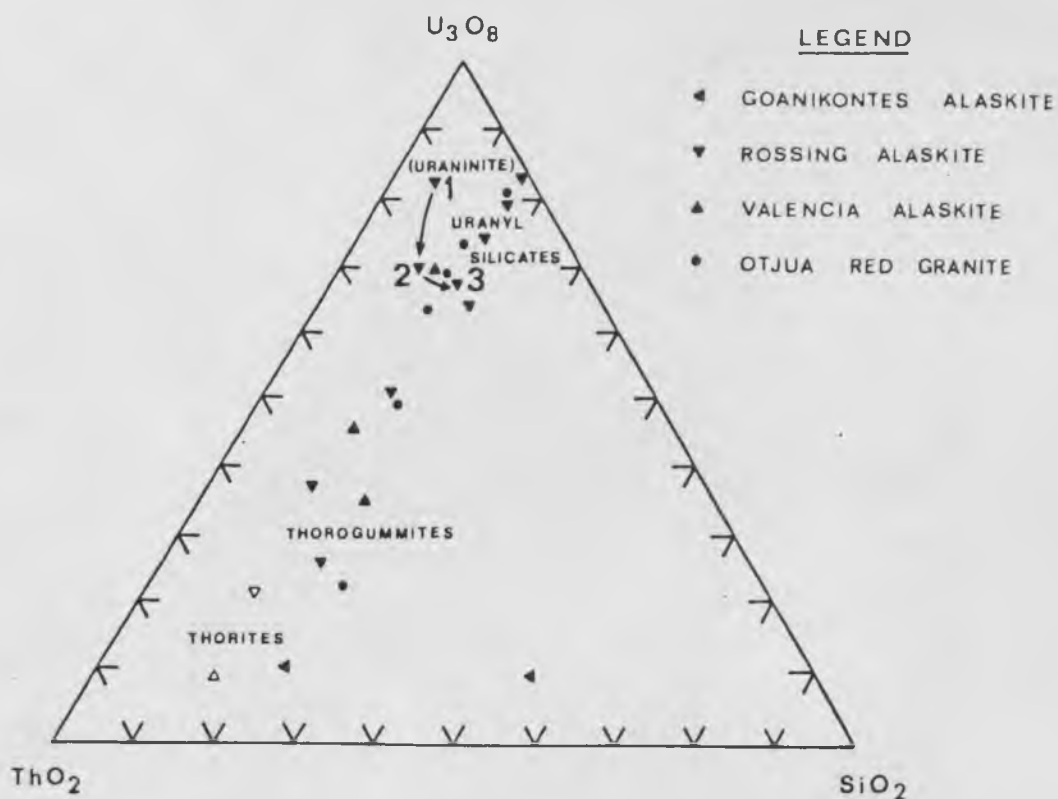


Fig. 26. U-Th-Si triangular diagram of the metamict thorites (open symbols), the thorogummites and the uranyl silicates. Arrows define path followed by a single uraninite during its alteration to uranyl silicate. Analyses 1, 2 and 3 are given in Table 11 and their positions within the altered uraninite are shown in Fig. 27.

The Th appears to increase during the course of alteration, although the intermediate spot 2 shows slightly higher Th than spot 3 which lies entirely within the uranyl silicate. This however may be due to an original inhomogeneous distribution of Th in the primary uraninite.

The partial alteration of uraninite exemplified by the sample shown in Plate 43 differs from the sequence of alteration of uraninite to gummite described by Frondel (1956). His typically altered uraninite crystal from a pegmatite consists of three zones, firstly a veined or embayed central uraninite core, secondly a zone of hydrated uranyl oxide, and thirdly an outer zone of uranyl silicate. This alteration sequence is assumed to take place at atmospheric conditions through the agency of meteoric waters. The absence of distinct zones of alteration

TABLE 11. Partial analyses of a single grain of uraninite (sample 122 A) showing incomplete alteration to uranyl silicate. For location of spots within the altered uraninite see Fig. 27, and for photomicrograph of the uraninite inclusion see Plate 34.

Fe_2O_3 (t) = total Fe as Fe_2O_3

	<u>Spot 1</u>	<u>Spot 2</u>	<u>Spot 3</u>
ThO_2	9.9	16.5	13.8
U_3O_8	68.4	57.2	56.1
K_2O	0.3	0.3	0.3
CaO	1.3	3.0	3.6
TiO_2	0.1	0.1	0.1
PbO	6.5	3.7	2.4
Fe_2O_3 (t)	0.1	0.1	0.1
Al_2O_3	0.3	1.0	0.5
SiO_2	4.5	8.1	13.5
ZrO_2	0.9	1.1	0.7
Total	92.3	91.1	91.1

in the Namibian uraninites suggests they developed in a different manner to that described above. The irregular distribution of uranyl silicate within the core of partially altered uraninite suggests the alteration is related to the passage of fluids during a deuteric stage of alteration. Ross et al. (1931) have previously assigned the internal alteration of uraninite to clarkeite, a hydrated oxide of U and Pb by reaction with late pegmatitic hydrothermal solutions.

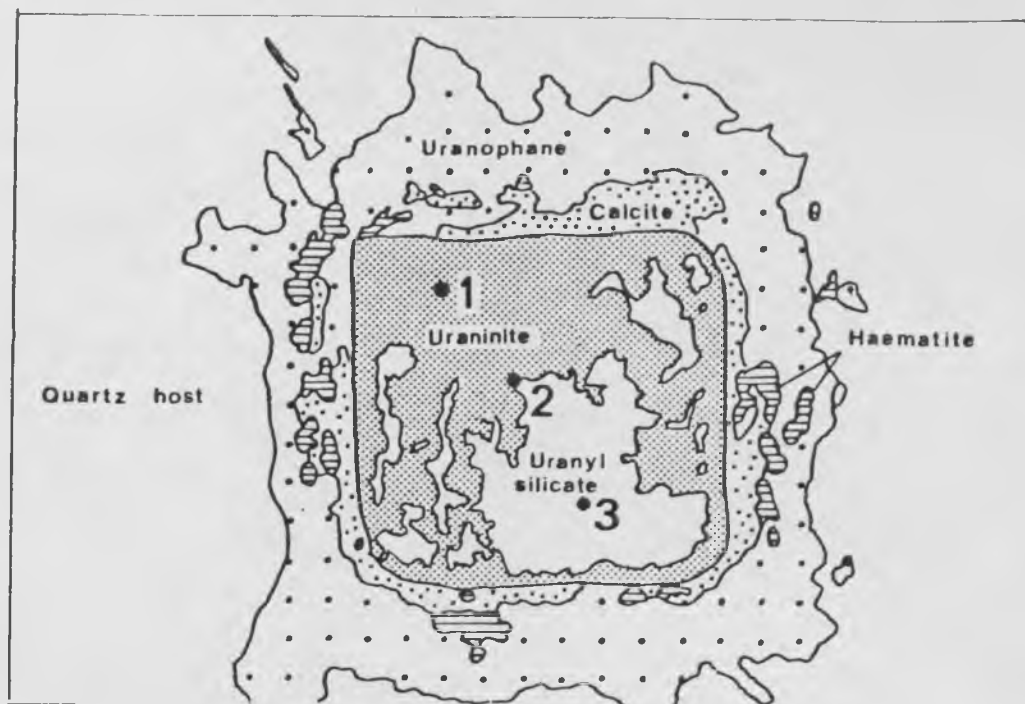


Fig. 27. Sketch illustrating the distribution of uranyl silicate in altered uraninite inclusion shown in the photomicrograph in Plate 43. The numbers 1, 2 and 3 indicate the positions where the grain was analysed, and they refer to analyses 1, 2 and 3 shown in Table 11.

VII.6. Thorogummite

Nine partial analyses of thorogummite are tabulated in Appendix 3E. These include three analyses of thorogummite from the Rössing alaskite, two from the Goanikontes alaskite, and single analyses from the Valencia alaskite and the Otjua red granite. The thorogummites contain major amounts of Th, U and Si and minor amounts of Ca, Pb, Zr, Fe, Al and Ti. When the Ca and Fe values exceed 10% the mineral should strictly be termed calciothorite and ferrothorite, respectively.

The analyses have been plotted on the U-Th-Si triangular diagram (Fig. 26) adjacent to the uranyl silicate analyses, and there appears to be a complete series between thorogummite and uranyl silicate. With the exception of one sample from the Goanikontes alaskite the

thorogummities appear to be restricted to a range of Si values between about 15 and 25%.

It has been mentioned in Chapter VI, section 4 (iv) B that some of the thorogummities display a peculiar internal variability in the distribution of the elements U, Th, Ca and Si. One of the grains which is shown in Plates 48 and 49 displays an inverse relationship between the distribution of U and Th, and this particular grain has been investigated in an attempt to establish the chemical variation which may exist within a single grain. Two partial analyses were determined, firstly from an area showing U enrichment and Th depletion, and secondly from an area displaying the reverse. The analyses are given in Table 12, and it is apparent that the two areas display very different chemical compositions, one of which is typical of uranyl silicate whilst the other is typical of thorogummite. As shown by the X-ray distribution maps in Plate 49B and C, the U rich zone appears to be enriched in Ca relative to the U poor zone. The mechanism involved in the development of such variable chemistry within a single grain is not known, but it may in part be due to the secondary alteration of the primary thorite to the secondary thorogummite.

VII.7. Uranophane

Eight analyses of uranophane are given in Appendix 3F. They include analyses from the Rössing and Goanikontes alaskites, the Otjua red granite, the lower biotite-cordierite gneiss unit of the Rössing Formation at Rössing, as well as the Etusis quartzite on Otjua 37. The uranophane is characterized by the presence of major

TABLE 12. Partial analyses of a single grain of thorogummite showing an inverse relationship between the distribution of U and Th (sample 588 C, shown in Plates 48 and 49).

	<u>Spot 1 - U poor zone</u>	<u>Spot 2 - U rich zone</u>
ThO ₂	40.8	8.2
U ₃ O ₈	19.9	64.3
CaO	0.7	5.8
TiO ₂	0.8	0.1
PbO	3.2	2.8
SiO ₂	14.8	13.8
ZrO ₂	1.0	0.9
Total	81.2	95.9

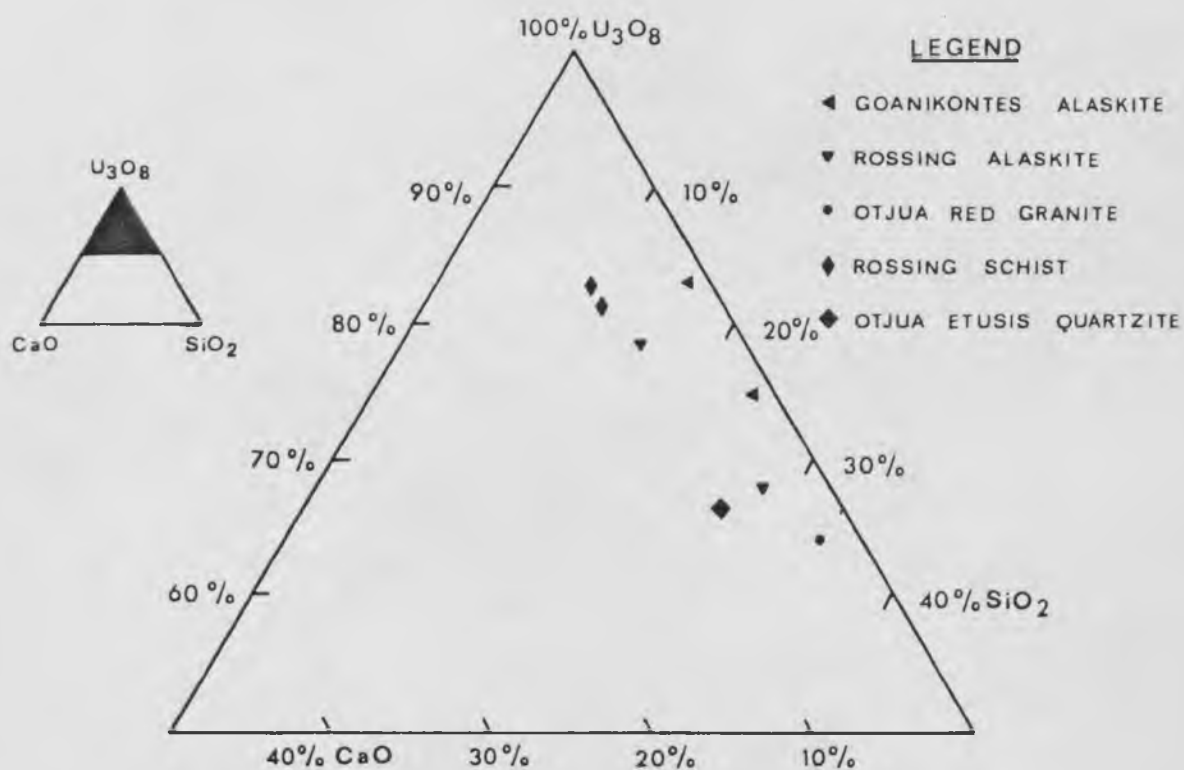


Fig. 28. U-Ca-Si triangular diagram of the uranophanes.

amounts of U and Si, and minor amounts of Ca, Pb and K. The analyses have been plotted on a U-Ca-Si triangular diagram (Fig. 28) which clearly displays their variability in U and Si, and their restricted range in Ca.

VII.8. Conclusions

The uraninites in the Rössing schists display a higher range of U/Th ratios than those in the Rössing alaskites, whilst the betafites show a lower range in U/Th and a higher range in Nb/Ta. This may be an indication that the uranium phases in the metasediments crystallized from different melts to those in the alaskites.

The transformation of uraninite to uranyl silicate is characterized by an increase in Si and Ca and a decrease in U and Pb. The calculated U, Th and Si content of the uranyl silicate and thorogummite indicates a complete series exists between the two minerals.

The variability in the concentration of U, Th and Ca within the thorogummites may in part be due to their alteration from primary thorite. The U poor zones are depleted in Ca relative to the U rich zones.

CHAPTER VIIIGEOCHRONOLOGYVIII.1. Introduction

Prior to the commencement of this study the only geochronological data pertaining to mineralized intrusives within the Damaran belt included two Rb/Sr whole rock ages, one for the Rössing alaskite (Kröner and Hawkesworth, 1977), and a second for the Valencia alaskite (Hawkesworth et al., 1981b). Recently Briquieu et al. (1980) have published U/Pb data on various minerals within the Goanikontes alaskite and they conclude that the primary uranium mineralization was contemporaneous with alaskite emplacement. A comprehensive geochronological investigation of known mineralized and radioactive granites and alaskites within the belt was undertaken in an attempt to:

- A. Determine the age and isotopic characteristics of the individual mineralized and radioactive granites and alaskites.
- B. Determine whether any relationships exist between mineralized granites and alaskites, and granites which are merely radiometrically anomalous.
- C. Determine the existence, if any, of characteristic isotopic features related to mineralized granites and alaskites.
- D. Determine the provenance of the uranium mineralization.

Seven intrusives were selected for the study including three mineralized alaskites, one mineralized red granite and three

radiometrically anomalous granites. The term 'mineralized' is defined here for a granitoid which displays a number of related features which include the presence of airborne and ground radiometric anomalies, the presence of primary and secondary uranium minerals, and assay values of uranium in excess of 20 ppm. The term 'anomalous' is used for granites which may display both airborne and radiometric anomalies, as well as secondary uranium minerals such as uranophane at the surface. The latter are distinguished from the former by their absence of primary uranium minerals and their lower uranium assay values which are normally below 20 ppm. Mineralized alaskites are typified by the Rössing, Valencia, Ida dome and Goanikontes bodies, whilst mineralized red granites are characterized by the red granite on Otjua 37. Anomalous granites are represented by the Salem granite and the leucogranite on Stinkbank 62 as well as the red granite on Namibfontein 91.

Two further whole rock Rb/Sr studies were performed on a basement gneiss from the Abbabis inlier, and a pre-F₂ Salem granite from Valencia 122. Neither are mineralized or radioactive, but the basement gneiss was investigated in an attempt to confirm the 1.9 ± 0.3 Ga age for the Abbabis gneisses (Jacob et al., 1978); and the pre-F₂ Valencia Salem granite was dated in an attempt to further constrain the age of the F₂ event in the central portion of the orogen.

Due to the decay of the radioactive isotopes ²³⁸U, ²³⁵U and ²³²Th to the radiogenic isotopes ²⁰⁶Pb, ²⁰⁷Pb and ²⁰⁸Pb, and the fact that the abundance of naturally occurring ²⁰⁴Pb does not change with time, the composition of these isotopes have been employed in a number of uranium provinces (Rosholt and Bartel, 1969; Stuckless, 1977, Gulson and Mizon, 1980) to give information about geological events such as magmatism or homogenization which may have happened before the time of

formation of the rock. Since isotopic studies on rocks from the Damaran orogen had previously been limited to the measurement of Rb- and Sr-isotopes, a study was made of the Pb-isotopic composition of a number of sulphide-bearing rocks from the belt. Sulphide ores were chosen for the investigation because they provide Pb-bearing minerals which are essentially U-free, and their present day measured Pb-isotope ratios are effectively the same as those at the time the ores were formed.

Sulphide deposits are well developed throughout the basement and supracrustal rocks of the Damaran belt (see Chapters II and III), and it was possible to sample most of the lithostratigraphic sequences within the basement and cover. Regionally, particular attention was paid to the high temperature central part of the belt between Swakopmund and Karibib, whilst stratigraphically the stratabound sulphide deposits associated with uraniferous alaskites were sampled in more detail.

VIII.2. Rb/Sr results

Since 1978 a number of authors have published over thirty whole rock results on Damaran granitoids and metasediments. The age and initial Sr-isotope ratios of these isochrons are listed in Table 13, and the distribution of the rock suites within the orogenic belt is shown in Fig. 29. During the course of this study the Rb/Sr whole rock isochron method (Faure, 1977) was used for dating the granitoids, and the ages were calculated using a decay constant of:

$$\lambda_{\text{Rb}} = 1.42 \times 10^{-11} \text{ yr}^{-1} \quad (\text{Steiger and Jäger, 1977})$$

Details of the sample preparation and laboratory techniques used are given in Appendix 1.

Due to the large scatter of data points shown by the Valencia

TABLE 13. Rb/Sr whole rock ages and initial $^{87}\text{Sr}/^{86}\text{Sr}$ ratios of the Damaran granitoids and metasediments. (Errors quoted apply to the last decimal places).

No. in Figure 29	Name	Age	Initial $^{87}\text{Sr}/^{86}\text{Sr}$	Reference
(i) Damaran Granitoids and Syenites				
1.	Rössing alaskite	458 ± 8	.759 ± 1	Kröner and Hawkesworth (1977)
2.	Oas syenite	840 ± 12	.7036 ± 13	Kröner (1981)
3.	Abbabis felsic dykes	766 ± 78	.7073 ± 12	" "
4.	Palmental diorite	750 ± 18	.7048 ± 1	" "
5.	Palmental granodiorite	651 ± 20	.7057 ± 1	" "
6.	Doros Salem syenite	573 ± 33	.7058 ± 1	" "
7.	Outlet Gorge Salem granite	554 ± 17	.7140 ± 4	" "
8.	Lofdal syenite	764 ± 60	.7030 ± 4	Hawkesworth et al. (1981b)
9.	Swakopmund Salem granite	563 ± 63	.707 ± 4	" "
10.	Sorris Sorris granite	495 ± 15	.7092 ± 15	" "
11.	Otjosondjou Salem granite	546 ± 30	.7054	" "
12.	Valencia alaskite	495 ± 12	.724 ± 2	" "
13.	Nomatsaus Donkerhuk granite	523 ± 8	.7074 ± 2	Blaxland et al. (1979)
14.	Onanis/Kamanab Donkerhuk granite	521 ± 15	.7117 ± 10	" "
15.	Goas Salem granite	515 ± 20	.7166 ± 6	" "
16.	Omaruru Salem granite	552 ± 19	.7056 ± 4	Haack et al. (1980)
17.	Omaruru leucocratic Salem granite	517 ± 11	.7120 ± 16	" "
18.	Omaruru quartzmonzonitic Salem granite	479 ± 10	.7076 ± 3	" "
19.	Omaruru quartz-rich Salem granite	474 ± 26	.714 ± 3	" "
20.	Omaruru quartzmonzonitic Salem granite	462 ± 19	.7087 ± 5	" "
21.	Palmental diorite	756 ± 36	.7070 ± 2	Kröner (1981)
22.	Palmental diorite	748 ± 38	.7060 ± 2	" "
23.	Horebis River red granite	633 ± 39	.712 ± 6	Downing (in prep.)
24.	Stinkbank Salem granite	601 ± 79	.710 ± 6	Marlow (1981)
25.	Onanis River Salem granite	554 ± 33	.712 ± 1	Downing (in prep.)
26.	Ida dome alaskite	542 ± 33	.724 ± 7	Marlow (1981)
27.	Otjua red granite	516 ± 23	.721 ± 4	" "
28.	Bloedkoppie granite	510 ± 9	.717 ± 1	Downing (in prep.)
29.	Stinkbank leucogranite	484 ± 25	.739 ± 5	Marlow (1981)
30.	Osombake granite	651 ± 20	.708	Esquevin and Menendez (1974)
31.	Dachsberg granite	508 ± 5	.722	" "
(ii) Damaran Metasediments				
32.	Karibib calc silicates	651 ± 34	.7101 ± 3	Kröner et al. (1978)
33.	Khan para-gneisses	464 ± 16	.7366 ± 3	" "
34, 35.	Kuleeb mica schists	548 ± 56	.715 ± 2	Hawkesworth et al. (1981b)

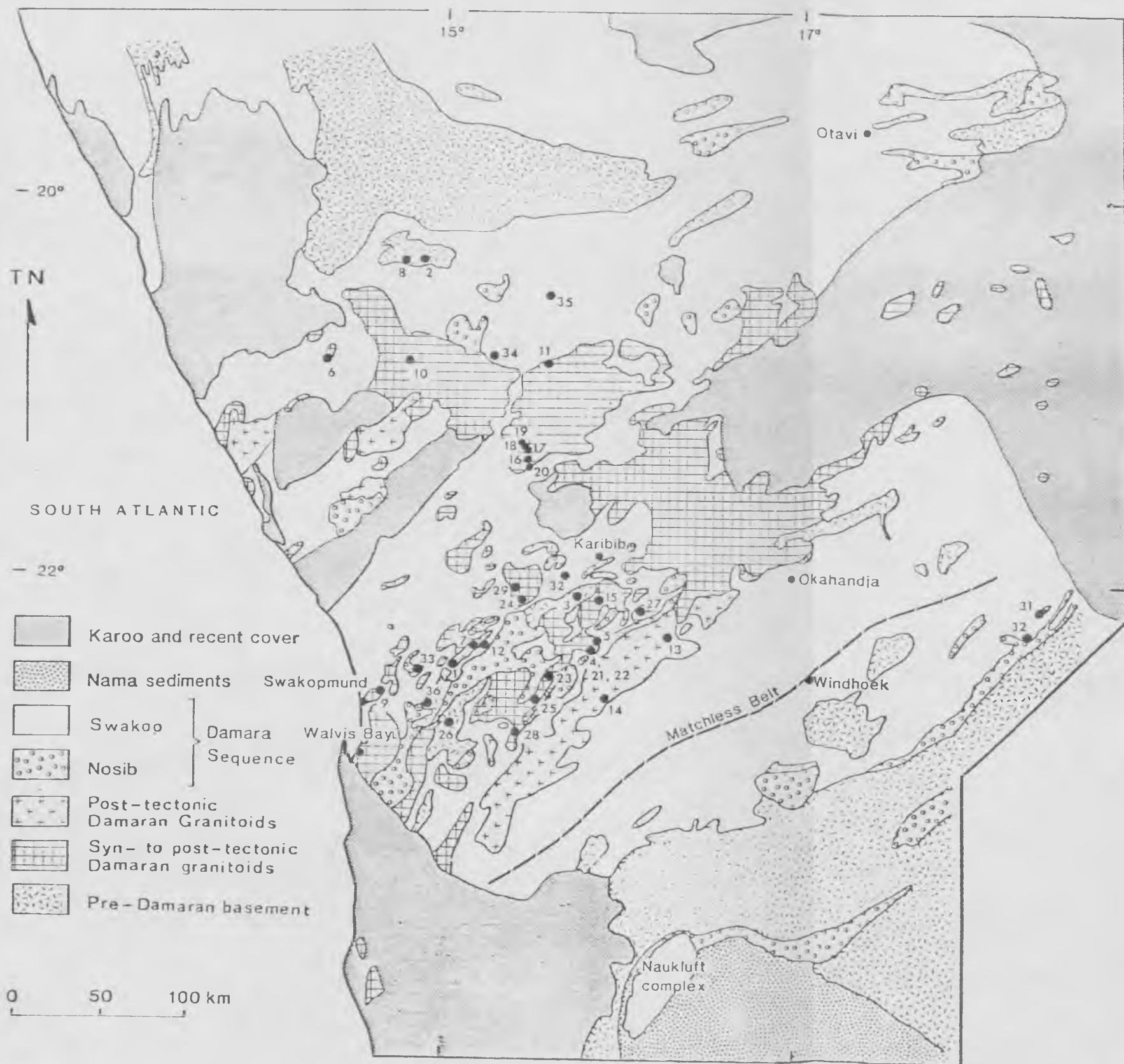


Fig. 29. Simplified geological map of the Damaran orogenic belt illustrating the sample localities of the Rb/Sr whole rock isochron suites. The numbers refer to those in Table 13, with the exception of site 36 which is the Goanikontes area.

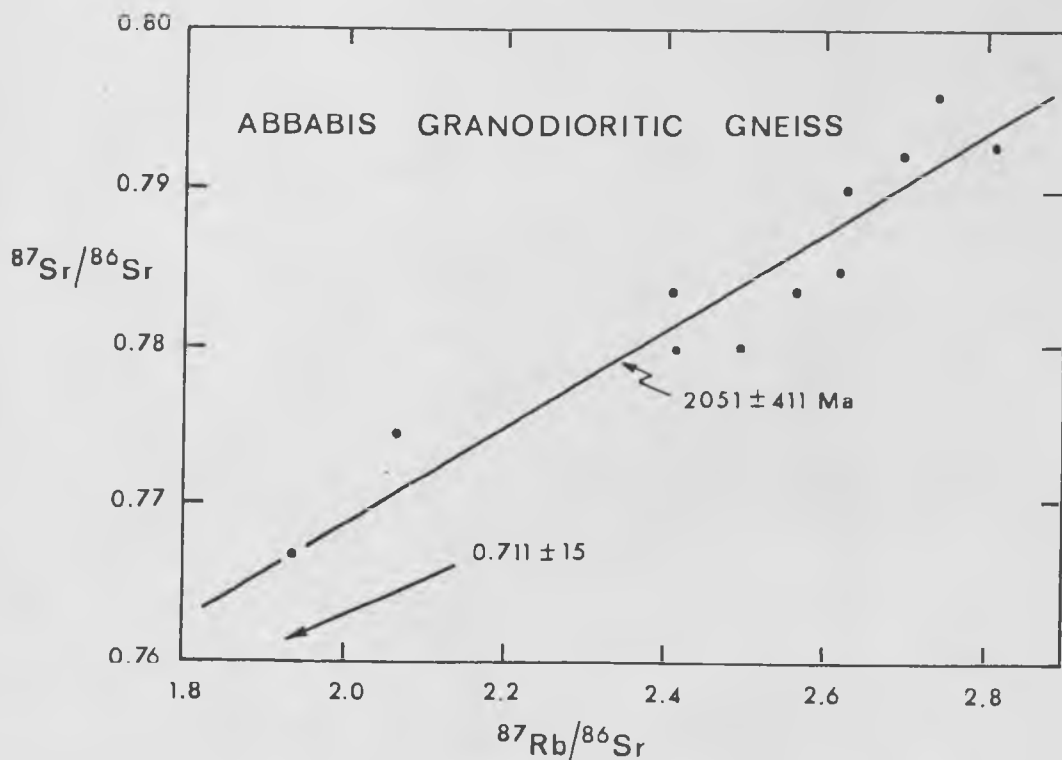


Fig. 30. Rb/Sr isochron diagram of the Abbabis granodioritic gneiss.

Salem granite suite and the Namibfontein red granite suite they are not discussed below, but the analytical results are given in Appendix 4.

(i) Abbabis gneiss

The granodioritic gneiss (Chapter II, section 3 (i)) was chosen for dating because it pre-dates the leucocratic gneiss on Ubib 76 and appears to represent one of the earlier events in the development of the Abbabis gneisses. Jacob et al. (1978) have reported a U/Pb zircon age of 1.9 ± 0.3 Ga for an orthogneiss on Abbabis 70, and the granodioritic gneiss was dated in an attempt to confirm this age for the emplacement of the Abbabis gneisses.

Eleven whole rock samples of the granodioritic gneiss were collected from an outcrop measuring about 1km across, just N.E. of the Usakos-Nordenburg road (Folder 1; I6). The eleven samples analysed (Appendix 4A) yield an age of 2051 ± 411 Ma. (M.S.W.D. = 58) with an

initial $^{87}\text{Sr}/^{86}\text{Sr}$ ratio of 0.711 ± 0.015 (Fig. 30). No great significance is placed on the age due to the large error, but it clearly corroborates the 1.9 ± 0.3 Ga age for the emplacement of the Abbabis gneisses.

(ii) Stinkbank Salem granite

The leucocratic facies of the Salem granite on Stinkbank 62 was dated because it is typical of many radioactive Salem granites within the Damaran belt. Twelve specimens of the granite were collected for whole rock Rb/Sr determination from an area about 1km square in the vicinity of the second ground radiometric anomaly described in Chapter VI, section 4 (i) (Folder 5, Q5). The samples of the granite analysed (Appendix 4B) yield an age of 601 ± 79 Ma (M.S.W.D. = 5.11) with an initial $^{87}\text{Sr}/^{86}\text{Sr}$ ratio of 0.710 ± 0.006 (Fig. 31). The granite is considered to be pre- or syn- F_2 in age, but there is a considerable scatter of points about the isochron, and therefore no major significance has been attached to the calculated age. It is important to note however, that the initial Sr-isotope ratio is within the error limits of a number of barren Salem granites reported from the belt (Haack et al., 1980; Hawkesworth et al., 1981b; Kröner, 1981; Downing, in prep.), and it is likely that it was derived from similar source regions.

(iii) Otjua red granite

Ten whole rock samples of the mineralized red granite on Otjua 37 were collected over an area of about 100m square in the vicinity of the N.W. ground radiometric anomaly described in Chapter IV, section 4 (ii), (Folder 2, F6). The data for these samples (Appendix 4Di) yield an age of 516 ± 23 Ma (M.S.W.D. = 0.87) with an

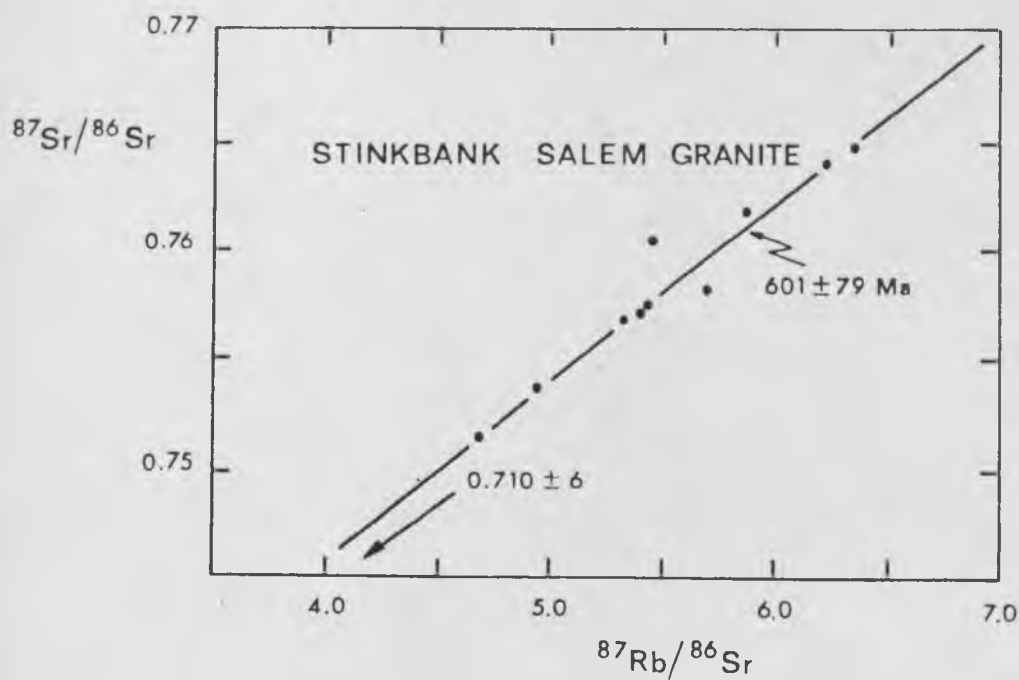


Fig. 31. Rb/Sr isochron diagram of the Stinkbank Salem granite

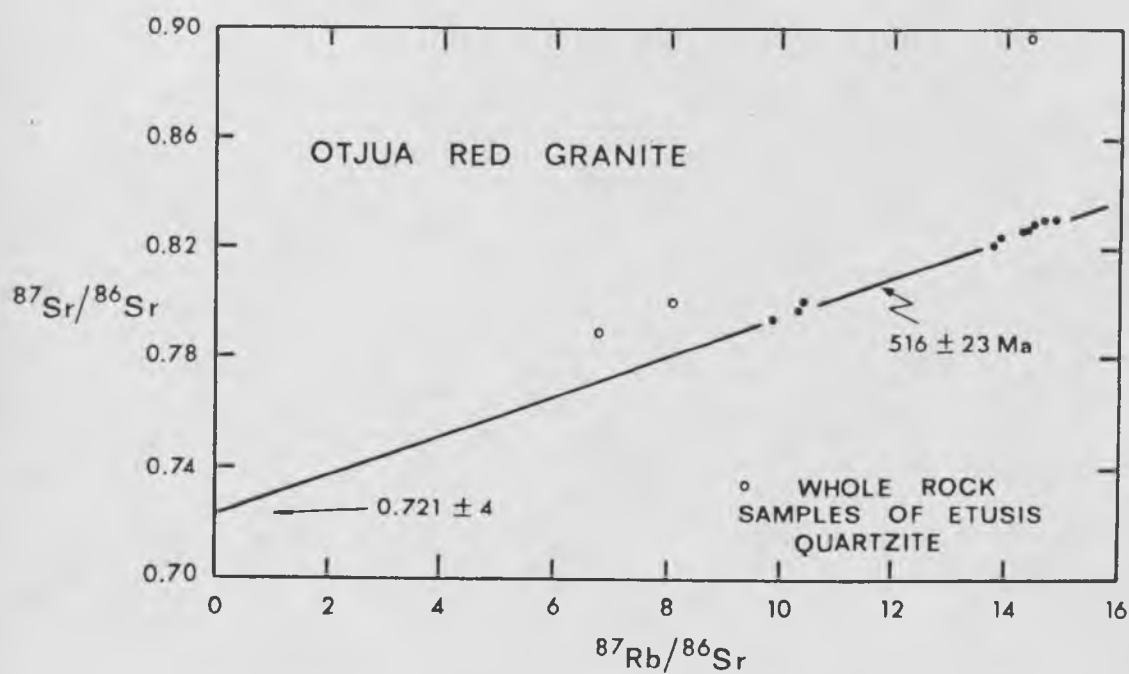


Fig. 32. Rb/Sr isochron diagram of the Otjua red granite

initial $^{87}\text{Sr}/^{86}\text{Sr}$ ratio of 0.721 ± 0.004 (Fig. 32).

In an attempt to establish whether the Etusis quartzite which hosts the red granite, represents the source of the mineralized red granite, three whole rock samples of the quartzite were collected from around the intrusion. The three quartzite data points (Appendix 4D ii) however, fall well above the Otjua red granite isochron (Fig. 32), suggesting that their initial Sr-isotope ratios at the time of intrusion were probably much higher than those of the red granite, and that the quartzite does not represent the source of the granite.

(iv) Stinkbank leucogranite

Eight whole rock samples of the radioactive leucogranite on Stinkbank 62 were collected from a railway cutting measuring about 20m in length, approximately 2.5km E. of the Stinkbank siding (Folder 5, 05). The samples analysed (Appendix 4F) yield an age of 484 ± 25 Ma (M.S.W.D. = 5.95) with an initial $^{87}\text{Sr}/^{86}\text{Sr}$ ratio of 0.739 ± 0.005 (Fig. 33). The age agrees satisfactorily with that of other leucogranites, namely the Donkerhuk (Blaxland et al., 1979), the Sorris Sorris (Hawkesworth et al., 1981) and the Bloedkoppie (Downing, in prep.), which give ages between 523 and 495 Ma. However, the initial Sr-isotope ratio is extremely high compared with those of the other leucogranites which vary between 0.707 and 0.717, indicating that the Stinkbank leucogranite may have a different source to that of the typical leucogranite of batholithic proportions.

(v) Ida dome alaskite

Mineralized alaskites are well developed in the vicinity of the Ida and Husab domes in the lower Swakop River area, and have been

described in detail by Jacob (1974b) who considers them to be of different ages, with the latest phases showing the strongest mineralization. One of the stronger radiometric anomalies, which runs along the eastern flank of the Ida dome at the stratigraphic level of the upper Khan Formation, has been drilled by a mining company, just south of the Swakop River.

Ten samples of quartered core (measuring about 30cm in length and 6cm in diameter), were selected from six boreholes sited within a few hundred metres of one another, and samples from the same borehole were collected within a distance of about 100m. All of the samples were collected from core which was radioactive to some degree, and which was unaffected by weathering and haematization. The alaskites exposed at the surface clearly post-date the strong F_2 fabric in the metasediments, and they display a weak fracture cleavage which is paralleled by trains of mafic material. Within this particular area of the Ida dome there is no sign of more than one phase of alaskite emplacement.

The data for the ten samples of alaskite (Appendix 4G) yield a reasonable Rb/Sr whole rock age of 542 ± 33 Ma (M.S.W.D. = 98.32), and an initial $^{87}\text{Sr}/^{86}\text{Sr}$ ratio of 0.724 ± 0.002 (Fig. 34). The weak fracture cleavage present within the Ida alaskite may be taken to indicate that a certain amount of deformation took place within the alaskites after intrusion, and it is likely that this deformation is related to late stage movements associated with doming.

(vi) Goanikontes alaskite

The alaskite in the Goanikontes area is intimately associated with, and locally may be seen to be formed by partial

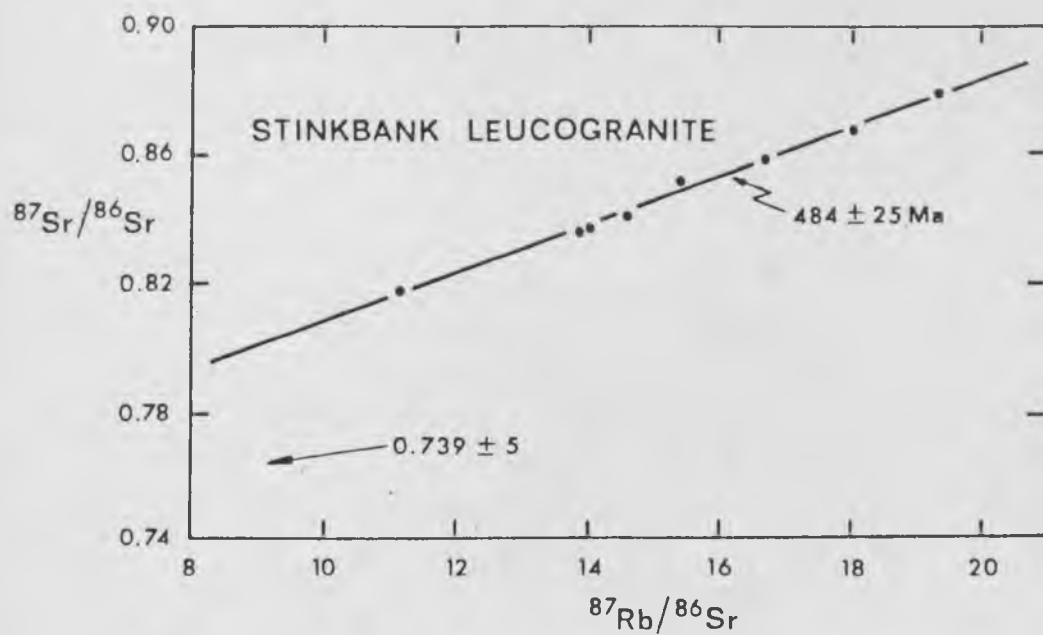


Fig. 33. Rb/Sr isochron diagram of the Stinkbank leucogranite

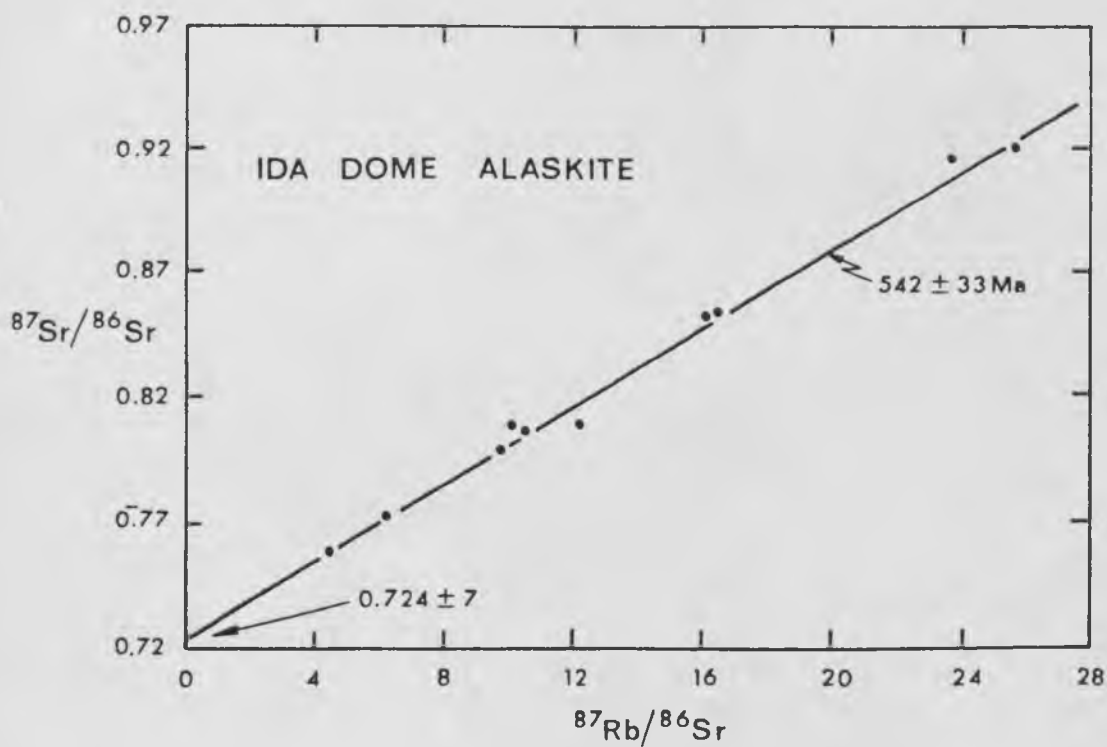


Fig. 34. Rb/Sr isochron diagram of the Ida dome alaskite

melting of the metasediments of the Khan Formation. Thirteen samples of mineralized alaskite were collected from an exploration cutting measuring about 100m in length, within the upper part of the Khan Formation, between the Swakop River and the exploration camp (Folder 3, M8). The samples of alaskite analysed (Appendix 4H i) fall about an "errorchron" corresponding to an age of 621 ± 100 Ma. (Fig. 35). However the field evidence indicates that the alaskite is essentially post-tectonic and cannot therefore have been formed before 550 Ma. (Coward, 1981b; Downing and Coward, 1981; Hawkesworth et al., 1981b). The post-tectonic nature of the Goanikontes alaskite has recently been confirmed by Briquieu et al. (1980) who obtained a U/Pb age of 508 ± 2 Ma. for the emplacement of the alaskite.

The available evidence all suggests that the calculated Rb/Sr whole rock age is too old. If an age of 510 Ma. is assumed for the intrusion, the initial Sr-isotope ratios can be calculated. Using the following equation:

$$\text{age} = \ln(\text{slope} + 1) / \lambda \quad (\text{Faure, 1977})$$

where λ is the decay constant for Rb, and the age is assumed to be 510 Ma., a slope of 0.00738 is obtained. This is the slope of a line on a Sr-isotope isochron diagram representing an age of 510 Ma. If this slope is substituted into the equation:

$$\left(\frac{87\text{Sr}}{86\text{Sr}}\right)_{t=510\text{Ma}} = \left(\frac{87\text{Sr}}{86\text{Sr}}\right)_{\text{measured}} - \left(\left(\frac{87\text{Sr}}{86\text{Sr}}\right)_{\text{measured}} \times \text{Slope}\right) \quad (\text{Faure, 1977})$$

the initial Sr-isotope ratios may be calculated for the Goanikontes alaskite (Table 14). Although the higher Rb/Sr alaskites tend to have lower Sr contents, there is no clear mixing relationship between $^{87}\text{Sr}/^{86}\text{Sr}$ and $1/\text{Sr}$ (Fig. 36).

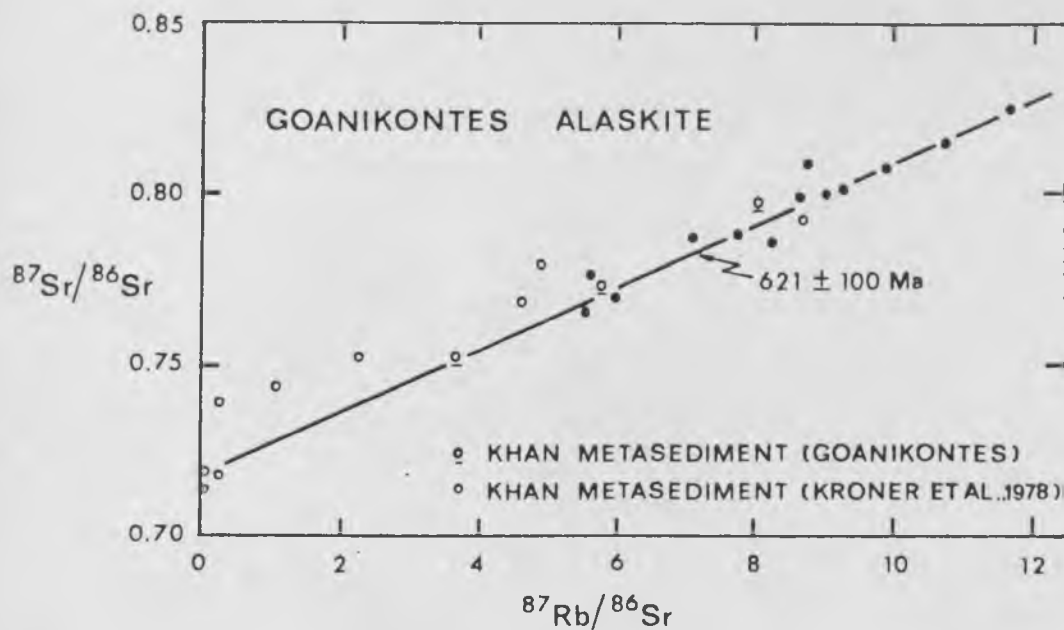


Fig. 35. Rb/Sr isochron diagram illustrating the relationship between the Goanikontes alaskite and the Khan metasediments, (one of the samples after Kröner et al., 1978 plots to the right of this figure). The alaskite is believed to have been emplaced at 508 ± 2 Ma. (U/Pb age on monazites, Briquet et al., 1980).

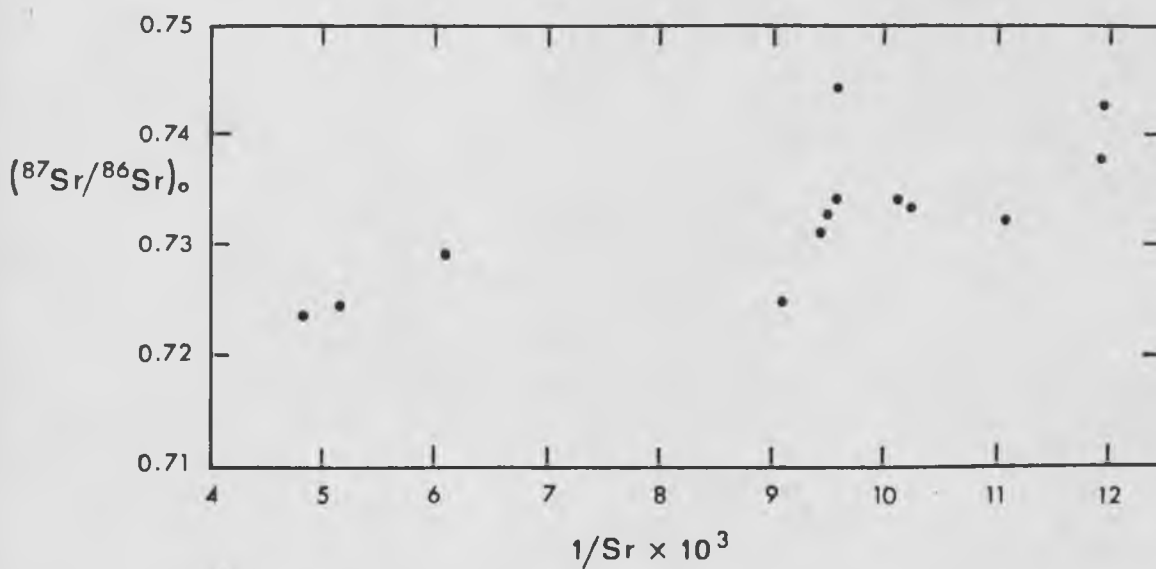


Fig. 36. $(^{87}\text{Sr}/^{86}\text{Sr})_t = 510$ Ma. vs $1/\text{Sr}$ diagram illustrating the non-linear nature of the Goanikontes alaskite samples.

TABLE 14. Initial Sr-isotope ratios calculated for the Goanikontes
alaskite at $t = 510$ Ma.

<u>Sample No.</u>	<u>G0</u>	<u>G1</u>	<u>G2</u>	<u>G3</u>	<u>G4</u>	<u>G5</u>	<u>G6</u>
$(^{87}\text{Sr}/^{86}\text{Sr})_0$	0.72926	0.73218	0.73410	0.73296	0.73420	0.73117	0.72381
$1/\text{Sr} \times 10^3$	6.08	11.10	9.58	9.50	10.14	9.45	4.23
<u>Sample No.</u>	<u>G7</u>	<u>G8</u>	<u>G9</u>	<u>G10</u>	<u>182</u>	<u>183</u>	
$(^{87}\text{Sr}/^{86}\text{Sr})_0$	0.72467	0.74276	0.73768	0.73327	0.74438	0.72408	
$1/\text{Sr} \times 10^3$	5.13	11.99	11.98	10.24	9.59	9.11	

Three whole rock samples of Khan metasediment were collected from the same locality as the mineralized alaskites on Goanikontes. The three samples analysed (Appendix 4H ii) plot on the alaskite "errorchron" (Fig. 35), strongly suggesting that the "old" age of the alaskite was inherited from its source rocks - the Khan metasediments. Kröner et al. (1978) have analysed ten samples of Khan metasediment from the vicinity of the Rössing mine, the Rössing mountain and the Ida dome; and many plot on a similar trend to the alaskites on the Rb/Sr isochron diagram (Fig. 35). Although some of the metasediments appear to have re-equilibrated isotopically around 470 Ma (Kröner et al., 1978) the age calculated for the alaskites is similar to that inferred for the early regional metamorphism in the central belt (650 - 620 Ma, Kröner, 1981), and that was probably the first high-grade event to effect these metasediments.

Examples of 'inherited isochrons' or 'pseudoisochrons' as they are sometimes referred to have been given by a number of authors. Brooks et al. (1976) propose that 'pseudoisochrons' reflect the age of the mantle from which magma originated, whilst Pankhurst and Pidgeon (1976) consider that they reflect an intermediate age between the last major

homogenization and magma genesis. Roddick and Compston (1977) concluded that the existence of 'inherited isochrons' demonstrate that: "(1) strontium isotopes were not well-mixed within the plutons during their emplacement and during the partial melting process that formed the magmas; and (2) the range of strontium isotopic equilibration is spatially limited, even during anatexis."

(vii) Valencia alaskite

Hawkesworth et al. (1981b) have recorded a 13 point isochron for the mineralized Valencia alaskite, yielding an age of 495 ± 12 Ma. (M.S.W.D. = 7.5) with an initial $^{87}\text{Sr}/^{86}\text{Sr}$ ratio of 0.722 ± 0.002 . However, field investigations have established that there are at least two major phases of alaskite emplacement on Valencia 122, one of which pre-dates the F_3 deformation, and one which post-dates it (Chapter V). Two whole rock samples of the pre- F_3 alaskite were collected from a boudinaged body within the Kuiseb schists (samples V31 and V41, folder 4, M8), whilst two samples of the post- F_3 alaskite were collected from a large undeformed body in the Karibib Formation (samples V11 and V21, folder 4, F6 - marked by an exploration pit). A further core sample of a strongly deformed, fine-grained pre- F_3 alaskite was obtained from the mining company exploring the area (sample 507).

The two post- F_3 alaskites analysed display high Rb/Sr ratios, whilst the three pre- F_3 alaskites show low ratios, and the strongly deformed, fine-grained variety has the lowest Rb/Sr ratio recorded from Valencia 122 (Appendix 4 I). The samples analysed by Hawkesworth et al. (1981) are mainly fine to medium grained, but one very coarse grained sample (DG 66) has the highest Rb/Sr ratio previously reported

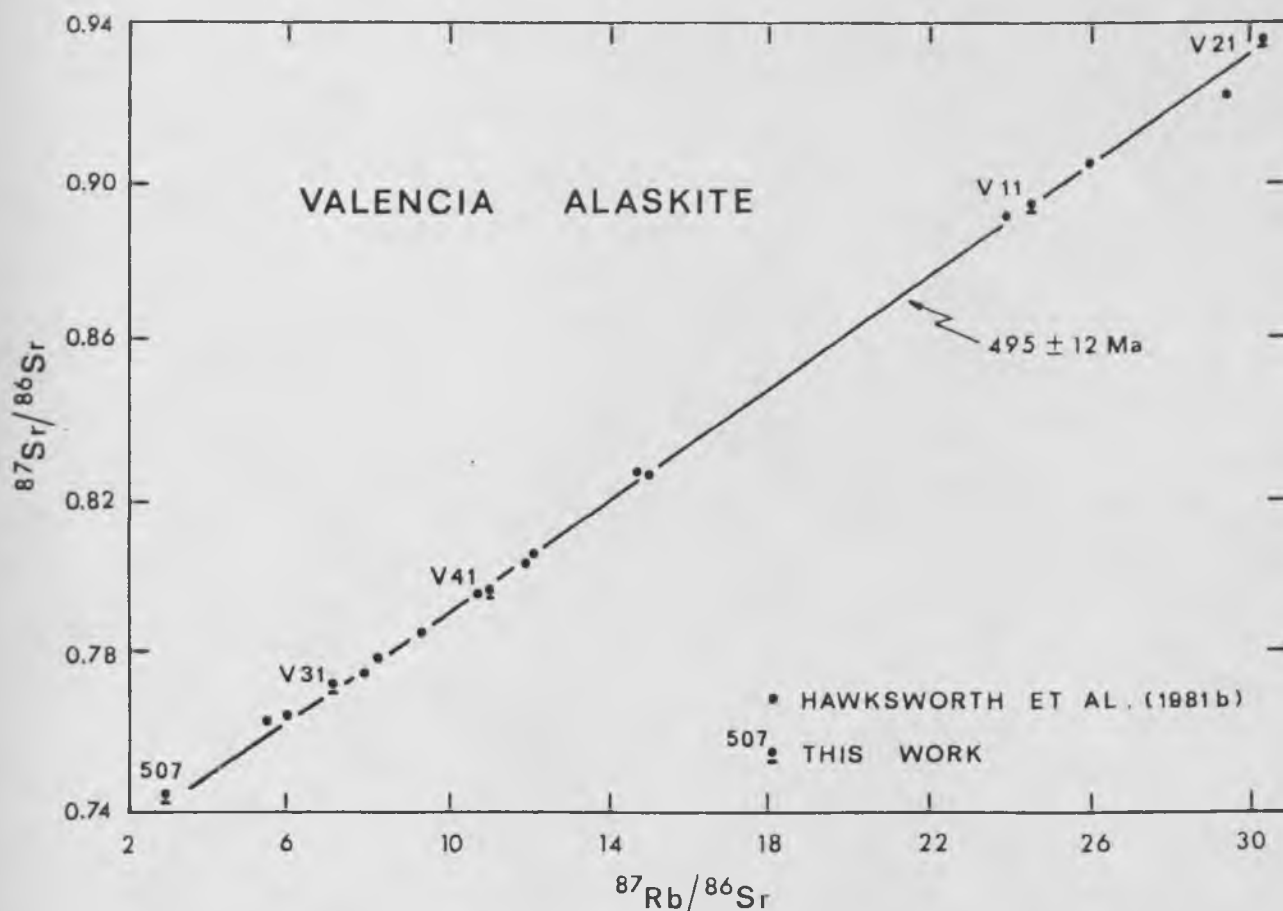


Fig. 37. Rb/Sr isochron diagram of the Valencia alaskite. The low Rb/Sr alaskites are considered to be pre- F_3 in age, whilst the high Rb/Sr alaskites are considered to be post- F_3 .

from Valencia 122. This suggests that the finer-grained alaskites are pre- F_3 in age and are characterized by low Rb/Sr ratios, whilst the coarser-grained ones are post- F_3 , and are characterized by high Rb/Sr ratios. However, all five of the new analyses lie along the $495 \pm 12 \text{ Ma}$. isochron and although the samples fall into two groups along the isochron, they cannot be distinguished in terms of their age (Fig. 37). The two groups are differentiated by their Rb/Sr ratios, and the group characterized by low Rb/Sr ratios include the pre- F_3 samples V31, V41 and 507, as well as the samples of Hawkesworth et al. (1981b) with a prefix '26/59' or '26/69'. The high Rb/Sr group includes the post- F_3 samples V11 and V21, as well as the samples of

Hawkesworth et al. (1981b) with a prefix 'DG'. It is considered that both the pre- and post-F₃ alaskites at Valencia were emplaced during the period 495 ± 12 Ma., and that the F₃ deformation, although intense, was a relatively short lived event.

(viii) Discussion

The initial Sr-isotope ratios of the granitoids listed in Table 13 are plotted against time in Fig. 38. In such a Sr-isotope diagram any rock, or system, evolves along a straight line whose slope reflects its Rb/Sr ratio, and the evolution of the bulk earth (Rb/Sr = 0.03, initial $^{87}\text{Sr}/^{86}\text{Sr} = 0.69898$ and age = 4.6 Ga) is shown for reference. In general a granitic rock plotting near the "Earth evolution line" is likely to have been only recently derived from the mantle, although perhaps by two- or multi-stage processes, and thus represents a new addition to the continental crust; those with higher $^{87}\text{Sr}/^{86}\text{Sr}$ ratios contain an increasing component of older, and hence pre-existing crustal strontium.

It is evident from Fig. 38 that there is a much greater range in initial Sr-isotope ratios in the younger granites. The alaskites exhibit the highest initial $^{87}\text{Sr}/^{86}\text{Sr}$ ratios, whilst those of the red granites are slightly more radiogenic than the other granites of comparable age. It is significant that the mineralized alaskites and granites, which are restricted to a late- to post-tectonic thermal event, are characterized by high initial Sr-isotope ratios. The mineralized red granite on Otjua 37 has a similar age and initial $^{87}\text{Sr}/^{86}\text{Sr}$ ratio to those of the mineralized Ida dome alaskite as well as the mineralized Valencia alaskite. This suggests that although the style of intrusion of the Otjua red granite is quite different from

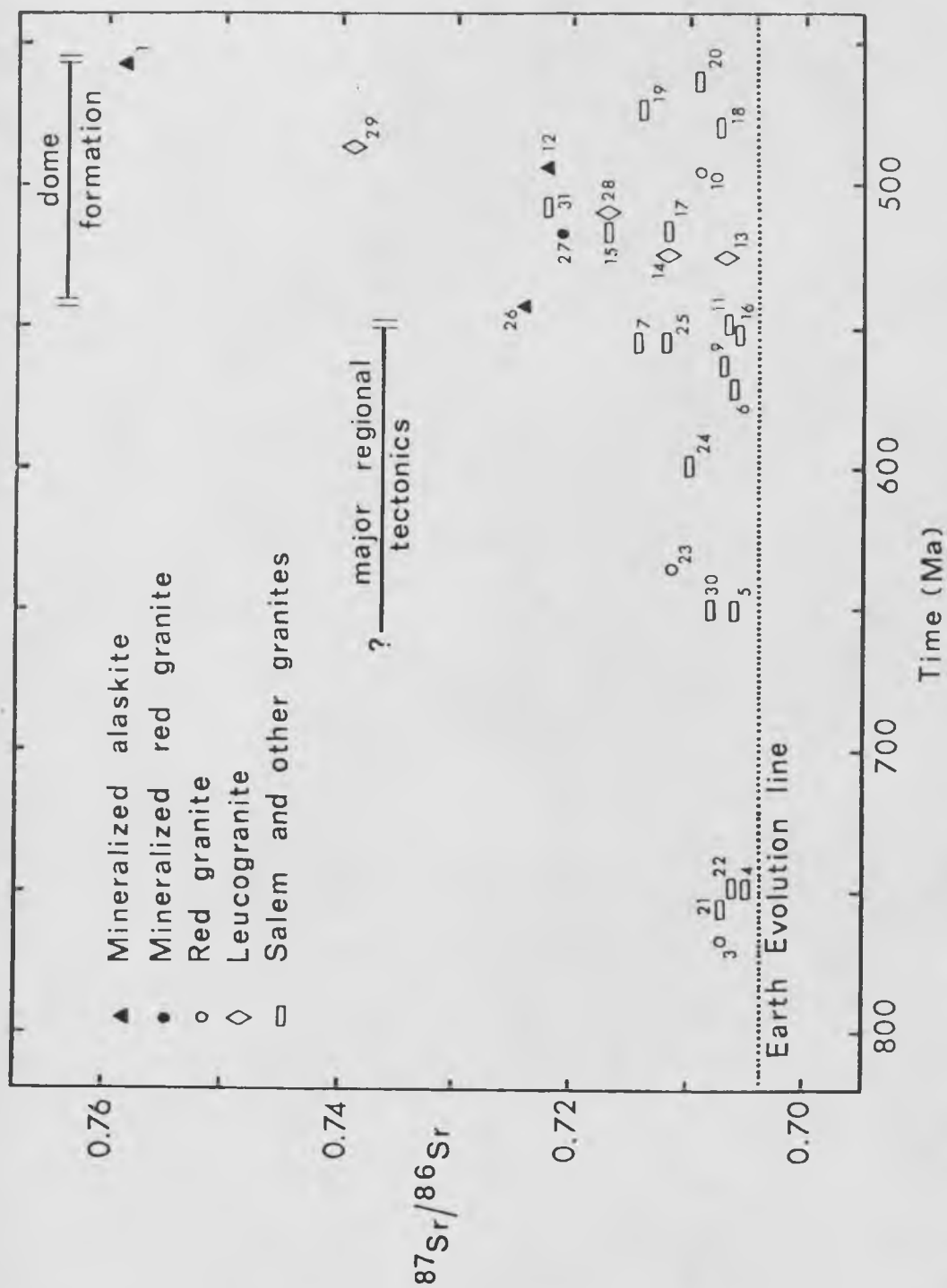


Fig. 38. Initial $^{87}\text{Sr}/^{86}\text{Sr}$ ratios in Damaran granitoids of various ages (numbers refer to Table 13 and Fig. 29). 'Major regional tectonics' is F₁ and F₂ of Coward (1981b) and Downing and Coward (1981), and F₁ of Haack et al. (1980).

that of the alaskites, their source rocks may well have come from similar units within the crust.

Hawkesworth and Marlow (1981) have compared the initial Sr-isotope ratios of the granites and alaskites formed between 550 and 450 Ma., with $^{87}\text{Sr}/^{86}\text{Sr}$ ratios calculated for Damaran metasediments and basement rocks at 500 Ma. The mineralized granites and alaskites have similar $^{87}\text{Sr}/^{86}\text{Sr}$ ratios to those of the Nosib and basement rocks, whilst the other granites have lower Sr-isotope ratios, and since they intrude the present erosion level they were clearly derived from deeper structural levels. Nd-isotope studies (Hawkesworth et al., 1981a; Hawkesworth and Marlow, 1981) indicate that the increase in $^{87}\text{Sr}/^{86}\text{Sr}$ with depth in the Damaran metasedimentary pile is accompanied by a marked decrease in $^{143}\text{Nd}/^{144}\text{Nd}$. Also, the high initial $^{87}\text{Sr}/^{86}\text{Sr}$ ratios of the alaskites are accompanied by low $^{143}\text{Nd}/^{144}\text{Nd}$ ratios providing further evidence to support the theory that both mineralized alaskites and granites are derived from Nosib and basement source rocks.

VII.3. Pb/Pb results

The Pb isotope ratios of 29 sulphide samples have been determined; six from the basement, 18 from the Damaran sedimentary cover, and five from various Damaran intrusions. The distribution of sampling sites within the Damaran belt is shown in Fig. 39, whilst the location, farm name, mineral analysed, host rock type, stratigraphic position and isotopic ratios are shown in Tables 15 and 16.

The samples in Tables 15 and 16 are listed in stratigraphic order with the exception of the five Damaran intrusives, which are listed at the top of the tables in their own structural order. The samples in

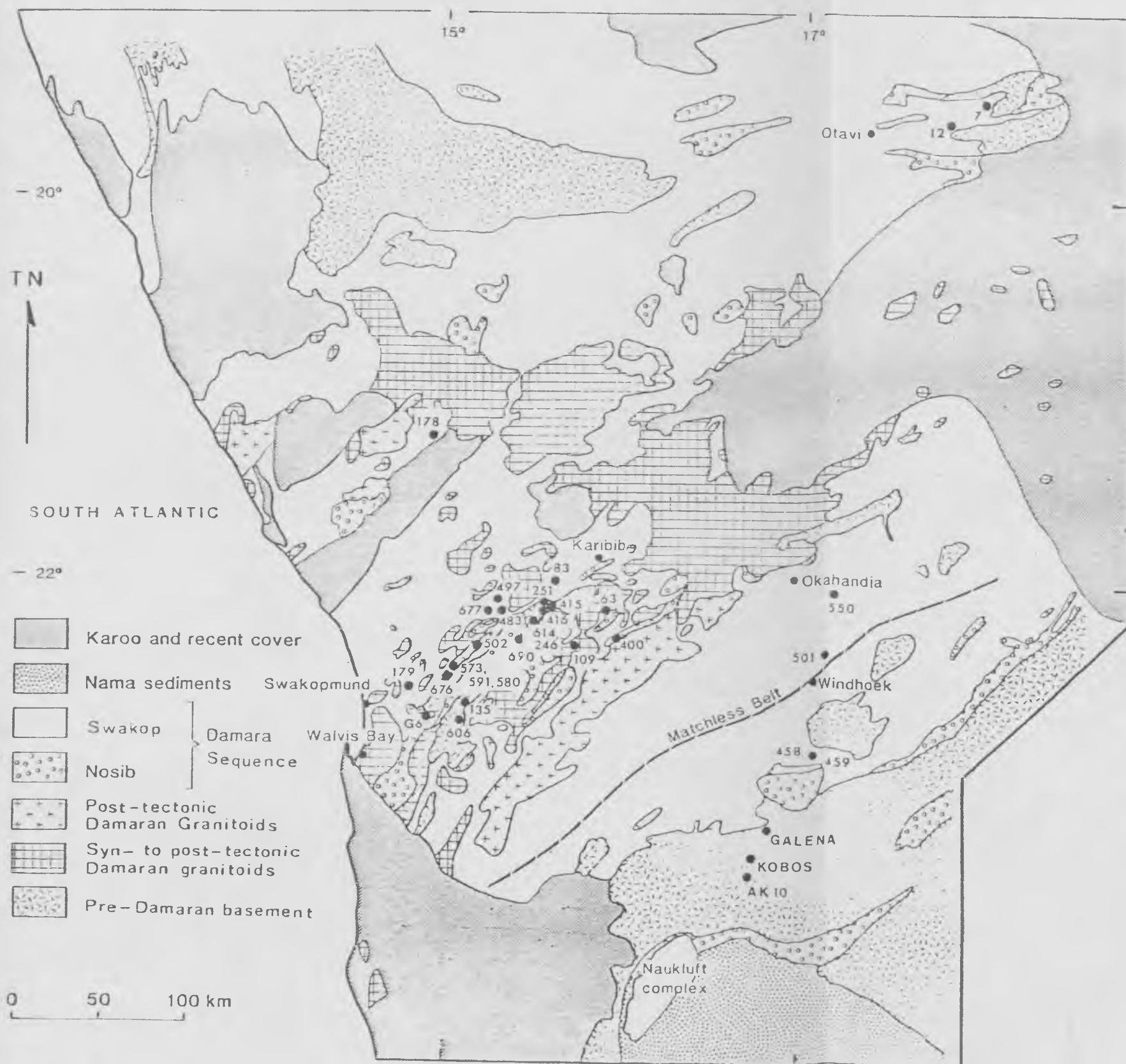


Fig. 39. Simplified geological map of the Damaran orogenic belt illustrating localities of the sulphide samples analysed. The numbers refer to those in Table 15. Samples 'GALENA', 'KOBOS' and 'AK 10' after Ruxton (1981).

TABLE 15. Location and characterization of sulphide samples analysed

Sample No.	Location	Farm	Mineral analyzed	Rock type	Stratigraphic Position
63	Henkert's mica prospect	Neu Schwaben 73	disseminated chalcopyrite	gabbro	Kuiseb Formation
573	Rössing mine	Namib Desert Park	" "	alaskite	Lower biotite-cordierite gneiss unit of Rössing Formation
677	2.5km S.W. of Ebony mine	Namibfontein 91	" "	pegmatite	Rössing Formation
G6	exploration pit	Goanikontes	" "	alaskite	Upper Khan Formation
676	Khan mine	Namib Desert Park	disseminated bornite	pegmatite	Khan Formation
109	Gamikaubmund mine	Ukuib 84	chalcopyrite in quartz vein	calc silicate	Tinkas Member
400	Audawip River	Otjimbingwe Reserve 104	disseminated chalcopyrite	" "	" "
178	Approx. 5km S. of Uis	Damaraland	galena in quartz vein	biotite schist	Kuiseb Formation
501	Otjihase mine	Otjihase 60	massive chalcopyrite	" "	" "
550	Bachran and Davidson's prospect	Ovitoto 55	" "	" "	" "
179	Namib mine	Namib Desert Park	massive galena	marble	Karibib Formation
83	Usakos mine	Mansfield 1	" "	" "	" "
7	Pick-Axe prospect	Olifantsfontein	disseminated galena	brecciated limestone	Middle Tsumeb Formation
12	Driehoek prospect	Driehoek	" "	colloform dolomite	Upper Abenab Subgroup
497	Ebony mine	Namibfontein 91	bornite in quartz vein	biotite schist	Rössing Formation
502	Kainkagchas mine	Valencia 122	massive chalcocite	calc silicate	" "
591	Rössing mine	Namib Desert Park	disseminated chalcopyrite	impure quartzite	Upper marble unit of Rössing Formation
580	" "	" "	" "	biotite schist	Lower biotite-cordierite gneiss unit of Rössing Formation
135	Muller's mine	" "	disseminated galena	fluorspar-bearing gneiss	Rössing Formation
606	Ida mine	" "	disseminated chalcopyrite	calc silicate	Upper Khan Formation
459	Oamites mine	Oamites 53	massive chalcopyrite	quartzite	Khan Formation
458	" "	" "	massive galena	" "	" "
690	Sphinx mine	Bergrus 94	chalcopyrite in quartz vein	" "	Etusis Formation
483	Breytenbach's prospect	Namibfontein 91	disseminated chalcopyrite	pyroxenite	Abbabis Formation
614	Abbisich River mine	Tswawis Suid 95	chalcopyrite in quartz vein	biotite schist	" "
246	" "	" "	" "	" "	" "
251	Renderson mine	Naob 69	disseminated chalcopyrite	calc silicate	" "
416	Near Ubib mine	" "	" "	amygdaloidal meta-basalt	" "
415	Ubib mine	" "	chalcopyrite in quartz vein	sillimanite-mica schist	" "

TABLE 16. Lead isotope ratios of sulphide samples analysed.
 Samples associated with uranium mineralization are
 marked by an asterisk.

Sample No.	$^{206}\text{Pb}/^{204}\text{Pb}$	$^{207}\text{Pb}/^{204}\text{Pb}$	$^{208}\text{Pb}/^{204}\text{Pb}$
63	17.541 ± 0.010	15.609 ± 0.011	38.468 ± 0.003
573*	27.727 ± 0.024	16.337 ± 0.030	40.123 ± 0.083
677	21.048 ± 0.006	15.881 ± 0.003	40.203 ± 0.010
G6*	64.740 ± 1.076	18.279 ± 0.213	38.861 ± 0.433
676	20.286 ± 0.056	15.961 ± 0.052	39.766 ± 0.130
109	21.503 ± 0.060	15.831 ± 0.048	41.990 ± 0.124
400	18.522 ± 0.020	15.691 ± 0.038	38.219 ± 0.097
178	18.157 ± 0.034	15.604 ± 0.032	37.779 ± 0.074
501	19.731 ± 0.017	15.804 ± 0.029	38.527 ± 0.093
550	24.732 ± 0.103	15.798 ± 0.084	37.395 ± 0.191
179	18.793 ± 0.021	15.680 ± 0.020	38.980 ± 0.054
83	18.186 ± 0.042	15.671 ± 0.052	38.025 ± 0.151
7	17.989 ± 0.024	15.652 ± 0.025	38.624 ± 0.080
12	17.995 ± 0.007	15.680 ± 0.008	38.280 ± 0.021
497	17.787 ± 0.009	15.705 ± 0.012	37.612 ± 0.038
502	23.599 ± 0.017	16.034 ± 0.017	40.126 ± 0.052
591	19.999 ± 0.005	15.824 ± 0.004	41.919 ± 0.011
580*	35.711 ± 0.032	16.776 ± 0.021	64.312 ± 0.087
135	18.131 ± 0.028	15.718 ± 0.027	38.841 ± 0.070
606	20.711 ± 0.006	15.869 ± 0.006	41.998 ± 0.017
459	18.439 ± 0.010	15.679 ± 0.009	37.974 ± 0.024
458	17.971 ± 0.015	15.628 ± 0.015	37.840 ± 0.035
690	20.352 ± 0.007	15.861 ± 0.007	38.017 ± 0.020
483*	206.510 ± 0.326	26.512 ± 0.044	38.455 ± 0.082
614	16.980 ± 0.016	15.537 ± 0.011	36.845 ± 0.028
246	29.772 ± 0.278	16.279 ± 0.162	39.036 ± 0.387
251	19.893 ± 0.015	15.840 ± 0.014	39.685 ± 0.036
416	18.055 ± 0.003	15.620 ± 0.003	39.857 ± 0.008
415	18.988 ± 0.014	15.753 ± 0.013	38.009 ± 0.036

Table 16 which show extremely radiogenic isotopic ratios, and which are associated with uranium mineralization, are marked with an asterisk. The samples collected from the Rössing uranium mine were taken from the local lithostratigraphic units of the Rössing Formation (Table 8), defined by Berning et al. (1976). The two samples from the Grootfontein-Otavi area, numbered 12 and 7, were collected from the upper part of the Abenab Subgroup and the middle part of the Tsumeb Subgroup respectively. Due to the greatly thickened sequences of carbonate shelf facies rocks in this area (S.A.C.S., 1980), the samples can not be correlated directly with those from the central belt of the Damaran orogen. However, if the mixtites of the Chuos Formation are considered to be synchronous in both areas, then the stratigraphic position of sample 12 approximates to that of the Rössing Formation, whilst that of sample 7 approximates to that of the Karibib Formation.

The minerals analysed include galena, chalcopyrite, bornite and chalcocite (Table 15), which occur as massive segregations in stratiform sulphide deposits, as disseminations in metasedimentary or metavolcanic stratiform sequences, or as disseminations in quartz veins in Damaran intrusives. Of the six samples collected from the basement, three occur as chalcopyrite in quartz veins which may not necessarily be of pre-Damaran age. However, the isotopic ratios of one of these (sample 614) are too low for it to be Damaran in age, whilst another of the three, (sample 415) occurs spacially and structurally close to a sequence of sulphide-bearing meta-basalts of pre-Damaran age, which probably represent the source of the sulphide mineralization in the quartz veins sampled. The last of the three (sample 246), displays extremely radiogenic isotopic ratios, but was sampled from the same copper deposit

as sample 614 and is therefore also likely to be pre-Damaran.

The 18 sulphide samples collected from the Damaran metasedimentary cover include four samples which occur as disseminated sulphide mineralizations in quartz veins, and a further 14 samples from stratiform type mineralizations. Sample 497 from the Ebony Mine on Namibfontein 91 represents one of the first four, and consists of disseminated bornite in a quartz vein cutting a sequence of biotite schists of the Rössing Formation. The schists, however, display a zone of disseminated copper carbonate mineralization which appears to be stratiform in nature, forming a mineralized zone some 2m thick and several metres along strike, and it is likely that the sulphide in the quartz vein was derived from this horizon. Sample 109 from the Gamikaubmund Mine on Ukuib 84, which consists of disseminated chalcopyrite in quartz veins cutting a sequence of calc silicates and schists of the Tinkas Member, may also be considered as a stratiform type mineralization, because the sulphide in the quartz veins is derived from disseminated chalcopyrite and bornite stratabound in the calc silicates. The origin of the sulphide mineralization in the quartz veins sampled at the Sphinx Mine (sample 690) and S. of Uis (sample 178) is uncertain and cannot be assumed to be stratiform in nature.

(i) U-Pb systematics

The Pb-isotope ratios of the sulphides analysed have been plotted on a $^{207}\text{Pb}/^{204}\text{Pb}$ vs $^{206}\text{Pb}/^{204}\text{Pb}$ diagram, against Stacey and Kramers (1975) average growth curve of the earth (Fig. 40). The Stacey and Kramers model for the evolution of the source region of conformable Pb-ore is a two-stage model, and their growth curve is drawn through analyses of conformable Pb-ores of different ages which

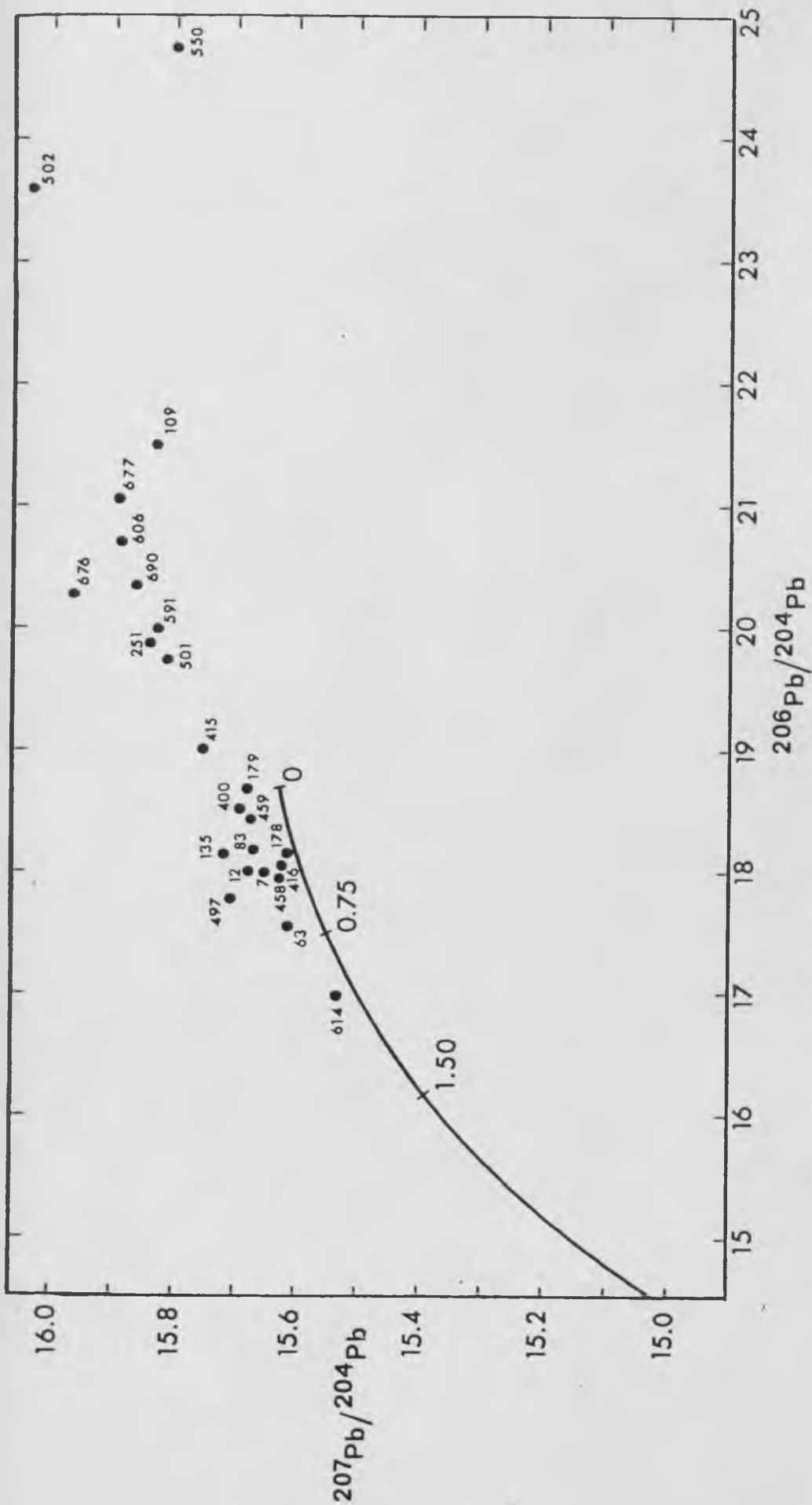


Fig. 40. $^{207}\text{Pb}/^{204}\text{Pb}$ vs $^{206}\text{Pb}/^{204}\text{Pb}$ variations in sulphides from the Damaran belt compared with the Pb-ore growth curve of Stacey and Kramers (1975). The numbers on the curve are two-stage model ages (in Ga) after Stacey and Kramers (1975). (Samples 483, G6, 580, 246 and 573 are all extremely radiogenic, plotting to the right of the figure).

are assumed to be of crustal derivation. All the samples plot above the growth curve and to the right of the predicted positions for ores of their age, indicating that their Pb-isotope ratios are relatively enriched in ^{207}Pb and ^{206}Pb .

There is no chronological order to the position of the stratiform samples above the growth curve, which one might expect from model leads, with the older samples falling on the left and the younger ones on the right. Only one exception to this can be seen in sample 614 from the basement, which falls well to the left of all the other samples analysed. The lack of chronological order above the growth curve suggests that the samples have been effected by a variable enrichment in ^{207}Pb and ^{206}Pb .

A three-stage growth model is envisaged for the evolution of the anomalous leads, in which they followed the evolution of average lead through its first and second stages as proposed by Stacey and Kramers (1975), and at around 2.0 Ga they entered a third stage of growth with increased $^{238}\text{U}/^{204}\text{Pb}$ values. If a tangent is drawn from the most primitive samples analysed (614 and 497), to the growth curve (Fig. 40), it intersects the curve at a point with $^{207}\text{Pb}/^{204}\text{Pb}$ and $^{206}\text{Pb}/^{204}\text{Pb}$ values of 15.34 and 15.8 respectively. This point on the curve represents a time of approximately 1.7 Ga (Table 9, Stacey and Kramers, 1975), and indicates a minimum age for the start of the third stage of growth of the anomalous leads. This is very significant in that it implies the existence of high U/Pb ratios within the basement at 1.7 Ga.

The Pb isotopic ratios of three samples analysed by Ruxton (1981), from the basement south of Windhoek (Fig. 39), as well as four of the basement samples from the central belt of the orogen, have been plotted

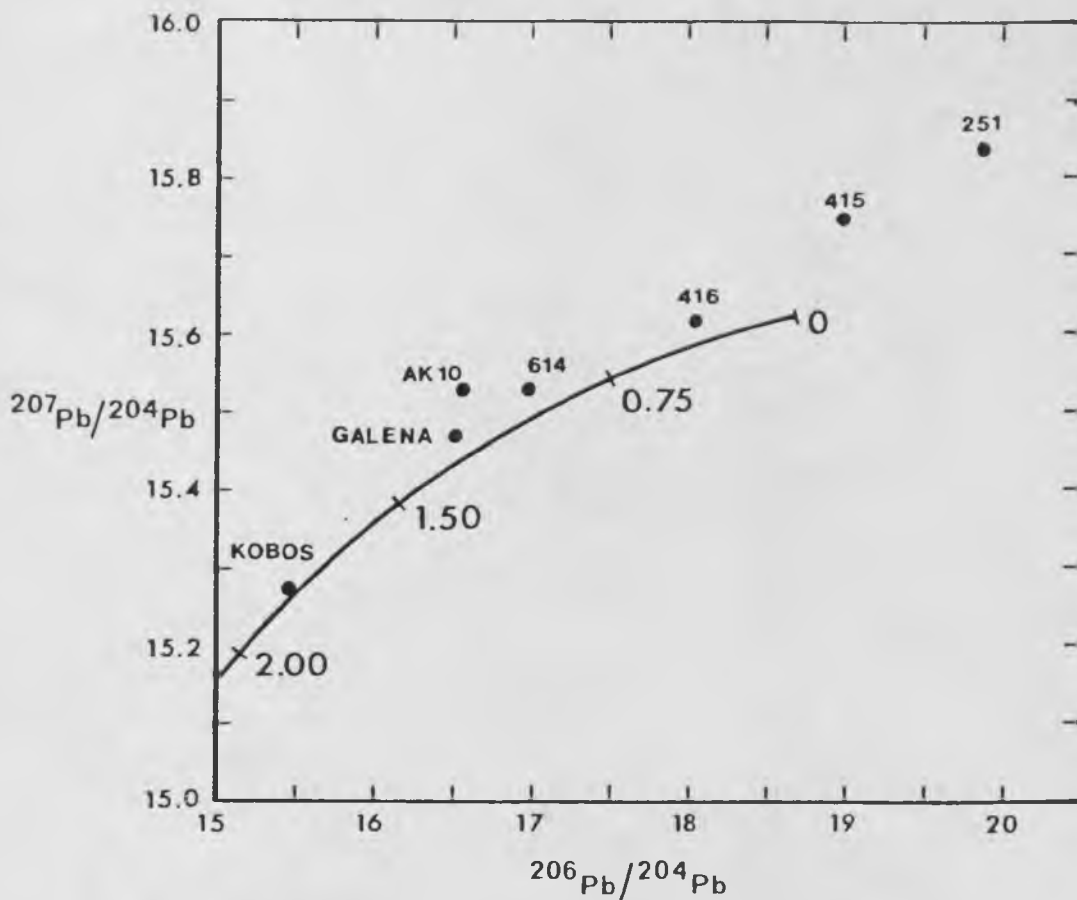


Fig. 41. $^{207}\text{Pb}/^{204}\text{Pb}$ vs $^{206}\text{Pb}/^{204}\text{Pb}$ variations in sulphides from the basement compared with the Pb-ore growth curve of Stacey and Kramers (1975). The numbers on the curve are two-stage model ages (in Ga.) after Stacey and Kramers (1975). Samples 'KOBOS', 'GALENA' and 'AK 10' after Ruxton (1981).

on a $^{207}\text{Pb}/^{204}\text{Pb}$ vs $^{206}\text{Pb}/^{204}\text{Pb}$ diagram relative to Stacey and Kramers average growth curve (Fig. 41). The sample KOBOS, which is non-radiogenic, falls on the growth curve and gives a model age of 1.90 ± 0.03 Ga (Ruxton, 1981). The remaining six radiogenic samples form a linear array which probably reflects the extent to which the isotopic ratios of the basement samples were effected during the Damaran metamorphism.

When the five samples from the Rössing Formation are considered (Fig. 42), they are seen to fall on an isochron (M.S.W.D. = 1.84) having a slope of 0.059681, which defines an age of 592 ± 60 Ma. (Stacey and Stern, 1972). It must be emphasized that the central portion of the orogen sampled for these five sulphides from the Rössing

sequence, represents a much smaller area than that sampled for the basement sulphides described above. Sample 606 from the Ida copper mine at the very top of the Khan Formation, also falls on this line, as do samples of two Damaran intrusives which invade rocks of the Rössing Formation. The first of these (sample 677) is from a pegmatite on Namibfontein 91, whilst the second (sample 573) is from an alaskite at the Rössing uranium mine.

The age of 592 Ma. defined by the isochron is interpreted as an M_1 homogenization event, indicating the time when uranium which existed within the basement and cover rocks, was mobilized and introduced into pre-existing sulphide mineralizations, resulting in the development of more radiogenic Pb isotope systems. The event corresponds to an early metamorphic event with associated granitic activity between 650 and 600 Ma. (Kröner et al., 1978; Hawkesworth et al., 1981b; Kröner, 1981; Downing and Coward, 1981). Only the data from the upper Khan and Rössing Formations fall on this isochron, and this may be due to the local availability of uranium in the host rocks. The presence of the alaskite from Rössing and the pegmatite from Namibfontein 91 falling on the line, suggests that the source material for both intrusives were rocks of the Rössing Formation. The initial Pb-isotope ratios of the samples at 592 Ma are assumed to be close to those of sample 497; firstly, because this sample provides the least radiogenic data on the isochron, and secondly, because it falls on the 800 Ma. "model isochron", which would represent a lower age for the deposition of the Rössing Formation. This is close to an upper age of 840 ± 12 Ma suggested for the deposition of the Rössing Formation, and an age of 800 ± 20 Ma. for the deposition of the overlying Chuos Formation (Kröner, 1981).

Five of the samples analysed were taken from slightly radioactive

material in the form of uraninite-bearing pyroxenite associated with uraniferous alaskite from Namibfontein 91 (sample 483); uraniferous alaskite (sample 573) and gneiss (sample 580) from the Rössing uranium mine; uraniferous alaskite from Goanikontes (sample G6); and biotite schist from Tsawisis Suid 95 (sample 246). The samples are shown on a $^{207}\text{Pb}/^{204}\text{Pb}$ vs $^{206}\text{Pb}/^{204}\text{Pb}$ diagram relative to Stacey and Kramers average growth curve (Fig. 43), and the data fall close to a 510 Ma. reference isochron consistent with remobilization at the time many uraniferous alaskites were emplaced.

Samples 614 and 246 were collected from the same abandoned copper deposit in the Abbisch River on Tsawisis Suid 95. The two samples however, show very different Pb isotopic compositions, the first being relatively primitive, whilst the second is extremely radiogenic. If the Abbisch River copper deposit is assumed to be stratiform in nature, the Pb-isotopic compositions of any number of sulphide samples from the deposit would originally have been identical, and it would be valid to draw an isochron through them on the $^{207}\text{Pb}/^{204}\text{Pb}$ vs $^{206}\text{Pb}/^{204}\text{Pb}$ diagram (Fig. 43). On such an isochron sample 614 would represent the initial isotopic composition of the system, and sample 246 would represent the composition of Pb in a system which was introduced to uranium at a certain time dependent upon the slope of the isochron. The slope of a line (M.S.W.D. = 0.0) drawn through samples 614 and 246 is 0.058005, which gives an age of $530 \pm \begin{matrix} 57 \\ - 59 \end{matrix}$ Ma. (Stacey and Stern, 1972). As this age is within error of a 510 Ma. emplacement age for the uraniferous alaskites, it is possible that the isochron may be real, representing the time of intrusion of a uranium-bearing liquid or magma into the area of the Abbisch River copper mine, even though the absence of any uraniferous material in this region argues against such a theory.

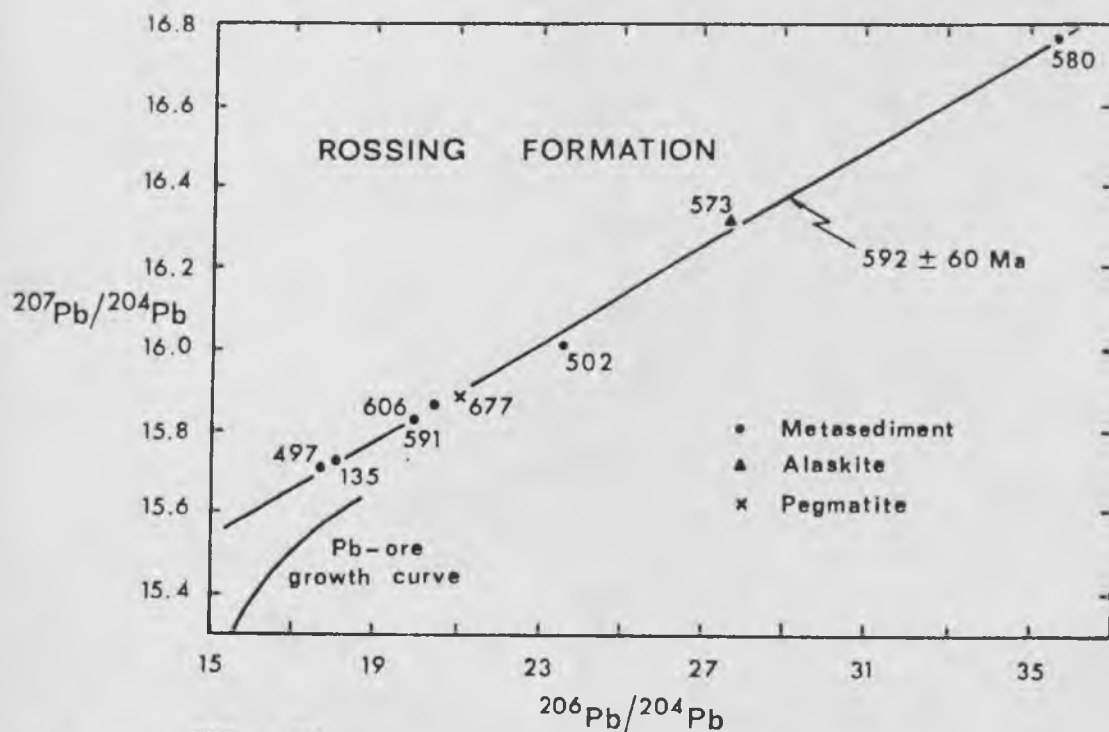


Fig. 42. $^{207}\text{Pb}/^{204}\text{Pb}$ vs $^{206}\text{Pb}/^{204}\text{Pb}$ diagram for sulphides from the Rössing Formation. The age of 592 ± 60 Ma is interpreted as an M_1 homogenization event.

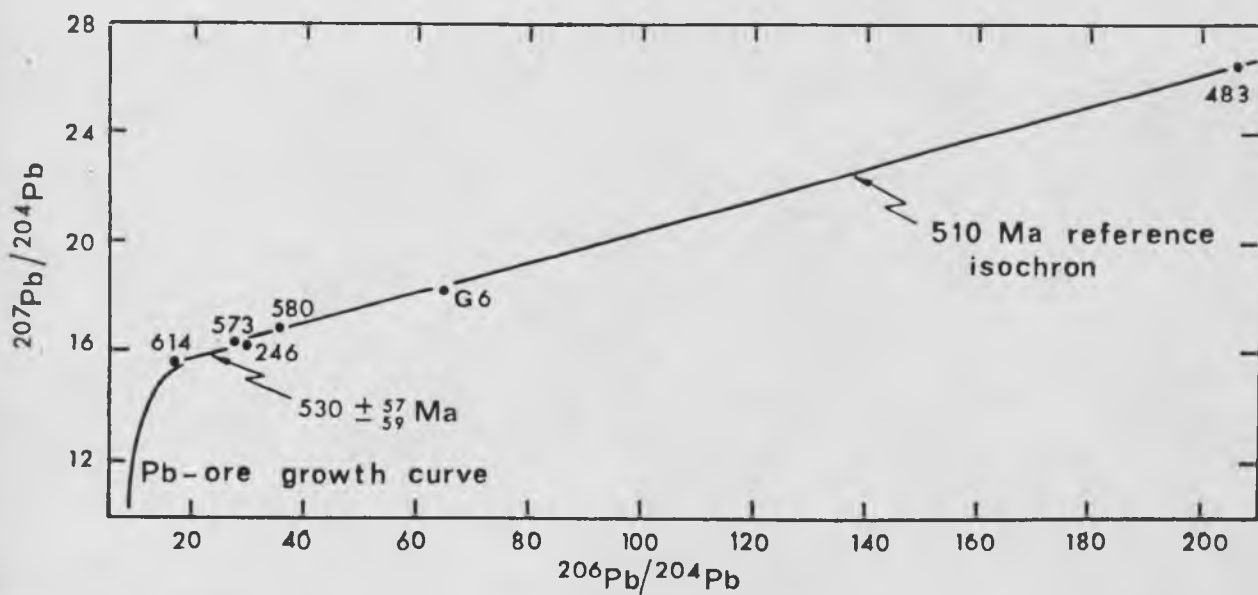


Fig. 43. $^{207}\text{Pb}/^{204}\text{Pb}$ vs $^{206}\text{Pb}/^{204}\text{Pb}$ diagram for the more radiogenic sulphides. Samples 573, 580, G6 and 483 are plotted relative to a 510 Ma reference isochron. The slope of a line drawn through samples 614 and 246 gives an age of 530 ± 57 Ma.

(ii) Th-Pb systematics

The data has also been plotted on a $^{208}\text{Pb}/^{204}\text{Pb}$ vs $^{206}\text{Pb}/^{204}\text{Pb}$ diagram, against Stacey and Kramers (1975) average growth curve for the earth (Fig. 44). The majority of analyses fall close to the average growth curve, and can be expected to have normal Th/U ratios. However, the five extremely radiogenic samples depart from the average growth curve, and display an enrichment in ^{206}Pb relative to ^{208}Pb , and in the case of sample 580 an enrichment in both ^{206}Pb and ^{208}Pb . The direction of departure from the average growth curve (Fig. 44), is a measure of the Th/U ratio, whilst its distance from its "model age" position on the average growth curve is a measure of its U/Pb and Th/Pb ratios. The four extremely radiogenic samples 573, 246, G6 and 483 all have approximately the same Th/Pb ratios, but their U/Pb ratios are extremely variable. Sample 580 has a normal Th/U ratio, but its enrichment in both ^{232}Th and ^{238}U , has led to increased Th/Pb and U/Pb ratios, respectively.

Sample 580 is a chalcopyrite from the lower biotite-cordierite gneiss unit of the Rössing Formation at the Rössing mine, whilst sample 591 is from the same deposit from the upper marble unit higher in the Rössing sequence (Table 8). Both samples show normal Th/U ratios, but the displacement of sample 580 to a more radiogenic position on Fig. 44 indicates that the leads in the metasediments at Rössing have been effected to a variable degree by the introduction of radiogenic ^{206}Pb and ^{208}Pb .

Samples 690, 502 and 550 from the Etusis, Rössing and Kuiseb Formations respectively, are enriched in ^{206}Pb relative to ^{208}Pb , indicating the depositional environment during the formation of certain sequences of these formations, was characterized by high U/Th ratios.

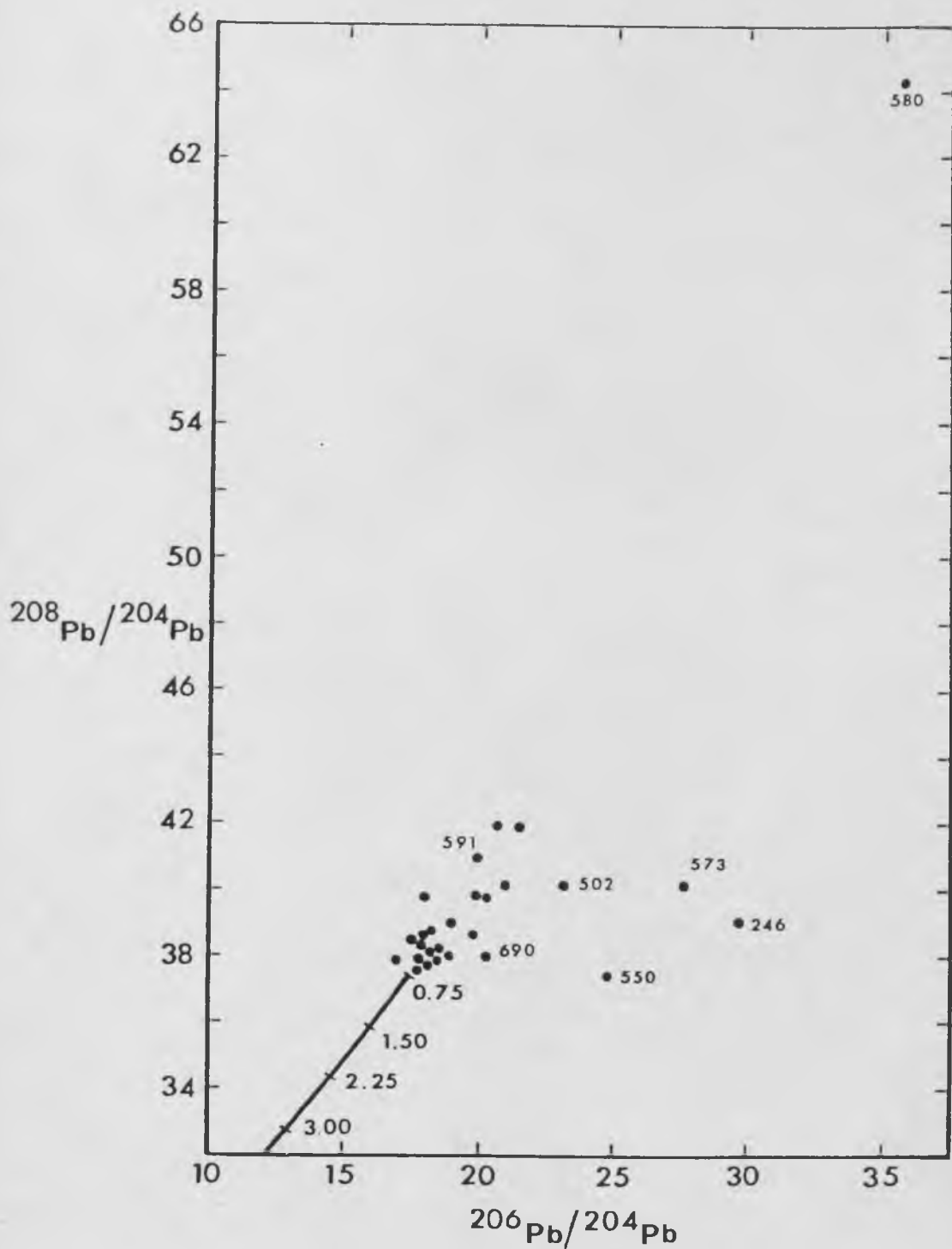


Fig. 44. $^{208}\text{Pb}/^{204}\text{Pb}$ vs $^{206}\text{Pb}/^{204}\text{Pb}$ variations in sulphides from the Damaran belt compared with the Pb-ore growth curve of Stacey and Kramers (1975). The numbers on the curve are two-stage model ages (in Ga) after Stacey and Kramers (1975). (Samples 483 and G6 are both extremely radiogenic, plotting to the right of the figure).

VIII.4. Conclusions

An eleven point whole rock Rb/Sr age of 2.0 ± 0.4 Ga for the granodioritic gneiss from the Abbabis inlier corroborates the U/Pb zircon age of 1.9 ± 0.3 Ga (Jacob et al., 1978) for the emplacement of the Abbabis gneisses. Pb-isotope results indicate that the basement was enriched in U/Pb at 1.7 Ga, and that the Damaran uranium province has been in existence for at least 1.7 Ga.

Five sulphides from the Rössing Formation define a Pb/Pb isochron which yields an age of 592 ± 60 Ma. The age is interpreted as an M_1 homogenization event, indicating the time when uranium which existed within the basement and cover rocks, was mobilized and introduced into the pre-existing sulphide mineralizations, resulting in the development of more radiogenic Pb-isotope systems.

The intrusion of the mineralized alaskites and granites is restricted to a late- to post-tectonic thermal event, whilst their initial Sr-isotope ratios are characteristically high in comparison with barren granites. The dramatic increase in the initial $^{87}\text{Sr}/^{86}\text{Sr}$ ratio with time displayed by the mineralized alaskites is particularly important when one considers that the only economic body to date is that of the Rössing alaskite, which shows the youngest age and the highest initial Sr-isotope ratio recorded from the belt.

The mineralized red granite on Otjua 37 has a similar age and initial Sr-isotope ratio to those of the mineralized alaskites at Valencia 122 and the Ida dome, and their source rocks may well have

come from similar units within the crust. The apparent increase in initial $^{87}\text{Sr}/^{86}\text{Sr}$ ratios with time shown by the mineralized alaskites, may also pertain with respect to the red granites, and economically viable red granites may well have been formed during the interval 500-450 Ma.

The radiometrically anomalous Stinkbank Salem granite has a similar age and initial Sr-isotope ratio to reported barren Salem granites. The much lower initial $^{87}\text{Sr}/^{86}\text{Sr}$ ratios recorded from the Salem granites, with respect to the mineralized red granites and alaskites, suggest that they were derived from less radiogenic source regions and it is unlikely that an economically viable deposit of Salem granite was formed at any time during the evolution of the Damaran orogen. The anomalous Stinkbank leucogranite however, has a similar age to other leucogranites within the belt, but its initial Sr-isotope ratio is extremely high relative to the others and is close to those of the mineralized granitoids. This suggests that the source of the Stinkbank leucogranite may well be related to that of the alaskites and for this reason the leucogranites should not be excluded as potential economic deposits.

The high $^{87}\text{Sr}/^{86}\text{Sr}$ and low $^{143}\text{Nd}/^{144}\text{Nd}$ ratios (Hawkesworth et al, 1981a; Hawkesworth and Marlow, 1981) in the mineralized alaskites, as well as the radiogenic Pb-isotope ratios in associated sulphides, indicate that the mineralized alaskites were derived from enriched crustal material which has been out of the mantle since 2.0 Ga. However, since the Nosib metasediments appear to consist of 2.0 Ga basement material (Hawkesworth and Marlow, 1981) it is not possible

to determine whether the mineralization was derived directly from the basement, or from the lower Damaran metasediments. At Goanikontes the alaskites appear to be derived directly from Khan material, whereas elsewhere alaskites have formed by in situ partial melting of basement lithologies.

CHAPTER IX
GEOCHEMISTRY

IX.1. Introduction

The economic potential of the Damaran uranium mineralization in particular has prompted several geochemical studies (Smith, 1965; Miller, 1973; Toens et al., 1979; Hawkesworth et al., 1981a). Smith (1965) reported a number of major element analyses of Salem granites, Kuiseb schists and red gneissic granites from the area around the Khan and Swakop Rivers, and considered the Nosib rocks and Kuiseb schists were isochemically transformed to red gneissic granites and Salem granites respectively. Miller (1973) published major and trace element data relating to the Salem granites in the vicinity of Otjosondjou, N.W. of Omaruru (Fig. 1), and was also of the opinion that the Salem granites were derived by extensive melting of the Kuiseb schists. Toens et al. (1979) have reported some 50 major and trace element analyses of a variety of rocks including mineralized alaskites from the area of the Khan and Swakop rivers. On the basis of discriminant analysis, using both major and trace element data they were able to separate mineralized alaskites from various other groups of rocks including Salem granites, banded gneisses and metasediments.

Toens et al. (1979) have published a number of chondrite normalized rare earth element (R.E.E.) patterns for mineralized and non-mineralized alaskites as well as Nosib rocks. They suggest that the mineralized alaskites tend to have a higher abundance of the heavier R.E.E., and on the basis of the similarity between some of the patterns they have

suggested that the mineralized alaskites from the Rössing area are derived from Nosib rocks. Hawkesworth et al. (1981a) have also reported R.E.E. patterns for a variety of Damaran granites and alaskites, and the mineralized alaskites display "concave-up" distribution patterns characterized by low concentrations of medium- and light-R.E.E. Bowden et al. (1979) have stressed the effect which migrating hydrothermal fluids may have on R.E.E. patterns associated with mineralized granites, and the distinction patterns shown by some of the mineralized alaskites may in part be due to magmatic fluids associated with the deuteritic alteration.

This particular geochemical study was initiated in an attempt to:

- A. Characterize the various granitoid suites which were investigated isotopically.
- B. Compare the major and some trace elements of mineralized granites and alaskites with barren granites, for the purpose of establishing geochemical criteria for the recognition of mineralized granitoids.
- C. Assess the various Damaran granitoids in terms of sedimentary protolith (S)- and igneous protolith (I)-type granites.

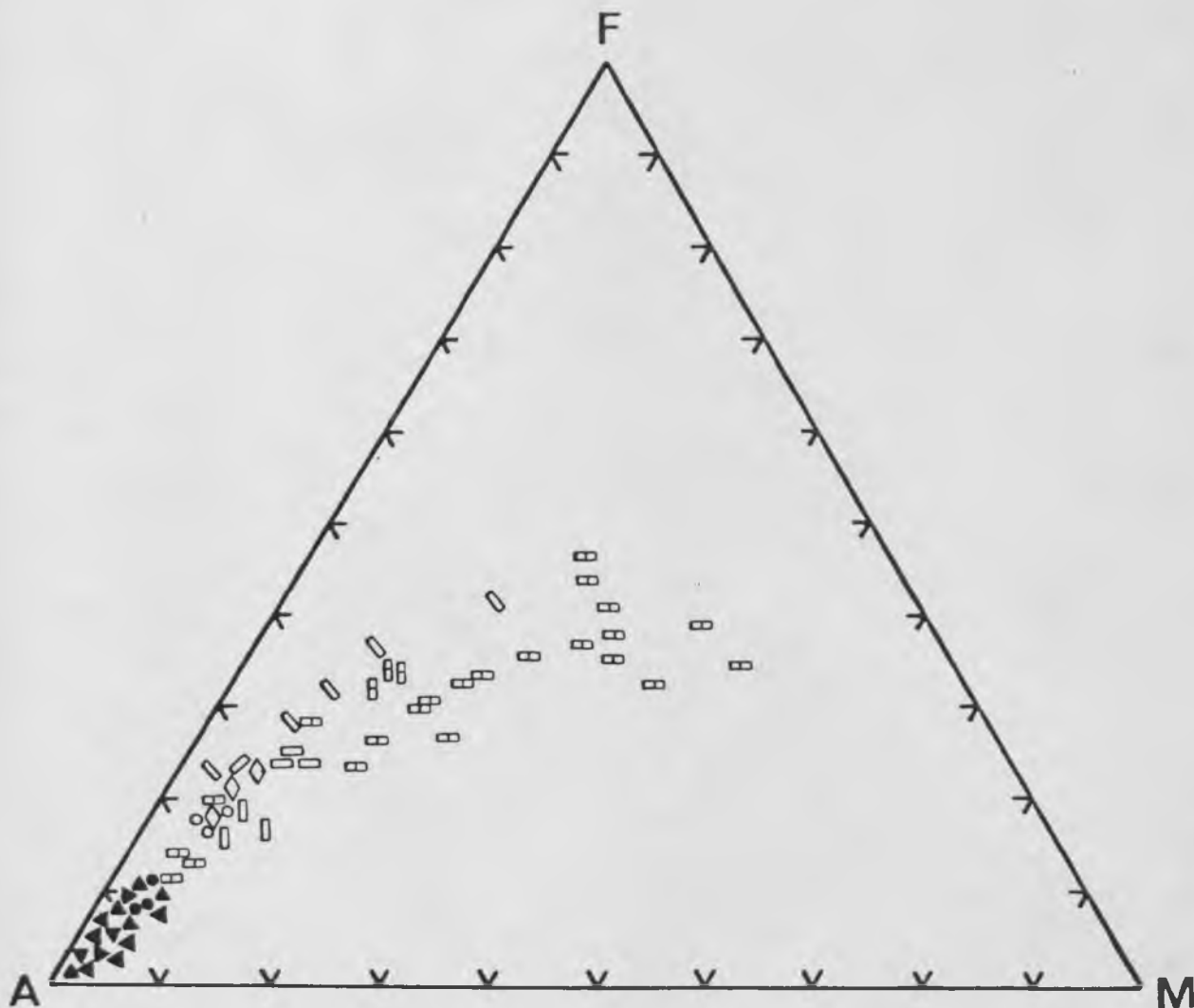
The major element chemistry of three samples from each of the whole rock Rb/Sr suites collected (Chapter VIII), have been determined by X.R.F. (Appendix 5). Samples showing the maximum spread in Rb/Sr values within each suite were selected for analysis. These same samples as well as some 20 other samples have been analysed for U, Th and Sm by epithermal neutron activation at the Open University (Appendix 5). The further 20 samples include additional samples from the whole rock Rb/Sr suites studied in this work, as well as samples of Salem granite

from Swakopmund and Otjosondjou, and samples of alaskite from Rössing and Valencia 122. The laboratory procedures and standard analytical conditions used during the X.R.F. at Leeds University and the neutron activation analysis at the Open University are given in Appendix 1.

IX.2. Geochemical characteristics of the Damaran granitoids

The major element data of the granitoids analysed (Appendix 5), as well as certain results reported by Miller (1973); Toens et al. (1979) and the Open University (unpublished) have been plotted on a conventional A.F.M. diagram (Fig. 45). The mineralized granites and alaskites are shown as filled symbols on Fig. 45, and they clearly fall in a separate field to the barren granitoids which are shown as open symbols. The mineralized alaskites from Rössing, Valencia 122, Goanikontes and the Ida dome, as well as the mineralized red granites from Otjua 37 are strongly enriched in alkalis relative to the barren granitoids, and the enrichment appears to be mainly due to an elevation in K_2O rather than Na_2O . This is compatible with observations by Toens et al. (1979) that the abundance of K-feldspar in alaskites is a favourable criteria for the recognition of uranium mineralization. The barren and radiometrically anomalous granitoids lie along a calc alkaline trend on the A.F.M. diagram, the former ranging in composition from diorites to adamellites (Miller, 1973), whereas the latter show a limited compositional range near the felsic end of the trend.

Brown (1979) has used the calcium oxide/alkalis vs silica diagram to distinguish calc alkaline granitoids from alkaline ones. All igneous rock series record a negative correlation between the calcium/alkali ratio and silica, but Brown (1979) considers the trends displaced towards higher calcium/alkali ratios are diagnostic of calc alkaline rocks,



LEGEND

- ▼ Rössing alaskite (Open University, unpubl.)
- ▲ Valencia alaskite
- ▶ Ida dome alaskite
- ◀ Goanikontes alaskite
- Otjua red granite
- Namibfontein red granite
- ◇ Stinkbank leucogranite
- ▭ Stinkbank Salem granite
- ▨ Valencia Salem granite
- ▮ Swakopmund Salem granite (Open University, unpubl.)
- ▩ Otjosondjou Salem granite (Miller, 1973)
- ◊ Swakop River Salem granite (Toens et al., 1979)

Fig. 45. A.F.M. diagram of the Damaran granitoids illustrating the alkali rich nature of the mineralized alaskites and granites. F = total Fe as Fe_2O_3 . Mineralized samples shown as filled symbols and barren samples shown as open symbols.

whilst those displaced towards lower calcium/alkali ratios are characteristic of alkaline suites. The major element data for the Damaran granitoids has been plotted on this diagram (Fig. 46) relative to typical calc-alkaline and alkaline trends of the Sierra Nevada batholith (Bateman and Dodge, 1970) and the Nigerian younger granites (MacLeod et al., 1971), respectively. The data appears to fall along two separate trends; an upper one paralleling the calc-alkaline Sierra Nevada line, and a lower one falling below the Nigerian alkaline trend. The upper trend contains the more mafic varieties of Salem granite from Otjosondjou (Miller, 1973), which display low initial $^{87}\text{Sr}/^{86}\text{Sr}$ ratios (Hawkesworth et al., 1981b), whilst the lower trend contains the more felsic and mineralized granites which display high initial $^{87}\text{Sr}/^{86}\text{Sr}$ ratios (Chapter VIII). The distribution of sample points on the calcium/alkalis vs silica diagram are considered to reflect the source of the granitoids in terms of their depth within the crust, rather than being an indication of their geochemical affinity. The samples displaying lower calcium/alkali ratios being derived from upper crustal levels, whilst those showing higher ratios being derived from lower levels within the crust.

Certain granites containing concentrations of metals such as tin have been shown by Stempok (1979) to fall within distinct fields on the normative Q-Or-Ab diagram. A high proportion of published analyses of rhyolites and granites, when plotted on such a diagram, fall close to the low-temperature minima of the feldspar-quartz cotectic (Tuttle and Bowen, 1958), and since the mineralized granites are considered to be derived by partial melting of the upper crust, they would also be expected to plot close to the low-temperature minimum. The position of the latter

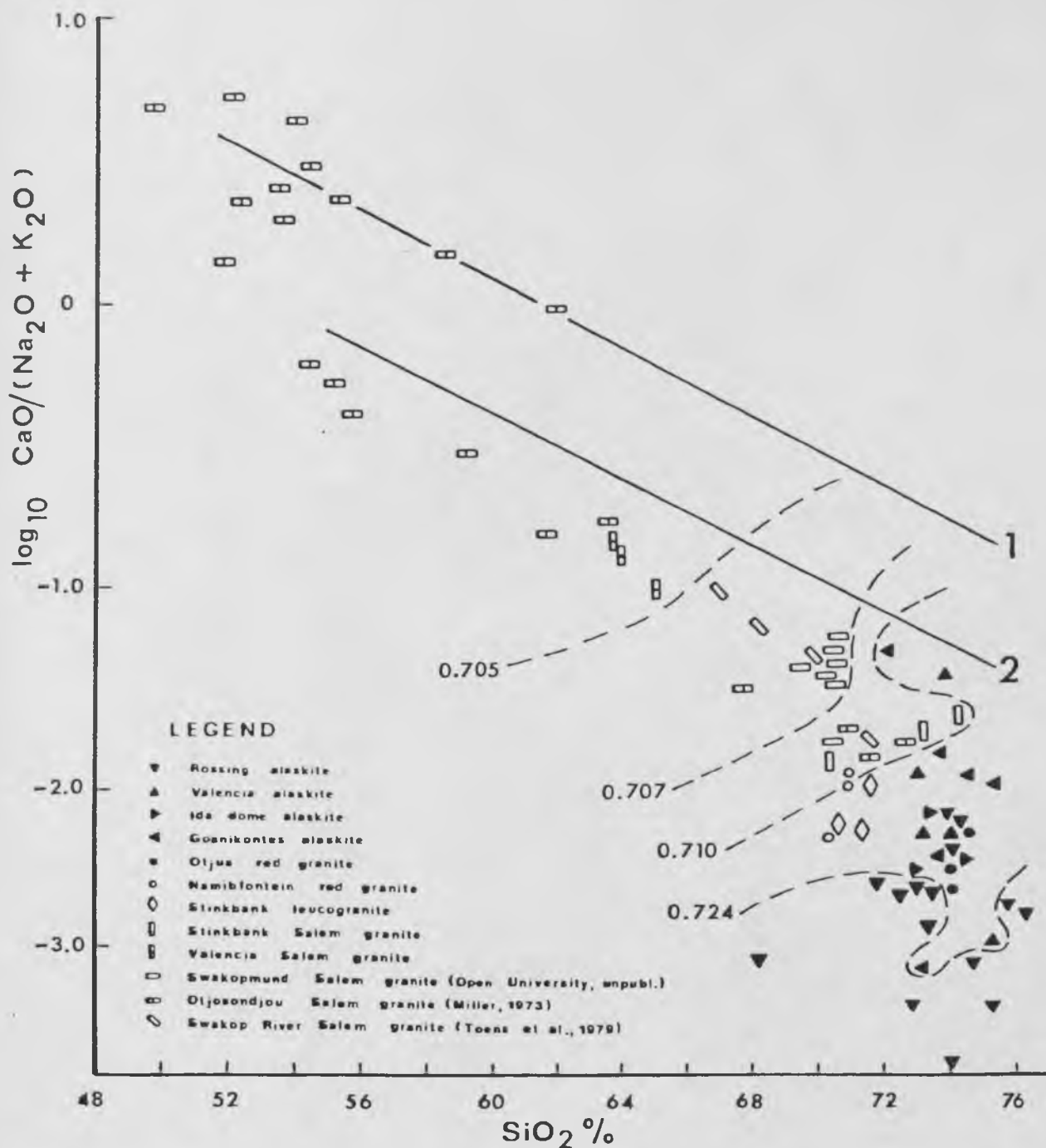
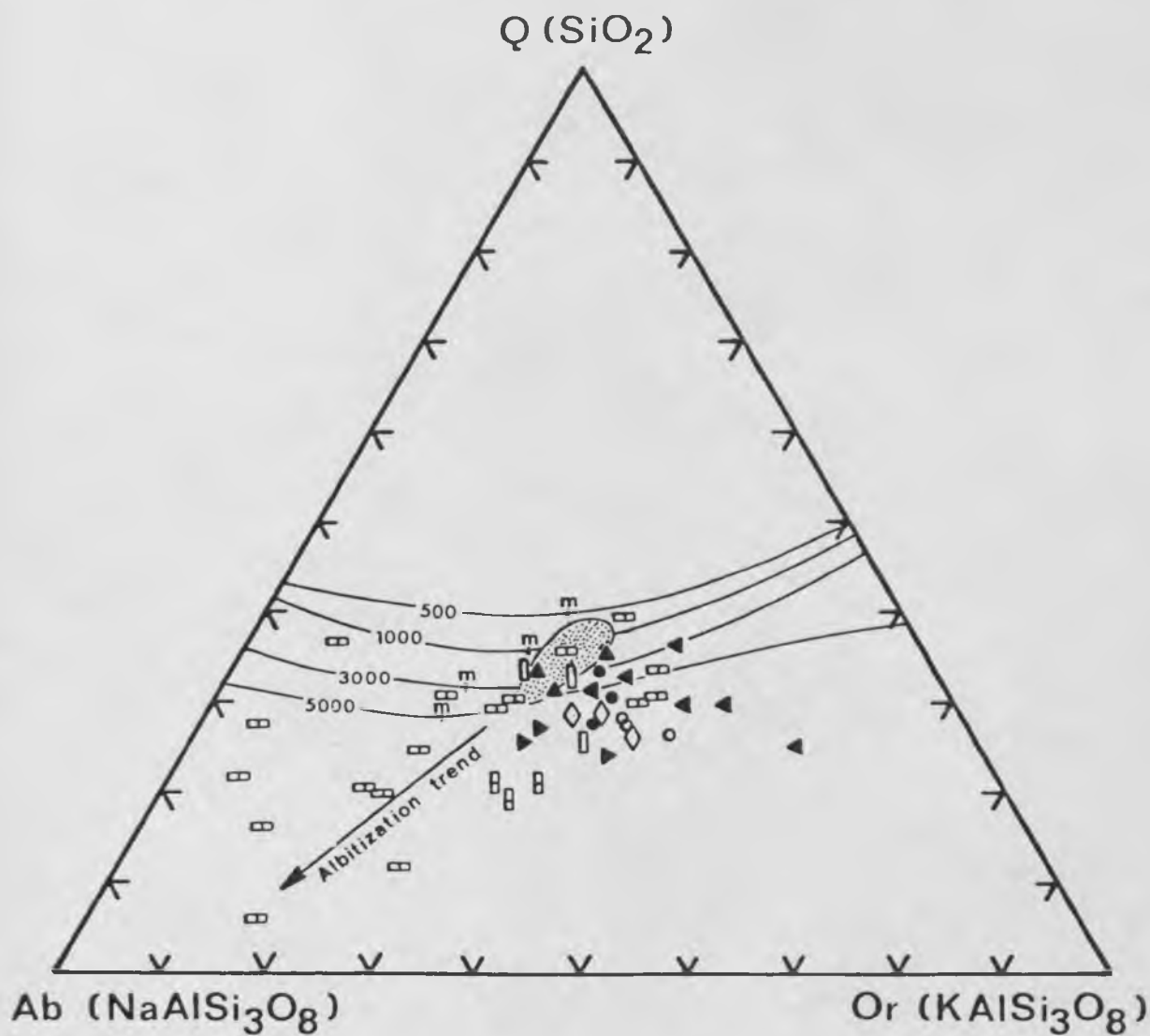


Fig. 46. Calcium oxide/alkalis vs silica diagram for various Damaran granitoids. Trend 1 = typical calc-alkaline trend of the Sierra Nevada batholith (Bateman and Dodge, 1970). Trend 2 = typical alkaline trend of the Nigerian younger granites (MacLeod et al., 1971). Dashed lines represent contours of initial $^{87}\text{Sr}/^{86}\text{Sr}$.

varies with pressure, and therefore the normative composition of the mineralized samples on the Q-Or-Ab diagram should give an indication of the depth at which melting took place. In an attempt to establish whether the Damaran granitoids fall in specific fields dependent upon their mineralized or barren nature, the C.I.P.W. normative compositions were calculated for the various granites analysed (Appendix 5). These are plotted on the normative Q-Or-Ab diagram (Fig. 47) for comparison with the normative compositions of the barren Salem granites from Otjosondjou (Miller, 1973). Many of the Damaran granitoids, particularly those from Otjosondjou show a considerable amount of scatter, and there is a large overlap between the mineralized and barren types. The scatter towards the Ab apex follows the albitization trend of Stempok and Skvor (1974), and it is considered that the large variation in normative composition shown by the Damaran granitoids is caused by alteration processes such as albitization which occurred during a deuteric stage of alteration. Petrological evidence for albitization within the Damaran granitoids is present in the form of albitic rims around feldspar grains (Plate 9).

The major element data have also been plotted on a variation diagram displaying SiO_2 vs TiO_2 , and the negative correlation between the two elements is illustrated in Fig. 48. A similar correlation is present for the same data between SiO_2 and MgO , and SiO_2 and Al_2O_3 . The mineralized granites and alaskites have a silica range between 65 and 78%, and they are enriched in SiO_2 and depleted in TiO_2 , MgO and Al_2O_3 relative to the barren granitoids. The major element characteristics of the mineralized red granites on Otjua 37 are similar to those of the mineralized alaskites.

When SiO_2 is plotted against Rb/Sr (Fig. 49) the distribution of barren



LEGEND

- ▲ Valencia alaskite
- ▶ Ida dome alaskite
- ◀ Goanikontes alaskite
- Otjua red granite
- Namibfontein red granite
- ◇ Stinkbank leucogranite
- ▭ Stinkbank Salem granite
- ⊞ Valencia Salem granite
- ⊞ Otjosondjou Salem granite (Miller, 1973)

Fig. 47. Normative Q-Or-Ab diagram for the Damaran granitoids. Feldspar-quartz cotectic lines at various confining pressures (500, 1000, 3000 and 5000 bars), low-temperature minima (m), and stippled area occupied by a high proportion of published analyses of rhyolites and granites, after Tuttle and Bowen (1958). Albitization trend after Stemprok and Skvor (1974).

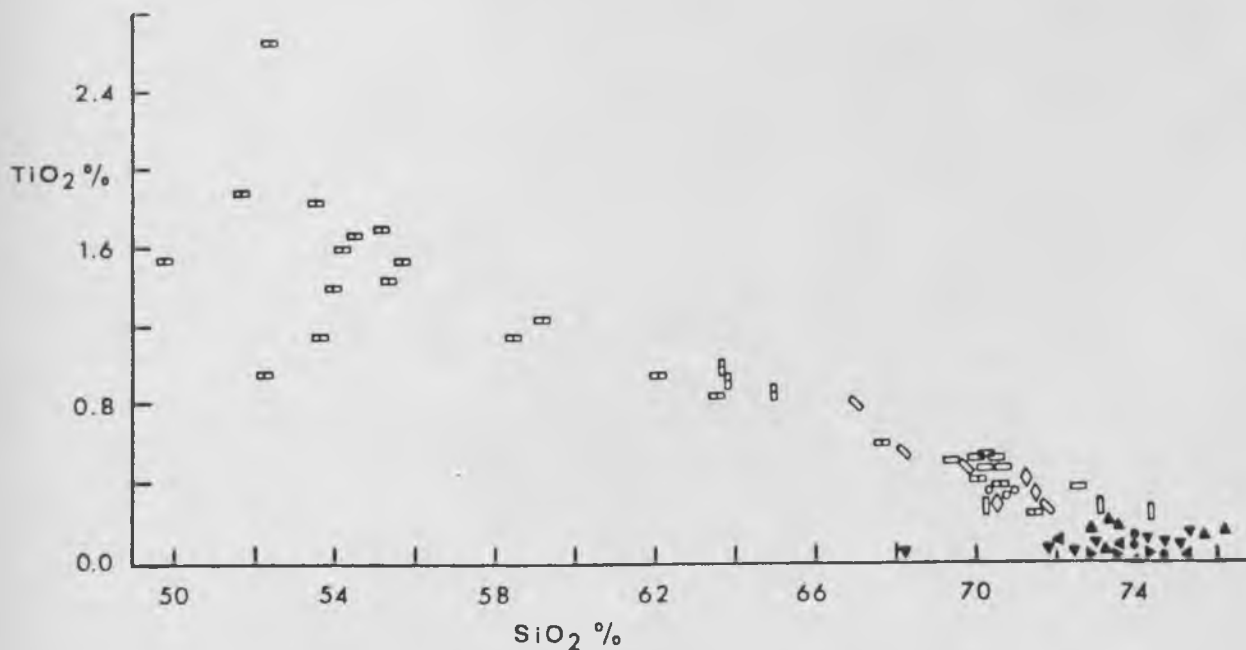


Fig. 48. Variation diagram illustrating the negative correlation between silica and titanium among the Damaran granitoids. For legend see Fig. 49 below.

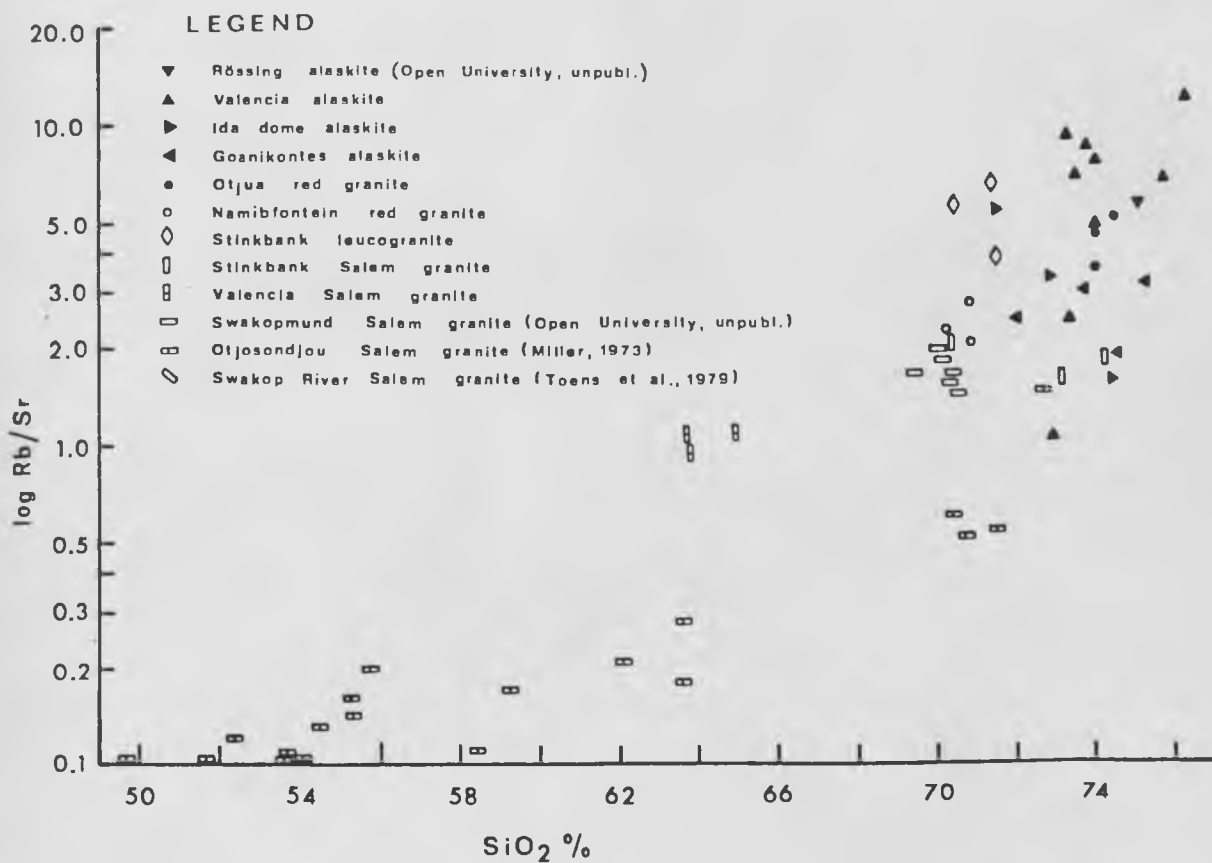


Fig. 49. Rb/Sr vs silica diagram for the Damaran granitoids.

granitoids is defined by a positive curve, expressing the higher Sr content of the more mafic granitoids and the higher Rb content of the more felsic varieties. The mineralized granites and alaskites are enriched in Rb and depleted in Sr relative to the barren granitoids. The distribution of the latter on a Rb vs Sr diagram (Fig. 50) is defined by a negative curve, expressing the enrichment of Rb and depletion of Sr in the more evolved granites. The mineralized samples fall within a separate but overlapping field which is characterized by a large spread in Rb (33-483 ppm) and a small range in Sr (16-209 ppm).

The elements K and Rb are very similar showing close geochemical coherence, and normal igneous rocks have K/Rb ratios which fall between 150 and 300 (Taylor, 1965; Shaw, 1968). Most Damaran granitoids fall well within these limits (Fig. 51) and only a few samples show slight departures to higher or lower ratios. The mafic Salem granites from Otjosondjou display ratios which average about 300, but a few samples, especially the aplitic ones (Miller, 1973), show ratios of up to 390. Slight deviations to lower values are shown by some samples of Rössing alaskite and a single sample of the Stinkbank leucogranite, but K/Rb ratios do not fall below 140. Pegmatites derived by fractionation of granites show an enrichment in Rb relative to K, and K/Rb ratios in these pegmatites may be expected to fall well below 100 (Taylor, 1965; Shaw, 1968). On the basis of the enrichment of the Damaran alaskites in incompatible elements Backström and Jacob (1979) suggest they represent crystallization products of highly fractionated melts. However, the absence of low K/Rb ratios among the typically pegmatitic alaskites indicates they have not undergone extreme fractionation, and that they are derived by partial melting of crustal rocks with normal

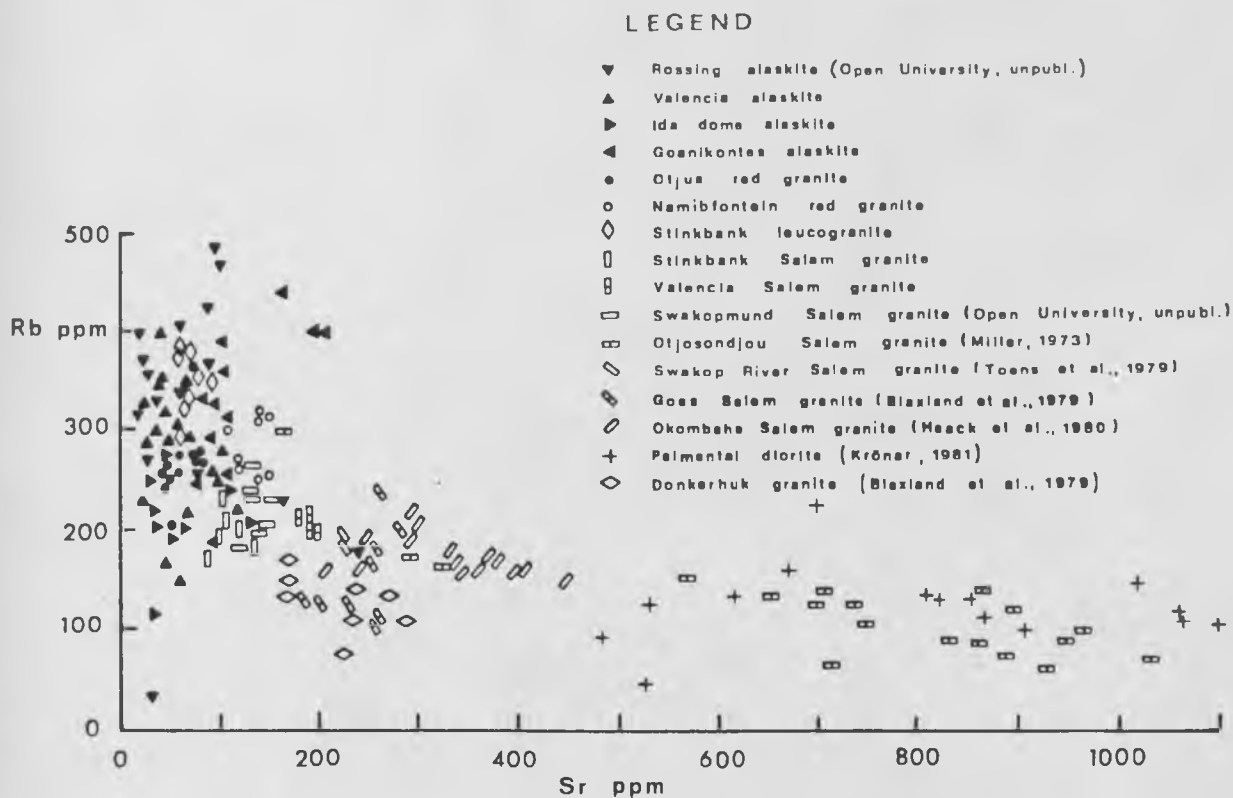


Fig. 50. Rb vs Sr diagram for the Damaran granitoids.

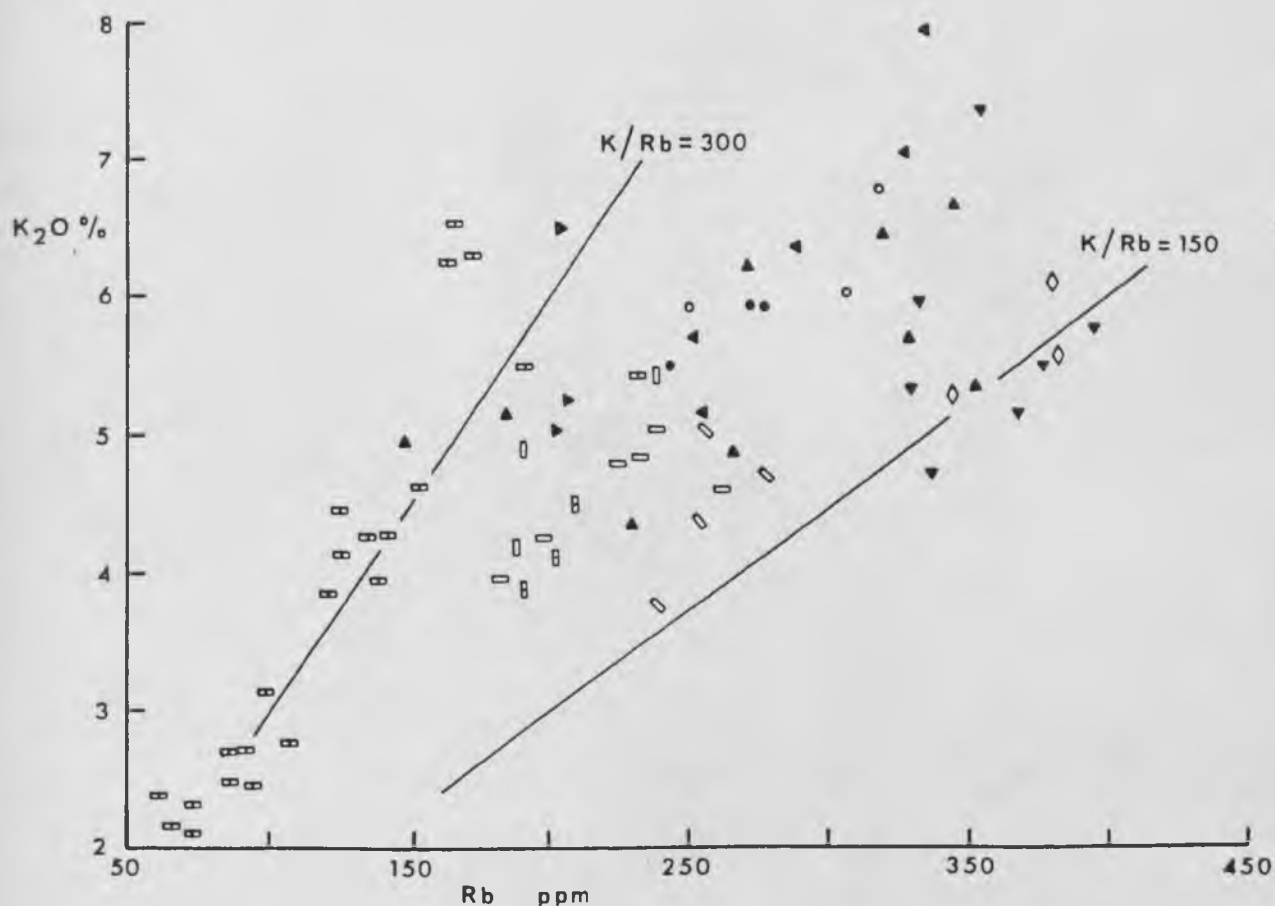


Fig. 51. Variation diagram illustrating the positive correlation between K_2O and Rb among the Damaran granitoids. For legend see Fig. 50 above.

K/Rb ratios (150-300, Taylor, 1965). Unusually low K/Rb ratios are also considered to serve as indicators of post-magmatic alteration by metasomatic fluids (Shaw, 1968; Vidal et al., 1979), and the absence of low ratios among the Damaran granitoids indicates these rocks have not undergone any major alteration by hydrothermal processes.

In an attempt to establish the relationship between U, Sm and Th within the Damaran granitoids, these elements have been plotted one against the other in Figures 52, 53 and 54. Samarium is a good example of a fairly immobile element whose behaviour during fractional crystallization is normally one of progressive enrichment, and therefore it makes a useful comparison with U and Th. One would expect Sm to increase with SiO_2 among the earlier barren Damaran granitoids because they are considered to represent fractionated products of material derived from the lower crust. The data relating to these intrusives is extremely limited, but there does not appear to be a positive correlation between Sm and SiO_2 . However, the mineralized granitoids display distinctly lower Sm values than the barren ones (Fig. 52), and there appears to be a progressive decrease in the Sm/U ratio as one passes from the mafic Salem granites at Otjosondjou, to the felsic ones at Stinkbank. The Th vs U diagram (Fig. 53) indicates the mineralized granites and alaskites are characterized by Th/U ratios of less than one, whilst the barren granitoids show Th/U ratios greater than one. Samarium appears to increase with Th in many of the Damaran granitoid suites (Fig. 54), but the mineralized samples are characterized by lower Sm/Th ratios than the barren samples. In conclusion it may be stated that the mineralized samples are characterized by low Sm values, low Sm/Th ratios and Th/U ratios of less than one.

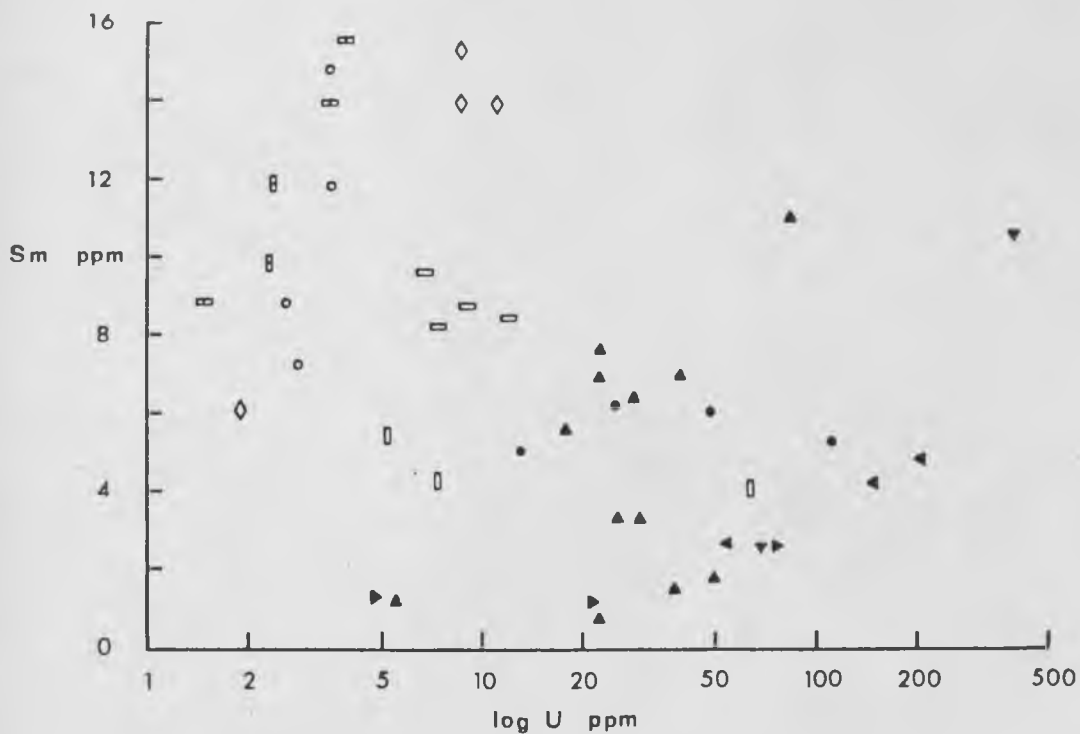


Fig. 52. Sm vs U diagram for the Damaran granitoids illustrating the distinctly lower Sm values among the mineralized samples. For legend see Fig. 50.

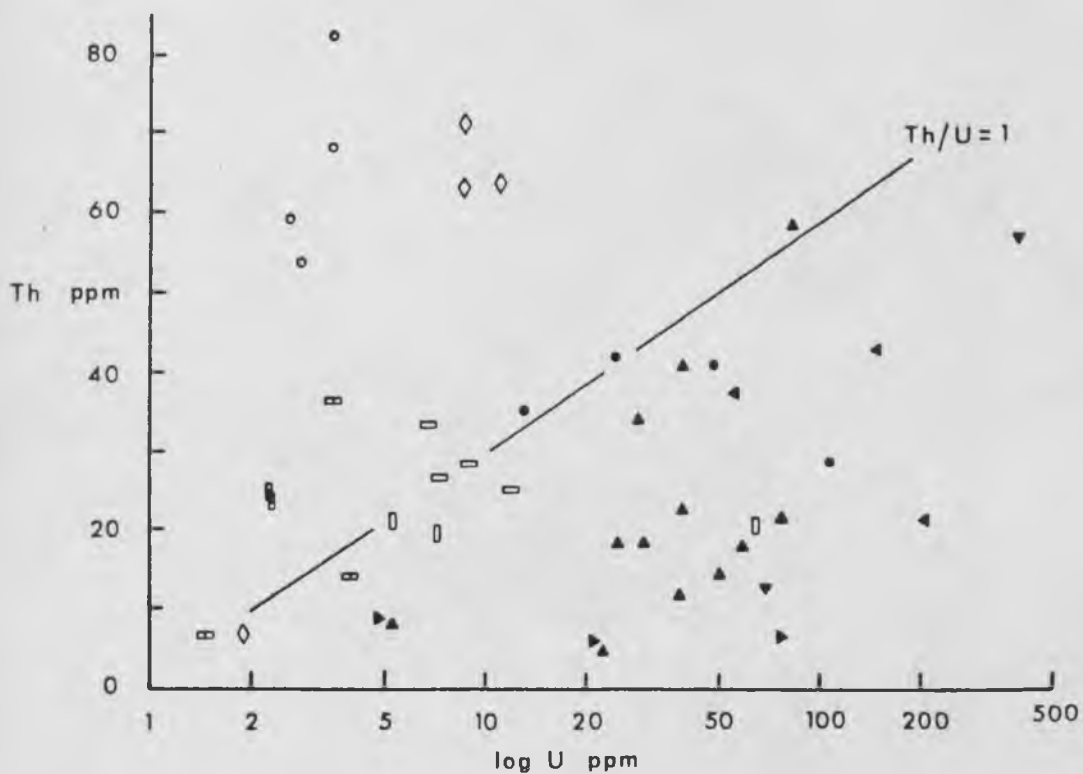


Fig. 53. Th vs U diagram for the Damaran granitoids. The mineralized granitoids are characterized by Th/U ratios of less than one. For legend see Fig. 50.

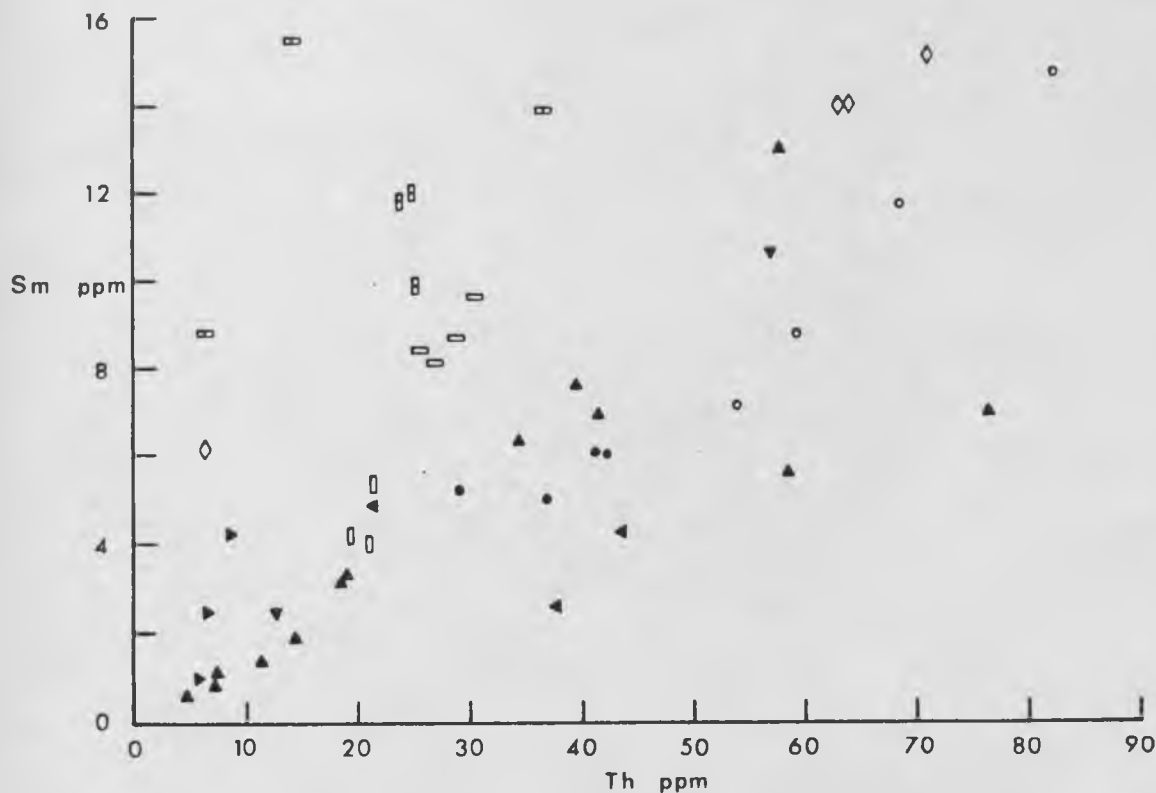


Fig. 54. Sm vs Th diagram for the Damaran granitoids. The mineralized granitoids are characterized by lower Sm/Th ratios than the barren samples. For legend see Fig. 50.

IX.3. Discussion

Using chemical, mineralogical and field criteria Chappell and White (1974) have distinguished two types of granitoid in the Tasman Orogenic Zone of eastern Australia. The differences between these two are interpreted as a reflection of different source rocks: partial melting of peraluminous sedimentary rocks is thought to produce "S-type" granitoids whereas "I-types" have an igneous source. S-type granites come from a sedimentary source that has been subjected to prior chemical fractionation, involving loss of sodium to sea water and evaporites and calcium to carbonates, with subsequent relative enrichment of the main sedimentary pile in aluminium. In contrast, this style of fractionation does not occur in igneous rocks and there is no enrichment of aluminium relative to alkalis and calcium in I-type granitoids. Ishihara (1977) proposed a similar classification

of the Japanese granitoids into a magnetite series and an ilmenite series. The former represent a "mantle-type" comparable with I-type granitoids of Chappell and White (1974), whilst the latter represent a "crust-type" comparable with S-type granitoids. The distinctive chemical and mineralogical properties of I- and S-type granitoids have been summarized by Ferguson et al. (1980), and they are shown in Table 17.

Isotopic evidence (Chapter VIII) suggests the mineralized and leucocratic granitoids are derived from Nosib and basement rocks, whilst the more mafic varieties were derived from deeper structural levels. These conclusions may be tested by applying the various chemical criteria for recognition of sedimentary and igneous protoliths, if it is assumed that the Abbabis basement and the Damaran cover rocks consist essentially of sedimentary material (i.e. that the upper Damaran crust represents a sedimentary protolith).

The mean Na_2O and mol. $\text{Al}_2\text{O}_3/(\text{Na}_2\text{O} + \text{K}_2\text{O} + \text{CaO})$ values of a number of Damaran granitoids are shown in Table 18. The major element data used for the calculations includes samples analysed in this work (Appendix 5) as well as analyses reported by Miller (1973), Toens et al (1979) and the Open University (unpublished). The mean Na_2O percentages for the various Damaran granitoids (Table 18) are close to the boundary figure of 3.2% set for S- and I-types by Chappell and White (1974), and they are therefore of little value in diagnosing the parentage of the various Damaran granitoids. The mean mol. $\text{Al}_2\text{O}_3/(\text{Na}_2\text{O} + \text{K}_2\text{O} + \text{CaO})$ values for the different granites however are well in excess of 1.1 (Table 18) and would therefore suggest an S-type source for both the mineralized and the barren granites. By contrast the C.I.P.W. normative corundum values for

TABLE 17. Distinctive chemical and mineralogical properties of I- and S-type granitoids, after Ferguson et al. (1980).

I-types	S-types
CHEMICAL CRITERIA	
Sodium normally high, $\text{Na}_2\text{O} \geq 3.2\%$ in felsic varieties, decreasing to 2.2% in more mafic types.	Sodium may be low, Na_2O normally $< 3.2\%$ in rocks with approximately 5% K_2O , decreasing to $> 2.2\%$ in rocks with approximately 2% K_2O .
Mol. $\text{Al}_2\text{O}_3 / (\text{Na}_2\text{O} + \text{K}_2\text{O} + \text{CaO}) < 1.1$	Mol. $\text{Al}_2\text{O}_3 / (\text{Na}_2\text{O} + \text{K}_2\text{O} + \text{CaO}) > 1.1$.
Broad spectrum of compositions from felsic to mafic	Relatively restricted in compositions to high SiO_2 types.
Regular inter-element variations within plutons, linear or near-linear variation diagrams.	Variation diagrams more irregular.
C.I.P.W. normative diopside or $< 1\%$ normative corundum.	Always have C.I.P.W. normative corundum.
$\text{Fe}^{3+} / (\text{Fe}^{2+} + \text{Fe}^{3+})$ high (usually > 0.2).	$\text{Fe}^{3+} / (\text{Fe}^{2+} + \text{Fe}^{3+})$ low (usually < 0.2).
Initial $^{87}\text{Sr}/^{86}\text{Sr}$ ratios generally low (usually < 0.708).	Initial $^{87}\text{Sr}/^{86}\text{Sr}$ ratios generally high (usually > 0.708).
$< 65\%$ SiO_2 most common	$> 65\%$ SiO_2 most common.
$\delta^{18}\text{O}$ values from 7.9 to 9.4.	$\delta^{18}\text{O}$ values from 9.9 to 12.0
MINERALOGICAL CRITERIA	
Hornblende present (hornblende-bearing xenoliths common).	Hornblende absent
Minor muscovite in very felsic rocks.	Muscovite common, sometimes abundant (2-3%).
Cordierite, garnet, andalusite and sillimanite absent.	Cordierite, garnet, andalusite and sillimanite may be present.
Accessories: Magnetite, allanite and primary sphene; sulphides uncommon; zircon, monazite and apatite can be present.	Accessories: Ilmenite, cassiterite and tourmaline; sulphides common; zircon, monazite and apatite can be present.

TABLE 18. Na_2O and mol. $\text{Al}_2\text{O}_3/(\text{Na}_2\text{O} + \text{K}_2\text{O} + \text{CaO})$ values
for various Damaran granitoids

	<u>n</u>	<u>Mean wt % Na_2O</u>	<u>Mean mol. $\frac{\text{Al}_2\text{O}_3}{(\text{Na}_2\text{O} + \text{K}_2\text{O} + \text{CaO})}$</u>
Mineralized granites and alaskites	33	3.4%	1.7
Radiometrically anomalous granites	9	3.5%	1.8
Barren granites	35	3.1%	1.9

the granites analysed (Appendix 5) are all less than 1%, and corundum is commonly absent from the calculations, which could indicate an I-type parentage for both the mineralized and barren granites.

Although the above data are contradictory, chemical and mineralogical evidence in terms of the other criteria proposed by Chappell and White (1974) are more consistent. For instance, the mineralized granites and alaskites display a limited range of SiO_2 between 65 and 78%, which is characteristic of S-type granitoids, whilst the barren granites display a wide range from 50 to 72% (Miller, 1973), which is common of I-types. It is difficult to assess the role of inter-element variation among the mineralized granites because only three samples have been analysed for each cogenetic suite. However, some 20 analyses of the barren Otjosondjou Salem granite (Miller, 1973) do display regular inter-element variation suggesting these rocks have an I-type parentage. With reference to the Sr-isotope composition of the Damaran granitoids (Chapter VIII), it is clear from Table 13 and Fig. 38 that the mineralized and leucocratic granitoids have the highest initial $^{87}\text{Sr}/^{86}\text{Sr}$ ratios, whilst the earlier granitoids (e.g. Oas syenite and Palmental diorite;

Kröner, 1981) have the lowest initial Sr-isotope ratios.

When the various mineralogical criteria for recognition of S- and I-types (Table 17) are applied to the Damaran granitoids, the leucocratic and mineralized varieties appear to be predominantly S-type in character, whilst the earlier mafic varieties show an affinity with I-types. The mineralogical features diagnostic of S-types shown by the Damaran intrusives include: the presence of muscovite as a common secondary constituent in all the granites as well as its presence as a major constituent in the leucogranites, the presence of metamorphic garnet in many of the granites as well as metamorphic sillimanite in the red granites and alaskites; and finally the abundance of sulphides in the alaskites. The mineralogical features suggestive of an I-type parentage for the more mafic granitoids include the presence of hornblende as a major constituent in some Salem diorites and granodiorites, and as a minor constituent in some red granites.

In conclusion, with the exception of certain chemical criteria, the majority of both chemical and mineralogical criteria proposed by Chappell and White (1974) indicate the mineralized granites and alaskites show an affinity for S-type granitoids, whilst the barren granites have a number of features in common with I-types. This substantiates the conclusions drawn from isotopic evidence (Chapter VIII) that the mineralized material was derived from the upper Damaran crust, whilst the more mafic granitoids were derived from deeper structural levels. Recent oxygen isotope investigations by U. Haack at Gottingen University (Kröner, pers. comm.) corroborate these ideas.

Various models proposed for the evolution of the Damaran belt (Sawyer, 1978; Barnes and Sawyer, 1980; Kröner, 1981; Coward, 1981a and b) suggest the Damaran granitoids were generated above a subduction zone.

However, the Sr-isotope ratios of the later Damaran granites (Table 13) are much higher than those normally observed above subduction zones (Hurley and Bateman, 1965; Kistler and Peterman, 1973; Hawkesworth, 1979), and they suggest derivation from a crustal source. Doubts concerning the significance of high initial Sr-isotope ratios in granites have been raised by several authors including Taylor and Forrester (1971), Vidal et al. (1979), Simpson et al. (1979) and Plant et al. (1980). The latter suggest that extensive initial high-temperature water-magma interaction within a few kilometres of the surface may lead to re-equilibration of the Sr-isotope systems to give values comparable with the sedimentary host rocks. Certainly, evidence of alteration is present within many Damaran granitoids, and has previously been recognized in the mineralized Goanikontes and Rössing alaskites by Valois and Walgenwitz (1979), and Cuney (1980), respectively. It is considered however, that this alteration is deuteric rather than hydrothermal, and that the magmatic fluids associated with the alteration had little effect on the Sr-isotope systems of the various mineralized granitoids. Vidal et al. (1979) consider the high initial Sr-isotope ratios shown by some granite-syenite complexes result from a post-magmatic geochemical readjustment by hydrothermal fluids. However, the complexes cited from Nigeria and the Indian Ocean are characterized by an abnormal negative correlation between K and Rb, which is clearly not present among the Damaran granitoids (Fig. 51). Also the large scale hydrothermal convective systems proposed by various authors including Taylor and Forrester (1971) and Simpson et al. (1979) are generally considered to act at higher structural levels than those required by the intermediate- to high-pressure Damaran metamorphism (Nash, 1971; Jacob, 1974a; Hoffer, 1975; Puhon, 1976; Cuney, 1980).

Plant et al. (1980) have distinguished two types of granite in the Scottish Caledonides; firstly metalliferous types containing high primary concentrations of elements such as Mo, Cu, Sn, U and F in silicate minerals; and secondly, mineralized granites containing the same elements in ore minerals. They consider that the metalliferous types have an isotopically juvenile sub-crustal source and that metalliferous mineralization only occurs when rising magma interacts with epizonal water during or after emplacement. The barren granitoids and the radioactive granites may be compared with some Scottish metalliferous types, in that their U content is well above that of average granitic rocks, but it is not present in high enough concentrations to form distinct primary uranium phases. However, the mineralized granites and alaskites cannot be compared with the Scottish mineralized granites firstly because they are considered to have a crustal source, and secondly, the uranium mineralization is primary in nature (for discussion see Chapter VI) and although migration of U-bearing fluids may have taken place during a deuteritic alteration, the primary uranium minerals crystallized in association with other accessory constituents prior to the alteration.

On the basis of tectonic setting, Rogers et al. (1978) proposed a classification of igneous uranium deposits in terms of two end members: (1) anatectic, migmatitic, pegmatite-alaskite bodies formed by remobilization of pre-existing basement; and (2) post-tectonic, alkali-rich granites in stocks probably derived directly from the mantle or deep crustal levels in the form of diapiric magmas. They consider the Rössing deposit to be an ideal example of an anatectic body, and the Bokan Mountain deposit of southern Alaska to represent an ideal example of a mantle

TABLE 19. Summary of principal differences between the Rössing and Bokan Mountain models for granitic uranium deposits, after Rogers et al. (1978).

<u>Characteristic</u>	<u>Rössing Model</u>	<u>Bokan Mt. Model</u>
Lithology	Pegmatite-alaskite-gneiss; anatectic granite and migmatite	Alkaline and/or peralkaline granite; associated syenites; commonly albite-riebeckite granite
Derivation	Reworked and recycled sialic crust	Mantle or lower crust
Initial Sr isotope ratios	Generally greater than 0.710	Generally less than 0.710
Th/U ratios	Generally less than 1.0	Generally greater than 1.0
Levels of erosion	Deep	Shallow
Levels of emplacement	Catazonal	Epizonal
Tectonic stage	Syntectonic	Post-tectonic
Age	Commonly Proterozoic to early Paleozoic	Any age (post-Archean)
Tectonic setting	Orogenic	Anorogenic or post-orogenic
Metamorphic rank of country rocks	Middle- to upper-amphibolite	Any rank (including unmetamorphosed)

derived uranium deposit. The principal differences between the two ideal end members, as summarized by Rogers et al. (1978) are shown in Table 19. It would appear that hydrothermal activity has a large role to play in the development of a uranium deposit of the "Bokan Mountain type", and the Scottish mineralized granites show many features in common with this type of uranium deposit.

TABLE 20. Th/U ratios of mineralized alaskites from various localities within the Damaran belt.

<u>Locality</u>	<u>Th/U ratios (Th and U values given in Appendix 5)</u>											
Valencia 122	0.3	0.6	0.2	0.7	1.1	1.2	0.7	3.4	1.5	0.3	3.3	1.8
Goanikontes	0.3	0.1	0.7									
Ida dome	0.3	1.8	0.1									
Rössing	0.2	0.2										

Limited geochemical data led Rogers et al. (1978) to suggest that the Rössing type deposits have very low Th/U ratios, and calculation of Th/U ratios from the new Th and U analyses (Appendix 5) suggest that this is a reliable criterion for the recognition of mineralized alaskites such as those at Rössing. Table 20 shows a number of Th/U ratios for mineralized alaskites from Valencia 122, Goanikontes, the Ida dome and Rössing, and a mean Th/U ratio of 0.9 has been calculated from the 20 ratios. Two of the alaskite samples from Valencia 122 however, show Th/U ratios well in excess of 1.0, but both samples were collected from an exploration pit only a few metres from the surface (Folder 4, F6), and it is possible they have both been effected by a recent loss of uranium. When these two samples are omitted from the mean calculation, a Th/U ratio of 0.7 is obtained.

The Rössing deposit is considered to represent an excellent example of an anatectic uranium deposit, formed by remobilization of pre-existing crust, but it must be emphasized that field evidence and age determinations (Kröner and Hawkesworth, 1977) indicate it is late- to post-tectonic in nature, and not syntectonic as proposed by Rogers et al. (1978). Since mantle derived uranium deposits, typified

by the Bokan Mountain deposit are also characterized by a post-tectonic nature, the tectonic stage of emplacement may not be a useful criteria for recognition of the different types of igneous uranium deposits.

IX.4. Conclusions

The mineralized red granites from Otjua 37 display identical major and trace element characteristics to the mineralized alaskites. However, these mineralized suites are geochemically quite distinct from the barren granitoids and they display an enrichment in total alkalis, silica and Rb/Sr, and a depletion in Sm, Sm/Th and Th/U.

The more mafic varieties of Salem granite from Otjosondjou display higher calcium/alkali ratios than the more leucocratic and mineralized Damaran granitoids. Since the latter contain the higher initial Sr-isotope ratios, the low calcium/alkali ratios are considered to reflect derivation from the upper crust, whilst lower ratios indicate derivation from deeper structural levels.

Application of Chappell and White's classification of igneous rocks into S- and I-types, indicates the mineralized granites and alaskites show an affinity with S-type granitoids, whilst barren granites have a number of features in common with I-types. This substantiates conclusions drawn from isotopic evidence (Chapter VIII) that the mineralized granites were derived from Nosib and basement source rocks, whilst the more mafic granitoids were derived from lower levels within the crust.

Rogers et al. (1978) consider that the Rössing body is an ideal example of an anatectic uranium deposit, and they suggest that such a

deposit is characterized by very low Th/U ratios. New data suggests that this ratio is a reliable criterion for the recognition of mineralized alaskites such as those at Rössing. The tectonic stage of emplacement however, is probably not a useful indicator for distinguishing the different types of igneous uranium deposits.

The secondary alterations seen within many of the Damaran intrusives are considered to be deuteric and associated with low-level magmatic fluids, rather than hydrothermal and related to high-level meteoric fluids. Geochemical evidence in the form of a normal positive correlation between K and Rb indicate that the alteration has not resulted in any major geochemical readjustments within the Damaran intrusives.

CHAPTER X

EVOLUTION OF THE DAMARAN URANIUM PROVINCE

The movement of uranium within the earth's crust is commonly shown to be related to active orogenic processes such as remobilization, magmatism and metamorphism (e.g. Adamek and Wilson, 1979; Dahlkamp, 1979), and in this chapter an attempt is made to follow the movement of uranium during the evolution of the Damaran orogenic belt. Although the development of the uranium province is intimately associated with the evolution of the Damaran orogeny, Pb-isotope data (Chapter VIII) indicate that rocks enriched in uranium were in existence as early as 1.7 Ga. It is considered that these rocks represent the original source of the Damaran uranium, and that they underwent processes including erosion, sedimentation, metamorphism, remobilization and magmatism during the Damaran orogenic event to produce the concentrations of primary mineralization within the Damaran granites and alaskites.

The whole rock Rb/Sr age of 2.0 ± 0.4 Ga (Chapter VIII) and the U-Pb age of 1.9 ± 0.3 Ga (Jacob et al., 1978) for two different Abbabis gneisses from a basement inlier within the central portion of the Damaran orogen, indicate that the area underwent a magmatic event around 2.0 Ga. Zircon ages of 1730 ± 30 Ma. and 1870 ± 30 Ma. for the emplacement of the Franzfontein granitic suite (Burger et al., 1976) on the northern margin of the orogen (Fig. 1), and a model Pb-Pb age of 1.90 ± 0.03 Ga for a thermal event along the southern margin (Ruxton, 1981) suggest that this magmatic event may have been widespread, but possibly not coeval from one area to the next.

Pb-isotope results (Chapter VIII) indicate that the basement underlying the central portion of the orogenic belt was enriched in U/Pb

at 1.7 Ga. This represents a minimum age for the development of the Damaran uranium province, and the introduction of U to the region may be related to the widespread 2.0 Ga magmatic event detailed above.

Little is known concerning the geological events which took place between the 2.0 Ga magmatic event and the initial stages of deposition of the Damara Sequence represented by fluviatile clastics of the Etusis Formation. There is however, some evidence for basement remobilization in the central belt around 1.1 Ga (Downing and Coward, 1981) when there was a widespread magmatic event along the southern margin of the orogen (Hugo and Schalk, 1971; Watters, 1974, 1976 and 1978; Ahrendt et al., 1978). The latter event is considered by Watters (1976) to have developed on the western and north-western margins of the sialic Kalahari plate as a result of the south-eastward subduction of oceanic crust. However, it is difficult to reconcile a 1.1 Ga event in the central zone with this model, if subduction was directed towards the S.E. If basement remobilization was operative at 1.1 Ga, it is probably related to the Kibaran orogenesis dated at 1.1 ± 0.2 Ga (Clifford, 1970).

Deposition of the Damara Sequence started around 1000 Ma with the inflow of clastic material into restricted basins which developed by rifting of the pre-existing sialic basement (Kröner, 1981). The thick sequence of clastics known as the Etusis Formation is represented predominantly by quartzite, but also by conglomerate and calc silicate units (Chapter III). Indications that some of these deposits were derived from radioactive source rocks are provided by the presence of:

- 1) Uranyl silicate inclusions in microcline grains which represent detrital constituents of quartzites exposed on Wolfkoppe 105 (Plate 24).
- 2) Th-bearing monazite grains which occur interstitially or as

inclusions in quartz and feldspar within weakly radioactive quartzites exposed on Namibfontein 91 (Plate 5).

3) Smoky quartz pebbles in fluvial, channel-type conglomerates exposed on the Langer Heinrich Mountain in the Namib Desert Park (Chapter III).

The rocks of the Etosis Formation are overlain conformably by interbedded gneisses, schists and calc silicates of the Khan Formation, which are considered to represent calcareous, feldspathic sandstones deposited in fairly shallow water basins. Stratiform copper deposits are present within the upper part of the formation at various localities within the central belt, and they are particularly well developed on the Ida dome in the Namib Desert Park.

The Khan Formation is overlain by the Rössing Formation which is characterized by a variable sequence of carbonates, quartzites, conglomerates and pelites. Stratabound copper deposits, similar to those within the Khan Formation, are well developed and the disseminated ore minerals which include chalcopyrite, bornite and chalcocite occur preferentially within the calc silicate units. Primary uranium minerals have been found within metasediments of the Rössing Formation at Rössing and Valencia 122 (Chapter VI). The mineralization occurs in the form of uraninite and betafite within calc silicates at Valencia (Plate 29), and schists of the lower biotite-cordierite gneiss unit at Rössing (Plates 26, 27 and 28). A number of points suggest that these primary uranium minerals represent recrystallized phases of syngenetic uranium which existed within the Rössing sediments prior to the emplacement of the uraniumiferous alaskites:

1) The most radioactive calc silicates of the Rössing sequence on Valencia 122 represent the host rocks to the more strongly developed

stratabound copper deposits (Chapter VI).

2) The Rössing schists contain an abundance of monazite grains, and because of the common association between primary uranium minerals and monazite in mineralized granitoids, the two phases could be derived from similar source rocks (Chapter VI).

3) Radiogenic Pb-isotope ratios of five sulphide samples from the Rössing Formation (Fig. 42) indicate that a homogenization event took place at 592 ± 60 Ma. which led to the mobilization of uranium which previously existed within basement and cover rocks (Chapter VIII).

The Rössing sequence is overlain by the Chuos mixtites, the Karibib marbles and the Kuiseb schists, and there is no indication of any stratabound U mineralization within any of these sequences. This is not surprising in the case of the Karibib Formation which is characterized by shallow water, carbonate, shelf facies deposits, because such sediments are not conducive towards the development of U deposits. However, the thick sequences of fine-grained, deep water sediments of the Kuiseb Formation are perhaps more appropriate for the deposition of U than certain other types of sediment within the Damara pile. The upper part of the Damara Sequence shows striking differences in its Sr-isotope and Nd-isotope compositions to the lower part, and Hawkesworth and Marlow (1981) concluded that these differences are due to the influx of much younger material at the time the upper Damara sediments were being deposited.

Derivation of uranium from a radioactive basement and its subsequent enrichment in certain geosynclinal sequences has previously been proposed by Ferguson et al. (1980) for the syngenetic uranium deposits of the Pine Creek geosyncline. Likewise, the association between radioactive

calc silicates and stratabound copper deposits such as those within the Rössing sequence on Valencia 122, has analogies with syngenetic uranium - base metal deposits in the East Alligator region (Hegge et al., 1980) and the Rum Jungle area (Fraser, 1980) of Australia. According to Samama (1973) uranium and copper are deposited under the same weathering conditions, and it is possible that many of the stratiform copper deposits in the Khan and Rössing Formations contained syngenetic uranium prior to its mobilization during the Damaran thermal event.

In terms of both assured and estimated tonnages of uranium, sandstone-type deposits in the U.S.A., Niger and Gabon represent the largest resources in the world (Dahlkamp, 1978), and 97% of the uranium deposits in the U.S.A. are in sandstone formations (Qidwai and Jensen, 1979). The latter are predominantly stream-laid quartzose, arkosic and tuffaceous sandstone and conglomerate lenses which commonly alternate and interfinger with mudstone beds; and V, Cu and Fe are the most abundant metals accompanying the U in these terrestrial rocks (Butler and Schnabel, 1955). The presence of frequent facies variations, which inhibit the rate of movement of uranium solutions, has been emphasized by Qidwai and Jensen (1979) as a useful criteria for the recognition of a good sandstone host. The variations in lithology and thickness shown by the Rössing Formation and the interbedded nature of the sandstone, limestone and mudstone units, now represented by sequences of quartzite, marble and calc silicate, indicate that these sediments were formed in an environment which favoured the deposition of uranium.

It has been suggested that the lower part of the Damara Sequence

may correlate with the copper- and uranium-rich metasediments of the Upper Roan Supergroup of Zaire and Zambia (Nicolayson, 1962; Rich et al., 1977). The Nosib Group was probably deposited between 1060 and 900 Ma. (Kröner, 1981), whilst the lower part of the Swakop Group is characterized by ages of around 800 Ma. (Chapter VIII). Apart from an upper age limit of 888 Ma. for the Roan Supergroup (Cahen, 1974) there is little geochronological evidence for correlation, and to do so merely for lithological reasons seems hazardous.

However, the stratiform copper deposits of the lower Damara Sequence may have been deposited in a very similar environment to the stratiform copper-uranium deposits of the Shaba region described by Francois (1974).

Between about 650 and 550 Ma. the Damaran belt underwent major regional deformation (F_1 and F_2 of Coward, 1981b; and Downing and Coward, 1981), and although early mafic granitoids were emplaced locally within the belt (e.g. Palmental diorites, Kröner, 1981) the major granite forming event post-dates the major regional deformation (Hawkesworth et al., 1981a and b; Hawkesworth and Marlow, 1981).

The earlier granitoids which tend to be more mafic in character, show relatively low Sr-isotope ratios and contain chemical and mineralogical features in common with I-type granitoids. These various factors are considered to reflect derivation from the lower crust or upper mantle. In contrast, the later granitoids are normally leucocratic in nature, commonly radioactive and occasionally mineralized. They display relatively high Sr-isotope ratios, and an affinity for S-type granitoids, and they are considered to be derived from basement and Nosib source rocks.

The mineralized granitoids include both red granites and alaskites, and the primary uranium phases identified within them consist of uraninite,

betafite and metamict thorite. These minerals are considered to be primary in nature because of their intimate association with the other accessory constituents (Plates 36, 37 and 42), as well as their presence as inclusions within the major constituents (Plates 38 and 40). Also, some excellent U/Pb results on various minerals within the uraniferous alaskites from Goanikontes (Briqueu et al., 1980) show that the time of mineralization (509 ± 1 Ma) and of alaskite emplacement (508 ± 2 Ma) are not distinguishable.

A definite pattern appears to be emerging with respect to the mineralized granites and alaskites within the Damaran belt. Their intrusion is restricted to a late- to post-tectonic thermal event, whilst their initial $^{87}\text{Sr}/^{86}\text{Sr}$ ratios are characteristically high in comparison with barren granites (Fig. 38). The dramatic increase in the initial Sr-isotope ratio with time displayed by the mineralized alaskites is particularly important when one considers that the only economic body to date is that of the Rössing alaskite (Kröner and Hawkesworth, 1977), which shows the youngest age (458 ± 8 Ma), and the highest initial $^{87}\text{Sr}/^{86}\text{Sr}$ ratio (0.759) recorded from the belt. This apparent increase in the initial Sr-isotope ratio with time, shown by the mineralized alaskites, may also pertain with respect to the red granites, and economically viable red granites may have been formed during the interval 500 - 450 Ma.

Yermolayev (1973) considers that the radioelements U and Th behave differently during successive grades of metamorphism. During progressive regional metamorphism at medium grades, recrystallization results in the loss of mainly U in the initial stages, but also of Th as the grade increases. During ultrametamorphism the dispersed U and Th is mobilized to produce melts of elevated radioactivity. Finally,

during retrograde metamorphism U and Th may be concentrated or redistributed by metasomatic fluids. Yermolayev (1973) shows that the highest U and Th concentrations of a group of ultrametamorphic granitoids from the Aldan, Baltic and Ukrainian Shields occur in the youngest varieties, and this feature which also characterizes the Damaran granitoids may well be dominant in many orogenic zones where the granitoids are mainly crustally derived.

Uranium- and thorium-bearing melts produced by anatexis may crystallize in-situ, or they may undergo fractional crystallization. The Damaran alaskites display K/Rb ratios in excess of those normally seen within pegmatites derived by fractionation (Chapter IX), and although they are typically pegmatitic in texture they are not considered to have undergone extreme fractionation. Cuney (1980) suggests that the pegmatitic textures are caused by the presence of a vapour phase during the crystallization of the alaskitic magma. It is unnecessary to postulate fractionation in the Damaran alaskites because the first liquids to form during the melting of rocks should resemble the last liquid fraction of a magma and be rich in silica, potash, alumina and water as well as U and other trace elements which tend to concentrate in residual granitic fluids (Klepper and Wyant, 1956).

In consideration of the processes leading to the formation of the mineralized alaskites, a number of authors have emphasized the importance of concentrating the uraniferous melts in favourable geochemical and structural traps (Jacob, 1974b; Berning et al., 1976; Backström and Jacob, 1979; Cuney, 1980). Carbonate sequences of the Rössing and Karibib Formations clearly represent important lithological boundaries against which the mineralized alaskites are "damned up" (e.g. the Ida dome).

Also regional structures associated with F_3 or later events have had an important effect on the emplacement of mineralized alaskites such as those at Valencia 122 and Goanikontes (Chapter V). The most important physiochemical processes leading to the crystallization of a uraniferous alaskitic magma appear to be an increase in CO_2 by decarbonation reactions at marble-alaskite contacts leading to the boiling of the magma and the subsequent deposition of uranium (Cuney, 1980).

Armstrong (1974) has suggested the use of the term "porphyry" uranium deposits for late magmatic differentiates containing very low concentrations of uranium in the range 0.03-0.05% U_3O_8 , and he considers the Rössing deposit to be the type example. Although the average grade of 0.035% U_3O_8 at Rössing (Wyllie, 1979) is very low, and the mineralization processes involving boiling of the magma and unmixing into a brine and a vapour phase are similar to those operating in porphyry copper deposits (Cuney, 1980), the term is not considered to be appropriate with respect to the Damaran alaskites for two reasons. Firstly, the alaskites are typically pegmatitic in texture rather than porphyritic, and secondly they do not represent magmatic differentiates but anatectic melts derived from upper crustal levels. If a "porphyry" type uranium deposit does exist it would be more appropriately applied to mantle derived uranium deposits which have undergone enrichment by fractionation and hydrothermal activity such as the Bokan Mountain deposit described by Rogers et al. (1978).

Within the mineralized granites and alaskites a deuteric alteration has resulted in the development of secondary uranium minerals after uraninite, betafite and thorite (Chapter VI). These secondary minerals

include an unidentified uranyl silicate, thorogummite, calcliothorite, ferrothorite and uranophane. Betafite commonly exhibits a well developed zonation which is primarily the result of a variation in the elements Si, Ca and U, and the concentrations of Si and U are occasionally inversely related (Plate 39). This characteristic variability in chemistry, and the presence of secondary rims around some betafite grains (Plate 41), are considered to be caused by the deuteritic alteration. Likewise, the peculiar internal variability in the distribution of U, Th, Ca and Si in many grains of thorogummite (Plate 49), may be a direct result of recrystallization during the deuteritic stage of alteration. Cuney (1980) considers the redistribution of uranium during the deuteritic alteration of the Rössing alaskites was probably related to CO₂ and NaCl-rich fluids, and that the uraninite was formed during both the magmatic and deuteritic stages. Geochemical evidence in the form of a normal positive correlation between K and Rb (Fig. 51) indicates that the alteration has not resulted in any major geochemical readjustments within the Damaran intrusives.

Moreau (1976) has compared the leucogranitic uranium mineralizations of the western Massif Central in France, with the uraniferous alaskites at Rössing. The geological setting of the French leucogranites within a thickened sialic crust, and the anatectic origin of the mineralizing fluids are both in common with the Damaran deposits. However, major concentrations of uranium within the French leucogranites appear to be related to secondary enrichment processes involving meteoric alteration (Eulry and Vargas, 1980), and since this is not a necessary factor in the formation of the Damaran deposits, a direct comparison is not considered to be justified. However, secondary uranium minerals have developed in both mineralized and radiometrically anomalous Damaran granitoids during a recent stage of surface enrichment and secondary

alteration. The minerals formed by a process of groundwater interaction with existing primary and secondary uranium minerals, removal of the uranyl ion in solution and subsequent precipitation in the near surface environment in available cracks, interstices and pore spaces. Where groundwaters are encountered in the Namib desert, they contain a high proportion of salts, particularly sulphates and carbonates (Backström, 1970) which are effective solvents. Briquet et al. (1980) suggest that the U/Pb chronometer of the primary uranium minerals in the alaskites at Goanikontes evolved as a closed system until recent times, indicating that uranium mobilization caused by weathering processes has been active only for the last 5 Ma.

REFERENCES

- ABBEY, S. 1978. Calibration Standards. IV. Studies in standard samples for use in the general analysis of silicate rocks and minerals. Part 5: 1977 Edition of "usable" values: X-ray Spectrometry, v. 7, No. 2, pp. 99-121.
- ADAMEK, P.M., and WILSON, M.R. 1979. The evolution of a uranium province in northern Sweden: Phil. Trans. R. Soc. Lond., A, v. 291, pp. 355-368.
- AHRENDT, H., HUNZIKER, J.C. and WEBER, K. 1978. Age and degree of metamorphism and time of nappe emplacement along the southern margin of the Damara Orogen/Namibia (S.W.-Africa): Geol. Rundschau, v. 67, pp. 719-742.
- ARMSTRONG, F.C. 1974. Uranium resources of the future - "porphyry" uranium deposits, in: Formation of uranium ore deposits: Vienna, I.A.E.A., pp. 625-635.
- ARNDT, N.T., NALDRETT, A.J. and PYKE, D.R. 1977. Komatiitic and iron-rich tholeiitic lavas of Munro Township, northeast Ontario: J. Petrol., v. 18, pp. 319-369.
- BARNES, J.F.H. 1981. Some aspects of the tectonic history of the Khan-Swakop region of the Damara belt, Namibia: Unpubl. Ph.D. thesis, Univ. Leeds, 466pp.
- BARNES, J.F.H. and DOWNING, K. 1979. Origin of domes in the central Damaran belt, Namibia: Revue de Geol. Dynam. et Geog. Physique, v. 21, pp. 383-386.
- BARNES, S.J. and SAWYER, E.W. 1980. An alternative model for the Damara mobile belt: Ocean crust subduction and continental convergence: Precambrian Res., v. 13, pp. 297-336.
- BATEMAN, P.C. and DODGE, F.C.W., 1970. Variations of major chemical constituents across the central Sierra Nevada batholith: Bull. geol. Soc. Am., v. 81, pp. 409-420.
- BECKINSALE, R.D., SUENSILPONG, S., NAKAPADUNGRAT, S., and WALSH, J.N. 1979. Geochronology and geochemistry of granite magmatism in Thailand in relation to a plate tectonic model: J. geol. Soc. Lond., v. 136, pp. 529-540.
- BERNING, J., COOKE, R., HIEMSTRA, S.A. and HOFFMANN, U. 1976. The Rössing uranium deposit. South West Africa: Econ. Geol., v. 71, pp. 351-368.
- BJØRLYKKE, H., 1931. Ein betafitmineral von Tangen bei Kragero: Norsk geol. Tidsskr., v. 12, pp. 73.

- BLAXLAND, A., GOHN, E., HAACK, U. and HOFFER, E. 1979. Rb/Sr ages of late-tectonic granites in the Damara orogen, Southwest Africa/Namibia: *Neues Jahrb. Mineral. Monatsh.*, v. 11, pp. 498-508.
- BOWDEN, P., BENNET, J.N., WHITLEY, J.E. and MOYES, A.B. 1979. Rare earths in Nigerian Mesozoic granites and related rocks. In: *Origin and distribution of the elements*, Pergamon Press, pp. 479-491.
- BRIGUEU, L., LANCELOT, J.R., VALOIS, J.P. and WALGENWITZ, F. 1980. Géochronologie U-Pb et genèse d'un type de minéralisation uranifère: les alaskites de Goanikontès (Namibia) et leur encaissant. *Bull. Centre Rech. Explor. Prod. Elf-Aquitaine*, v. 4, pp. 789-811.
- BROOKS, C., JAMES, D.E. and HART, S.R. 1976. Ancient lithosphere: Its role in young continental volcanism: *Science*, v. 193, pp. 1086-1094.
- BROWN, G.C. 1979. The changing pattern of batholith emplacement during Earth history, in: Atherton, M.P. and Tarney, J. eds., *Origin of granite batholiths: Geochemical evidence*, pp. 106-115.
- BURGER, A.J., CLIFFORD, T.N. and MILLER, R. McG. 1976. Zircon U-PB ages of the Franzfontein granitic suite, northern South West Africa: *Precambrian Res.*, v. 3, pp. 415-431.
- BURKE, K., DEWEY, J.F. and KIDD, W.S.F. 1977. World distribution of sutures - the sites of former oceans: *Tectonophysics*, v. 40, pp. 69-100.
- BUTLER, A.P. Jr. and SCHNABEL, R.W. 1955. Distribution and general features of uranium occurrences in the United States. Contributions to the geology of uranium and thorium by the U.S. Geological Survey and Atomic Energy Commission for the United Nations. International Conference on peaceful uses of atomic energy, Geneva, Switzerland, 1955: U.S. Geol. Survey Prof. Paper 300, pp. 27-40.
- CAHEN, L. 1974. Geological background to the copper-bearing strata of southern Shaba (Zaire), in: Bartholomé, P. ed., *Gisements stratiformes et provinces cuprifères*, Liege, pp. 57-77.
- CANN, J.R. 1970. Rb, Sr, Y, Zr and Nb in some ocean floor basaltic rocks: *Earth Planet. Sci. Lett.*, v. 10, pp. 7-11.
- CARMICHAEL, I.S.E., 1964. The petrology of Thingmuli, a Tertiary volcano in eastern Iceland. *J. Petrol.*, v. 5, pp. 435-460.

- CARMICHAEL, I.S.E., TURNER, F.J., and VERHOOGEN, J. 1974. *Igneous Petrology*, McGraw-Hill, New York, 739 pp.
- CHAPPELL, B.W. and WHITE, A.J.R. 1974. Two contrasting granite types: *Pacific Geology*, v. 8, pp. 173-174.
- CLIFFORD, T.N. 1970. The structural framework of Africa, in: Clifford, T.N. and Gass, I.G. ed., *African magmatism and tectonics*, Oliver and Boyd, Edinburgh, pp. 1-26.
- COBBOLT, P.R., COSGROVE, J.W., and SUMMERS, J.M. 1971. Development of internal structures in deformed anisotropic rocks: *Tectonophysics*, v. 12, pp. 23-53.
- CORNER, B., and HENTHORN, D.I. 1978. Results of a palaeomagnetic survey undertaken in the Damara mobile belt, South West Africa, with special reference to the magnetization of the uraniferous pegmatitic granites: Rep. Atomic Energy Board, PEL-260, Pretoria, 28pp.
- COWARD, M.P. (1981a). The junction between Pan African mobile belts in Namibia: its structural history: *Tectonophysics*, (in press).
- COWARD, M.P. (1981b). Tectonic history of the Damara belt, in Miller, R. McG. ed., *Geodynamic evolution of the Damara orogen*. *Geol. Soc. S. Afr., Spec. Publ.*, (in press).
- COWARD, M.P. (1981c). Pan African gneiss domes, diapirs and sheath folds: *Journ. Struct. geol.*, v.3, No. 1, pp. 91.
- COX, K.G. and HORNING, G., 1966. The petrology of the Karroo basalts of Basutoland: *Am. Mineral.*, v. 51, pp. 1414-1432.
- CUNEY, M. 1980. Preliminary results on the petrology and fluid inclusions of the Rössing uraniferous alaskites. *Trans. geol. Soc. S. Afr.*, v. 83, pp. 39-45.
- DAHLKAMP, F.J. 1978. Classification of uranium deposits. *Mineral. Deposita*. v. 13, pp. 83-104.
- DAHLKAMP, F.J. 1979. Uranium occurrences in northern Saskatchewan, Canada, and their mode of origin. *Phil. Trans. R. Soc. Lond., A*, v. 291, pp. 369-384.
- DAVIES, C.S. and COWARD, M.P. 1981. The structural evolution of the Gariep arc in southern Namibia, (South West Africa): *Precambrian Res.*, (in press).
- DIXON, J.M. 1975. Finite strain and progressive deformation in models of diapiric structures: *Tectonophysics*, v. 28, pp. 89-124.

- DOWNING, K.N. and COWARD, M.P. 1981. The Okahandja Lineament and its significance in Damaran tectonics in Namibia: Geol. Rundschau, (in press).
- DOWNING, K.N. in prep. Tectonic significance of the Okahandja Lineament. Unpubl. Ph.D. thesis, Univ. Leeds, (in prep.).
- ESQUEVIN, S. and MENENDEZ, R. 1974. Age Rb/Sr des granites du permien Diana (Omakuara et Sandflats, S.W.A.). Unpubl. S.N.P.A. report for Aquitaine S.W.A., Mineral Exploration.
- EULRY, M. and VARGAS, J.M. 1980. Le rôle des altérations antéliasiques dans la métallogenèse de la périphérie du mont Lozère (France). Cas de l'uranium. In: Samama, J.C. ed., Les paléosurfaces et leur métallogenèse. pp. 15-175.
- FAUPEL, J., 1973. Geological and mineralogical investigation of the Donkerhoek-Granite, Karibib District, South West Africa: N. Jb. Geol. Palaont. Mh. pp. 327-341.
- FAURE, G. 1977. Principles of Isotope Geology: John Wiley and Sons Inc., New York, 464 pp.
- FERGUSON, J., CHAPPELL, B.W. and GOLEBY, A.B. 1980. Granitoids in the Pine Creek geosyncline: Proceedings of the International Uranium Symposium on the Pine Creek Geosyncline, I.A.E.A., Vienna, pp. 73-90.
- FLOYD, P.A., and WINCHESTER, J.A. 1975. Magma types and tectonic discrimination using immobile elements: Earth Planet. Sci. Lett., v. 27, pp. 211-218.
- FRANCOIS, A. 1974. Stratigraphie, tectonique et minéralisations dans l'arc cuprifère du shaba (République du Zaïre), in: Bartholemé, P. ed., Gisements stratiforms et provinces cuprifères, Liege, pp. 79-101.
- FRASER, W.J. 1980. Geology and exploration of the Rum Jungle uranium field: Proceedings of the International Uranium Symposium on the Pine Creek Geosyncline, I.A.E.A., Vienna, pp. 287-298.
- FRONDEL, C. 1956. Mineral composition of gummite: Am. Mineral., v. 41, pp. 539-568.
- FRONDEL, C. 1958. Systematic mineralogy of uranium and thorium: U.S.G.S., Bull. 1064, 400 pp.
- GEVERS, T.W. 1931. The fundamental complex of western Damaraland, South West Africa: Unpubl. D.Sc. thesis, Univ. Cape Town, 163 pp.
- GULSON, B.L. and MIZON, K.J. 1980. Lead isotope studies at Jabiluka: Proceedings of the International Uranium Symposium on the Pine Creek Geosyncline, I.A.E.A., Vienna, pp. 439-455.

- GUNN, B.M. 1966. Modal and element variation in Antarctic tholeiites. *Geochim. Cosmochim. Acta*, v. 30, pp. 881-920.
- HAACK, U., GOHN, E. and KLEIN, J.A. 1980. Rb/Sr ages of granitic rocks along the middle reaches of the Omaruru River and the timing of orogenic events in the Damara belt (Namibia). *Contrib. Mineral. Petrol.*, v. 74, pp. 349-360.
- HARTNADY, C.J.H. 1974. An ERTS-1 view of the southwestern part of the Damaran mobile belt. 12th ann. Rep., *Precambrian Res. Unit.*, Univ. Cape Town, pp. 60.
- HARTNADY, C.J.H. 1979. Overthrust tectonics, stratigraphic problems and metallogenesis in the Khomas Ridge Province, Damara orogenic belt. 16th ann. Rep., *Precambrian Res. Unit.*, Univ. Cape Town, pp. 73-89.
- HAWKESWORTH, C.J. 1979. $^{143}\text{Nd}/^{144}\text{Nd}$, $^{87}\text{Sr}/^{86}\text{Sr}$ and trace element characteristics of magmas along destructive plate margins, in: Atherton, M.P. and Tarney, T., eds., *Origin of granite batholiths: Geochemical evidence*, pp. 76-89.
- HAWKESWORTH, C.J. and MARLOW, A.G. 1981. Thermal evolution of the Damara high temperature belt, Namibia, in Miller, R. McG. ed., *Geodynamic evolution of the Damara orogen South West Africa/Namibia: Geol. Soc. S. Afr., Spec. Publ.*, (in press).
- HAWKESWORTH, C.J., KRAMERS, K.D. and MILLER, R. McG. 1981a. Old model Nd ages in Namibian Pan-African rocks: *Nature*, v. 289, p. 278-282.
- HAWKESWORTH, C.J., GLEDHILL, A., RODDICK, J.C., MILLER, R. McG. and KRONER, A. 1981b. Rb/Sr geochronology and its bearing on models for the thermal evolution of the Damara orogenic belt, Namibia, in: Miller, R. McG., ed., *Geodynamic evolution of the Damara Orogen: Geol. Soc. S. Afr., Spec. Publ.*, (in press).
- HEGGE, M.R., MOSHER, D.V., EUPENE, G.S. and ANTHONY, P.J. 1980. Geologic setting of the East Alligator uranium deposits and prospects: *Proceedings of the International Uranium Symposium on the Pine Creek Geosyncline, I.A.E.A., Vienna*, pp. 259-272.
- HOFFER, E. 1975. Die zeitliche Beziehung zwischen Tektogenese und Metamorphose: Ein Beitrag zur Rekonstruktion der thermischer Geschichte des Damara-Orogens, in: *Bericht des Sonderforschungsbereiches 48, Univ. Göttingen, West Germany*, pp. 170-183.

- HOFFMANN, C. 1976. Granites and migmatites of the Damara belt, South West Africa. Petrography and melting experiments: Geol. Rundschau, v. 65, pp. 939-966.
- HOGARTH, D.D. 1961. A study of pyrochlore and betafite. Canadian Mineral., v. 6, pp. 610-633.
- HOLDER, M.T. 1981. Mechanisms of emplacement of granite plutons: Unpubl. Ph.D. thesis, Leeds University, 226 pp.
- HUGO, P.J. and SCHALK, K.E.L. 1971. The isotope ages of certain granites and acid lavas in the Rehoboth and Maltahöhe districts, South West Africa: Unpubl. Repr. Ann. geol. Surv., S. Afr., v. 9, pp. 103-105.
- HURLEY, P.M., BATEMAN, P.C., FAIRBAIRN, H.W. and PINSON, W.H. Jr. 1965. Investigation of $^{87}\text{Sr}/^{86}\text{Sr}$ ratios in the Sierra Nevada plutonic province: Bull. geol. Soc. Am., v. 76, pp. 165-174.
- ISHIHARA, S. 1977. The magnetite-series and ilmenite-series granitic rocks: Ming. Geol., v. 27, pp. 293-305.
- JACOB, R.E. 1974a. Geology and metamorphic petrology of part of the Damara orogen along the lower Swakop River, South West Africa: Precambrian Res. Unit., Univ. Cape Town, Bull. 17, 201 pp.
- JACOB, R.E. 1974b. The radioactive mineralization in part of the central belt, South West Africa, and its possible origin: Atomic Energy Board, Pretoria, PIN-234 (BR), 17 pp.
- JACOB, R.E. and HAMBLETON-JONES, B.B. 1979. Geological and geochemical setting of granites in the eugeosynclinal portion of the Damara orogen, Rössing area, South West Africa: Phil. Trans. R. Soc. Lond., A, v. 291, pp. 307-319.
- JACOB, R.E., KRONER, A. and BURGER, A.J. 1978. Areal extent and first U-Pb age of the pre-Damara Abbabis complex in the central Damara belt of South West Africa (Namibia): Geol. Rundschau, v. 67, pp. 706-718.
- KENNEDY, W.Q. 1964. The structural differentiation of Africa in the Pan African (± 500 Ma) tectonic episode: 8th ann. Rep. Res. Inst. Afr. Geol., Univ. Leeds, pp. 48-49.
- KISTLER, R.W. and PETERMAN, Z.E. 1973. Variations in Sr, Rb, K, Na and initial $^{87}\text{Sr}/^{86}\text{Sr}$ in Mesozoic granitic rocks and intruded wall rocks in central California: Bull. geol. Soc. Am., v. 84, pp. 3489-3512.
- KLEPPER, M.R. and WYANT, D.G. 1956. Uranium provinces: Contributions to the geology of uranium and thorium by the U.S. Geological Survey and Atomic Energy Commission for the United Nations. International Conference on peaceful uses of atomic energy, Geneva, Switzerland, 1955: U.S. Geol. Survey Prof. Paper 300, pp. 17-25.

- KRONER, A. 1981. Rb-Sr geochronology and tectonic evolution of the Pan African Damara belt of Namibia, southwestern Africa: Amer. Jour. Sci. (in press).
- KRONER, A. and JACKSON, M.P.A. 1974. Geological reconnaissance of the coast between Luderitz and Marble Point, South West Africa, in: Kröner, A., ed., Contributions to the Precambrian geology of southern Africa: Precambrian Res. Unit, Univ. Cape Town, Bull. 15, pp. 79-103.
- KRONER, A. and HAWKESWORTH, C.J. 1977. Late Pan-African emplacement ages for the Rössing alaskitic granite (Damara belt) and the Rooi Lepel bostonite (Gariep belt) in Namibia and their significance for the timing of metamorphic events: 20th ann. Rep. Res. Inst. Afr. Geol., Univ. Leeds, pp. 14-17.
- KRONER, A. and DOPKE, H.H. Age and formation of dome structures in the central Damara belt of Namibia (South West Africa): Geol. Rundschau, (in press).
- KUNO, H. 1968. Differentiation of basalt magma, in: Hess, H.H. and Poldervaart, A., eds., Basalts: The Poldervaart Treatise on rocks of basaltic composition, v. 2, New York, Interscience, pp. 623-688.
- LISLE, R.J. 1977. Estimation of the tectonic strain ratio from the mean shape of deformed elliptical markers. Geol. Mijnb., v. 56, pt. 2, pp. 140-144.
- MACDONALD, G.A. and KATSURA, T. 1964. Chemical composition of Hawaiian Lavas: J. Petrol., v. 5, pp. 83-133.
- MACLEOD, W.N., TURNER, D.C. and WRIGHT, E.P. 1971. The geology of the Jos Plateau, Vol. 1, general geology: Bull. geol. Surv. Nigeria, No. 32, 110 pp.
- MARLOW, A.G. 1981. Geology and Rb-Sr geochronology of mineralized and anomalous granites and alaskites, Namibia, in: Miller, R. McG. ed., Geodynamic evolution of the Damara orogen: Geol. Soc. S. Afr., Spec. Publ., (in press).
- MARTIN, H. 1965. The Precambrian geology of South West Africa and Namaqualand: Precambrian Res. Unit, Univ. Cape Town, 159 pp.
- McINTYRE, G.A., BROOKS, C., COMPSTON, W. and TUREK, W. 1966. The statistical assessment of Rb-Sr isochrons: J. Geophys. Res., v. 71, pp. 5459-5468.
- MIDDLEMOST, E.A.K. 1975. The basalt clan: Earth-Sci. Rev., v. 11, pp. 337-364.

- MILLER, R. McG. 1973. The Salem granite suite: genesis by means of partial melting of the Khomas schist: Mem. 64, geol. Surv. S. Afr., 106 pp.
- MILLER, R. McG. 1980. The Okahandja Lineament, a fundamental tectonic boundary in the Damara orogen of South West Africa/Namibia: Trans. geol. Soc. S. Afr., v. 82, pp. 349-361.
- MOREAU, M. 1976. "L'uranium et les granitoids: essai d'interprétation", in: Jones, M.J. ed., geology, Mining and extractive processing of uranium. Institute of Mining and Metallurgy, Lond., pp. 83-102.
- NASH, C.R. 1971. Metamorphic petrology of the S.J. area, Swakopmund district, South West Africa: Univ. Cape Town, Precambrian Res. Unit, Bull. 9, 77 pp.
- NICOLAYSEN, L.O. 1962. Stratigraphic interpretation of age measurements in southern Africa, in: Engel, A.E.J. and Leonard, B.F., eds., Petrological Studies: A volume in honour of A.F. Buddington, pp. 569-598.
- PANKHURST, R.J. and PIDGEON, R.T. 1976. Inherited isotope systems and the source region pre-history of early Caledonian granites in the Dalradian Series of Scotland: Earth Planet. Sci. Lett., v. 31, pp. 55-68.
- PEARCE, J.A. 1975. Basalt geochemistry used to investigate post tectonic environments on Cyprus: Tectonophysics, v. 25, pp. 41-67.
- PEARCE, J.A. and CANN, J.R. 1971. Ophiolite origin investigated by discriminant analysis using Ti, Zr and Y: Earth Planet. Sci. Lett., v. 12, pp. 339-349.
- PEARCE, J.A. and CANN, J.R. 1973. Tectonic setting of basic volcanic rocks determined using trace element analyses: Earth Planet. Sci. Lett., v. 19, pp. 290-300.
- PEARCE, T.H., GORMAN, B.E., and BIRKETT, T.C. 1975. The TiO_2 - K_2O - P_2O_5 diagram: A method of discriminating between oceanic and non-oceanic basalts: Earth Planet. Sci. Lett., v. 24, pp. 419-426.
- PEARCE, J.A. and NORRY, M.J. 1979. Petrogenetic implications of Ti, Zr, Y, Nb variation in volcanic rocks: Contrib. Mineral. Petrol., v. 69, pp. 33-47.
- PLANT, J., BROWN, G.C., SIMPSON, P.R., and SMITH, R.T. 1980. Signatures of metalliferous granites in the Scottish Caledonides: Trans. Instn. Min. Metall. (Sect. B: Appl. earth sci.) v. 89, pp. 198-210.

- PORADA, H. 1979. The Damara-Ribeira orogen of the Pan African-Brasiliano cycle in Namibia (Southwest Africa) and Brazil as interpreted in terms of continental collision: *Tectonophysics*, v. 57, pp. 237-265.
- PUHAN, D. 1976. Metamorphic temperature determined by means of the dolomite-calcite solvus geothermometer - Examples from the Central Damara Orogen (South West Africa): *Contr. Mineral. Petrol.*, v. 58, pp. 23-28.
- QIDWAI, H.A. and JENSEN, M.L. 1979. Methodology and exploration for sandstone-type uranium deposits: *Mineral Deposita (Berl.)*, v. 14, pp. 137-152.
- RAGAN, D.M. 1973. *Structural geology: an introduction to geometrical techniques*. 2nd rev. ed., New York, Lond., J. Wiley and Sons, 208 pp.
- RAMSAY, J.G. 1967. *Folding and fracturing of rocks*. McGraw-Hill, 568 pp.
- RICH, R.A., HOLLAND, H.D. and PETERSON, U. 1977. Hydrothermal uranium deposits, Elsevier, Amsterdam, 264 pp.
- RODDICK, J.C. and COMPSTON, W. 1977. Strontium isotopic equilibration: A solution to a paradox: *Earth Planet. Sci. Lett.*, v. 34, pp. 238-246.
- ROGERS, J.J.W., RAGLAND, P.C., NISHIMORI, R.K., GREENBERG, J.K. and HAUCK, S.W. 1978. Varieties of granitic uranium deposits and favourable exploration areas in the eastern United States: *Econ. Geol.* v. 73, pp. 1539-1555.
- ROSHOLT, J.N. and BARTEL, A.J. 1969. Uranium, thorium and lead systematics in Granite Mountains, Wyoming: *Earth Planet. Sci. Lett.*, v. 7, pp. 141-147.
- ROSS, C.S., HENDERSON, E.P. and POSNJAK, E. 1931. Clarkeite: a new uranium mineral: *Am. Mineral.*, v. 16, pp. 213-220.
- RUXTON, P. 1981. Sedimentation and diagenesis of Cu-bearing rocks of the southern margin of the Damara orogenic belt of Namibia and Botswana, Ph.D. thesis, Univ. Leeds. (in prep.).
- SAMAMA, J.C. 1973. Ore deposits and continental weathering. A contribution to the problem of geochemical inheritance of heavy metal contents of basement areas and of sedimentary basins, in: Amstutz, G.C. and Bernard, A.J., ed., *Ores in sediments*, Springer-Verlag, pp. 247-265.
- SAWYER, E.W. 1978. Damaran structural and metamorphic geology of an area south-east of Walvis Bay, South West Africa/Namibia, unpubl. M.Sc. thesis, Univ. Cape Town, 205 pp.

- SHAW, D.M. 1968. A review of K-Rb fractionation trends by covariance analysis. *Geochim. Cosmochim. Acta*, v. 32, pp. 573-601.
- SIMPSON, P.R., BROWN, G.C., PLANT, J., and OSTLE, D. 1979. Uranium mineralization and granite magmatism in the British Isles: *Phil. Trans. R. Soc. Lond., A.*, v. 291, pp. 385-412.
- SMITH, D.A.M. 1965. The geology of the area around the Khan and Swakop Rivers in South West Africa: *Geol. Surv. S. Afr.*, Memoir 3 (South West Africa series), 113 pp.
- SMITH, D.A.M. 1966. Geological map 2215A - Ebony and 2215B - Usakos: *Geol. Surv. S. Afr.*
- SNELLING, A.A. 1980. Uraninite and its alteration products, Koongarra uranium deposit: *Proceedings of the International Uranium Symposium on the Pine Creek Geosyncline, I.A.E.A., Vienna*, pp. 487-498.
- SOUTH AFRICAN COMMITTEE FOR STRATIGRAPHY (S.A.C.S.) 1980. The Damara Sequence, in Kent, L.E., *Compl., Stratigraphy of Southern Africa. I. Lithostratigraphy of South Africa, South West Africa/Namibia and the Republics of Bophuthatswana, Transkei and Venda*, *Handb. geol. Surv. S. Afr.*, 8.
- STACEY, J.S. and STERN, T.W. 1972. Revised tables for the calculation of lead isotope ages: *Natl. Tech. Information Service, Springfield, Virginia 22151, U.S.A.*, 35pp.
- STACEY, J.S. and KRAMERS, J.D. 1975. Approximation of terrestrial lead isotope evolution by a two-stage model: *Earth Planet. Sci. Lett.*, v. 26, pp. 207-221.
- STACKELBERG, M. von and ROTTENBACH, E. 1940. Dichte und struktur des zirkons, III und IV: *Zeitschr Kristallographie*, v. 97, pp. 173-182.
- STEIGER, R.H. and JAGER, E. 1977. Subcommittee on geochronology: Convention on the use of decay constants in geo- and cosmochronology: *Earth Planet. Sci. Lett.*, v. 36, pp. 359-362.
- STEINNES, E. 1971. Epithermal neutron activation analysis of geological material, in: Branfelt, A.O. and Steinnes, E., eds., *Activation Analysis in Geochemistry and Cosmochemistry*, pp. 113-128.
- STEMPROK, M. 1963. Distribution of Sn-W-Mo formation deposits around granites, in: *Symp. Problems of post-magmatic ore deposition, Prague*, v. 1, pp. 69-72.

- STEMPROK, M. 1979. Mineralized granites and their origin: Episodes, No. 3, pp. 20-24.
- STEMPROK, M. and SKVOR, P. 1974. Composition of tin-bearing granites from the Krusne Hory metallogenic province of Czechoslovakia: Sb. Geol. Ved., Loziskova Geol., Mineral, v. 16, pp. 7-87.
- STEPHANSSON, O. and JOHNSON, K. 1976. Granite diapirism in the Rum Jungle area, northern Australia: Precambrian Res., v. 3, pp. 159-185.
- STUCKLESS, J.S. 1977. A synthesis of uranium related studies in the Precambrian rocks of the Granite Mountains of Wyoming, in: NURE, Uranium Geol. Symp. Grand Junction, pp. 125-133.
- TAYLOR, H.P. and FORRESTER, R.W. 1971. Low ¹⁸O igneous rocks from intrusive complexes of Skye, Mull and Ardnamurchan, Western Scotland: J. Petrol, v. 12, pp. 465-497.
- TAYLOR, S.R. 1965. The application of trace element data to problems in petrology: Phys. Chem. Earth, v. 6, pp. 133-213.
- TOENS, P.D., OSTHUYZEN, E.J., JACOB, R.E., BRITS, R.J.N., HAMBLETON-JONES, B.B. and SMIT, M.C.B. 1979. A mineralogical, petrological and geochemical study of a suite of rocks from the Damara orogenic belt, South West Africa: Rep. Atomic Energy Board, PEL-269, Pretoria, 31 pp.
- TUTTLE, O.F. and BOWEN, N.L. 1958. Origin of granite in the light of experimental studies in the system NaAlSi₃O₈-KAlSi₃O₈-SiO₂-H₂O: Mem. geol. Soc. Am., v. 74, 153 pp.
- VALOIS, J.P. and WALGENWITZ, F. 1979. Pétrographie des alaskites de la série métamorphique de Goanikontes, Namibie: Bull. Cent. Rech. Explor. Prod. Elf-Aquitaine, v. 3, pp. 351-367.
- VIDAL, P., DOSSO, L., BOWDEN, P. and LAMEYRE, J. 1979. Strontium isotope geochemistry in syenite-alkaline granite complexes: Physics Chem. Earth, v. 11, pp. 223-321.
- VILJOEN, M.J. and VILJOEN, R.P. 1969. The geology and geochemistry of the lower ultramafic unit of the Onverwacht Group and a proposed new class of igneous rock: Upper Mantle Project: Spec. Publ. Geol. Soc. S. Afr., 2, pp. 221-244.
- VON BACKSTROM, J.W. 1970. The Rössing uranium deposit near Swakopmund, South West Africa. A preliminary report: Panel proceed, 13-17 April, 1970, Uranium Exploration Geology. I.A.E.A. Vienna, pp. 143-150.

- VON BACKSTROM, J.W. and JACOB, R.E. 1979. Uranium in South Africa and South West Africa (Namibia): *Phil. Trans. R. Soc. Lond., A.* v. 291, pp. 307-319.
- WAGER, L.R. 1960. The major element variation of the layered series of the Skaergaard intrusion: *J. Petrol.*, v. 1, pp. 364-398.
- WATTERS, B.R. 1974. Stratigraphy, igneous petrology and evolution of the Sinclair Group in southern South West Africa: *Precambrian Res. Unit, Univ. Cape Town, Bull.* 16, 235 pp.
- WATTERS, B.R. 1976. Possible late Precambrian subduction zone in South West Africa: *Nature*, v. 259, pp. 471-473.
- WATTERS, B.R. 1978. Petrogenesis of the felsic rock units of the late-Precambrian Sinclair Group, South West Africa: *Geol. Rundschau*, v. 67, pp. 743-773.
- WYLLIE, R.J.M. 1979. Rössing uranium reaches rated production: *World Mining*, January, pp. 43-52.
- YAKOWITZ, H., MYKLEBUST, R.L. and HEINRICH, K.F.J. 1973. "FRAME" an on-line correction procedure for quantitative electron probe microanalysis: *Nat. Bureau Stnds.*
- YERMOLAYEV, N.P. 1973. Uranium and thorium in regional and contact metamorphism. *Geochem. Int.*, v. 10, No. 2, pp. 418-423.
- YORK, D. 1969. Least-squares fitting of a straight line with correlation errors: *Earth Planet. Sci. Lett.*, v. 5, pp. 320-324.

APPENDIX 1. ANALYTICAL TECHNIQUES AND LABORATORY PROCEDURES1A. Preparation of whole rock samples

Whole rock samples weighing between 10 and 15 kg were broken down by jaw crusher until a size of $< 0.5\text{cm}$ was reached. The sample was then halved several times with a riffle splitter to obtain a representative sample of about 100 - 150 g. This was then ground further with the jaw crusher until the whole sample passed through a -30 sieve. Between each sample the jaw crushers were cleaned with a wire brush, compressed air and acetone soaked cloth.

Samples were then ground in an agate barrel Tema grinder to -100 mesh powder for about five minutes, or longer if necessary, until the powder felt completely smooth and homogeneous.

1B. Preparation of whole rock powders for mass spectrometry

- 1) Accurately weigh about 0.2 g of the -100 mesh powder into a 30 ml Teflon beaker, moisten with quartz distilled water, add 8 - 10 ml of 40% HF and 2 ml conc. HNO_3 ;
- 2) leave for at least two hours;
- 3) evaporate to dryness under IR lamps;
- 4) add 2 ml conc. HNO_3 and re-evaporate;
- 5) add 6 - 8 ml of 6 M HCl and re-evaporate;
- 6) dissolve in 3 - 4 ml of 2.5 M HCl, and transfer to centrifuge tube and centrifuge for a few minutes;
- 7) load clean ion-exchange column with 1 ml of sample solution and let it soak the resin;
- 8) wash column with two lots of 1 ml each of 2.5 M HCl;
- 9) wash column with 45 ml of 2.5 M HCl to remove unwanted elements;
- 10) elute Sr with 12 ml of 2.5 M HCl collecting in the cleaned Teflon beaker;
- 11) evaporate to dryness, or if sample is to be stored, transfer solution into a quartz micro-beaker and then complete the evaporation;
- 12) clean a Ta filament

(single filament bead) by outgassing in a vacuum chamber, applying DC at 5A for 5 minutes at $< 2.10^{-5}$ torr; 13) insert filament in a DC circuit, load filament centre with a microdrop of 1 M H_2PO_5 , apply DC of 1.15A until acid is almost evaporated; 14) dissolve Sr salt residue in quartz distilled water and load filament centre with a microdrop of sample solution; 15) evaporate by gently applying DC current.

The bead is then ready to be mounted in the turret to be placed in the source chamber of the mass spectrometer.

1C. Preparation of sulphide samples for mass spectrometry

(i) Galena

Outside Pb-free laboratory: 1) Remove a small grain of galena from sample, place in clean 25 ml pyrex beaker, add 10 ml of 6 M S.B. HCl and place on hot plate for 2 hours at 250° until dry; 2) Remove from hot plate, add 20 ml of 2.5 M S.B. HCl and leave to dissolve; 3) Pour sample away into sink, discarding 90% of solution to reduce quantity of Pb; 4) Cover beaker with parafilm for transport to Pb-free laboratory.

Inside the Pb-free laboratory: 5) Remove parafilm from beaker and dry sample on hot plate; 6) Add 2 or 3 drops of $HClO_4$ to beaker, then add just enough distilled water to cover bottom of beaker, remove from hot plate before sample is totally dry, i.e. before smoking stops; 7) Add 10 ml of distilled water to sample beaker, wait a few minutes and pour sample into clean electro-deposition teflon cell, then fix on the top of the cell and place over electromagnetic separator; 8) After 5 - 20 minutes Pb-oxide will be taken up by the anode turning it black. (If no black deposit appears on the anode after 20 minutes,

put the solution back into the sample beaker, add a few drops of HClO_4 and place on hot plate to dryness, then repeat steps 6) and 7); 9) Draw a drop of $\text{HNO}_3 - \text{H}_2\text{O}_2$ solution into a pipette, run it over the anode to take up the Pb and blow sample solution out of pipette into a clean teflon microbeaker, and dry on hot plate; 10) clean a Re filament (single filament bead) by outgassing in a vacuum chamber, applying DC at 5A for 5 minutes at $< 2.10^{-5}$ torr; 11) Place a drop of H_3PO_4 on top of sample in the teflon microbeaker; 12) insert Re filament in a DC circuit, load filament centre with a drop of silica gel, apply current of 0.9A and wait until dry; 13) load filament centre with a drop of sample solution and apply current of 1.6A, followed by 2.4A, followed by 3.0A.

The bead is then ready to be mounted in the turret to be placed in the source chamber of the mass spectrometer.

(ii) Chalcopyrite, bornite and chalcocite

Outside Pb-free laboratory: 1) Remove a small grain of sulphide from sample, place about 100 mg into a clean 25 ml pyrex beaker and wash by adding 5 ml of acetone, 5 ml of HCl and 10 ml of water; 2) Place on hot plate for a few minutes, then pour away and wash again with water; 3) Dissolve sample in solution of 6 M HCl and HNO_3 (ratio 3:1) over hot plate until dry; 4) Remove from hot plate, add a microbeaker ($\frac{3}{4}$ full) of bromic acid and leave for 2 - 3 hours until sample goes into solution; 5) Put a micro-beaker ($\frac{3}{4}$ full) of bromic acid through ion-exchange column to condition resin; 6) pass sample solution through column, and wash sample beaker after removing the residue; 7) When sample solution has passed through the column, add a solution of bromic acid and distilled water (ratio 1:1) to flush through any unwanted material, then pass through 2 ml of 3 M HCl;

8) Place clean sample beakers under ion exchange column and take off Pb by passing through 6 M HCl, then dry on hot plate; 9) go to step 5 in galena procedure.

1D. Mass spectrometry analysis

Isotopic measurements were made on a VG-Micromass 30 mass spectrometer equipped with a 30cm radius, 90° - sector analyser and Faraday collector. Filament current: 2.2A for Pb measurements and 2.8A for Sr measurements; electromagnetic field : 3.5 Gauss for Pb and 2.0 Gauss for Sr; magnetic current peak switching, delay time : 1.5 seconds; counting time : 1.1 seconds; vacuum : source $< 5 \cdot 10^{-7}$ torr; analyser collector $< 2 \cdot 10^{-8}$ torr; on-line Digico Micro 16V computer for collection and reduction of data produced on a teletype.

In the case of Sr samples, measurements were made at 88 mass units (m.u.) (peak), 87.5 m.u. (intended for correction of tailing effects from ^{87}Sr), 87 m.u. (peak), 86 m.u. (peak), 85 m.u. (intended for checking possible interference from ^{85}Rb), and 84.5 m.u. (background). Rb was usually absent, but when it was present, interference of ^{87}Rb on ^{87}Sr was corrected assuming $^{87}\text{Rb}/^{85}\text{Rb} = 0.3815$, the amount of ^{87}Rb being expressed as a % of ^{87}Sr . The analytical results are shown in Appendix 4, the error on the $^{87}\text{Rb}/^{86}\text{Sr}$ ratio being $\pm 2\%$ (2 σ), and that on the $^{87}\text{Sr}/^{86}\text{Sr}$ ratio being quoted as two standard errors of the mean. The average of six analyses made on the NBS 987 Sr standard during the course of the study was 0.71023 ± 2 (1 σ).

In the case of Pb samples, measurements were made at 208 m.u. (peak), 207 m.u. (peak), 206 m.u. (peak), 204.5 m.u. (intended for correction of tail contribution to ^{204}Pb), and 203.5 m.u. (background). The analytical results are shown in Table 16, the errors (2 σ) being

quoted to three decimal places. The average of 7 analyses of the SRM 981 Pb standard during the course of this study was: $^{207}\text{Pb}/^{206}\text{Pb} = 0.9150 \pm 4 (2 \sigma)$; $^{206}\text{Pb}/^{204}\text{Pb} = 16.95 \pm 1 (2 \sigma)$; $^{208}\text{Pb}/^{206}\text{Pb} = 2.168 \pm 1 (2 \sigma)$.

IE. Isochron Fitting

Isochrons were fitted using a combination of the techniques given by Macintyre et al. (1966) and York (1969), and ages were calculated using a decay constant of $1.42 \times 10^{-11} \text{ yr}^{-1}$ (Steiger and Jäger, 1977). Three models were tested to find the best fit. One allowed the x co-ordinate to vary and not the y, the second allowed the y co-ordinate to vary and not the x, and the third model allowed both to vary. The third model normally gave the best fit.

IF. Preparation of fusion discs for major element analysis

A quantity of 0.4 g of rock powder and 2.6 g of dehydrated Spectroflux 110 Johnson Matthey Ltd., London (Li tetraborate based) are accurately weighed and transferred into a Au-Pt crucible. The mixture is carefully stirred then melted in a furnace (1000°C for about $\frac{1}{2}$ hour), and subsequently cooled on a refractory slab, and an aluminium heat sink. The mixture is re-weighed and made up to its initial weight with flux. Re-melt gently over Meker burner and transfer on to refractory triangle over Amal burner at full blast. Stir melt briefly at intervals with Pt wire. When melt is uniform in aspect and moves freely inside the crucible, it is given a final stir and quickly poured out into the middle of a copper wire ring standing on a stainless steel hot plate. The melt is immediately pressed down with the flat surface of an aluminium cylinder and a disc is obtained, which is kept in a numbered polythene zip fastened bag.

1G. Preparation of pellets for analysis of Rb and Sr

Weigh 7 g of -100 mesh rock powder and mix well in agate mortar with a few drops of Moviol organic binder. Transfer into hardened steel mould and, using a hydraulic press exert pressure (about 330 kg/cm^2) for a few minutes. Release pressure gently. Allow pellet (normally 4mm thick and 30mm in diameter) to dry in an oven at 110°C .

1H. X-ray fluorescence spectrometry analysis

The instrument used was a Philips PW 1212 automatic spectrometer. For all the calibrations described below computer programmes devised in Leeds correct for instrument drift, a standard being always present to monitor this.

(i) Standard analytical conditions for major elements

X-ray power : 36kV, 44mA; Ag tube; gas flow proportional counter; vacuum path ($\approx 5.10^{-1}$ torr); spinner on; analysis lines K_α except for Fe (K_β). Specific conditions of operation for each element given in Table 1/1.

(ii) Standard analytical conditions for Rb and Sr

X-ray power : 80kV, 24mA; Mo tube; scintillation counter; vacuum path; spinner on; analysis lines K_α ; coarse collimator; discriminator : Base Line 10; window : 26; counting times : 100 seconds (peak), 40 seconds (background); LiF 220 analysing crystal. The precision of the results shown in Appendix 4 was found to be $\pm 1.5\%$ (2σ). The average values obtained on USGS and NIM standards during the course of this study, compared with values quoted by Abbey (1978) are given in Table 1/2. For geochronological purposes the Rb/Sr ratios obtained from this technique were converted to $^{87}\text{Rb}/^{86}\text{Sr}$ by taking into account the $^{87}\text{Sr}/^{86}\text{Sr}$ ratio of the sample.

TABLE 1/1 - Specific analytical conditions in XRF major element analysis

	Si	Ti	Al	Fe	Mn	Mg	Ca	K	Na	P
Collimator	F	F	C	F	F	C	F	F	C	F
Analysing crystal	2	1	2	1	1	2	1	1	2	2
Discriminator	E	A	A	B	B	A	A	A	A	B
Counting time (seconds)	40	10	40	10	10	100	10	10	100	40

F - Fine : 160 μ spacing
 C - Coarse : 480 μ spacing
 1 - LiF 200
 2 - TLAp
 A - Base Line : 28; Window : 40
 B - Base Line : 30.5; Window : 35
 E - Base Line : 20; Window : 48

TABLE 1/2

Average Rb and Sr values obtained on U.S.G.S. and N.I.M. standards
(values in ppm)

<u>Sample Number</u>	<u>G2</u>	<u>GSP</u>	<u>AGV</u>	<u>BCR</u>	<u>NIM-G</u>	<u>NIM-N</u>	<u>NIM-S</u>
Average Rb obtained	170	255	67	47	325	3	540
Standard Rb value	170	250	67	47	330	5	550
Average Sr obtained	481	230	668	335	8	261	61
Standard Sr value	480	230	660	330	10	260	64

(iii) Standard analytical conditions for Cr, Co, Ni, Zn, Y, Zr and Ba

X-ray power : 80kV, 18mA for Zn, Y, Zr and Ba; 60kV, 24mA for Cr, Co and Ni; Ag tube for Cr, Co, Ni, Zn and Zr; W tube for Y and Ba; all on scintillation counter except for Cr (gas flow proportional counter); vacuum path; spinner on; analysis lines K_{α} except for Zr (K_{β}); fine collimator; discriminator: Base Line 30; Window 40; counting times : 100 seconds (peak), 40 seconds (background); all on LiF 100 analysing crystal except Ba (LiF 110).

II. Epithermal neutron activation analysis

Analysis of U, Th and Sm was carried out at the Open University by epithermal neutron activation. Powdered rock samples (0.3 g each) are sealed in polythene capsules and irradiated in batches of 10 at the University of London Reactor Centre, Ascot. Each sample is separated by an iron foil used to measure the neutron flux variation between the irradiation standard (Ailsa Craig microgranite) and unknowns. After irradiating in an epithermal flux of approximately 10^9 neutrons $\text{cm}^{-2} \text{sec}^{-1}$ for 25 to 30 hours, samples are allowed to 'cool' down for a further week in order to allow the intense short half-life activity due to Al, Na and Mn to decay away.

Samples are immediately returned to the Open University where U, Th and Sm are determined by measuring the 90 - 110 KeV spectrum on the LEPS (low energy photon spectrometer) detector for 3000 seconds for each sample in a batch sequentially. Spectral data is recorded on paper tape, and peak areas are compared with those of the Ailsa Craig standard (U = 4.36 ppm, Th = 17.1 ppm, Sm = 25.1 ppm). For further details concerning epithermal neutron activation the reader is referred to Steinnes (1971).

APPENDIX 2. CONTOUR FIGURES FOR THE STEREOGRAMS SHOWN IN

FIGURES 15, 17, 18, 19 AND 20.

(CONTOUR FIGURES REFER TO PERCENTAGES PER 1% AREA)

<u>Fig.</u>	<u>Stereogram No.</u>	<u>n</u>	<u>Contours</u>
15	1	24	1, 8, 15, 22
"	2	18	1, 10, 19, 28
"	3	165	1, 6, 11, 16
"	4	121	1, 6, 11, 16
"	5	46	1, 6, 11, 16
"	6	36	1, 7, 13, 19
17	1	57	1, 6, 11, 16
"	5	50	1, 4, 7, 10
"	6	36	1, 7, 13, 19
"	7	57	1, 5, 9, 13
"	8	73	1, 5, 9, 13
"	9	248	0.5, 2, 3, 4
18	4	264	0.5, 2, 3, 4
"	5	29	1, 8, 15, 22
"	6	150	0.5, 4, 8, 11
"	7	93	1, 5, 9, 13
"	9	52	1, 5, 9, 13
"	10	89	1, 3, 5, 9
"	12	34	1, 5, 9, 13
19	1	104	1, 4, 7, 10
"	2	73	1, 3, 5, 7
"	3	14	1, 11, 21, 31
"	4	118	1, 5, 9, 13
"	5	48	1, 4, 7, 10
"	7	124	1, 3, 5, 7
20	1	60	1, 5, 9, 13
"	2	29	1, 4, 7, 10
"	3	152	0.5, 4, 8, 12

APPENDIX 3. PARTIAL ANALYSES OF THE URANIUM MINERALS

(0.0. indicates not present; - indicates not analysed)

3A. Uraninite

	<u>504 A</u>	<u>588 D</u>	<u>588 B1</u>	<u>122 A1</u>	<u>588 B2</u>	<u>588 Y</u>
ThO ₂	6.1	6.7	6.4	9.9	16.5	5.7
U ₃ O ₈	86.1	80.6	79.7	68.4	54.4	73.7
K ₂ O	-	-	-	0.3	-	0.2
CaO	0.2	0.6	0.7	1.3	0.8	0.8
TiO ₂	0.2	0.2	0.2	0.1	-	0.1
PbO	10.2	9.8	9.7	6.5	2.6	16.2
Fe ₂ O ₃ (t)	-	-	-	0.1	-	0.1
Al ₂ O ₃	-	-	-	0.3	-	0.2
SiO ₂	0.4	0.4	0.4	4.5	7.4	0.6
ZrO ₂	1.2	1.1	1.2	0.9	0.1	0.9
Total	104.4	99.4	98.3	92.3	81.8	98.5
U/Th	14.1	12.0	3.1	6.9	3.3	12.9
	<u>588 X</u>	<u>123 X</u>	<u>09 B</u>	<u>504 B</u>	<u>504 F1</u>	<u>484 A</u>
ThO ₂	5.7	6.3	4.9	3.9	7.9	1.2
U ₃ O ₈	70.0	76.7	77.0	89.2	82.9	77.5
K ₂ O	0.2	0.4	0.2	0.1	0.1	0.3
CaO	0.7	0.7	0.4	0.3	0.4	0.7
TiO ₂	0.1	0.0	0.1	0.0	0.0	0.0
PbO	8.0	4.5	9.2	6.7	6.3	7.6
Fe ₂ O ₃ (t)	0.1	0.1	0.1	0.0	0.0	3.1
Al ₂ O ₃	0.3	0.1	0.1	0.0	0.1	0.0
SiO ₂	0.8	0.3	0.4	0.2	0.1	0.1
ZrO ₂	0.9	1.0	0.8	0.5	0.5	0.5
Total	86.8	90.1	93.2	100.9	98.3	90.0
U/Th	12.3	12.2	15.7	22.9	10.5	64.6

APPENDIX 3A CONTINUED

	<u>576 D1</u>	<u>576 D2</u>	<u>576 D3</u>	<u>576 D4</u>	<u>588 E</u>	<u>523 B</u>
ThO ₂	5.9	5.5	5.4	5.2	5.9	4.8
U ₃ O ₈	71.7	73.9	72.1	76.1	64.7	56.0
K ₂ O	-	-	-	-	-	-
CaO	0.5	0.8	0.2	0.4	0.8	0.2
TiO ₂	-	-	-	-	-	-
PbO	6.7	6.8	8.5	7.0	4.1	3.5
Fe ₂ O ₃ (t)	-	-	-	-	-	0.0
Al ₂ O ₃	-	-	-	-	-	-
SiO ₂	0.2	0.1	0.2	0.1	4.8	0.0
ZrO ₂	0.2	0.1	0.3	0.3	0.2	-
Total	85.2	87.2	86.7	89.1	80.5	64.5
U/Th	12.2	13.4	13.4	14.6	11.0	11.7
	<u>574 E1</u>	<u>574 E2</u>	<u>574 E3</u>	<u>574 E4</u>	<u>574 E5</u>	
ThO ₂	6.1	6.7	6.1	6.5	6.4	
U ₃ O ₈	56.6	57.5	59.7	59.5	60.0	
K ₂ O	-	-	-	-	-	
CaO	0.4	0.1	0.2	0.2	0.2	
TiO ₂	-	-	-	-	-	
PbO	4.5	4.4	4.5	4.6	4.3	
Fe ₂ O ₃ (t)	0.0	0.0	0.0	0.0	0.0	
Al ₂ O ₃	-	-	-	-	-	
SiO ₂	0.1	0.0	0.0	0.0	0.0	
ZrO ₂	-	-	-	-	-	
Total	67.7	68.7	70.5	70.8	70.9	
U/Th	9.3	8.6	9.8	9.2	9.4	

APPENDIX 3A CONTINUED

504 A	Alaskite drill core, Valencia 122
588 D	Alaskite, Rössing
588 B1	" "
122 A1	" "
588 B2	" "
588 Y	" "
588 X	" "
123 X	" "
09 B	Red granite, Otjua 37
504 B	Alaskite drill core, Valencia 122
504 F1	" " "
484 A	Pyroxenite, Breytenbach copper prospect, Namibfontein 91
576 D1	Lower biotite-cordierite gneiss unit of Rössing Formation, Rössing.
576 D2	" " " " "
576 D3	" " " " "
576 D4	" " " " "
588 E	Alaskite, Rössing
523 B	Alaskite drill core, Valencia 122
574 E1	Alaskite, Rössing
574 E2	" "
574 E3	" "
574 E4	" "
574 E5	" "

3B. Betafite

	<u>579 A</u>	<u>G7 F1</u>	<u>G7 F2</u>	<u>G7 F3</u>	<u>G7 F4</u>	<u>G6 D1</u>
ThO ₂	3.0	1.7	2.0	2.3	2.6	1.1
U ₃ O ₈	18.6	28.9	28.4	25.0	27.9	33.6
CaO	1.4	13.0	12.7	5.1	5.1	0.0
TiO ₂	22.0	17.4	17.5	15.3	11.5	14.9
PbO	1.6	0.0	-	-	-	-
Fe ₂ O ₃ (t)	2.8	1.4	1.3	0.7	0.7	0.6
Al ₂ O ₃	0.0	0.1	0.1	0.3	0.3	0.3
SiO ₂	0.0	0.0	0.0	9.0	12.0	9.4
ZrO ₂	0.0	0.0	0.0	0.0	0.0	0.3
Nb ₂ O ₅	26.7	24.1	23.3	21.1	17.8	14.8
Ta ₂ O ₅	2.6	10.0	8.4	10.6	10.8	8.6
WO ₃	1.6	1.5	1.3	0.2	0.1	0.4
Total	80.3	98.1	95.0	89.6	88.8	84.0
U/Th	6.2	17.0	14.2	10.9	10.7	30.6
Nb/Ta	10.3	2.4	2.8	2.0	1.7	1.7
	<u>G6 D2</u>	<u>G6 A</u>	<u>522 A1</u>	<u>522 A2</u>	<u>522 A3</u>	<u>522 A4</u>
ThO ₂	0.3	0.2	0.3	0.2	0.2	0.2
U ₃ O ₈	53.1	32.4	33.4	34.1	33.4	31.7
CaO	0.0	0.2	11.8	6.6	18.3	16.8
TiO ₂	8.1	18.3	22.1	20.0	22.6	23.9
PbO	-	-	-	-	-	-
Fe ₂ O ₃ (t)	0.7	1.1	-	-	-	-
Al ₂ O ₃	0.2	0.1	-	-	-	-
SiO ₂	5.6	1.5	2.3	6.0	0.1	1.2
ZrO ₂	0.3	0.5	0.5	0.6	0.3	0.3
Nb ₂ O ₅	16.8	22.5	18.0	18.6	17.0	15.4
Ta ₂ O ₅	2.5	9.7	6.0	5.4	5.9	3.1
WO ₃	0.8	0.7	3.1	3.2	3.5	4.8
Total	88.4	87.2	97.5	94.7	101.3	97.4
U/Th	177.0	162.0	111.3	170.5	167.0	158.5
Nb/Ta	6.7	2.3	3.0	3.4	2.9	5.0

APPENDIX 3B CONTINUED

	<u>522 A5</u>	<u>522 A6</u>	<u>123 A1</u>	<u>123 A3</u>	<u>123 A4</u>
ThO ₂	0.2	0.2	0.6	0.6	0.7
U ₃ O ₈	33.2	30.0	32.7	30.4	28.9
CaO	16.7	8.2	13.0	9.5	6.8
TiO ₂	22.8	21.9	18.9	15.3	17.5
PbO	-	-	-	-	-
Fe ₂ O ₃ (t)	-	-	-	-	-
Al ₂ O ₃	-	-	-	-	-
SiO ₂	1.0	6.5	0.1	0.1	1.2
ZrO ₂	0.3	0.3	0.2	0.3	0.2
Nb ₂ O ₅	18.3	20.6	24.4	27.6	25.6
Ta ₂ O ₅	5.8	5.4	3.5	3.9	3.6
WO ₃	3.2	2.5	3.6	3.6	3.9
Total	101.5	95.6	97.0	91.3	88.4
U/Th	166.0	150.0	54.5	50.7	41.3
Nb/Ta	3.2	3.8	7.0	7.0	7.1

579 A Lower biotite-cordierite gneiss unit of Rössing Formation, Rössing
G7 F1 Alaskite, Goanikontes

G7 F2 " "
G7 F3 " "
G7 F4 " "
G6 D1 " "
G6 D2 " "
G6 A " "

522 A1 Calc silicate of Rössing Formation, Valencia 122

522 A2 " " "
522 A3 " " "
522 A4 " " "
522 A5 " " "
522 A6 " " "

123 A1 Alaskite, Rössing

123 A3 " "
123 A4 " "

3C. Metamict thorite

	<u>504 D</u>	<u>123 A</u>
ThO ₂	47.3	58.9
U ₃ O ₈	6.0	20.3
K ₂ O	-	0.1
CaO	0.9	2.1
TiO ₂	0.0	0.0
PbO	1.6	0.9
Fe ₂ O ₃ (t)	-	0.1
Al ₂ O ₃	-	0.1
SiO ₂	9.6	12.8
ZrO ₂	0.5	0.9
Total	65.9	96.2

504 D Alaskite drill core, Valencia 122

123 A Alaskite, Rössing

3D. Uranyl silicate

	<u>09 A</u>	<u>09 C</u>	<u>09 D</u>	<u>09 F</u>	<u>09 X</u>	<u>504 B</u>
ThO ₂	11.84	3.03	18.46	28.23	11.08	15.14
U ₃ O ₈	47.05	67.99	53.17	42.32	63.15	56.37
K ₂ O	0.89	1.22	1.53	0.74	1.85	-
CaO	1.74	1.72	1.59	5.93	1.49	0.41
TiO ₂	0.00	0.00	0.00	0.00	0.00	0.14
PbO	0.43	0.00	0.54	0.50	0.34	4.28
Fe ₂ O ₃ (t)	0.67	0.48	0.33	1.36	0.14	-
Al ₂ O ₃	0.24	0.16	0.11	0.19	0.15	-
SiO ₂	9.61	13.09	12.08	15.09	12.12	9.71
ZrO ₂	2.41	0.86	0.41	0.80	0.65	1.00
Total	74.89	88.55	88.22	95.15	90.97	87.05

APPENDIX 3D CONTINUED

	<u>504 C</u>	<u>504 F2</u>	<u>121 A</u>	<u>121 Y</u>	<u>122 A3</u>	<u>122 A2</u>	<u>122 B1</u>
ThO ₂	27.3	0.5	3.9	29.6	13.8	16.5	12.4
U ₃ O ₈	43.0	69.4	71.1	34.4	56.1	57.2	48.5
K ₂ O	-	-	0.3	0.2	0.3	0.3	0.1
CaO	3.3	8.3	6.4	2.8	3.6	3.0	4.6
TiO ₂	0.1	0.1	0.1	0.0	0.1	0.1	0.1
PbO	2.6	5.0	1.4	1.3	2.4	3.7	2.3
Fe ₂ O ₃ (t)	-	-	0.3	0.1	0.1	0.1	0.1
Al ₂ O ₃	-	-	0.2	0.1	0.5	1.0	0.2
SiO ₂	13.5	13.5	14.6	10.8	13.5	8.1	14.4
ZrO ₂	1.1	1.2	1.1	0.7	0.7	1.1	2.1
Total	90.9	98.0	99.4	80.0	91.1	91.1	84.8

09 A Red granite, Otjua 37

09 C " "

09 D " "

09 F " "

09 X " "

504 B Alaskite drill core, Valencia 122

504 C " " "

504 F2 " " "

121 A Alaskite, Rössing

121 Y " "

122 A2 " "

122 A3 " "

122 B1 " "

3E. Thorogummite

	<u>588 A</u>	<u>588 C1</u>	<u>588 C2</u>	<u>G9 C1</u>	<u>G9 C2</u>	<u>G9 D1</u>	<u>G9 D2</u>	<u>504 X</u>	<u>09 E</u>
ThO ₂	33.7	40.8	8.2	8.8	19.3	36.0	22.6	36.5	32.5
U ₃ O ₈	25.5	19.9	64.3	6.7	5.5	6.0	5.5	30.1	14.2
K ₂ O	-	-	-	0.1	2.0	0.5	0.0	-	0.0
CaO	0.8	0.7	5.8	43.2	0.5	1.0	30.8	1.2	2.5
TiO ₂	-	0.8	0.1	0.4	2.1	0.0	0.0	0.1	0.2
PbO	1.9	3.2	2.8	0.0	-	1.1	0.0	2.5	0.0
Fe ₂ O ₃ (t)	0.1	-	-	0.6	4.5	1.8	0.1	-	1.1
Al ₂ O ₃	-	-	-	0.0	8.5	2.2	0.2	-	1.4
SiO ₂	9.2	14.8	13.8	2.4	29.4	13.0	6.2	17.4	15.3
ZrO ₂	-	1.0	0.9	0.0	0.8	0.5	0.3	0.6	9.2
Total	71.2	81.2	95.9	6.2	72.6	62.1	65.7	88.4	76.4

588 A Alaskite, Rössing
588 C1 " "
588 C2 " "
G9 C1 " Goanikontes
G9 C2 " "
G9 D1 " "
G9 D2 " "
504 X " drill core, Valencia 122
09 E Red granite, Otjua 37

3F. Uranophane

	<u>122 A4</u>	<u>122 B2</u>	<u>G9 A</u>	<u>G9 B</u>	<u>09 J</u>	<u>581 A</u>	<u>581 B</u>	<u>461 A</u>
U ₃ O ₈	58.8	71.5	75.6	67.2	58.5	62.6	64.1	60.3
K ₂ O	1.1	0.1	4.2	4.2	1.5	0.1	0.2	-
CaO	3.6	5.9	1.1	1.0	2.2	5.7	5.8	6.7
TiO ₂	0.0	0.0	0.0	0.1	0.0	0.0	0.0	0.0
PbO	0.3	1.5	1.7	-	0.0	1.2	1.1	1.5
Fe ₂ O ₃ (t)	0.3	0.0	0.1	0.0	0.0	0.0	0.0	-
Al ₂ O ₃	8.8	0.1	0.1	-	0.4	0.0	0.0	-
SiO ₂	23.9	13.7	14.3	21.0	30.8	8.5	7.6	23.4
ZrO ₂	0.0	0.5	0.1	1.2	0.0	0.1	0.5	0.5
Total	96.8	93.3	97.2	94.7	93.4	78.2	79.3	92.4

122 A4	Alaskite, Rössing
122 B2	" "
G9 A	" Goanikontes
G9 B	" "
09 J	Red granite, Otjua 37
581 A	Biotite-amphibole schists unit of Khan Formation, Rössing
581 B	" " " "
461 A	Etusis quartzite, Otjua 37.

APPENDIX 4. RB/SR WHOLE ROCK ANALYTICAL RESULTS

(Errors quoted apply to the last two decimal places)

4A. Granodioritic gneiss, 2051 ± 411 Ma. (M.S.W.D. = 58)

<u>Sample No.</u>	<u>Rb</u>	<u>Sr</u>	<u>$^{87}\text{Rb}/^{86}\text{Sr}$</u>	<u>$^{87}\text{Sr}/^{86}\text{Sr}$</u>
qs 1	103	145	2.07	0.77449 ± 07
qs 2	130	135	2.81	0.79285 ± 13
qs 3	122	130	2.74	0.79599 ± 11
qs 4	116	140	2.41	0.77986 ± 12
qs 5	118	131	2.63	0.79028 ± 13
qs 6	124	150	2.41	0.78367 ± 07
qs 7	123	133	2.70	0.79225 ± 36
qs 8	107	125	2.49	0.77999 ± 08
qs 10	115	128	2.62	0.78494 ± 06
qs 11	116	132	2.56	0.78364 ± 08
qs 12	98	147	1.94	0.76689 ± 03

4B. Stinkbank Salem granite. 601 ± 79 Ma. (M.S.W.D. = 5.11)

<u>Sample No.</u>	<u>Rb</u>	<u>Sr</u>	<u>$^{87}\text{Rb}/^{86}\text{Sr}$</u>	<u>$^{87}\text{Sr}/^{86}\text{Sr}$</u>
1S1	207	121	4.96	0.75350 ± 05
1S2	191	118	4.70	0.75139 ± 05
1S3	197	121	4.74	0.75008 ± 05
1S4	173	88	5.72	0.75773 ± 15
1S5	214	115	5.42	0.75689 ± 10
1S6	218	108	5.88	0.76152 ± 10
1S7	239	110	6.36	0.76447 ± 04
1S8	226	105	6.25	0.76366 ± 06
1S9	189	101	5.47	0.75955 ± 19
1S10	202	108	5.44	0.75703 ± 08
1S11	209	114	5.34	0.75655 ± 09
1S12	200	121	4.78	0.75045 ± 08

4C. Valencia Salem granite, 711 ± 199 Ma.; initial $^{87}\text{Sr}/^{86}\text{Sr}$ ratio
= 0.705 ± 0.009 (M.S.W.D. = 2.44)

V1	206	203	2.95	0.73443 ± 05
V2	207	195	3.08	0.73646 ± 14
V3	191	194	2.86	0.73422 ± 08
V4	206	194	3.09	0.73582 ± 05
V5	216	197	3.18	0.73795 ± 08
V6	204	192	3.08	0.73645 ± 05
V8	210	191	3.18	0.73638 ± 11
V9	217	202	3.12	0.73621 ± 08
V10	203	197	3.00	0.73573 ± 09
V11	199	200	2.89	0.73431 ± 06

4D. Otjua red granite and metasediment(i) Otjua red granite, 516 ± 23 Ma. (M.S.W.D. = 0.87)

<u>Sample No.</u>	<u>Rb</u>	<u>Sr</u>	<u>$^{87}\text{Rb}/^{86}\text{Sr}$</u>	<u>$^{87}\text{Sr}/^{86}\text{Sr}$</u>
03	365	77	13.84	0.82262 ± 04
04	385	78	14.39	0.82619 ± 63
05	274	77	10.36	0.79643 ± 23
06	270	80	9.87	0.79397 ± 09
07	251	52	14.15	0.82573 ± 17
08	268	56	13.90	0.82370 ± 07
09	244	48	14.87	0.83046 ± 06
010	258	52	14.58	0.82930 ± 17
011	205	57	10.42	0.79927 ± 06
012	250	50	14.66	0.82956 ± 07

(ii) Etusis quartzite on Otjua 37

013	131	56	6.80	0.78892 ± 05
014	116	42	8.09	0.80074 ± 11
015	149	30	14.48	0.89805 ± 05

4E. Namibfontein red granite

N1	306	111	8.06	0.76891 ± 08
N2	313	141	6.44	0.76871 ± 14
N3	319	141	6.59	0.77133 ± 05
N4	315	146	6.28	0.76924 ± 01
N6	252	121	6.08	0.75946 ± 18
N7	255	155	4.81	0.78937 ± 08
N8	270	123	6.43	0.77065 ± 14
N9	265	121	6.37	0.76860 ± 04

4F. Stinkbank leucogranite, 484 ± 25 Ma. (M.S.W.D. = 5.95)

<u>Sample No.</u>	<u>Rb</u>	<u>Sr</u>	<u>$^{87}\text{Rb}/^{86}\text{Sr}$</u>	<u>$^{87}\text{Sr}/^{86}\text{Sr}$</u>
S1	380	66	16.83	0.85592 ± 24
S2	383	58	19.50	0.87584 ± 09
S3	345	90	11.22	0.81749 ± 08
S4	343	71	14.13	0.83656 ± 09
S5	380	61	18.17	0.86318 ± 06
S6	327	65	14.65	0.84056 ± 09
S7	349	73	14.02	0.83412 ± 03
S8	305	58	15.47	0.84549 ± 12

4G. Ida dome alaskite, 542 ± 33 Ma. (M.S.W.D. = 98.32)

1/1	337	81	12.20	0.80950 ± 12
1/2	243	114	6.21	0.77243 ± 08
2	224	28	23.85	0.91441 ± 05
3/2	197	55	10.41	0.80626 ± 05
4/1	274	49	16.42	0.85161 ± 06
4/2	207	132	4.56	0.75750 ± 08
5/1	204	61	9.76	0.79911 ± 10
5/2	250	29	25.84	0.91844 ± 15
6/1	116	34	10.13	0.80931 ± 09
6/2	203	37	16.34	0.85127 ± 05

4H. Goanikontes alaskite and metasediment(i) Alaskites

<u>Sample No.</u>	<u>Rb</u>	<u>Sr</u>	<u>$^{87}\text{Rb}/^{86}\text{Sr}$</u>	<u>$^{87}\text{Sr}/^{86}\text{Sr}$</u>
G0	440	164	7.81	0.78690 \pm 06
G1	288	90	9.35	0.80120 \pm 05
G2	256	104	7.16	0.78698 \pm 04
G3	359	105	9.96	0.80650 \pm 04
G4	294	99	8.69	0.79834 \pm 09
G5	328	106	9.03	0.79885 \pm 04
G6	398	207	5.60	0.76512 \pm 06
G7	402	195	6.00	0.76896 \pm 03
G8	252	83	8.83	0.80797 \pm 03
G9	335	84	11.74	0.82439 \pm 20
G10	191	98	5.69	0.77530 \pm 05
182	387	104	10.83	0.81260 \pm 04
183	314	110	8.33	0.78558 \pm 01

(ii) Khan metasediments

G11	299	149	5.82	0.77219 \pm 09
G12	284	223	3.70	0.75224 \pm 04
G13	302	109	8.08	0.79724 \pm 13

4I. Valencia alaskite

V11	230	28	24.54	0.89565 \pm 08
V21	287	28	30.27	0.93718 \pm 16
V31	149	60	7.19	0.77343 \pm 10
V41	271	72	11.07	0.79808 \pm 05
507	185	179	3.01	0.74391 \pm 05

APPENDIX 5. MAJOR AND TRACE ELEMENT ANALYSES AND NORMATIVE COMPOSITIONS

	<u>N1</u>	<u>N3</u>	<u>N6</u>	<u>V3</u>	<u>V8</u>	<u>V10</u>
SiO ₂	70.88	70.30	70.90	63.80	64.96	63.74
TiO ₂	0.33	0.32	0.33	0.91	0.85	0.96
Al ₂ O ₃	13.84	14.05	14.13	15.49	15.45	15.84
Fe ₂ O ₃ (t)	2.29	2.28	2.38	5.67	5.36	5.73
MnO	0.04	0.04	0.05	0.10	0.10	0.11
MgO	0.82	0.75	0.82	2.17	2.07	2.23
CaO	1.36	1.01	1.37	3.43	3.06	3.67
K ₂ O	6.08	6.78	5.93	3.88	4.48	4.10
P ₂ O ₅	0.17	0.17	0.16	0.28	0.27	0.29
Na ₂ O	3.35	3.03	3.33	4.01	3.84	3.98
L.O.I.	nil	nil	0.16	1.16	0.66	1.00
Total	99.12	98.73	99.40	99.74	100.44	100.66
Q	24.25	23.38	24.55	15.08	15.76	13.91
Or	35.69	40.07	35.04	22.93	26.47	24.23
Ab	28.35	25.64	28.18	33.93	32.49	33.67
An	4.89	3.90	5.75	12.81	11.69	13.25
C	-	0.30	0.13	-	-	-
Di	0.61	-	-	1.93	1.40	2.48
Hy	2.91	3.06	3.31	7.25	7.14	7.15
Mt	1.25	1.24	1.29	3.08	2.91	3.12
Il	0.63	0.61	0.63	1.73	1.61	1.84
Ap	0.39	0.39	0.37	0.65	0.63	0.67
Total	98.97	98.59	99.25	99.39	100.10	100.32
U	3.5	2.6	3.5	2.6	2.3	2.3
Th	68.4	59.1	82.3	24.4	25.0	23.8
Sm	11.8	8.8	14.7	12.0	9.9	11.9

APPENDIX 5 CONTINUED

	<u>S1</u>	<u>S2</u>	<u>S3</u>	<u>4/2</u>	<u>5/2</u>	<u>6/2</u>
SiO ₂	70.52	71.26	71.49	74.41	72.89	73.44
TiO ₂	0.28	0.41	0.34	0.01	0.02	0.01
Al ₂ O ₃	14.08	14.11	14.54	14.46	14.41	14.69
Fe ₂ O ₃ (t)	2.37	3.30	2.66	0.46	1.18	0.50
MnO	0.02	0.04	0.03	0.01	0.01	0.01
MgO	0.80	0.95	0.87	0.36	0.35	0.40
CaO	1.03	1.01	1.31	0.89	0.82	1.17
K ₂ O	6.09	5.56	5.26	5.25	6.49	5.05
P ₂ O ₅	0.15	0.18	0.19	0.11	0.11	0.09
Na ₂ O	3.39	3.55	3.83	4.55	3.99	4.67
L.O.I.	nil	1.16	2.50	1.83	2.00	1.66
Total	98.73	100.73	100.52	100.51	100.27	100.03
Q	23.93	25.45	24.87	25.61	22.73	24.15
Or	35.99	32.86	31.08	31.02	38.35	29.84
Ab	28.69	30.04	32.41	38.50	33.76	39.52
An	4.13	3.84	5.26	3.53	2.24	4.21
C	0.40	0.85	0.62	-	-	-
Di	-	-	-	0.14	0.915	0.81
Hy	3.28	4.15	3.59	1.17	1.26	0.77
Mt	1.29	1.79	1.45	0.25	0.64	0.27
Il	0.53	0.78	0.65	0.02	0.04	0.02
Ap	0.35	0.42	0.44	0.26	0.26	0.21
Total	98.59	100.18	100.37	100.50	100.20	100.00
U	11.0	1.9	8.6	4.8	21.6	76.4
Th	63.6	6.4	71.2	8.5	5.9	6.4
Sm	13.9	6.1	15.3	3.9	1.1	2.6

APPENDIX 5 CONTINUED

	<u>1s 2</u>	<u>1s 7</u>	<u>1s 9</u>	<u>01</u>	<u>02</u>	<u>09</u>
SiO ₂	67.13	70.32	74.29	74.00	74.01	74.52
TiO ₂	0.26	0.27	0.24	0.11	0.08	0.08
Al ₂ O ₃	13.81	14.59	14.33	14.45	13.78	13.19
Fe ₂ O ₃ (t)	2.10	2.28	2.24	1.09	1.35	0.94
MnO	0.04	0.04	0.04	0.02	0.02	0.02
MgO	0.74	1.44	0.75	0.48	0.46	0.36
CaO	1.58	1.48	1.68	0.85	0.70	0.96
K ₂ O	4.90	5.43	4.19	5.94	5.94	5.48
P ₂ O ₅	0.11	0.14	0.10	0.09	0.09	0.08
Na ₂ O	3.58	3.68	4.00	3.97	3.51	3.45
L.O.I.	1.50	1.33	2.33	1.83	0.83	nil
Total	100.25	99.67	101.86	101.00	99.94	99.08
Q	28.85	22.63	29.96	25.60	28.53	30.85
Or	28.96	32.09	24.76	35.10	35.10	32.38
Ab	30.29	31.14	33.85	33.59	29.70	29.19
An	7.12	6.43	7.68	3.63	2.89	4.24
C	0.01	0.30	0.40	0.16	0.52	0.03
Di	-	-	-	-	-	-
Hy	3.01	4.86	3.17	1.84	2.03	1.48
Mt	1.14	1.24	1.22	0.59	0.73	0.51
Il	0.49	0.51	0.46	0.21	0.15	0.15
Ap	0.26	0.32	0.23	0.21	0.21	0.19
Total	100.13	99.52	101.73	100.93	99.86	99.02
U	64.5	5.3	7.2	47.9	13.0	112.6
Th	20.9	21.3	19.3	41.3	35.6	28.9
Sm	4.1	5.4	4.2	6.0	5.0	5.2

APPENDIX 5 CONTINUED

	<u>G1</u>	<u>G2</u>	<u>G5</u>	<u>G6</u>	<u>G8</u>	<u>G9</u>
SiO ₂	75.34	72.02	74.56	73.12	73.64	73.95
TiO ₂	0.03	0.10	0.01	0.02	0.05	0.06
Al ₂ O ₃	13.41	15.64	14.77	14.19	13.87	13.55
Fe ₂ O ₃ (t)	0.39	0.86	0.35	0.83	0.44	0.46
MnO	0.01	0.03	0.02	0.04	0.02	0.01
MgO	0.29	0.61	0.21	0.16	0.48	0.46
CaO	1.25	2.35	1.48	0.50	1.51	0.90
K ₂ O	6.35	5.17	7.05	9.40	5.70	7.73
P ₂ O ₅	0.06	0.09	0.11	0.06	0.08	0.08
Na ₂ O	2.52	3.38	2.86	1.98	3.16	2.46
L.O.I.	0.65	nil	0.06	0.22	1.00	2.83
Total	99.65	100.25	101.42	100.30	98.94	99.66
Q	33.33	26.63	27.65	24.20	29.64	27.74
Or	37.52	30.55	41.66	55.55	33.68	45.68
Ab	21.32	28.60	24.20	16.75	26.74	20.82
An	5.81	11.12	6.62	2.07	6.83	3.10
C	0.26	0.41	0.01	-	-	-
Di	-	-	-	0.02	0.11	0.67
Hy	0.97	2.03	0.80	1.03	1.39	1.08
Mt	0.21	0.47	0.19	0.45	0.24	0.25
Il	0.06	0.19	0.02	0.04	0.10	0.11
Ap	0.14	0.21	0.26	0.14	0.19	0.19
Total	99.62	100.21	101.41	100.25	98.92	99.64
U	-	-	-	206.7	54.7	150.9
Th	-	-	-	21.4	37.7	43.4
Sm	-	-	-	4.8	2.6	4.2

APPENDIX 5 CONTINUED

	<u>V11</u>	<u>V31</u>	<u>507</u>	<u>V21</u>	<u>V41</u>	<u>N7</u>	<u>S4</u>	<u>06</u>
SiO ₂	73.79	73.23	72.91	-	-	-	-	-
TiO ₂	0.09	0.05	0.17	-	-	-	-	-
Al ₂ O ₃	13.21	13.56	13.92	-	-	-	-	-
Fe ₂ O ₃ (t)	1.11	0.62	1.31	-	-	-	-	-
MnO	0.02	0.01	0.04	-	-	-	-	-
MgO	0.49	0.39	0.78	-	-	-	-	-
CaO	1.07	0.97	1.24	-	-	-	-	-
K ₂ O	4.35	4.77	5.16	-	-	-	-	-
P ₂ O ₅	0.11	0.15	0.15	-	-	-	-	-
Na ₂ O	4.12	4.00	3.14	-	-	-	-	-
L.O.I.	2.66	1.50	1.83	-	-	-	-	-
Total	98.36	97.95	98.82	-	-	-	-	-
Q	30.15	28.53	31.17	-	-	-	-	-
Or	25.71	29.37	30.49	-	-	-	-	-
Ab	34.86	33.85	26.57	-	-	-	-	-
An	4.59	3.83	5.17	-	-	-	-	-
C	0.04	0.20	1.27	-	-	-	-	-
Di	-	-	-	-	-	-	-	-
Hy	1.91	1.36	2.68	-	-	-	-	-
Mt	0.60	0.34	0.71	-	-	-	-	-
Il	0.17	0.10	0.32	-	-	-	-	-
Ap	0.26	0.35	0.35	-	-	-	-	-
Total	98.29	97.93	98.73	-	-	-	-	-
U	22.2	4.8	22.4	17.9	5.3	2.8	8.6	25.3
Th	76.2	6.9	39.3	58.6	7.7	54.0	63.1	42.1
Sm	6.8	1.1	7.6	5.6	1.1	7.2	13.9	6.1

APPENDIX 5 CONTINUED

Valencia alaskites: (for Rb/Sr data see Hawkesworth et al., 1981)

	<u>26/59 140m</u>	<u>26/59 217m</u>	<u>26/69 86m</u>	<u>26/69 133m</u>	<u>26/69 137m</u>	<u>DG 64</u>	<u>DG 66</u>
U	22.6	28.5	38.4	38.8	25.0	49.9	83.2
Th	4.8	34.3	11.6	41.3	18.2	14.2	58.6
Sm	0.7	6.4	1.4	6.9	3.2	1.7	13.0

Rössing alaskites: (for Rb/Sr data see Hawkesworth et al., 1981)

	<u>772004</u>	<u>772006</u>
U	390.2	68.8
Th	57.0	12.7
Sm	10.6	2.5

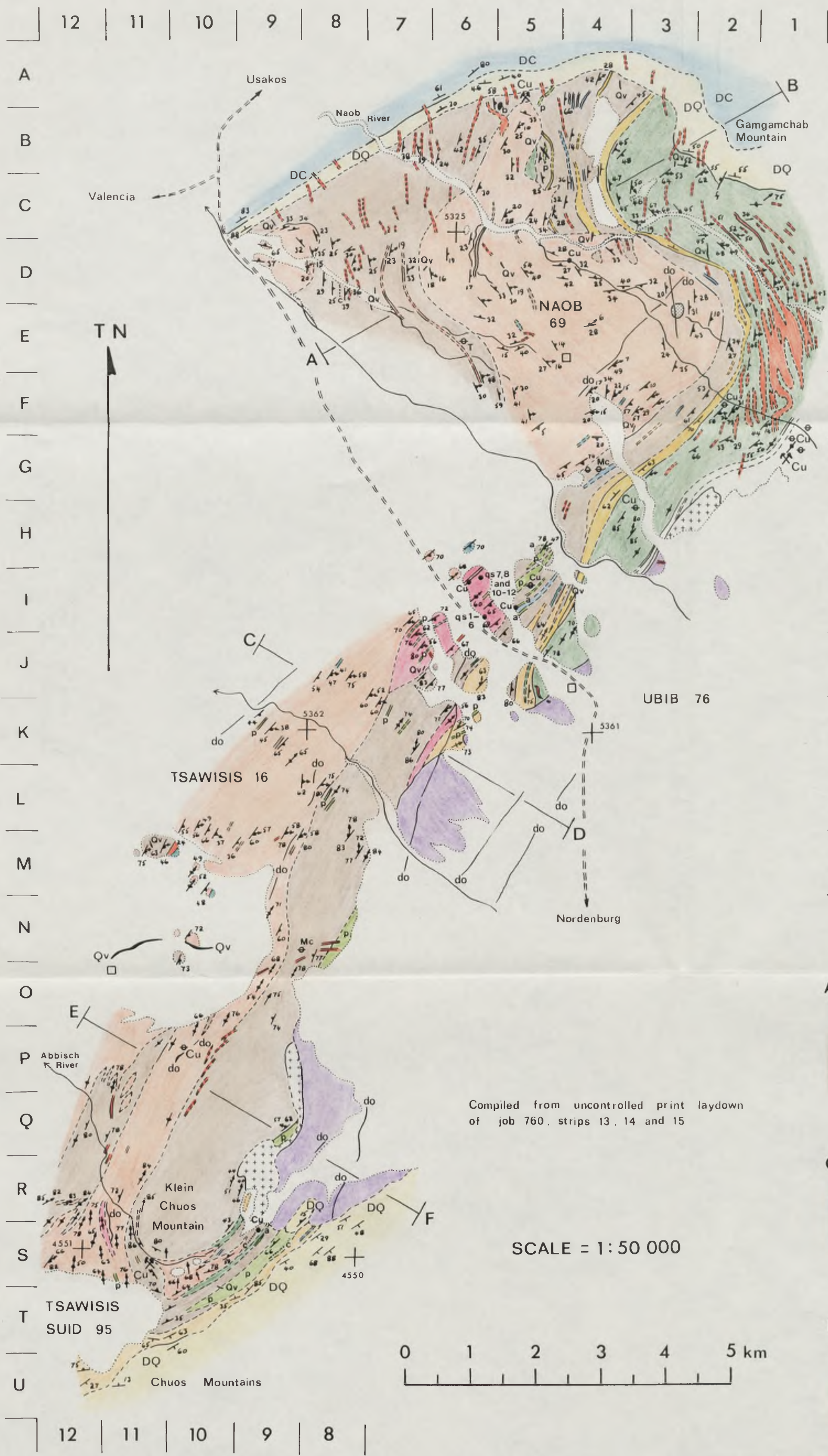
Salem granite near Swakopmund: (for Rb/Sr data see Hawkesworth et al., 1981)

	<u>SM1</u>	<u>SM3</u>	<u>SM5</u>	<u>SM6</u>
U	6.7	9.1	12.0	7.3
Th	30.3	28.7	25.3	26.6
Sm	9.6	8.7	8.4	8.2

Salem granite near Otjosondjou: (for major elements and other trace elements see Miller, 1973).

	<u>RM584</u>	<u>RM596</u>	<u>RM598</u>
U	1.5	3.9	3.5
Th	6.3	14.0	36.3
Sm	8.8	15.5	13.9

FOLDER 1 — GEOLOGICAL MAP OF PART OF THE ABBABIS INLIER

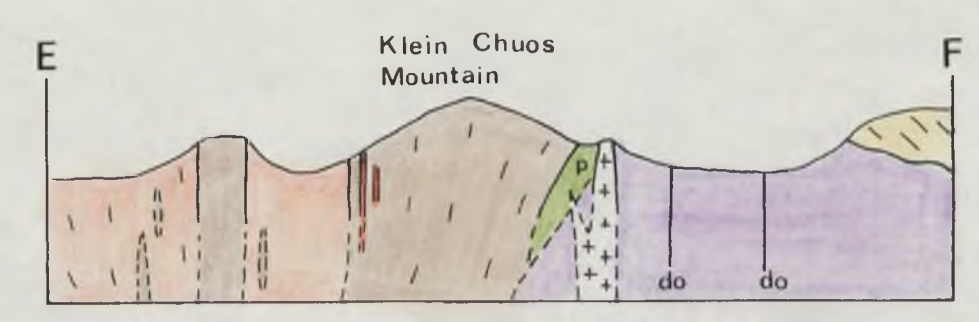
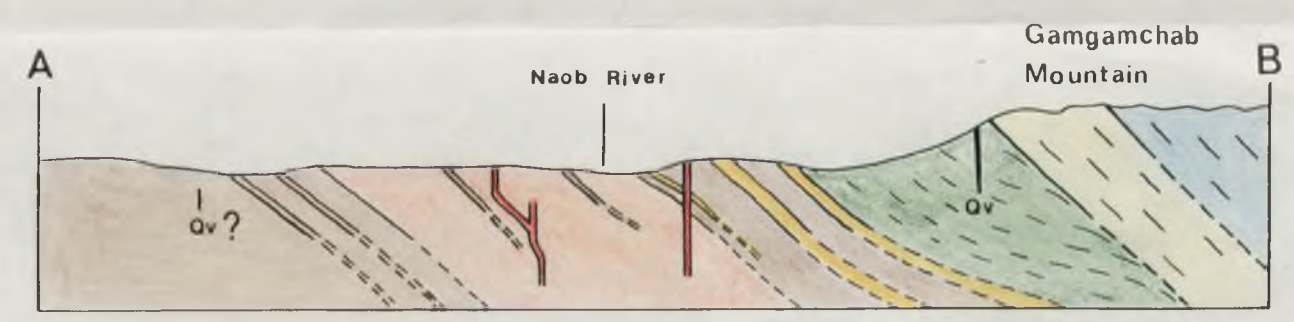
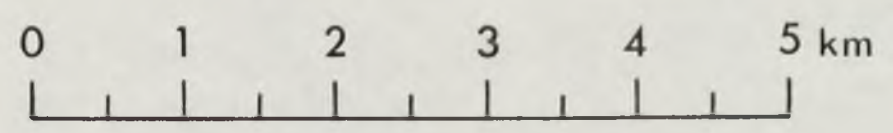


LEGEND

- | | | | |
|---|--|---|--------------------|
| A | | SOIL, SAND, CALCRETE ETC. | RECENT |
| | | DOLERITE | KARROO |
| B | | BRECCIA | |
| C | | PEGMATITE | DAMARAN GRANITOIDS |
| | | MUSCOVITE-BEARING LEUCOGRANITE | |
| | | GARNET-BEARING LEUCOGRANITE | |
| | | SALEM DIORITE | |
| D | | MARBLE AND CALC SILICATE | DAMARA SEQUENCE |
| | | QUARTZITE | |
| E | | LEUCOCRATIC GNEISS AND AUGEN GNEISS | ABBABIS GNEISSES |
| | | GRANODIORITIC GNEISS | |
| F | | AGGLOMERATE | ABBABIS FORMATION |
| | | PYROXENITE AND AMPHIBOLITE | |
| | | META-BASALT | |
| | | SCHIST | |
| | | CALC SILICATE | |
| | | MARBLE | |
| | | FINE GRAINED QUARTZITE | |
| | | COARSE GRAINED QUARTZITE | |
| | | CONGLOMERATE | |
| H | | DIP OF BEDDING | |
| | | VERTICAL BEDDING | |
| I | | DIP OF S ₂ FOLIATION | |
| | | VERTICAL S ₂ FOLIATION | |
| | | PLUNGE OF L ₂ OR EARLIER LINEATION | |
| J | | GEOLOGICAL BOUNDARY | |
| | | INFERRED GEOLOGICAL BOUNDARY | |
| | | OUTCROP BOUNDARY | |
| | | FAULT, TICK ON DOWNTHROWN SIDE | |
| K | | ABANDONED COPPER MINE | |
| | | EXPLORATION PIT FOR COPPER | |
| | | COPPER SHOWING | |
| | | EXPLORATION PIT FOR MICA | |
| | | EXPLORATION PIT FOR TALC | |
| L | | QUARTZ VEIN | |
| | | RIVER | |
| | | ROAD | |
| | | FARMHOUSE | |
| M | | PRINCIPAL POINT OF PHOTO. NO. 5325 | |
| | | WHOLE ROCK SAMPLE SITE | |

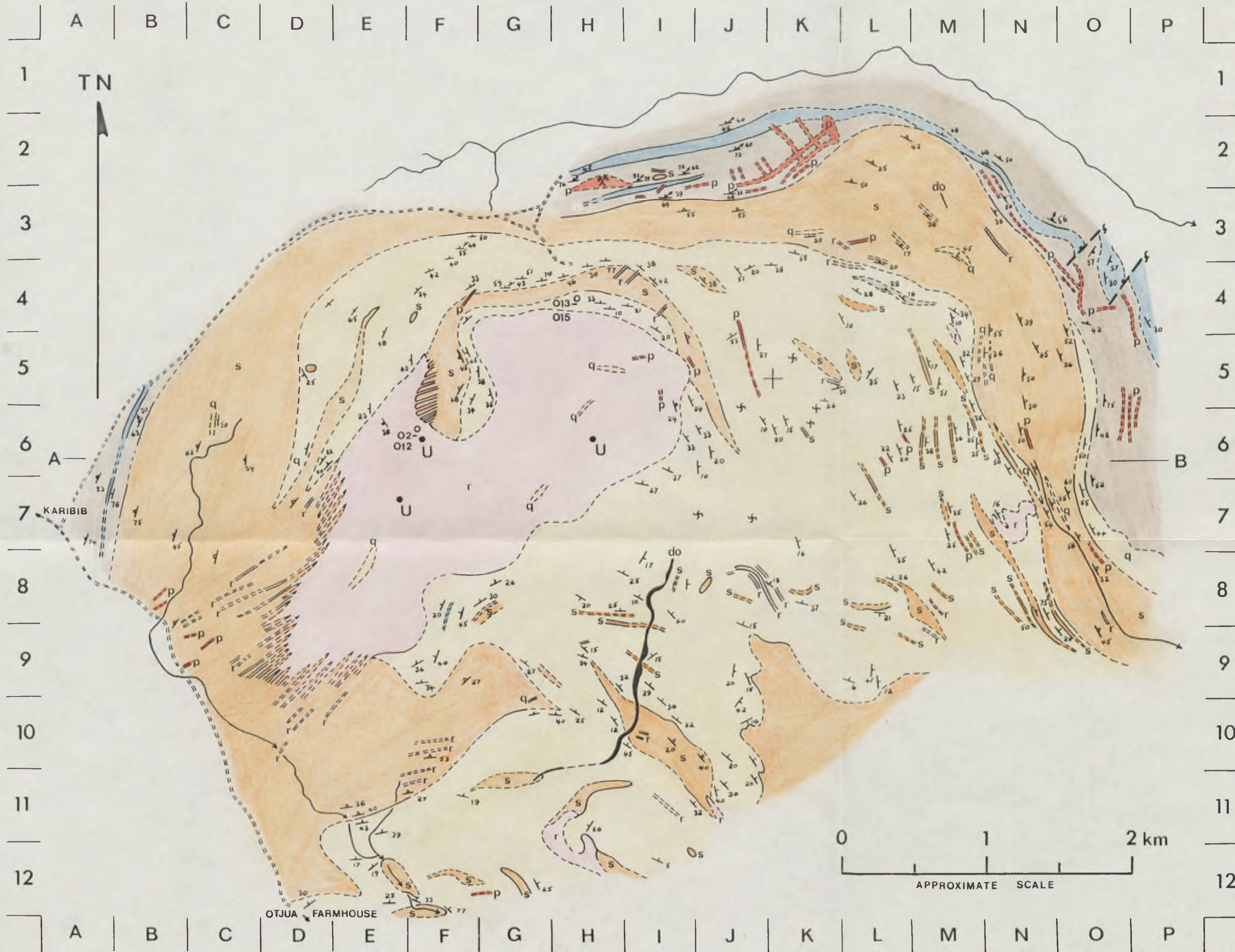
Compiled from uncontrolled print laydown of job 760, strips 13, 14 and 15

SCALE = 1:50 000



Vertical scale = horizontal scale in all sections

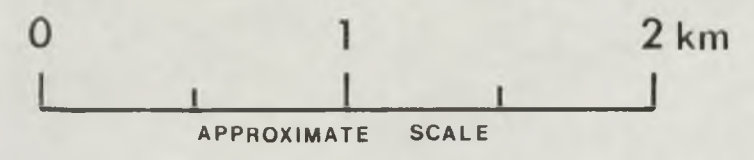
FOLDER 2 — GEOLOGICAL MAP OF PART OF OTJUA 37



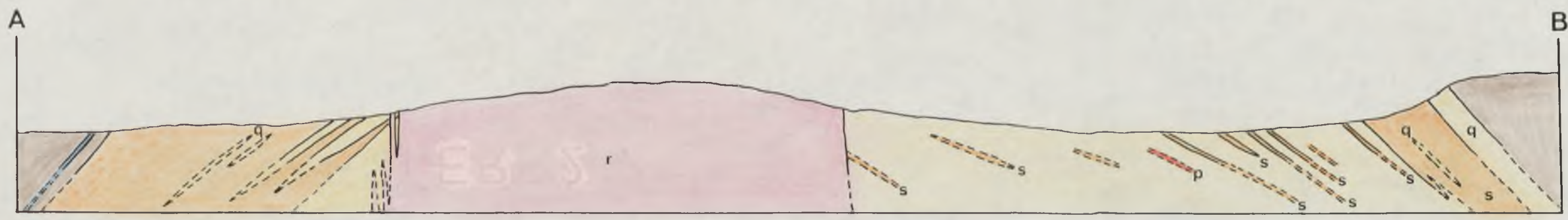
LEGEND

- | | | | |
|--|---------------|---|--------------------|
| | DOLERITE | | KARROO |
| | PEGMATITE | } | DAMARAN GRANITOIDS |
| | RED GRANITE | | |
| | SALEM GRANITE | | |
| | MARBLE | } | DAMARA SEQUENCE |
| | SCHIST | | |
| | CALC SILICATE | } | ETUSIS FORMATION |
| | QUARTZITE | | |
-
- DIP OF BEDDING
 - VERTICAL BEDDING
 - SUB-HORIZONTAL BEDDING
 - DIP OF S₂ FOLIATION
 - PLUNGE OF L₂ LINEATION
 - DIP OF S₃ FOLIATION
 - DIP OF IGNEOUS FLOW FABRIC
 - FAULT, TICK ON DOWNTHROWN SIDE
 - GEOLOGICAL BOUNDARY
 - INFERRED GEOLOGICAL BOUNDARY
 - BECKER'S LITHIUM MINE
 - SECONDARY URANIUM MINERALIZATION AND GROUND RADIOMETRIC ANOMALY
 - RIVER
 - FARM TRACK
 - PRINCIPAL POINT OF PHOTOGRAPH
 - WHOLE ROCK SAMPLE SITE

Compiled from X2 enlargement of photo. no. 0656, strip 7, job 578



APPROXIMATE SCALE =
1:25 000



Vertical scale = horizontal scale

FOLDER 3 — GEOLOGICAL MAP OF PART OF GOANIKONTES



- ### LEGEND
- SOIL, SAND, CALCRETE, ETC. RECENT
 - DOLERITE KARROO
 - MIXTITE
 - MARBLE
 - QUARTZITE
 - SCHIST
 - MARBLE
 - QUARTZITE
 - GNEISS, SCHIST AND CALC SILICATE
 - AMPHIBOLITE
 - GNEISS
 - SCHIST
 - QUARTZITE
- CHUOS FORMATION

ROSSING FORMATION

KHAN FORMATION

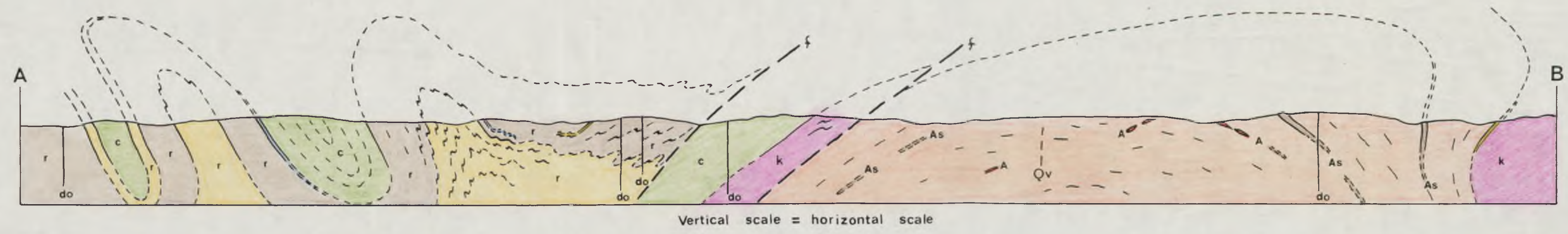
DAMARA SEQUENCE

ABBABIS GNEISS

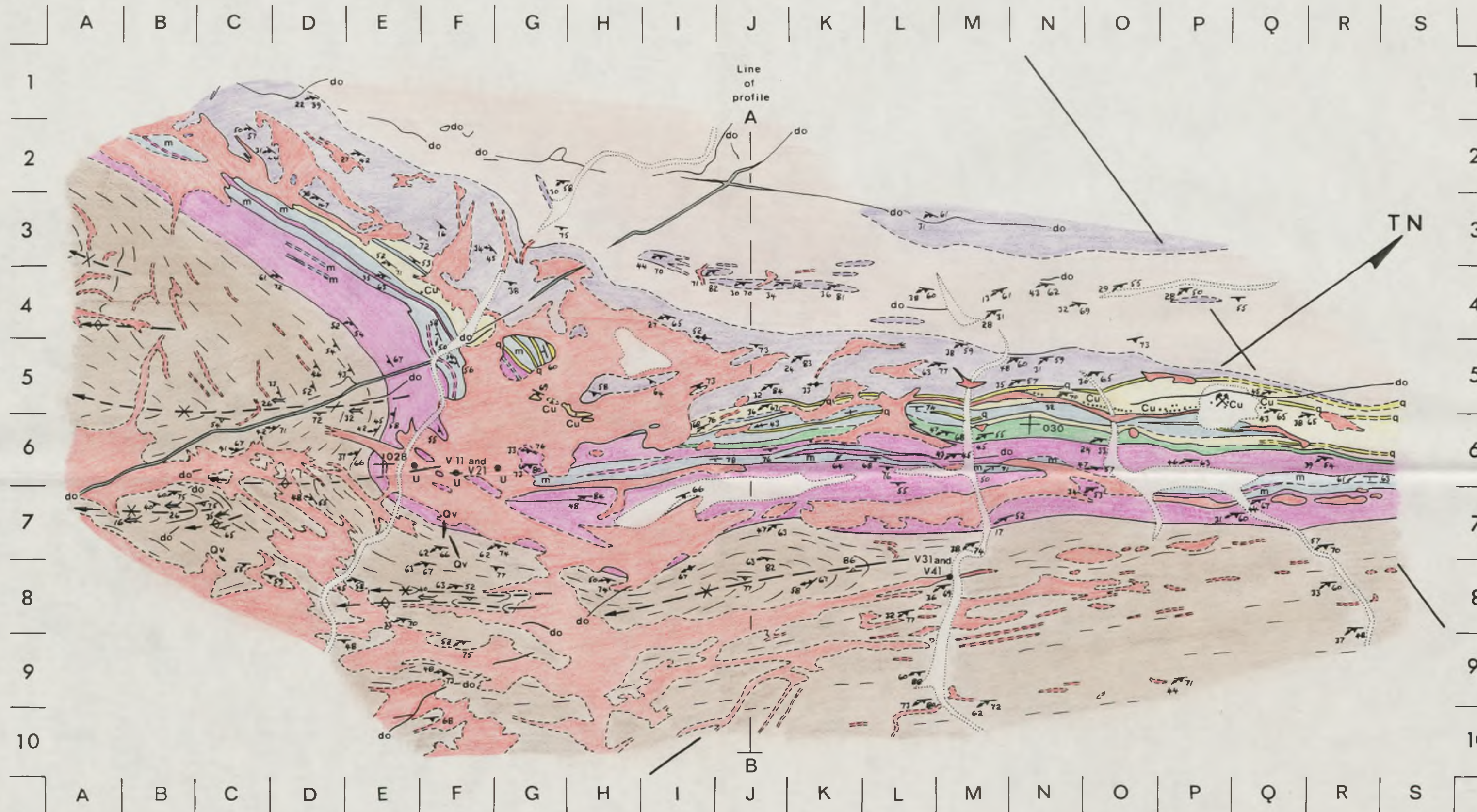
ABBABIS FORMATION
- DIP OF BEDDING
 - DIP OF S₂ FOLIATION
 - VERTICAL S₂ FOLIATION
 - SUB-HORIZONTAL S₂ FOLIATION
 - PLUNGE OF L₃ OR EARLIER LINEATION
 - PLUNGE OF F₃ FOLD AXIS
 - PLUNGE OF F₄ FOLD AXIS
 - F₄ ANTICLINAL AXIS
 - F₄ SYNCLINAL AXIS
 - GEOLOGICAL BOUNDARY
 - INFERRED GEOLOGICAL BOUNDARY
 - OUTCROP BOUNDARY
 - FAULT
 - URANIUM MINERALIZATION
 - QUARTZ VEIN
 - TRACK
 - FARMHOUSE
 - EXPLORATION CAMP
 - PRINCIPAL POINT OF PHOTOGRAPH
 - FIDUCIAL MARK OF PHOTOGRAPH
 - SITE OF WHOLE ROCK SAMPLES G0-G13, 182 AND 183

Compiled from X2 enlargement of photo. no. 4840, strip 21, job 760

APPROXIMATE SCALE = 1 : 25 000

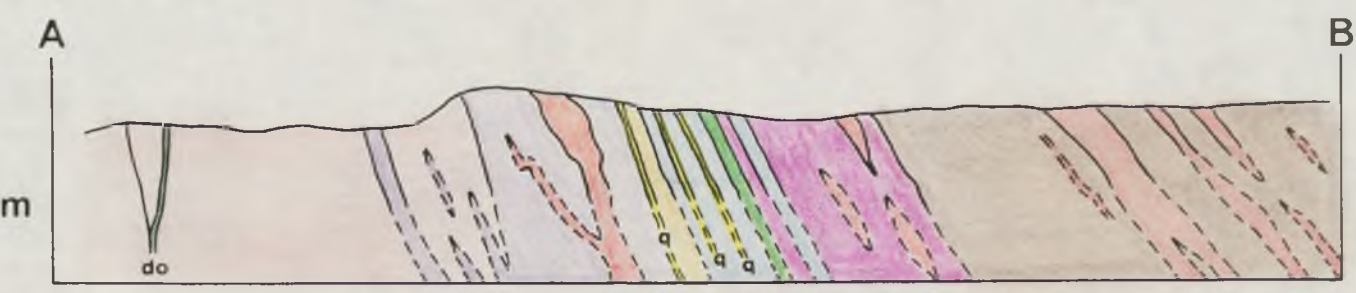
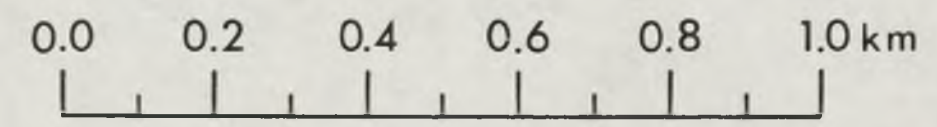


FOLDER 4 — GEOLOGICAL MAP OF PART OF VALENCIA 122



LEGEND

- | | | |
|--|----------------------------------|--------------------|
| | SOIL, SAND, CALCRETE ETC. | RECENT |
| | DOLERITE | KARROO |
| | ALASKITE | DAMARAN GRANITOIDS |
| | SALEM GRANITE | |
| | BIOTITE-ORTHOCLASE SCHIST | DAMARA SEQUENCE |
| | MARBLE | |
| | MIXTITE | |
| | SCHIST | KUISEB FORMATION |
| | MARBLE | |
| | QUARTZITE | KARIBIB FORMATION |
| | GNEISS, SCHIST AND CALC SILICATE | |
| | | CHUOS FORMATION |
| | | ROSSING FORMATION |
| | | KHAN FORMATION |
-
- DIP OF BEDDING
 - VERTICAL BEDDING
 - DIP OF S₂ FOLIATION
 - VERTICAL S₂ FOLIATION
 - STRIKE OF S₂ FOLIATION
 - DIP OF S₃ FOLIATION
 - PLUNGE OF L₃ AND EARLIER LINEATIONS
 - PLUNGE OF F₃ FOLD HINGE
 - F₃ ANTICLINAL AXIS
 - F₃ SYNCLINAL AXIS
 - GEOLOGICAL BOUNDARY
 - INFERRED GEOLOGICAL BOUNDARY
 - OUTCROP BOUNDARY
 - SECONDARY URANIUM MINERALIZATION
 - SECONDARY COPPER MINERALIZATION
 - KAINKAGCHAS COPPER MINE (ABANDONED)
 - EXPLORATION PIT
 - QUARTZ VEIN
 - PRINCIPAL POINT OF PHOTO. NO. 028
 - WHOLE ROCK SAMPLE SITE

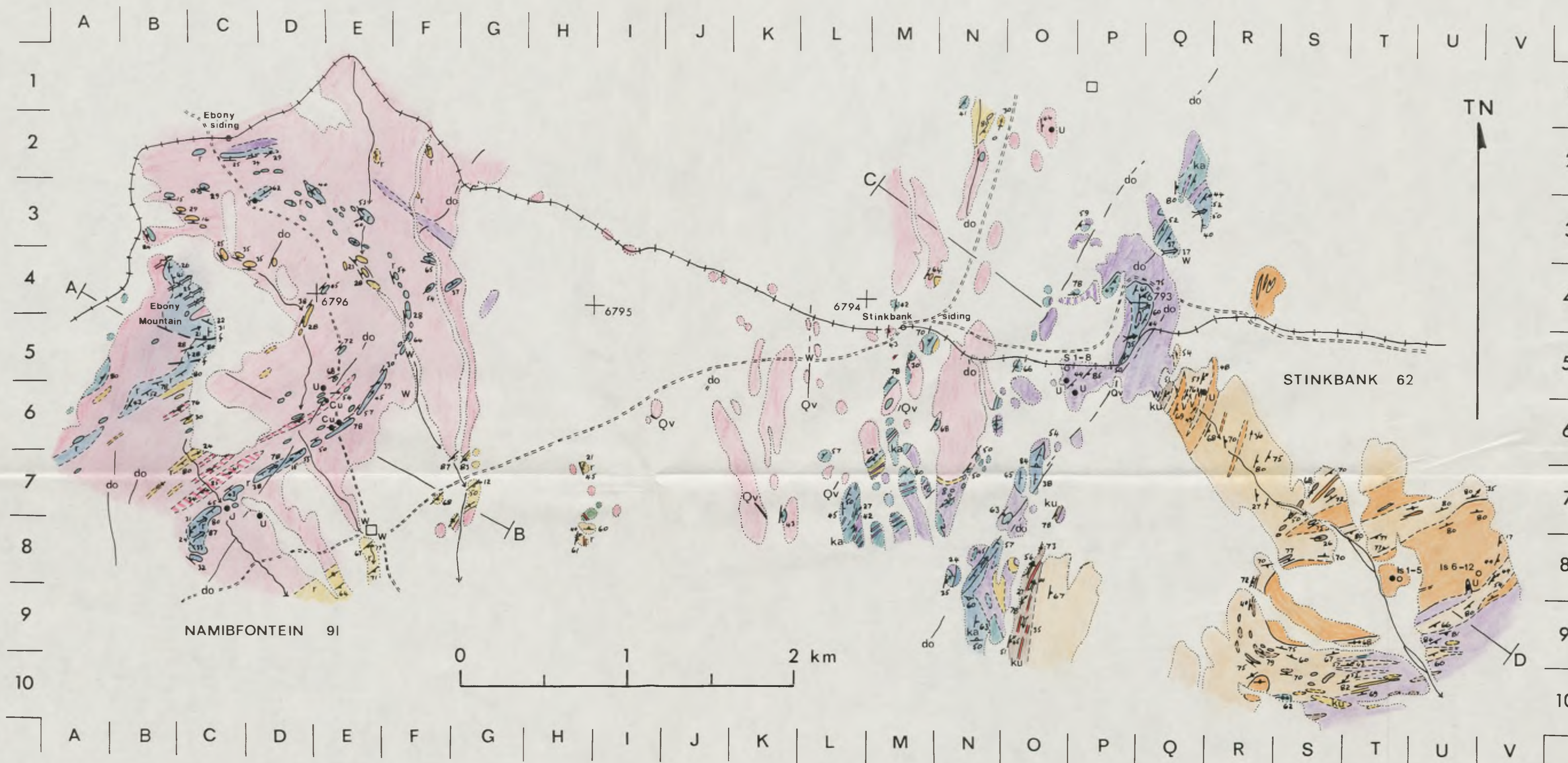


SCALE = 1 : 10 000

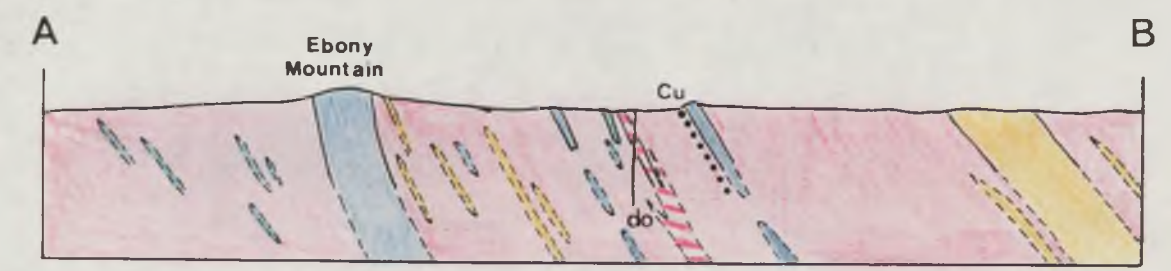
Vertical scale = horizontal scale

Compiled from uncontrolled print laydown of in-house job strip 13

FOLDER 5 — GEOLOGICAL MAP OF PART OF NAMIBFONTEIN 91 AND STINKBANK 62



LEGEND		
[White box]	SOIL, SAND, CALCRETE, ETC.	RECENT
[do box]	DOLERITE	KARROO
[Red box]	RED PEGMATITE	DAMARAN GRANITOIDS
[Pink box]	RED GRANITE	
[Purple box]	RHEOMORPHIC LEUCOGRANITE	
[Light purple box]	LEUCOGRANITE	
[Green box]	GABBRO	
[Orange box]	PRE-F ₂ RED GRANITE	SALEM GRANITE
[Light orange box]	LEUCOCRATIC SALEM GRANITE	
[ku box]	QUARTZITE	KUISEB FORMATION
[ka box]	CALC SILICATE	
[ka box]	BIOTITE SCHIST	KARIBIB FORMATION
[ka box]	MARBLE	
[r box]	CALC SILICATE	ROSSING FORMATION
[r box]	SCHIST AND QUARTZITE	
[r box]	MARBLE	DAMARA SEQUENCE
[r box]	CALC SILICATE	
[Symbol]	DIP OF BEDDING	
[Symbol]	DIP OF S ₂ FOLIATION	
[Symbol]	VERTICAL S ₂ FOLIATION	
[Symbol]	PLUNGE OF L ₂ LINEATION	
[Symbol]	DIP OF S ₃ FOLIATION	
[Symbol]	PLUNGE OF F ₂ FOLD HINGE	
[Symbol]	PLUNGE OF F ₃ FOLD HINGE	
[Symbol]	F ₃ ANTICLINAL AXIS	
[Symbol]	F ₃ SYNCLINAL AXIS	
[Symbol]	DIP OF IGNEOUS FLOW FABRIC	
[Symbol]	GEOLOGICAL BOUNDARY	
[Symbol]	INFERRED GEOLOGICAL BOUNDARY	
[Symbol]	OUTCROP BOUNDARY	
[Symbol]	FAULT TICK ON DOWNTHROWN SIDE	
[Symbol]	SECONDARY URANIUM MINERALIZATION	
[Symbol]	SECONDARY COPPER MINERALIZATION	
[Symbol]	ABANDONED PROSPECTING PIT	
[Symbol]	QUARTZ VEIN	
[Symbol]	RIVER	
[Symbol]	FARM TRACK	
[Symbol]	FARMHOUSE	
[Symbol]	WINDPUMP	
[Symbol]	RAILWAY	
[Symbol]	PRINCIPAL POINT OF PHOTO. NO. 6795	
[Symbol]	WHOLE ROCK SAMPLE SITE	



Vertical scale = horizontal scale in both sections

Compiled from uncontrolled print laydown of job 596, strips 6 and 7

SCALE = 1:42 000